LA-12359-MS
NPR-44

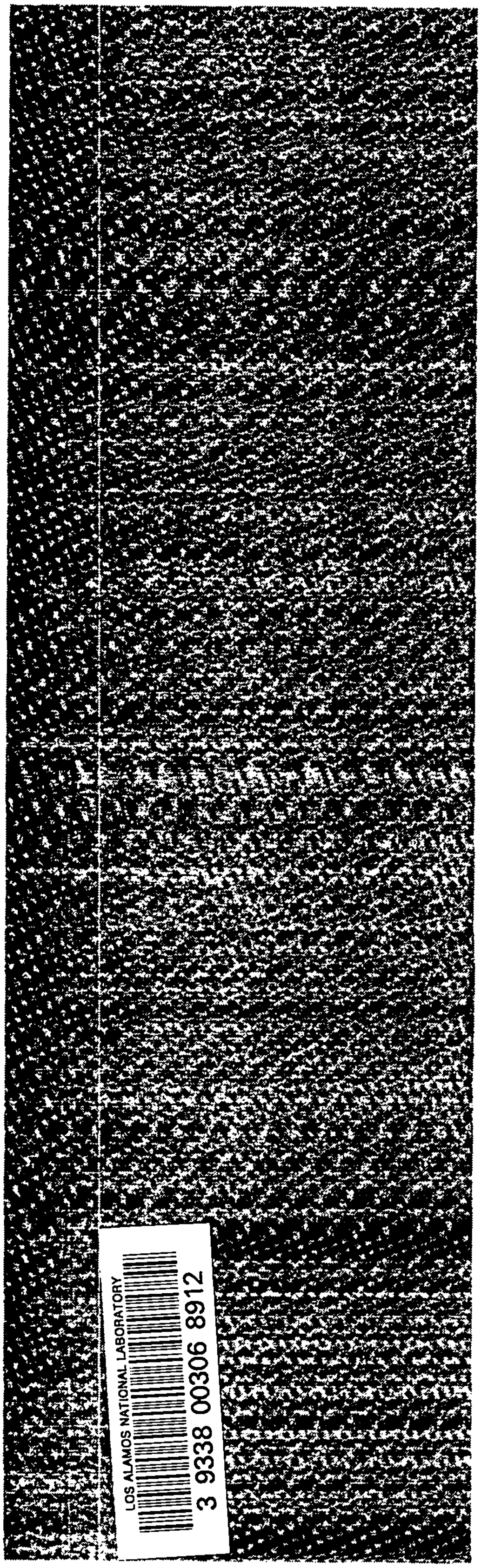

Seismic Buckling Capacity of Unstiffened, Free-Standing Steel Containments

Los Alamos

Los Alamos National Laboratory is operated by the University of California for the United States Department of Energy under contract W-7405-ENG-36.

Edited by Lilly Shelley, MEE Division

An Affirmative Action/Equal Opportunity Employer

LA-12359-MS
NPR-44

UC-731 and UC-706
Issued: July 1992

Seismic Buckling Capacity of Unstiffened, Free-Standing Steel Containments

Charles R. Farrar
Thomas A. Duffey
Peggy A. Goldman
Joel G. Bennett

Los Alamos
Los Alamos National Laboratory
Los Alamos,New Mexico 87545

CONTENTS

FIGURES

TABLES

SEISMIC BUCKLING CAPACITY OF UNSTIFFENED, FREE-STANDING STEEL CONTAINMENTS

by

Charles R. Farrar, Thomas A. Duffey, Peggy A. Goldman, and Joel G. Bennett

ABSTRACT

An investigation of the seismic buckling capacity of two unstiffened, free-standing steel containments is reported. The first structure studied is a proposed next-generation containment whose geometry is driven by the need for a passive cooling mechanism. For the second structure, a survey of commercial nuclear reactor containments was used to develop a generic design indicative of existing unstiffened, free-standing containments. This generic structure is also assumed to be indicative of a smaller scale version of the next-generation, passively cooled containments.

A simple three-degree-of-freedom (3-DOF), axisymmetric model of the containments is analyzed using response spectrum methods to determine the zero-period acceleration that would produce a case of incipient buckling. Then, more refined numerical time-history analyses were performed using the ABAQUS finite element code. The numerical models were subjected to measured earthquake acceleration-time histories and to artificial earthquake acceleration-time histories whose response spectra matched the Reg. Guide 1.60 design spectra, an eastern U.S. site-specific design spectra, and a spectrum that includes soil-structure interaction effects.

The effects of containment construction methods and the effects of the internal negative air pressure on containment buckling are examined; applications of the work presented in this study to the development of a simplified margins assessment method are discussed; and a summary of buckling concerns, which the authors feel have been inadequately addressed in Code Case N-284, is presented. In the conclusion, the level of safety of a proposed next-generation containment design for seismically induced buckling is compared with the level of safety of existing commercial nuclear power plant containments for this failure mode.

I. INTRODUCTION

The passive cooling mechanisms currently being considered for the next generation of nuclear reactors require that the containment shells have a large surface area. It is not desirable to have circumferential ring stiffeners on the exterior of the shells because these stiffeners would impede the flow of air over the shell surface, thus reducing the efficiency of a convective cooling mechanism. It is desirable, however, to keep the thickness of these containments below 4.45 cm (1.75 in.). Thicknesses in excess of 4.45 cm require field heat-treating of the welds, which increases the construction costs of the reactor. Such thin containment shells require careful consideration of elastic buckling in the design and safety review process.

This study investigates the buckling capacity of such a containment subjected to seismic excitations. Also investigated is the buckling capacity of a generic containment whose geometry is indicative of existing unstiffened, free-standing containments and smaller scale passively cooled containments. Two specific topics are examined: (1) the ability to use simple, lumped-mass models and beam theory to accurately predict buckling, and (2) the sensitivity of buckling to the damping that the structure is assumed to exhibit when responding to a seismic excitation.

A current conceptual design configuration for a passively cooled containment structure consists of a thin-walled steel cylindrical vessel with a hemispherical upper steel closure.[1] The lower closure is ellipsoidal in shape and is cast in concrete. The free-standing cylindrical steel vessel is surrounded by a reinforced-concrete shield building. A clearance exists between the shield building and the steel containment structure, and it is assumed here that, when subjected to dynamic loading, the gap between the steel containment and the surrounding concrete shield building is sufficient to prevent any interaction (impact) of these two structures. Based upon a 28.65-m (1128-in.) containment vessel radius and a 4.45-cm wall thickness, the radius-to-thickness ratio (R/t) of this containment is 645. To put the ratio into perspective, a typical soft drink can has an R/t of approximately 260.

Several existing commercial nuclear power plants[2-6] have containments similar in geometry to the containment being proposed for the next-generation containment. Table I summarizes some of the geometric properties of these free-standing, unstiffened steel containments in use today. On the basis of these properties, a generic containment design was developed that has the same general configuration as the next-generation design described above. This hypothetical containment has a radius of 20.00 m (787.5 in.) and a wall thickness of 4.45 cm, resulting in an R/t of 450. The authors feel that, in addition to representing existing containment structures, this geometry will also represent smaller scale versions of the next generation of passively cooled containments.

The question that motivated this study is, "At what earthquake acceleration levels do such containments fail, that is, allow a leak path for radioactive material to the outside environment?" Currently, at an eastern U.S. site,[7] a peak acceleration level of 0.3 g's is being proposed for a next-generation reactor's SSE-level earthquake. Although buckling of the containment does not necessarily imply that a leak path to the outside environment will be provided, failure is conservatively defined to occur when the containment buckles. Given the failure acceleration level, suitable seismic hazard curves can be used to determine the annual probability of exceedance of an earthquake with this peak acceleration level. It can then be determined whether or not the reactor satisfies safety goals for the probability of release of radioactive material to the environment.

Because of the relative stiffnesses of the hemispherical upper closure and the cylindrical-shell section, the buckling behavior of these containment structures is similar to that of a free-standing cylindrical shell with a fixed base. The spherical upper closure acts as a concentrated top mass, in addition to maintaining the circular shape of the top of the shell. Thus, the extensive literature on cylindrical shell buckling is directly applicable to this study.

Table I

GEOMETRIC PROPERTIES OF EXISTING COMMERCIAL NUCLEAR REACTOR CONTAINMENTS[a]

PLANT	RADIUS	HEIGHT OF CYLINDRICAL PORTION	WALL THICKNESS
Waterford No. 3 (Louisiana)	21.3 m (840 in.)	41.1 m (1620 in.)	4.83 cm (1.90 in.)
Davis-Besse (Ohio)	19.8 m (780 in.)	57.3 m (2256 in.)	3.81 cm (1.50 in.)
St. Lucie (Florida)	21.3 m (840 in.)	38.4 m (1512 in.)	4.85 cm (1.91 in.)
Prairie Island (Minnesota)	16.0 m (630 in.)	46.8 m (1842 in.)	3.81 cm (1.50 in.)
Kewaunee (Wisconsin)	16.0 m (630 in.)	47.4 m (1866 in.)	3.81 cm (1.50 in.)
Generic Design	20.0 m (787.5 in.)	40.0 m (1575 in.)	4.45 cm (1.75 in.)

[a] All containments listed have ellipsoid bases embedded in concrete and hemispherical upper closures.

II. PREVIOUS STATIC AND DYNAMIC BUCKLING STUDIES

In 1979 Miller[8] presented an extensive review of metal containment shell buckling design methods. His review is based on a comparison of data from a large number of static buckling tests with theoretical predictions for stiffened and unstiffened shells. Cylindrical shell buckling, as a result of axial loading and external pressure loading, is emphasized in this work, along with limited data on torsional buckling. This work forms the basis for the methods presented in the ASME Boiler and Pressure Vessel Code, Section III, Code Case N-284 (Ref. 9) and accounts for imperfections introduced in the manufacture of shells, at least for small models. No mention of any dynamic buckling data is made in Ref. 8.

The investigation of dynamic buckling has received considerably less attention than that of quasi-static buckling. Buckling of cylindrical shells subjected to pulse loading of high intensity and short duration is reported by Anderson and Lindberg[10] for radial loading and by Lindberg and Herbert[11] for axial impact loading. No results have been reported for shear or torsional pulse loading, nor have pulse buckling investigations considered transient loading of a repetitive nature to be similar to that of seismic loading (these works are limited to single pulses).

Babcock et al.[12] present a complete description of the dynamic buckling of containment shells under time-dependent loading, as well as a proposed experimental/analytical program to address unresolved issues in dynamic buckling analysis. The primary issue addressed was the validity of the commonly used 'freezing-in-time' analysis technique,[13] a method for reducing a dynamic buckling problem to a problem of static buckling.

Results of the proposed buckling program were subsequently reported by Butler et al.[14] In this experimental/analytical program, a polycarbonate scale model of a containment building was mounted on a shake table and excited with scaled earthquake transients and single-frequency harmonic transients to deduce the base excitation levels that cause buckling. The scale model consisted of a cylindrical shell, fixed at its base, with a top-ring mass to simulate the mass of the containment's hemispherical closure. Experimental results were compared with analytical results, employing the 'freezing-in-time' technique with some success. It is important to point out, however, that in the experimental program, the mass of the aluminum ring attached to the top of the cylinder was increased beyond the scaled mass of the hemispherical closure. This distortion artificially lowered the fundamental mode of the cylindrical portion of the containment so that its frequency did not coincide with the shell modes of the cylinder. In fact, as suggested by the authors, it is the interaction of these shell modes with the fundamental shear-bending mode that might invalidate the 'freezing-in-time' technique and result in substantial differences in static and dynamic buckling levels for a given stress level.

Nakamura et al.[15] examined failures that occurred to short cylinders that buckled in shear because of horizontal seismic loads. But the loadings applied to the 20 stainless steel shell models tested were static, and, thus, provided no further insight into the validity of the static ('freezing-in-time') analysis method. In this experimental/analytical paper, somewhat thicker shells (R/t approximately equal to 200) were tested, and the mode of failure was plastic shear buckling. The authors emphasize the need for additional experimental data for other values of R/t. It is noteworthy that the authors believe that buckling behavior, under dynamic loads, is not yet clearly understood.

Kokubo et al,[16] consider static and dynamic buckling over a range of R/t ratios up to 1250. Dynamic buckling experiments were performed on cylindrical shells with added top mass by laterally exciting the shells at the base. The added top mass was selected such that the axial stress in the shell being tested was equal to the axial stress of an actual full-size reactor vessel, that is, the mass was not arbitrarily increased to separate the fundamental shear/bending mode from higher shell modes, as was done in Ref. 14. The initiation of dynamic shear buckling is nearly the same as that of static buckling, independent of the input frequency. However, it is important to note that the lowest shell mode for which results are reported had a frequency of approximately 200 Hz, whereas testing was performed with excitations in the 10- to 60-Hz frequency range (it appears that the fundamental shear-bending mode frequency was approximately 42 Hz). Thus, the shell modes are well above the shear-bending mode. On full-scale containments, the fundamental shear-bending mode and the lowest shell modes are typically intermingled.

Galletly et al.[17] present experimental data on short, steel cylindrical shells with fixed bases subjected to transverse edge shearing loads. They confirm two possible modes of buckling: (1) an axisymmetric bulge that occurs over part of the circumference near the base of the shell because of the axial compression induced by vertical force or moment loading, and (2) a buckling mode caused by transverse shearing forces. The shells they tested are somewhat thicker ($125 < R/t < 190$) than those of interest in this study, and plastic buckling predominates. This work confirms that the shear buckling mode is not as sensitive to imperfections as the axial compression mode is. However, results are limited to static load application only.

Finally, Sauve et al.[18] point out that the 'freezing-in-time' method has not been investigated significantly. They further claim that dynamic buckling differs from static buckling only in that the portion of load-carrying capacity represented by inertia may determine the lowest-energy buckling mode; and that this buckling mode may differ substantially from the lowest-energy static buckling mode. They also mention that dynamic buckling mode shapes are often more localized, and that it is conservative to calculate dynamic buckling loads directly using static analysis. However, it would seem that for dynamic loading over a significant time period, shell modes may be amplified, introducing imperfections and, consequently, lowering buckling loads.

It is clear from the above references that the differences between static and dynamic buckling and the validity of the 'freezing-in-time' analysis method (as currently recommended by the ASME Code) have not been fully investigated and that experimental investigations of dynamic buckling are very limited. The interaction of the shell modes with the buckling mode during dynamic excitation has been identified as a possible cause of reduced buckling capacity, but this phenomenon has not been verified or quantified experimentally. It is clear that although a wide range of static buckling data exist for axially loaded cylindrical shells, data on shear buckling is rather limited, even for static loading.

III. BUCKLING OF CONTAINMENTS: ASME CODE CASE N-284

A. Discussion of Code Case

Based primarily on work by Miller[19] that summarizes the previous experimental buckling results of others, the ASME adopted Code Case N-284. This case presents detailed procedures for the buckling analysis and for the design of metal containment shells.

N-284 is based on the assumption that the internal stress field that controls the buckling of the shell consists of the longitudinal membrane (axial), σ_ϕ, circumferential membrane (hoop), σ_θ, and in-plane shear, $\sigma_{\phi\theta}$, stresses. These are the only three stress components considered in the buckling analyses for cylindrical shells.

For the case of dynamic loading of a cylindrical shell, the stress results from a dynamic shell analysis are screened for the maximum value of the axial compression, hoop compression, and in-plane shear stress at each area of interest in the shell. The maximum value of each is taken together with the other two concurrent stress components to form a set of quasi-static buckling stress components. For each area of interest on the shell, these three sets of quasi-static buckling stress components, which correspond to the three maximum values, are used to investigate the buckling capacity of the shell. N-284 also requires that the results of the dynamic analysis be reviewed for additional sets of "quasi-static" stress components that may represent a more severe condition than those defined above.

N-284 presents interaction curves that provide a means for assessing the buckling capacity of a containment when subjected to a multidimensional state of stress, as described above, and formulas for allowable values of stress components that, when acting individually, will cause buckling. Tests have shown that geometric imperfections can greatly reduce the buckling capacity of a cylindrical shell.[20] To account for the inevitable initial imperfections that will exist in an actual containment structure, "Capacity Reduction" factors are used to reduce allowable buckling stress values. The allowable values are effectively further reduced by an appropriate factor of safety.

N-284 has plastic buckling provisions for cases in which the buckling stress exceeds the yield stress of the material. However, because of the thin containment shell being investigated, buckling will occur when stresses are well below the yield stress. N-284 also provides for the occurrence of high local discontinuity membrane stresses, such as stresses that would occur around penetrations, at the base connection, and with other abrupt changes in geometry. These stresses are locally high, but they decrease rapidly with distance from the discontinuity, that is, they are high over a region that may be small compared with the buckling wave length. N-284 states that, when these high discontinuity stresses occur, average values of membrane stress components within a meridional distance of $\sqrt{Rt}$ of a point of fixity or $0.5\sqrt{Rt}$ on each side of a discontinuity should be used.

B. Interaction Surfaces

Design interaction surfaces are presented in N-284 to determine whether or not elastic buckling of the containment would occur. The surfaces are of the general form

$$f(\sigma_\phi, \sigma_\theta, \sigma_{\phi\theta}) = 1. \tag{1}$$

The surface functions to indicate whether a given stress state lies in the "no buckling" or the "buckling" region. Thus, although no buckling occurs for $f \leq 1$, the design buckling limit is exceeded for $f > 1$. Here, σ_ϕ, σ_θ, $\sigma_{\phi\theta}$ is the state of stress at a particular point on the containment shell at a particular instant in the transient response. In most cases, the design interaction surface is nonlinear. In view of the nonlinearity, it does not provide a measure of the degree by which the buckling criteria may have been exceeded.

N-284 is actually based on a unique design interaction surface in terms σ_ϕ, σ_θ, and $\sigma\phi\theta$. This surface is given by the following two expressions:

For $\sigma_\phi < 0.5\sigma_\theta$ (axial compression plus hoop compression plus shear),

$$\frac{\sigma_\theta}{K\left(\sigma_{\theta_D} - \sigma_h\right)\left(1 - \dfrac{\sigma_\phi}{0.5K\sigma_h}\right) + K\sigma_h} = 1\,, \tag{2}$$

where

$$K = 1 - \left(\frac{\sigma_{\phi\theta}}{\sigma_{\phi\theta_D}}\right)^2, \tag{3}$$

and the subscript D denotes the limiting axial, hoop, or shear stress. These values are the stress components, which, when acting alone, will produce incipient buckling, as defined by N-284. σ_h is a buckling parameter associated with hoop stress, which is also defined in N-284.

For $\sigma_\phi \geq 0.5\,\sigma_\theta$ (axial compression plus hoop compression plus shear),

$$\frac{\sigma_\phi - 0.5K\sigma_h}{K\left(\sigma_{\phi_D} - 0.5\sigma_h\right)} + \left(\frac{\sigma_\theta}{K\sigma_h}\right)^2 = 1. \tag{4}$$

If either σ_ϕ or σ_θ is tensile, then it is set to zero, per N-284. As a result, the above surface simplifies to the following special cases:

For $\sigma_\theta{}^* \leq 0$ (axial compression plus shear),

$$\frac{\sigma_\phi}{\sigma_{\phi_D}} + \left(\frac{\sigma_{\phi\theta}}{\sigma_{\phi\theta_D}}\right)^2 = 1. \tag{5}$$

For $\sigma_\phi{}^* \leq 0$ (hoop compression plus shear),

$$\frac{\sigma_\theta}{\sigma_{\theta_D}} + \left(\frac{\sigma_{\phi\theta}}{\sigma_{\phi\theta_D}}\right)^2 = 1. \tag{6}$$

For the cases in which only a single component of stress is present, the interaction surface reverts to

$$\frac{\sigma_\phi}{\sigma_{\phi_D}} = 1\,, \quad \frac{\sigma_\theta}{\sigma_{\theta_D}} = 1 \quad \text{or} \quad \frac{\sigma_{\phi\theta}}{\sigma_{\phi\theta_D}} = 1. \tag{7}$$

---

[*] Negative values of σ_ϕ and σ_θ correspond to tensile stresses.

C. Allowable Buckling Stresses

Allowable buckling stresses for the containments being considered are determined, using the procedures of N-284, for the following geometrical parameters and material properties:

$R/t = 645$
R = radius of cylindrical shell = 28.65 m,
t = thickness = 0.0445 m,
L = length of cylindrical shell = 35.97 m (1416 in.), and
E = elastic modulus of steel = 2.0×10^5 MPa (29×10^6 psi).

$R/t = 450$
R = radius of cylindrical shell = 20.00 m,
t = thickness = 0.0445 m,
L = length of cylindrical shell = 40.00 m (1575 in.), and
E = elastic modulus of steel = 2.0×10^5 MPa.

Because these containments have no ring stiffeners, N-284 considers the effective length of these containments to be the length of the cylindrical portion, plus one-third the height of the hemispherical dome. These effective lengths are 45.52 m (1792 in.) and 46.67 m (1838 in.) for the containment with an R/t=645 and an R/t=450, respectively. The allowable buckling stresses are a function of this length. The allowable buckling stresses that result from N-284 are as follows:

$R/t = 645$
Axial compression: $\sigma_{\phi o}$ = 188 MPa (27,200 psi),
In-plane shear: $\sigma_{\phi\theta o}$ = 36.5 MPa (5290 psi),
Hoop compression: $\sigma_{\theta o}$ = 7.29 MPa (1060 psi), and
σ_{ho} = 7.19 MPa (1040 psi).

$R/t = 450$
Axial compression: $\sigma_{\phi o}$ = 269 MPa (39,000 psi),
In-plane shear: $\sigma_{\phi\theta o}$ = 47.1 MPa (6830 psi),
Hoop compression: $\sigma_{\theta o}$ = 8.45 MPa (1230 psi), and
σ_{ho} = 8.36 MPa (1210 psi).

Capacity reduction factors (using the procedures of N-284) are

$R/t = 645$
Axial compression: $\alpha_{\phi} = 0.207$,
In-plane shear: $\alpha_{\phi\theta} = 0.711$, and
Hoop compression: $\alpha_{\theta} = 0.800$.

$R/t = 450$

Axial compression: $\alpha_\phi = 0.265$,

In-plane shear: $\alpha_{\phi\theta} = 0.745$, and

Hoop compression: $\alpha_\theta = 0.800$.

For cylinders with an R/t of either 645 or 450, there is little or no conservatism in these capacity reduction factors for the axial stress component, that is, the test data available[19] show that the theoretical buckling capacity and the measured buckling capacity are related almost exactly by the values given above.

Based upon a factor of safety (FS) of 1.67 (Level C service limits), the allowable buckling stresses are

$R/t = 645$

$\sigma_{\phi D} = \sigma_{\phi_0}\,\alpha_\phi/FS$ = 23.2 MPa (3370 psi),

$\sigma_{\phi\theta D} = \sigma_{\phi\theta_0}\,\alpha_{\phi\theta}/FS$ = 15.5 MPa (2250 psi),

$\sigma_{\theta D} = \sigma_{\theta_0}\,\alpha_\theta/FS$ = 3.49 MPa (506 psi), and

$\sigma_h = \sigma_{h_0}\,\alpha_\theta/FS$ = 3.45 MPa (500 psi).

$R/t = 450$

$\sigma_{\phi D} = \sigma_{\phi_0}\,\alpha_\phi/FS$ = 42.7 MPa (6190 psi),

$\sigma_{\phi\theta D} = \sigma_{\phi\theta_0}\,\alpha_{\phi\theta}/FS$ = 21.0 MPa (3050 psi),

$\sigma_{\theta D} = \sigma_{\theta_0}\,\alpha_\theta/FS$ = 4.05 MPa (587 psi), and

$\sigma_h = \sigma_{h_0}\,\alpha_\theta/FS$ = 4.01 MPa (581 psi).

D. Determination of Acceleration Level for Incipient Buckling

The procedure for determining the acceleration level that will produce incipient buckling, as defined by the ASME Boiler and Pressure Vessel Code Case N-284, is as follows:

1. Axial (σ_ϕ) and hoop (σ_θ) stresses are partitioned into components resulting from static loads (dead and live loads) and dynamic loads. Note that the shear stress, $\sigma_{\phi\theta}$, consists of a component resulting only from the dynamic loads.

2. The dynamic stresses are caused by seismic loading, and they are a linear function of the acceleration level to which input acceleration-time histories are normalized, or, in the case of response spectrum analysis, they are linear functions of the zero-period acceleration (ZPA) for a given spectrum.

3. Using the appropriate interaction curve (Eqs. (2)-(7)), the axial, hoop, and shear stresses are written in terms of static- and dynamic-stress components, and a linear multiplier is used on dynamic stresses to scale (up or down) the nominal dynamic stresses until the interaction equation is equal to 1 (that is,

the stress state lies on the interaction curve or surface). Thus, the minimum value of acceleration level that causes the equation to be satisfied is the peak acceleration level, or the ZPA that will produce a state of incipient buckling.

The procedure is illustrated for the case of interaction Eq. (5). First, the calculated stress components (σ_ϕ, σ_θ, $\sigma_{\phi\theta}$), at a generic point in the cylindrical shell at a given time, which is determined on the basis of a transient elastic solution of the equations of motion of the shell or by response spectrum analysis methods, are partitioned into the components that result from static and dynamic loads,

$$\sigma_\phi = \sigma_{\phi_{St}} + \sigma_{\phi_{Dy}},$$

$$\sigma_\theta = \sigma_{\theta_{St}} + \sigma_{\theta_{Dy}}, \text{ and} \tag{8}$$

$$\sigma_{\phi\theta} = \sigma_{\phi\theta_{Dy}},$$

where the subscript St denotes the respective stress components that result from the static dead and live loads, and the subscript Dy denotes the stress components that result from the seismic excitation.

Next, the dynamic load components are scaled by the factor, g/g_i, where g_i is the peak acceleration level of excitation used in the transient solution, or the ZPA in a response spectrum analysis. Now, based upon a small-deflection elastic response, linear superposition applies. Therefore, the seismic portion of the stress response can be linearly scaled as follows:

$$\sigma_\phi = \sigma_{\phi_{St}} + \left(\frac{g}{g_i}\right) \sigma_{\phi_{Dy}},$$

$$\sigma_\theta = \sigma_{\theta_{St}} + \left(\frac{g}{g_i}\right) \sigma_{\theta_{Dy}}, \text{ and} \tag{9}$$

$$\sigma_{\phi\theta} = \left(\frac{g}{g_i}\right) \sigma_{\phi\theta_{Dy}}.$$

Substituting Eqs. (9) into the Interaction equation (Eq. (5)) yields

$$\frac{\sigma_{\phi\,St} + \sigma_{\phi_{Dy}}\left(\frac{g}{g_i}\right)}{\sigma_{\phi_D}} + \left(\frac{\sigma_{\phi\theta_{Dy}}\left(\frac{g}{g_i}\right)}{\sigma_{\phi\theta_D}}\right)^2 = 1. \tag{10}$$

This equation can be written as a quadratic in g, the value of acceleration to cause incipient buckling. The resulting acceleration value is

$$g = \frac{\dfrac{-\sigma_{\phi_{Dy}}}{g_i\,\sigma_{\phi_D}} + \sqrt{\dfrac{\sigma^2_{\phi_{Dy}}}{g_i^2\,\sigma^2_{\phi_D}} - 4\left(\dfrac{\sigma_{\phi\theta_{Dy}}}{g_i\,\sigma_{\phi\theta_D}}\right)^2\left(\dfrac{\sigma_{\phi_{St}}}{\sigma_{\phi_D}} - 1\right)}}{2\left(\dfrac{\sigma_{\phi\theta_{Dy}}}{g_i\,\sigma_{\phi\theta_D}}\right)^2}. \qquad (11)$$

Physically, this process can be viewed in the axial stress-shear stress plane as moving from the point (σ_ϕ, $\sigma_{\phi\theta}$) outward, or inward along a ray with the slope proportional to the ratio of the dynamic stresses, until the interaction curve is contacted.

The same procedure was used to determine incipient buckling acceleration values for all forms of the interaction surface given above (Eqs. (2)-(7)). The equations necessary to determine the incipient buckling acceleration values from Eqs. (2)-(7) were roots of either quartic, quadratic, or linear expressions. Eight additional possible combinations of stresses must be considered; each leads to a unique expression for incipient buckling acceleration level*

Case 1: $(\sigma_\phi < 0.5\,\sigma_\theta,\ \sigma_\phi > 0,\ \sigma_\theta > 0,\ \sigma_{\phi\theta} \neq 0)$

The incipient buckling acceleration level (using Eq. (2)) is given by the minimum positive root of the following quadratic:

$$(D + F)\,\sigma_{\phi\theta}^2 g^2 + \left(\frac{\sigma_{\theta_{Dy}}}{g_i} + N\,\sigma_{\phi_{Dy}}\right) g + G = 0\,, \qquad (12)$$

where

$$D = \frac{J}{\sigma_{\phi\theta_D}^{\ 2}\, g_i^2}\,,$$

$$F = \frac{2B}{\sigma_{\phi\theta_D}^{\ 2}\, g_i^2}\,,$$

$$G = \sigma_{\theta_{St}} - J + JC - 2B\,,$$

---

* In the following discussion, compresive axial (σ_ϕ) and hoop (σ_θ) stresses are considered positive. Tensile axial and hoop stresses are set equal to zero.

$$N = \frac{J}{B\,g_i},$$

$$J = \sigma_{\theta_D} - \sigma_h ,$$

$$B = 0.5\sigma_h , \text{ and}$$

$$C = \frac{\sigma_{\phi_{St}}}{B}.$$

Case 2: $(\sigma_\phi < 0.5\,\sigma_\theta, \sigma_\phi > 0, \sigma_\theta > 0, \sigma_{\phi\theta} = 0)$

The incipient buckling acceleration level (using Eq. (2)) is given by

$$g = \frac{-G}{\left(\frac{\sigma_{\theta_{Dy}}}{g_i} + N\,\sigma_{\phi_{Dy}}\right)} \qquad (13)$$

Case 3: $(\sigma_\phi \geq 0.5\,\sigma_\theta, \sigma_\phi > 0, \sigma_\theta > 0, \sigma_{\phi\theta} \neq 0)$

The incipient buckling acceleration level (using Eq. (4)) is given by the minimum positive real root of the following quartic:

$$\sigma_{\phi\theta}^4\,U g^4 + \frac{\sigma_{\phi_{Dy}}\sigma_{\phi\theta}^2}{Q}\,g^3$$

$$-\left[\frac{2\sigma_{\phi\theta}^2}{\sigma_{\phi\theta_D}^2\,g_i^2}\left(1 + \frac{0.5\sigma_h}{H}\right) - \frac{\sigma_{\phi_{St}}\,\sigma_{\phi\theta}^2}{H\,\sigma_{\phi\theta_D}^2 g_i^2} + \frac{\sigma_{\theta_{Dy}}^2}{\sigma_h^2 g_i^2}\right] g^2 \qquad (14)$$

$$-\left(\frac{2\sigma_{\theta_{St}}\,\sigma_{\theta_{Dy}}}{\sigma_h^2 g_i} + \frac{\sigma_{\phi_{Dy}}}{H g_i}\right) g + S = 0 ,$$

where $H = \sigma_{\phi_D} - 0.5\,\sigma_h$,

$$U = \left(1 + \frac{\sigma_h}{2H}\right) \Big/ \left(\sigma_{\phi\theta_D}^4\,g_i^4\right),$$

$Q = H\, \sigma_{\phi\theta_D}{}^2\, g_i^3$, and

$$S = 1 - \frac{\sigma_{\phi St}}{H} + \frac{0.5\sigma_h}{H} - \frac{\sigma_{\theta St}{}^2}{\sigma_h{}^2}$$

Case 4: $(\sigma_\phi \geq 0.5\, \sigma_\theta,\ \sigma_\phi > 0,\ \sigma_\theta > 0,\ \sigma_{\phi\theta} = 0)$:

The incipient buckling acceleration level (using Eq. (4)) is given by the minimum positive root of

$$\left(\frac{\sigma_{\theta_{Dy}}}{\sigma_h\, g_i}\right)^2 g^2 + \left[\frac{2\sigma_{\theta St}\, \sigma_{\theta_{Dy}}}{\sigma_h{}^2\, g_i} + \frac{\sigma_{\phi_{Dy}}}{H\, g_i}\right] g - S = 0\,. \qquad (15)$$

Case 5: $(\sigma_\theta > 0,\ \sigma_{\phi\theta} \neq 0\,,\ \sigma_\phi = 0)$

The incipient buckling acceleration level (using Eq. (6)) is given by the positive root of the following quadratic expression for g:

$$\left(\frac{\sigma_{\phi\theta}}{g_i\, \sigma_{\phi\theta_D}}\right)^2 g^2 + \frac{\sigma_{\theta_{Dy}}}{g_i\, \sigma_{\theta_D}}\, g + \left(\frac{\sigma_{\theta_{St}}}{\sigma_{\theta_D}} - 1\right) = 0\,. \qquad (16)$$

Case 6: $(\sigma_{\phi\theta} \neq 0,\ \sigma_\theta = 0,\ \sigma_\phi = 0)$

The incipient buckling acceleration level (using the third equation of Eqs. (7)) is given by

$$g = g_i\, \frac{\sigma_{\phi\theta_D}}{\sigma_{\phi\theta}}\,. \qquad (17)$$

Case 7: $(\sigma_\phi > 0,\ \sigma_\theta = 0,\ \sigma_{\phi\theta} = 0)$

The incipient buckling acceleration level (using the first equation of Eqs. (7)) is given by

$$g = \frac{g_i}{\sigma_{\phi_{Dy}}}\left(\sigma_{\phi_D} - \sigma_{\phi_{St}}\right). \tag{18}$$

Case 8: $(\sigma_\phi > 0, \sigma_\theta = 0, \sigma_{\phi\theta} = 0)$

The incipient buckling acceleration level (using the second equation of Eqs. (7)) is given by

$$g = \frac{g_i}{\sigma_{\theta_{Dy}}}\left(\sigma_{\theta_D} - \sigma_{\theta_{St}}\right). \tag{19}$$

Care must be taken in using the above scaling procedures because only the dynamic stresses are being scaled. Furthermore, a sign change on the total stress component could occur, which would invalidate results. For instance, the axial stress component could be $\sigma_\phi = \sigma_{\phi St} + \sigma_{\phi Dy} > 0$, even though $\sigma_{\phi Dy} < 0$. Now, in scaling up the acceleration level, the new total σ_ϕ stress component becomes

$$\sigma_{\phi_{St}} + \sigma_{\phi_{Dy}}\left(\frac{g}{g_i}\right) = \sigma_\phi \tag{20}$$

This new scaled stress component could be less than zero, which is inconsistent with the development of Eqs. (11)-(19). Similar arguments apply to $\sigma_{\theta St}$ and $\sigma_{\theta Dy}$. A check should therefore be made to see that a change in sign of either σ_θ or σ_ϕ has not occurred as a result of the scaling process.

IV. DETERMINATION OF APPROPRIATE DAMPING

Damping values are typically specified in terms of equivalent viscous damping and have been shown to be stress-level dependent. A single viscous, modal damping value is used for seismic applications; this value is considered valid for all modes of the structure.

The damping values for welded steel structures given in Table I of Regulatory Guide 1.61 (Ref. 21) are 2% or 4%, with the lower value corresponding to an Operating-Basis Earthquake (OBE), assumed to produce stress levels approximately two-thirds of yield, and the higher value corresponding to a Safe-Shutdown Earthquake (SSE), assumed to produce stress levels approximately 90% of yield.[22] These damping values, as stated in Regulatory Position 1, should be used as modal damping values for all modes considered in time-history dynamic seismic analysis. However, Regulatory Position 3 states that if the maximum combined stresses are significantly lower than the yield stress for the SSE, or half the yield stress for the OBE (both of which are the case for the containments being considered when subjected to the proposed SSE), then damping values lower than those specified in Table I should be used to avoid underestimating the amplitudes of vibrations or dynamic stresses.

Newmark and Hall[23] recommend a damping value in the range of 0.5% to 1.0% for steel structures at a stress level below one-fourth of the yield stress. More recently[24] they recommended a damping value for use at the working stress level (no more than half the yield point) of 2% to 3%; the 2% value represents a near lower bound and is considered to be "highly conservative."

ASCE 4-86 (Ref. 25) and the Seismic Design Criteria proposed by Lawrence Livermore National Laboratory (LLNL)[7] have adopted the 2%/4% damping values of Regulatory Guide 1.61. Currently, the committee updating ASCE 4-86 is considering modifications that would recommend using 2% damping when the failure mechanism being considered is elastic stability.

The Electric Power Research Institute's [EPRI] methodology for seismic margins assessment[26] recommends 3% of critical damping for welded steel structures at stress levels up to one-half the yield stress. Further guidance is provided by Priestley et al.[27] They recommend damping values of 2% and 5% in the horizontal and vertical directions, respectively, for storage tanks anchored on firm soil or rock.

Damping values listed in commercial nuclear power plant Safety Analysis Reports (SARs) vary from 1% to 4%. For example, the analysis of Waterford Unit No. 3 used 2% damping for both the OBE and the SSE.[2] The Updated SAR for Davis-Besse Station No. 1 states that 2% damping was used when analyzing for the "maximum probable" and the "maximum possible" earthquakes.[3] The Reg. Guide 1.61 values of 2% and 4% (Ref. 4) were used for the seismic analysis of St. Lucie Unit No. 2. One-percent damping was specified for Kewaunee's containment structure when the structure was subjected to both the OBE and the design basis earthquake (DBE).[5] The Updated SAR for Prairie Island Nuclear Generating Station also states that the containment was assumed to exhibit 1% damping during both the OBE and the DBE.[6] The Watts Bar[28,29] and Sequoyah[30] SARs utilized 1% damping for OBE and SSE events. In a second analysis approach given in the Watts Bar SAR, the Reg. Guide 1.61 values of 2% and 4% were used.

In 1982 Stevenson and Thomas compared the damping values used by the U.S., Canada, and Japan.[31] The U.S. nuclear industry uses values of 2% to 4% for welded steel structures. Canada uses values of 3%, and Japan uses a value of 1%.

In thin unstiffened cylindrical shells, buckling occurs at very low stress levels (less than one-tenth of the yield stress for the containments being considered). Based on Reg. Guide 1.61, the previously cited works, and the stress level dependence of damping, 1% equivalent viscous damping is considered appropriate for the buckling analysis of welded steel containments. The authors feel that this value is consistent both with Regulatory Position 3 of Regulatory Guide 1.61 and with the stress-level dependence of damping. The sensitivity of buckling to this parameter is examined in the subsequent analyses.

V. SIMPLIFIED BUCKLING ANALYSIS OF THE CONTAINMENT

Initially, a simplified 3-DOF response spectrum analysis of the containment shells was performed to obtain estimates of buckling capacity in terms of peak ground acceleration levels. Only a symmetrical shell is considered in this analysis.

A. Simplified Model

The 3-DOF model of the containments is shown in Fig. 1. The first DOF is horizontal motion, similar to that of a short cantilever beam, and it results from the shear-bending mode of response. The second DOF is identical to the first, but it acts in the orthogonal horizontal direction (not shown in Fig. 1). The third DOF corresponds to axial motion in the vertical direction. Referring to Fig. 1, m denotes either m_h or m_v, where m_h is the participating mass for the horizontal translation mode, and m_v is the participating mass for the vertical translation mode. For both cases, the participating mass is assumed to be concentrated at the top of the cylindrical portion of the containment.

Other geometric parameters needed in the subsequent analysis are

A = cross-sectional area of the containment,
I = area moment of inertia of the containment cross section, and
c = distance from the neutral axis to the outer fiber of the shell.

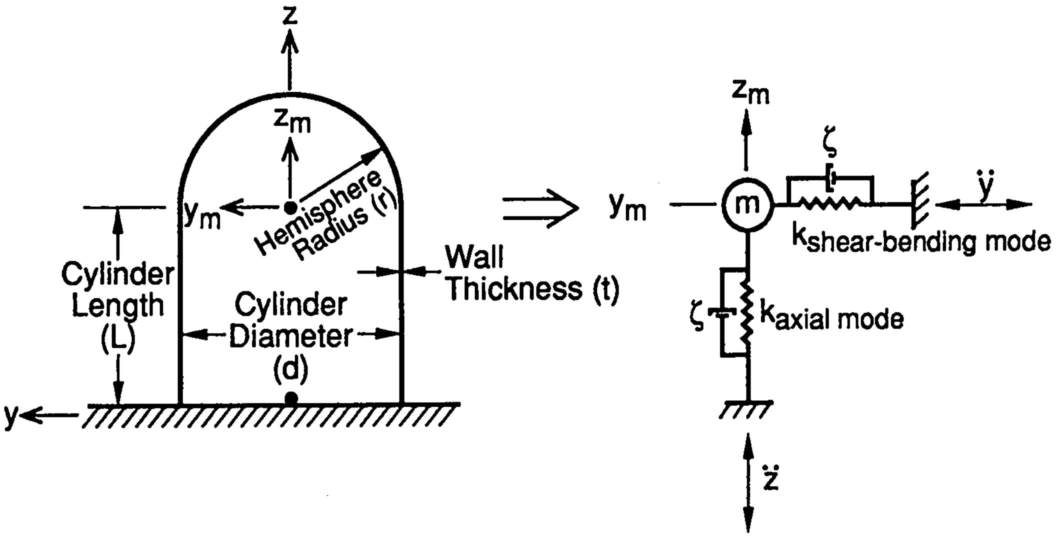

Fig. 1 Three DOF model of the Containment.

B. Determination of Resonant Frequencies

Because the structures being considered were modeled as axisymmetric, the two shear-bending modes associated with the horizontal DOFs have the same resonant frequency. Using the BOSOR finite difference structural computer code,[32] the resonant frequency for the horizontal shear-bending mode, f_h, was determined to be 7.13 Hz for the R/t=645 containment and 7.06 Hz for the R/t=450 containment. The displacement shape in this mode, which is similar for both structures, is depicted in Fig. 2 for the R/t = 645 containment.

The resonant frequency for the vertical translation mode, f_v, is estimated as

$$f_v = \frac{1}{2\pi}\sqrt{\frac{K_v}{m_v}}, \tag{21}$$

where K_V is the axial stiffness of the cylindrical shell. These quantities are defined as

$$K_V = AE/L, \tag{22}$$

$$m_V = m_{sp} + 1/3\ m_C, \tag{23}$$

m_{sp} = the mass of the hemispherical dome,
for R/t = 645: 1.78 x 10^6 kg (3.92 x 10^6 lbm),
for R/t = 450: 8.68 x 10^5 kg (1.91 x 10^6 lbm),
m_C = the mass of the cylindrical portion of the containment, for R/t = 645: 2.23 x 10^6 kg (4.92 x 10^6 lbm), and
for R/t = 450: 1.74 x 10^6 kg (3.82 x 10^6 lbm).

The participating mass for vertical motion was determined by Rayleigh's Method.[33]

Combining Eqs. (21)-(23) results in a fundamental vertical translation mode natural frequency of f_V = 21.1 Hz and 22.2 Hz for the containments with R/t = 645 and R/t = 450, respectively.

C. Dynamic Amplification

Response spectra from four sources are next used to determine the dynamic amplification factors associated with these three modes. The sources are

1. NRC Regulatory Guide 1.60 site-independent design spectra[34] shown in Fig. 3.

2. An eastern U.S. site-specific design spectra given in Ref. 35 (these spectra are currently acceptable to Department of Energy for the design of nonreactor facilities at Savannah River Site). These spectra are shown in Fig. 4.

3. The eastern U.S. site-specific design spectra, determined recently (1990), which account for the higher frequency content observed in eastern U.S. seismic events[7] are shown in Fig. 5.

4. A spectrum was calculated for the base of a containment that rests on a common basemat foundation and includes soil-structure interaction effects,[36] (see Fig. 6).

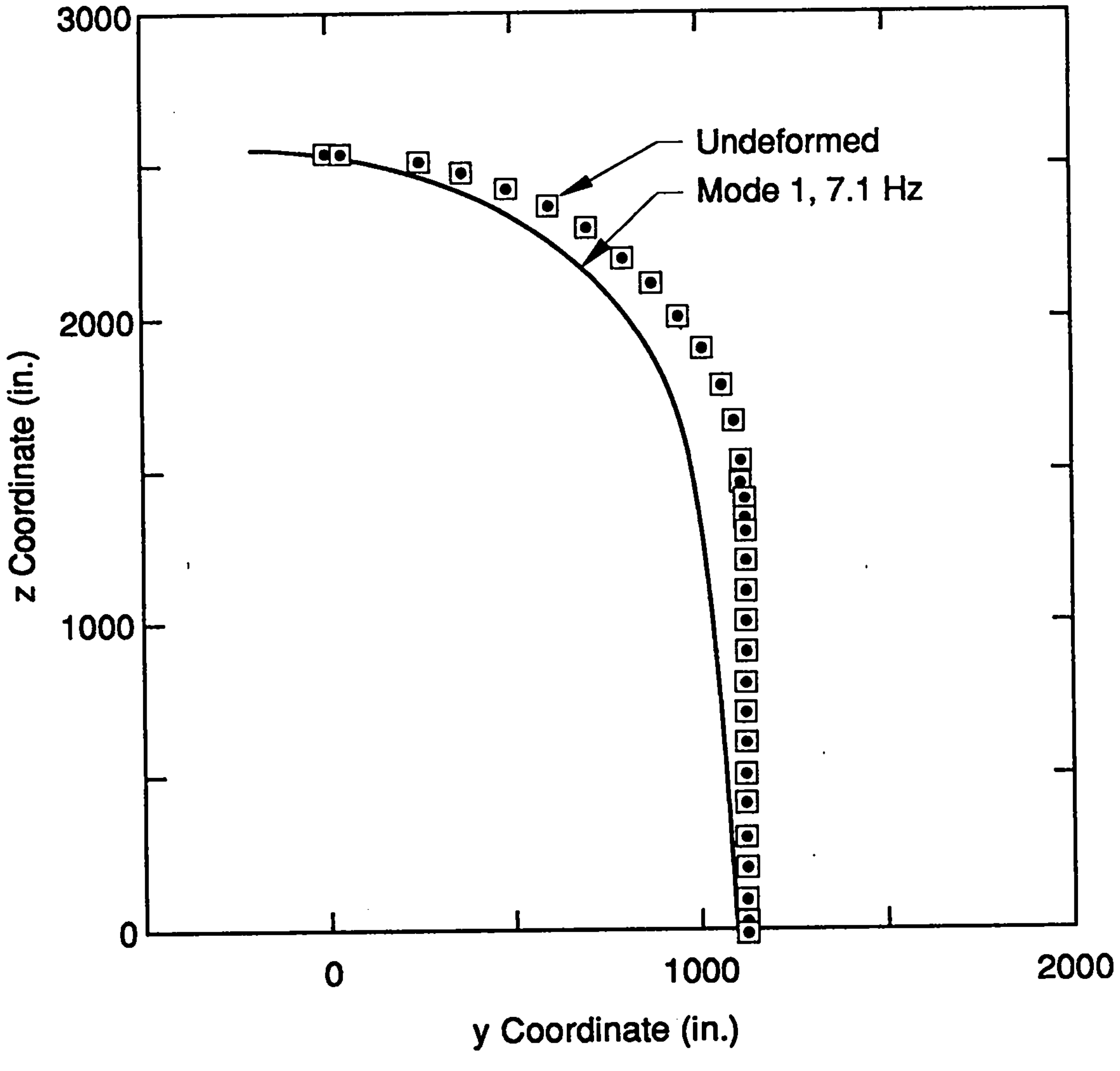

Fig. 2. The shear-bending mode of the R/t = 645 containment calculated with BOSOR.

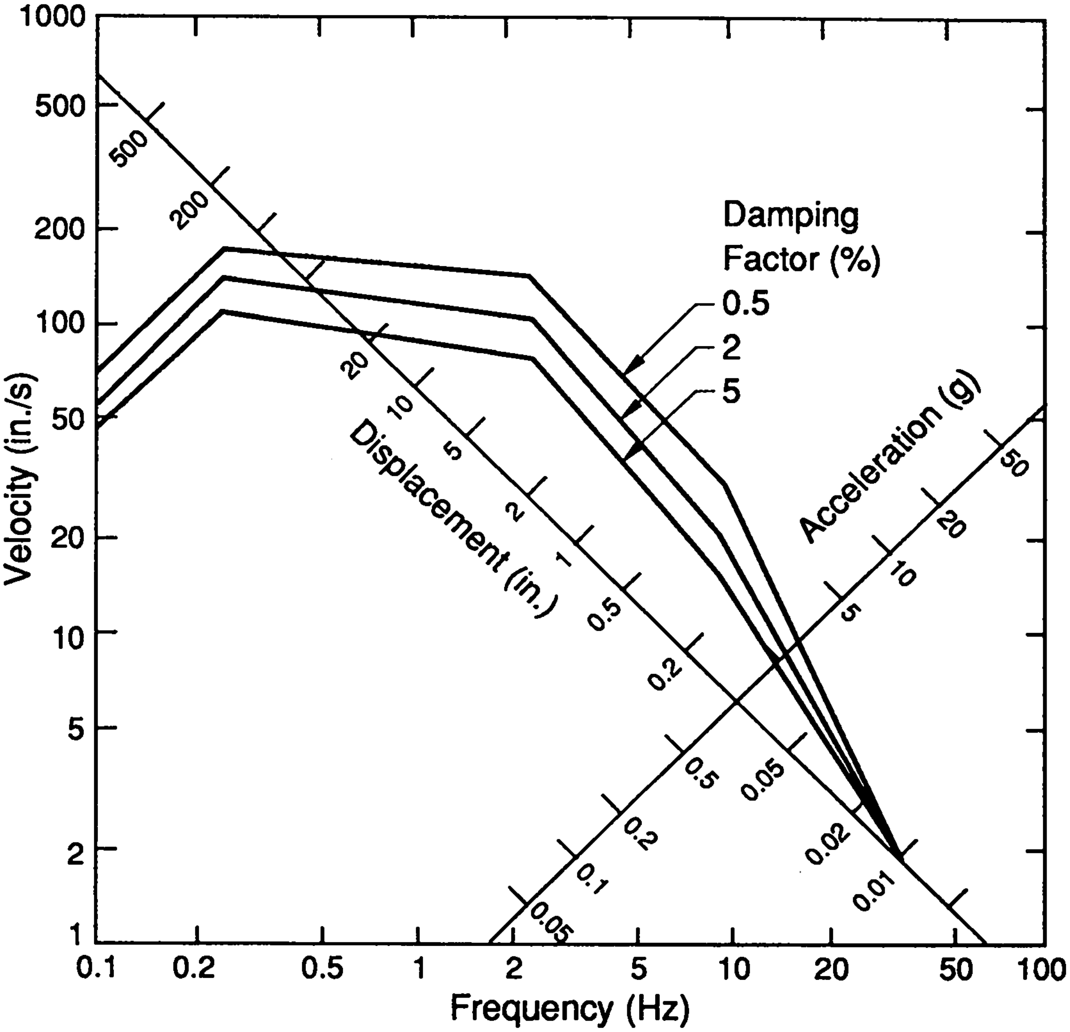

Fig. 3 NRC Regulatory Guide 1.60 Spectra.

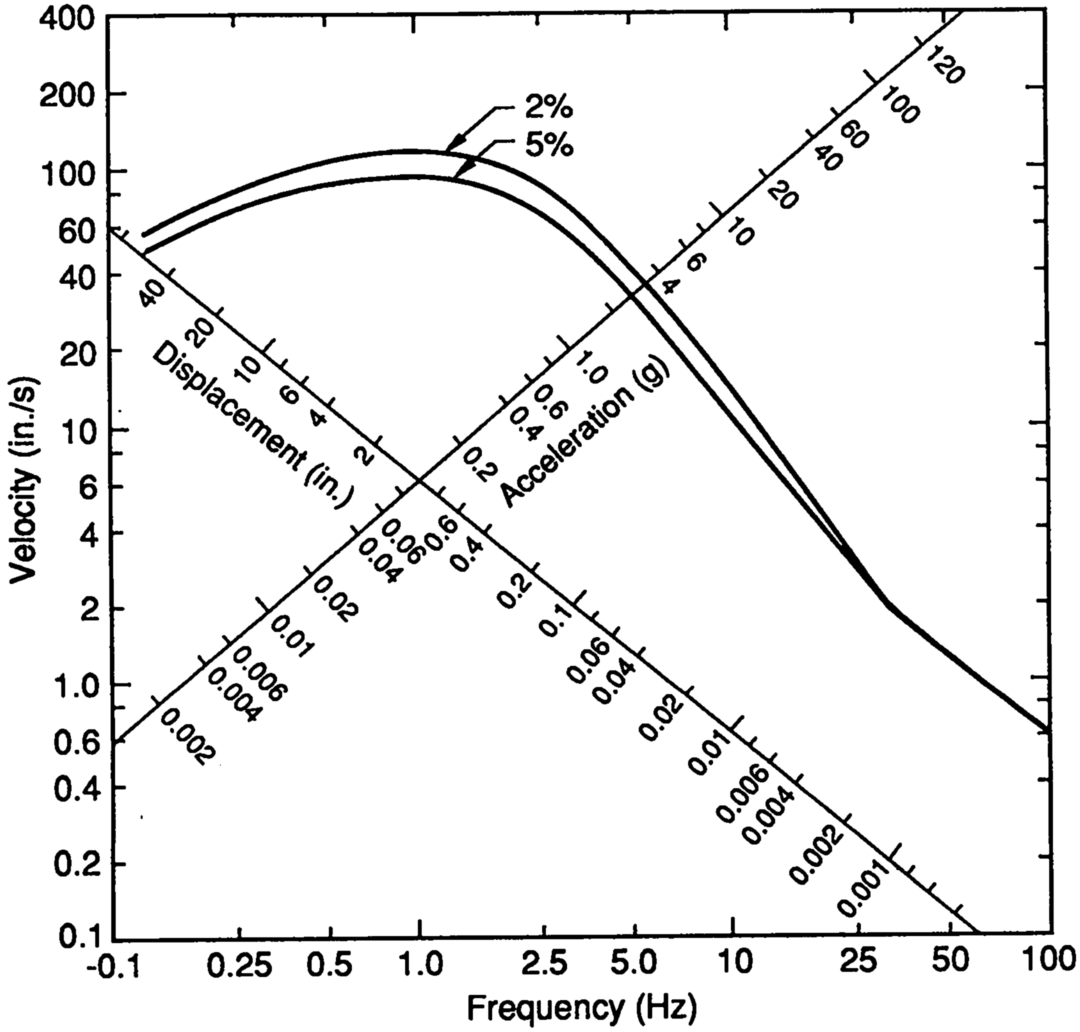

Fig. 4 Eastern U.S. site-specific spectra given in UCRL-53582.

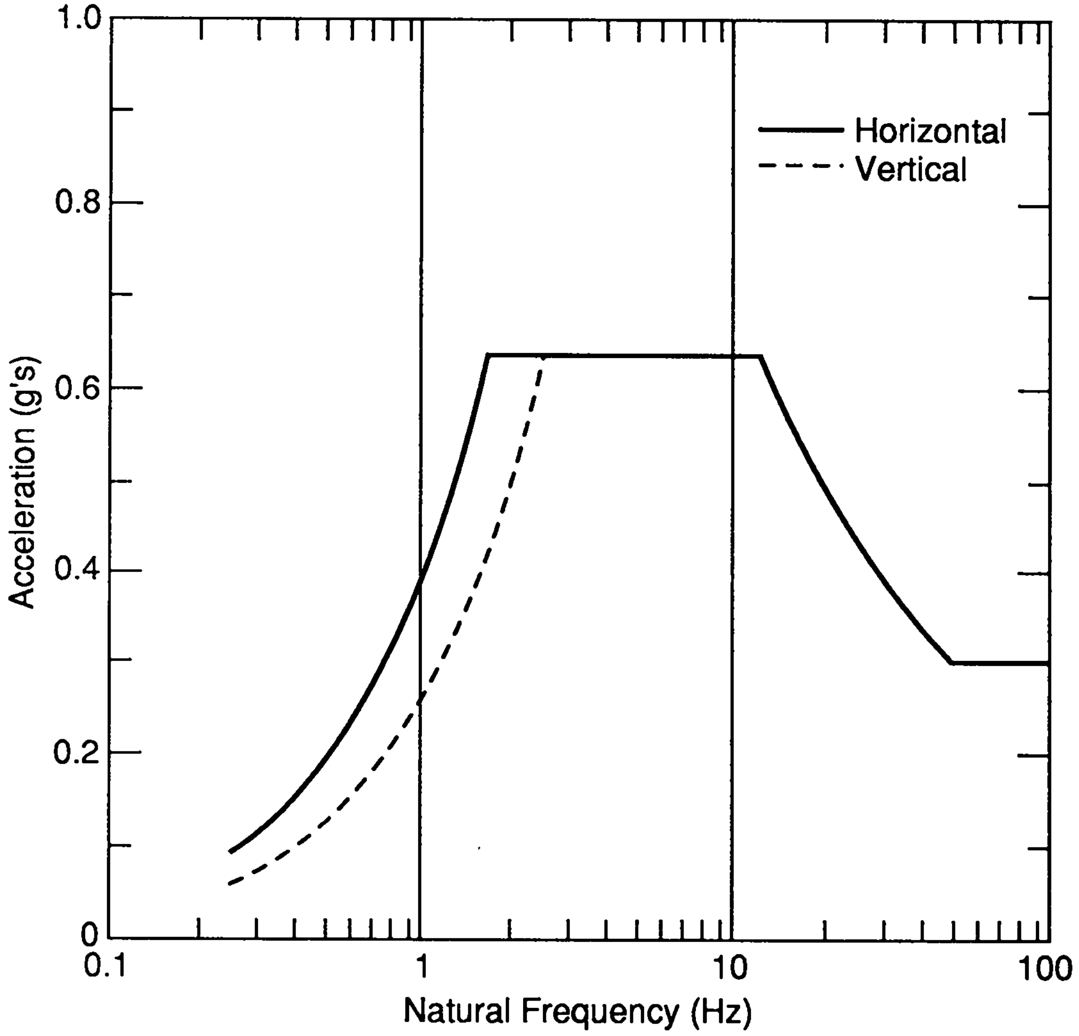

Fig. 5 Eastern U.S. site-specific spectra given n LLNL's Preliminary Title I Seismic Design Criteria for New Production Reactors.

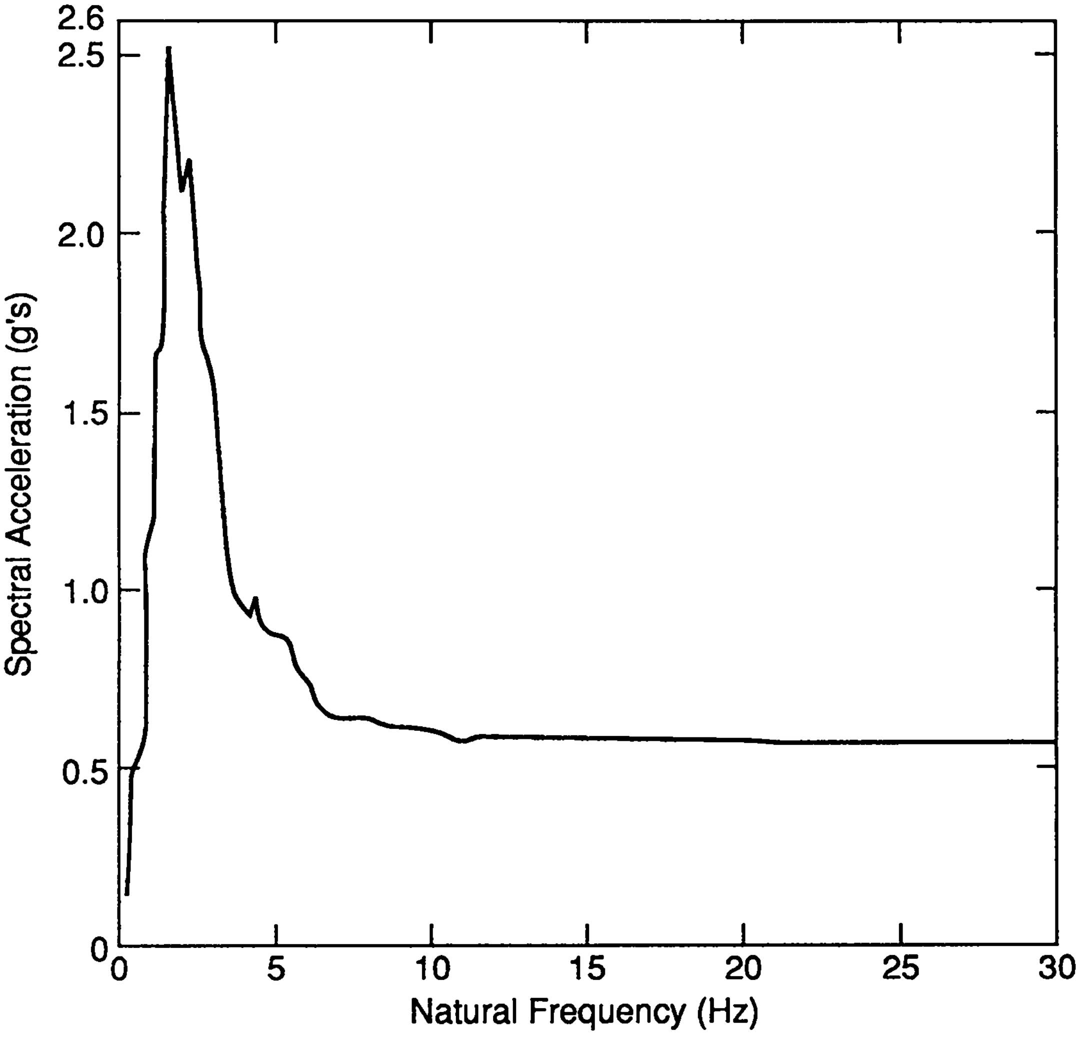

Fig. 6 Spectrum corresponding to the seismic input at the base of the containment determined from soil-structure interaction analysis.

The amplification factors obtained from the 1% damping spectra are used here, based on the arguments set forth in Section IV. The amplification factors corresponding to the 2% and 4% damping spectra have also been determined. All dynamic amplification factors are presented in Table I. Because the 1% damping curves were not shown explicitly for the Reg. Guide 1.60 spectra or for the spectra given in Ref. 35, the values in Table II are interpolated or extrapolated from log-log plots.

Note that Reg. Guide 1.60 specifies that a linear interpolation between spectra is acceptable when the spectrum corresponding to the damping value of interest is not given explicitly. ASCE 4-86, 2.2.1.b also specifies a linear interpolation between spectra if the higher damping spectrum is within twice the damping of the lower spectrum. The LLNL Seismic Design Criteria[7] specifies a method for obtaining spectral accelerations as a function of frequency, damping, and ZPA. Because only one spectrum was given in the SSI analysis (corresponding to 5% damping), and because both modes being considered were either very close to or in the ZPA portion of the spectrum, no attempt was made to estimate the amplification factors for the other damping values being considered.

D. Axial Stresses from Beam Theory

The maximum longitudinal stress at the base of the cylindrical shell is determined from simple beam theory. The longitudinal stress caused by bending, which is induced from the horizontal component of acceleration, is considered along with the longitudinal stress caused by the static dead and live loads, including the normal operating negative air-pressure effects and the longitudinal stress caused by the vertical inertial loading. These stress components are as follows:

$$\sigma_{\phi Dyh} = \frac{Mc}{I}, \qquad (24)$$

$$\sigma_{\phi Dyv} = \frac{P_{Dy}}{A}, \qquad (25)$$

$$\sigma_{\phi St} = \frac{P_{St}}{A} + \frac{pR}{2t}, \qquad (26)$$

where $\sigma_{\phi Dyh}$ = the longitudinal dynamic stress that results from the horizontal seismic input component,

$\sigma_{\phi Dyv}$ = the longitudinal dynamic stress that results from the vertical seismic input component,

$\sigma_{\phi St}$ = the longitudinal static stress,

M = the bending moment at the base of the containment caused by the horizontal seismic input component,

P_{St} = longitudinal static load,

P_{Dy} = longitudinal dynamic load, and

p = the negative air pressure maintained during normal operating conditions.

TABLE II

DYNAMIC AMPLIFICATION FACTORS

		Amplification			
Mode	Damping	Reg. Guide 1.60	Ref. 35	Ref. 7.	SSI
f_h	1%	4.0	3.7	3.2	-
f_v	1%	1.8	1.6	2.0	-
f_h	2%	3.7	2.9	2.7	-
f_v	2%	1.7	1.5	1.8	-
f_h	4%	3.0	2.3	2.3	-
f_v	4%	1.6	1.4	1.6	-
f_h	5%	-	-	-	1.15
f_v	5%	-	-	-	1.0

The longitudinal dead load is given by

$$P_{St} = m_t g_o, \tag{27}$$

where m_t = $m_{sp} + m_c$, and
g_o = the acceleration caused by gravity, in g's.

The same negative air pressure (0.69 kPa (0.1 psi)) (Ref. 37) is assumed to be maintained during normal operating conditions in both containments. The parameters listed above give a maximum longitudinal static stress of

$R/t=645$
$\sigma_{\phi St} = 5.14$ MPa (745 psi).

$R/t=450$
$\sigma_{\phi St} = 4.73$ MPa (685 psi).

The bending moment is determined from

$$M = D_{AH}\, g\, m_h\, L \tag{28}$$

where D_{AH} = dynamic amplification factor for the horizontal translation mode, and
g = horizontal ZPA in g's.

Rayleigh's method is again employed to determine m_h. Because the containment is similar to a short beam, the horizontal displacement of the cylinder, when responding in its fundamental shear-bending mode, is assumed to be a linear function of the height of the cylinder. This assumption appears reasonable when the fundamental shear-bending mode shown in Fig. 2 is examined. Referring to Fig. 1, the horizontal displacement, y, of any point along the axis of the cylinder is

$$y = \frac{z}{L} y_m, \qquad (29)$$

where y_m is the displacement at the top of the cylindrical portion ($z = L$) of the containment. The assumption is now made that the mass of the hemisphere can be considered as a lumped mass located at the centroid of the hemisphere. This assumption also seems reasonable if Fig. 2 is examined. The displacement of the hemisphere's centroid, y_h, can be expressed as

$$y_h = y_m\left(1 + \frac{a}{L}\right), \qquad (30)$$

where a is the distance of the hemisphere's centroid above the top of the cylindrical portion of the containment. Standard statics texts show that

$R/t = 645$

$a = \frac{R}{2} = 14.3$ m (564 in.) .

$R/t = 450$

$a = \frac{R}{2} = 10.0$ m (394 in.) .

The maximum kinetic energy of the cylinder can now be expressed in terms of y_m as

$$\int_0^L \frac{m_c}{2L}\left(\dot{y}_m \frac{z}{L}\right)^2 dz + \frac{m_{sp}}{2} \dot{y}_m^{\,2}\left(1 + \frac{a}{L}\right)^2, \qquad (31)$$

where $\dot{y}_m$ is the maximum velocity of the top of the cylindrical portion of the cylinder. A lumped mass of

$$\frac{m_c}{3} + m_{sp}\left(1 + \frac{2a}{L} + \left(\frac{a}{L}\right)^2\right) \tag{32}$$

located at the top of the cylinder will have the same maximum kinetic energy. Substituting the appropriate values into Eq. (32) gives the participating mass for the horizontal translation mode, when all the mass is lumped at the top of the cylindrical portion of the containment, as

$R/t=645$
$m_h = 4.23 \times 10^6$ kg (9.30×10^6 lbm).

$R/t=450$
$m_h = 1.94 \times 10^6$ kg (4.26×10^6 lbm).

Finally, the longitudinal inertial load is given by

$$P_{Dy} = 0.67\, D_{AV}\, g\, m_v \tag{33}$$

where D_{AV} = dynamic amplification factor for the vertical translation mode, and

0.67 = factor specified in ASCE 4-86 , Section 2.2.2.2 (Ref. 25), which relates the vertical acceleration to horizontal acceleration. The factor is 0.82 for the SSI analysis. For eastern U.S. site-specific spectra given by LLNL,[7] the vertical spectra are given explicitly and, for this, the factor is 1.

The axial dynamic stress components at the base of the containments that result from a 0.3-g's ZPA earthquake are summarized in Tables III and IV.

E. Shear Buckling Considerations

The maximum in-plane shear stress in the cylindrical shell occurs at positions 90° around the shell from the point of maximum longitudinal compressive stress.

Based on Ref. 38, the maximum shear stress, for a cantilever cylindrical shell loaded by a transverse concentrated force, P, on its end is

$$(\sigma_{\phi\theta})_{Max} = \frac{P}{\pi R t} \, . \tag{34}$$

This value is twice that of the average shear stress. The horizontal shear force is given by

$$P = D_{AH}\, g\, m_h \, . \tag{35}$$

TABLE III

DYNAMIC COMPONENTS OF LONGITUDINAL STRESS RESULTING FROM A 0.3-g's ZPA EARTHQUAKE, R/t = 645

Spectrum	Amplification Horizontal	$\sigma_{\phi Dyh}$ MPa (psi)	Amplification Vertical	$\sigma_{\phi Dyv}$ MPa (psi)
Reg. Guide 1.60 Damping = 1%	4.0	15.6 (2260)	1.8	1.12 (162)
Reg. Guide 1.60 Damping = 2%	3.7	14.4 (2090)	1.7	1.06 (153)
Reg. Guide 1.60 Damping = 4%	3.0	11.7 (1690)	1.6	0.993 (144)
Ref. 35 Damping = 1%	3.7	14.4 (2090)	1.6	0.993 (144)
Ref. 35 Damping = 2%	2.9	11.3 (1640)	1.5	0.931 (135)
Ref. 35 Damping = 4%	2.3	8.97 (1300)	1.4	0.869 (126)
Ref. 7 Damping = 1%	3.2	12.5 (1810)	2.0	1.85 (269)
Ref. 7 Damping = 2%	2.7	10.5 (1530)	1.8	1.67 (242)
Ref. 7 Damping = 4%	2.3	8.97 (1300)	1.6	1.48 (215)
SSI Damping = 5%	1.15	8.22 (1190)	1.0	1.40 (202)

Combining Eqs. (34) and (35) leads to the following maximum value of shear stress resulting from the seismic input

$$\sigma_{\phi\theta_{Dy}} = \frac{D_{AH}\, g\, m_h}{\pi R t} \, . \qquad (36)$$

The shear stress components at the base of the containment, which results from a 0.3 g's-ZPA earthquake are summarized in Table V.

TABLE IV

DYNAMIC COMPONENTS OF LONGITUDINAL STRESS RESULTING FROM A 0.3-g's ZPA EARTHQUAKE, R/t = 450

Spectrum	Amplification Horizontal	$\sigma_{\phi Dyh}$ MPa (psi)	Amplification Vertical	$\sigma_{\phi Dyv}$ MPa (psi)
Reg. Guide 1.60 Damping = 1%	4.0	16.3 (2360)	1.8	0.917 (133)
Reg. Guide 1.60 Damping = 2%	3.7	15.1 (2190)	1.7	0.862 (125)
Reg. Guide 1.60 Damping = 4%	3.0	12.2 (1770)	1.6	0.814 (118)
Ref. 35 Damping = 1%	3.7	15.1 (2190)	1.6	0.814 (118)
Ref. 35 Damping = 2%	2.9	11.8 (1710)	1.5	0.765 (111)
Ref. 35 Damping = 4%	2.3	9.38 (1360)	1.4	0.710 (103)
Ref. 7 Damping = 1%	3.2	13.0 (1890)	2.0	1.51 (219)
Ref. 7 Damping = 2%	2.7	11.0 (1600)	1.8	1.37 (199)
Ref. 7 Damping = 4%	2.3	9.38 (1360)	1.6	1.21 (176)
SSI Damping = 5%	1.15	8.58 (1250)	1.0	1.14 (165)

F. Combining Stresses and Evaluating the Interaction Equations

The stress components can be combined, assuming that three components of input are acting simultaneously. ASCE 4-86 (Ref. 25) specifies a 100-40-40 rule for combining stresses when performing a response spectrum analysis such as that used in Sections D and E above. The input in one direction is assumed to act in full; in the other orthogonal directions, only 40% of the inputs are assumed to occur. All possible combinations of stresses must therefore be examined (100% vertical, with 40% in both horizontal directions; 40% vertical and 40% in one horizontal direction, with 100% in the other horizontal direction, etc.). The 40% reduction is applied only to the stresses resulting from the seismic excitation. This method of combining stresses is used to compensate for the loss of phasing information that occurs when a response spectrum analysis is performed and the observations that actually measured earthquake acceleration components are randomly phased. Because of the symmetry in the model being considered, and because the axial stresses and the in-plane shear stresses are primarily a function of the horizontal component of

TABLE V

DYNAMIC COMPONENTS OF SHEAR STRESS RESULTING
FROM A 0.3-g's ZPA EARTHQUAKE

Spectrum	Amplification Horizontal	R/t=645 $\sigma_{\phi\theta Dy}$ MPa (psi)	R/t=450 $\sigma_{\phi\theta Dy}$ MPa (psi)
Reg. Guide 1.60 Damping = 1%	4.0	12.4 (1800)	8.14 (1180)
Reg. Guide 1.60 Damping = 2%	3.7	11.5 (1665)	7.52 (1090)
Reg. Guide 1.60 Damping = 4%	3.0	9.31 (1350)	6.11 (886)
Ref. 35 Damping = 1%	3.7	11.5 (1665)	7.52 (1090)
Ref. 35 Damping = 2%	2.9	9.00 (1305)	5.90 (856)
Ref. 35 Damping = 4%	2.3	7.14 (1035)	4.68 (679)
Ref. 7 Damping = 1%	3.2	9.93 (1440)	6.52 (945)
Ref. 7 Damping = 2%	2.7	8.38 (1215)	5.50 (797)
Ref. 7 Damping = 4%	2.3	7.14 (1035)	4.68 (679)
SSI Damping = 5%	1.15	6.54 (950)	4.29 (622)

excitation, the controlling load case results when 100% of the input is applied in one of the horizontal directions. The N-284 interaction curve is considered only for this case. Two critical locations at the base of the containment must be considered. These points are shown in Fig. 7. Point 1 in Fig. 7 experiences the maximum longitudinal stress, while point 2 experiences the maximum in-plane shear stress.

The circumferential component of static stress, $\sigma_{\theta St}$, which arises from the negative internal pressure, must also be considered. This stress component is

For R/t=645

$$\sigma_{\theta St} = \frac{pR}{t} = 0.445 \text{ MPa } (64.5 \text{ psi}) .$$

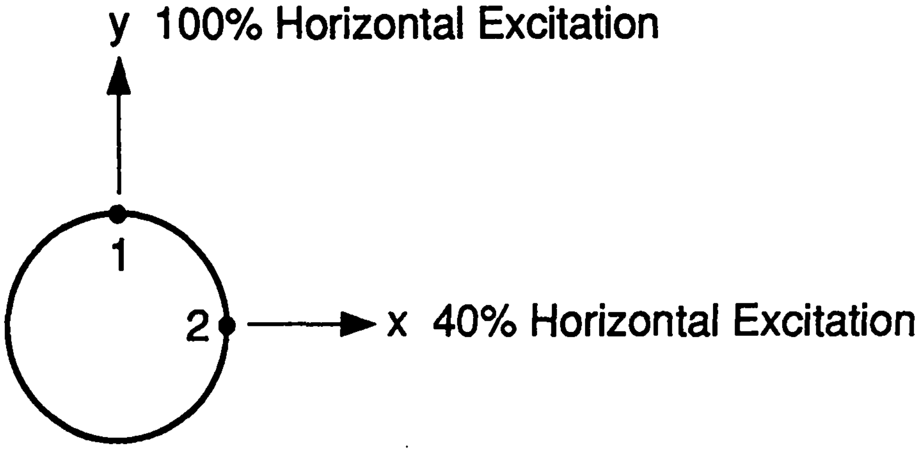

Fig. 7. Point at the base of the containment for which the buckling interaction equation was considered.

TABLE VI

STRESS VALUES TO BE USED WITH N-284 BUCKLING INTERACTION EQUATIONS, R/t = 645

	POINT 1			POINT 2		
Spectrum	σ_ϕ MPa (psi)	σ_θ MPa (psi)	$\sigma_{\phi\theta}$ MPa (psi)	σ_ϕ MPa (psi)	σ_θ MPa (psi)	$\sigma_{\phi\theta}$ MPa (psi)
Reg. Guide 1.60 Damping = 1%	21.2 (3070)	0.445 (64.5)	4.97 (720)	11.8 (1710)	0.445 (64.5)	12.4 (1800)
Reg. Guide 1.60 Damping = 2%	20.0 (2900)	0.445 (64.5)	4.59 (666)	11.3 (1640)	0.445 (64.5)	11.5 (1665)
Reg. Guide 1.60 Damping = 4%	17.2 (2490)	0.445 (64.5)	3.72 (540)	10.2 (1480)	0.445 (64.5)	9.31 (1350)
Ref. 35 Damping = 1%	20.0 (2900)	0.445 (64.5)	4.59 (666)	11.3 (1640)	0.445 (64.5)	11.5 (1665)
Ref. 35 Damping = 2%	16.8 (2440)	0.445 (64.5)	3.60 (522)	10.1 (1460)	0.445 (64.5)	9.00 (1305)
Ref. 35 Damping = 4%	14.5 (2100)	0.445 (64.5)	2.86 (414)	9.10 (1320)	0.445 (64.5)	7.14 (1035)
Ref. 7 Damping = 1%	18.3 (2660)	0.445 (64.5)	3.97 (576)	10.9 (1580)	0.445 (64.5)	9.93 (1440)
Ref. 7 Damping = 2%	16.3 (2370)	0.445 (64.5)	3.35 (486)	10.0 (1450)	0.445 (64.5)	8.38 (1215)
Ref. 7 Damping = 4%	14.7 (2130)	0.445 (64.5)	2.86 (414)	9.31 (1350)	0.445 (64.5)	7.14 (1035)
SSI Damping = 5%	13.8 (2020)	0.445 (64.5)	2.62 (380)	8.87 (1300)	0.445 (64.5)	6.54 (950)

For R/t=450

$\sigma_{\theta St}$ = 0.310 MPa (45.0 psi).

Tables VI and VII summarize the stress component values that must be considered for the two points in question on each containment.

Table VIII summarizes the results of substituting these stress values into the appropriate interaction equations given in Section III. B. A review of Table VIII shows that the critical location on the structure, in terms of buckling, is not always in the same location when different damping values are examined. This difference results because the ratio between the amplification factors in the vertical and horizontal translation modes changes with the different damping levels.

TABLE VII

STRESS VALUES TO BE USED WITH N-284 BUCKLING INTERACTION EQUATIONS, R/t = 450

	POINT 1			POINT 2		
Spectrum	σ_ϕ MPa (psi)	σ_θ MPa (psi)	$\sigma_{\phi\theta}$ MPa (psi)	σ_ϕ MPa (psi)	σ_θ MPa (psi)	$\sigma_{\phi\theta}$ MPa (psi)
Reg. Guide 1.60 Damping = 1%	21.4 (3100)	0.310 (45.0)	3.25 (472)	11.6 (1680)	0.310 (45.0)	8.14 (1180)
Reg. Guide 1.60 Damping = 2%	20.1 (2920)	0.310 (45.0)	3.01 (436)	11.1 (1610)	0.310 (45.0)	7.52 (1090)
Reg. Guide 1.60 Damping = 4%	17.3 (2500)	0.310 (45.0)	2.44 (354)	9.93 (1440)	0.310 (45.0)	6.11 (886)
Ref. 35 Damping = 1%	20.1 (2920)	0.310 (45.0)	3.01 (436)	11.1 (1610)	0.310 (45.0)	7.52 (1090)
Ref. 35 Damping = 2%	16.8 (2440)	0.310 (45.0)	2.36 (342)	9.72 (1410)	0.310 (45.0)	5.90 (856)
Ref. 35 Damping = 4%	14.4 (2090)	0.310 (45.0)	1.88 (272)	8.76 (1270)	0.310 (45.0)	4.68 (679)
Ref. 7 Damping = 1%	18.4 (2670)	0.310 (45.0)	2.61 (378)	10.5 (1530)	0.310 (45.0)	6.52 (945)
Ref. 7 Damping = 2%	16.3 (2370)	0.310 (45.0)	2.20 (319)	9.69 (1410)	0.310 (45.0)	5.50 (797)
Ref. 7 Damping = 4%	14.6 (2120)	0.310 (45.0)	1.88 (272)	8.96 (1300)	0.310 (45.0)	4.68 (679)
SSI Damping = 5%	13.8 (2000)	0.310 (45.0)	1.72 (249)	8.61 (1250)	0.310 (45.0)	4.29 (622)

The procedure used to determine the ZPA value that corresponds to incipient buckling for a generic state of stress is presented in Section III D. Table IX summarizes the resulting values of the ZPA that led to the condition of incipient buckling, as defined by N-284.

The hazard curves, shown for an eastern U.S. site in Fig. 8 (Ref 39), can be used to estimate the probability that an earthquake with a ZPA given in Table IX, or greater, will occur in a given year. As an example, the annual probability of exceedance of a 0.26-g's ZPA earthquake (obtained from the analysis of the R/t = 645 structure using the Reg. Guide 1.60 spectrum and assuming 1% damping) ranges from 1.15×10^{-5} to 1×10^{-3}, depending on which hazard curve is used (LLNL or EPRI, mean or median). This range decreases to 1×10^{-5} to 9×10^{-4} for a 0.29-g's ZPA, and further reduces to 7×10^{-6} to 6×10^{-4} for a 0.35-g's ZPA earthquake.

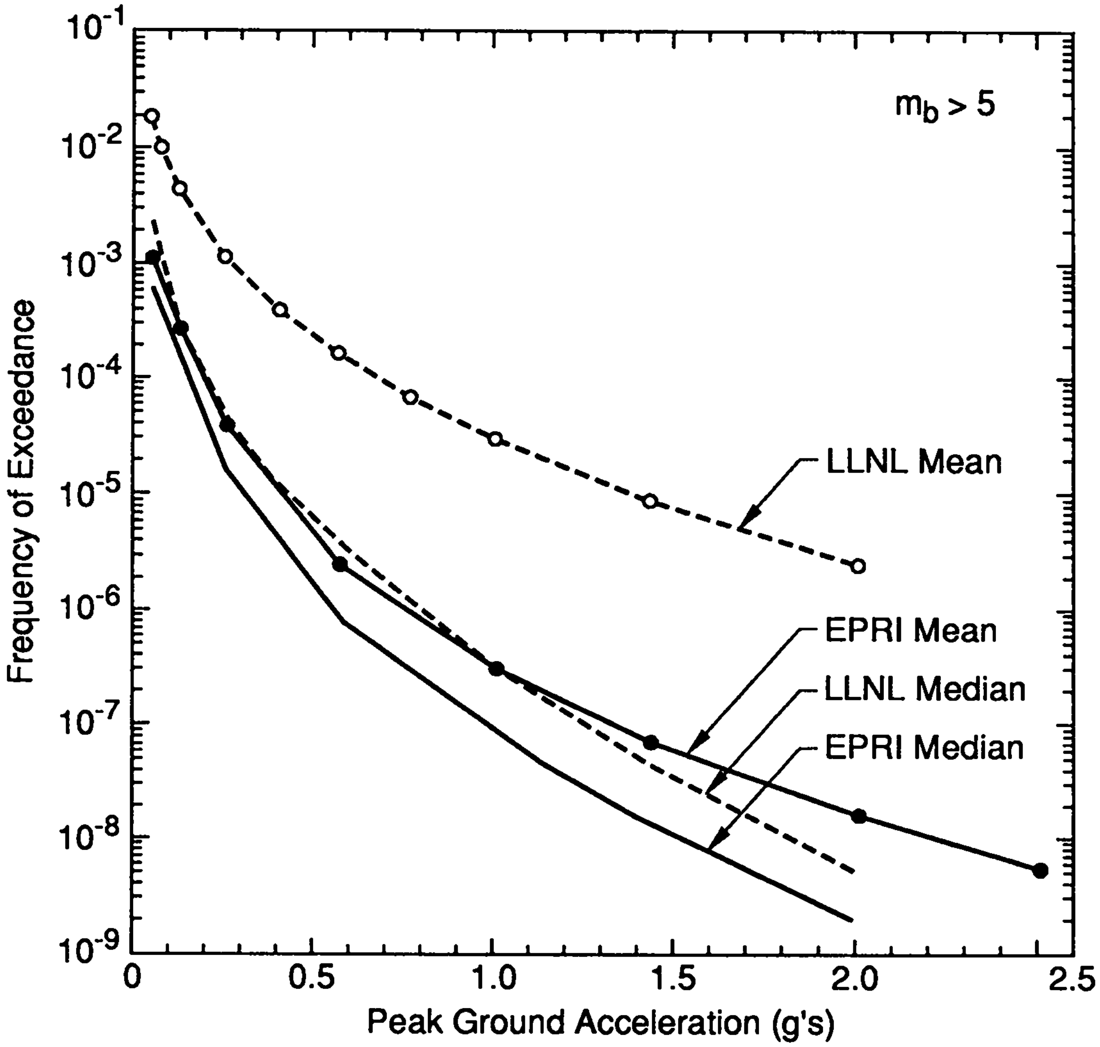

Fig. 8 Typical seismic hazard curves for an eastern U.S. site.

TABLE VIII

N-284 INTERACTION EQUATION VALUES

	Reg. Guide 1.60 Spectra			Ref. 35 Spectra			Ref. 7 Spectra			SSI Spectrum
Point	1%	2%	4%	1%	2%	4%	1%	2%	4%	5%
R/t=645										
1	1.03	0.96	0.79	0.96	0.76	0.63	0.84	0.72	0.63	0.60
2	1.57	1.17	0.70	1.17	0.67	0.48	0.80	0.59	0.48	0.45
R/t=450										
1	0.50	0.46	0.39	0.46	0.38	0.31	0.41	0.36	0.31	0.30
2	0.29	0.27	0.22	0.27	0.22	0.18	0.24	0.21	0.19	0.18

TABLE IX

FREE-FIELD ZPA VALUES THAT WILL PRODUCE AN INCIPIENT BUCKLING CONDITION

Damping	Reg. Guide 1.60 Spectra	Ref. 35 Spectra	Ref. 7 Spectra	SSI Spectrum[a]
R/t=645				
1%	0.26 g's	0.29 g's	0.33 g's	-
2%	0.29 g's	0.36 g's	0.38 g's	-
4%	0.35 g's	0.46 g's	0.45 g's	-
5%	-	-	-	0.49 g's
R/t=450				-
1%	0.58 g's	0.63 g's	0.72 g's	
2%	0.63 g's	0.80 g's	0.85 g's	-
4%	0.77 g's	1.04 g's	1.00 g's	-
5%	-	-	-	1.09 g's

[a] This analysis assumes that the 0.55-g's ZPA given in the SSI spectrum is a linear function of the free-field ZPA.

The primary limitation of this simplified analysis is that it cannot adequately handle the circumferential components of stress that arise when the containment is subjected to multiple components of seismic excitation. A three-dimensional finite element analysis was performed to gain a better understanding of the effects of the hoop stress component on containment buckling.

VI. NUMERICAL ANALYSIS OF THE CONTAINMENTS

A. Selection of the Analysis Method

Using ABAQUS,[40] a conventional finite element modal analysis was performed to determine the frequencies of the various response modes of the containment shell. Axisymmetric half models of the containment shells, shown in Figs. 9 and 10, were generated using the eight-node quadratic shell element in ABAQUS. The results are shown in Figs. 11 and 12 for some of the lower shell modes. These results were confirmed by performing a similar analysis with the BOSOR finite difference code. The fundamental shear-bending mode (n=1), shown in Fig. 13 for the R/t=645 structure, occurs at approximately 7.1 Hz for both structures, as mentioned earlier. Even within a frequency band of 1 Hz about the fundamental shear-bending mode, a large number of shell modes can be seen in Figs. 11 and 12. Because ABAQUS does not allow one to specify the particular modes to be used in a response spectrum analysis, the excessive number of low-frequency shell modes between the fundamental shear-bending mode and the fundamental axial translation mode makes it impractical to solve this problem by using the commonly used modal response spectrum approach. Therefore, the transient-time integration approach was chosen, and both the measured and the artificial earthquake acceleration-time histories were used as input to the base of the structure.

B. Specification of the Seismic Input

Actual recorded earthquake signals were first used in the time-history analysis. Various combinations of seismic excitation were applied to the base of the ABAQUS containment models in the two horizontal directions (global X and Y) and in the vertical direction (global Z). The seismic acceleration-time histories used in this study are the strong motion portions (6-s duration) of the 1940 El Centro N-S component; the 1949 Olympia N86E component; and the 1935 Helena west component, scaled to a peak acceleration of 0.3 g's. These acceleration-time histories are shown in Fig. 14. The strong motion portions of these signals were aligned in time so that they would simulate an actual seismic event.

A correlation analysis[41] was performed between the El Centro and Helena, El Centro and Olympia, and Helena and Olympia acceleration-time histories. These three signals were uncorrelated and they satisfied the ASCE 4-86 (Ref. 25) criteria concerning the magnitude of the correlation coefficient (all were less than 0.3). Therefore, the use of these three different earthquakes in the study assured that the three input components were randomly phased

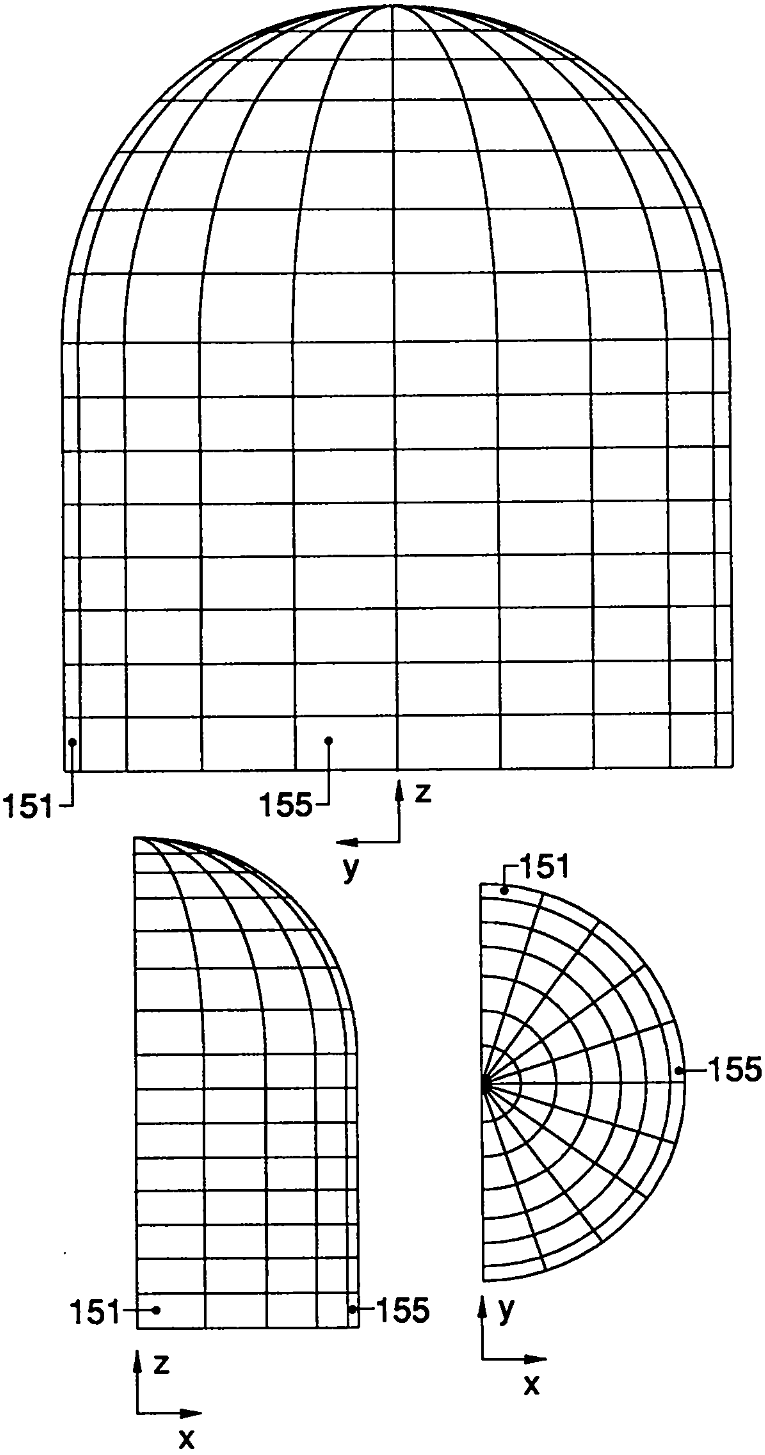

Fig. 9 Axisymmetric finite element model of the R/t = 645 containment.

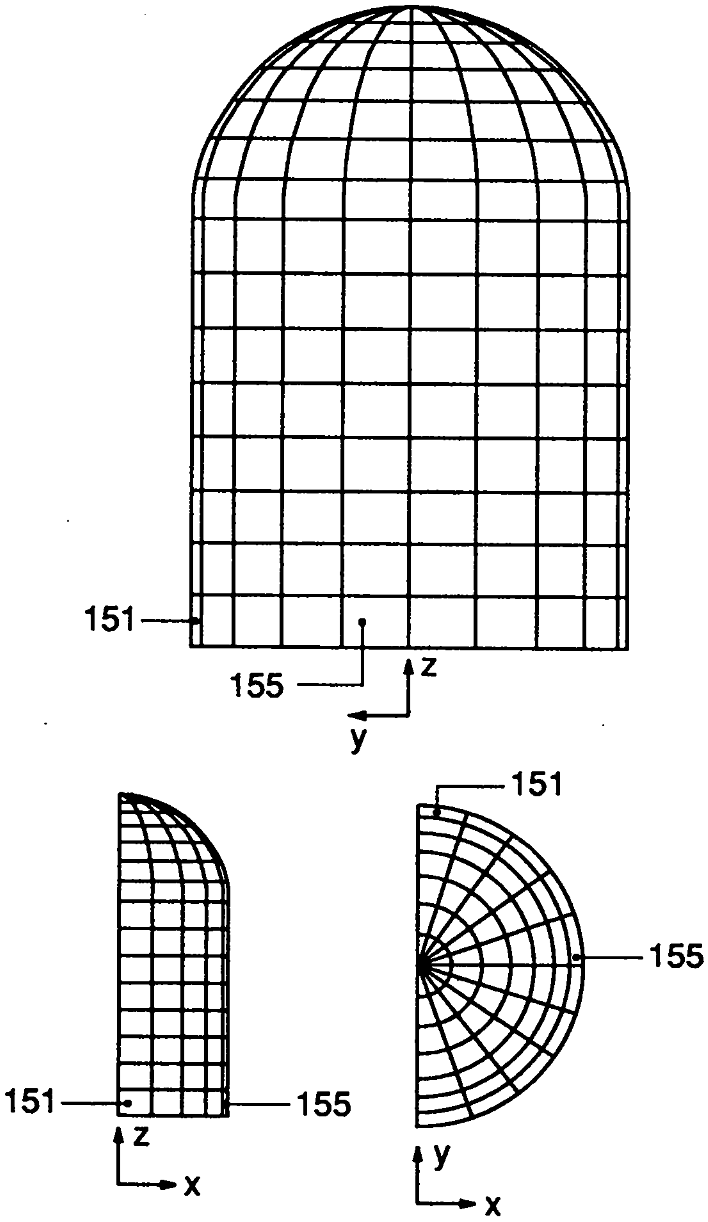

Fig. 10 Axisymmetric finite element model of the R/t = 450 containment.

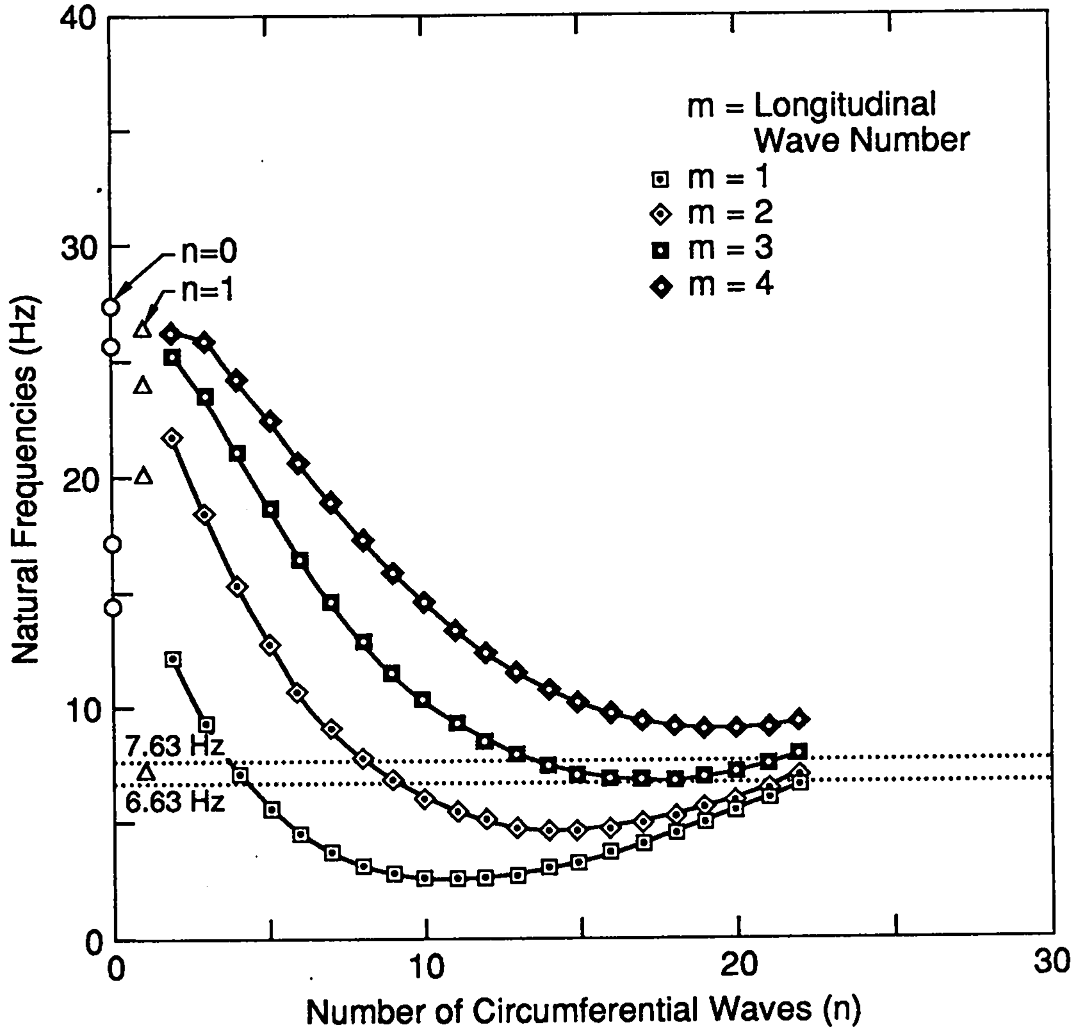

Fig. 11 Natural frequencies of the R/t=645 containment structure.

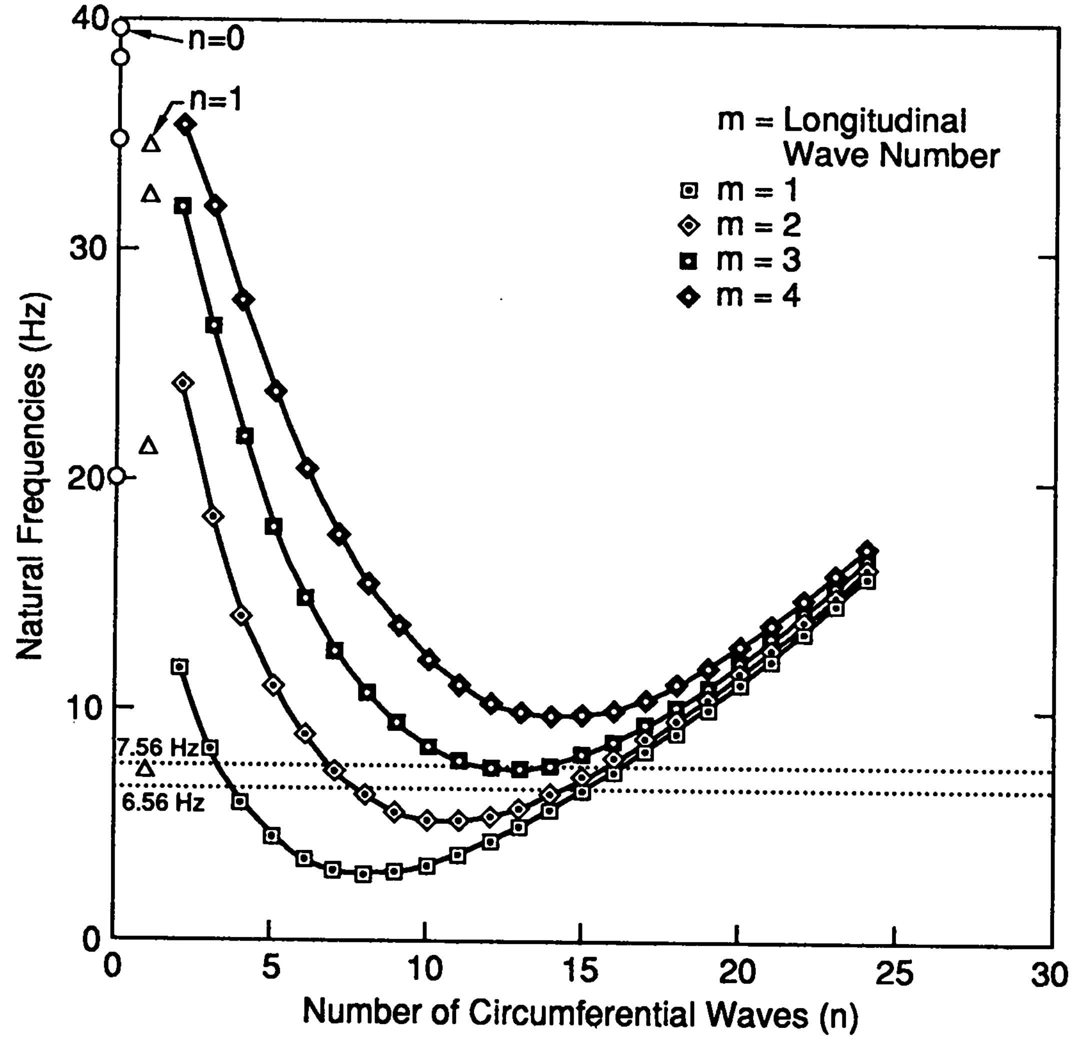

Fig. 12 Natural frequencies of the R/t=450 containment structure.

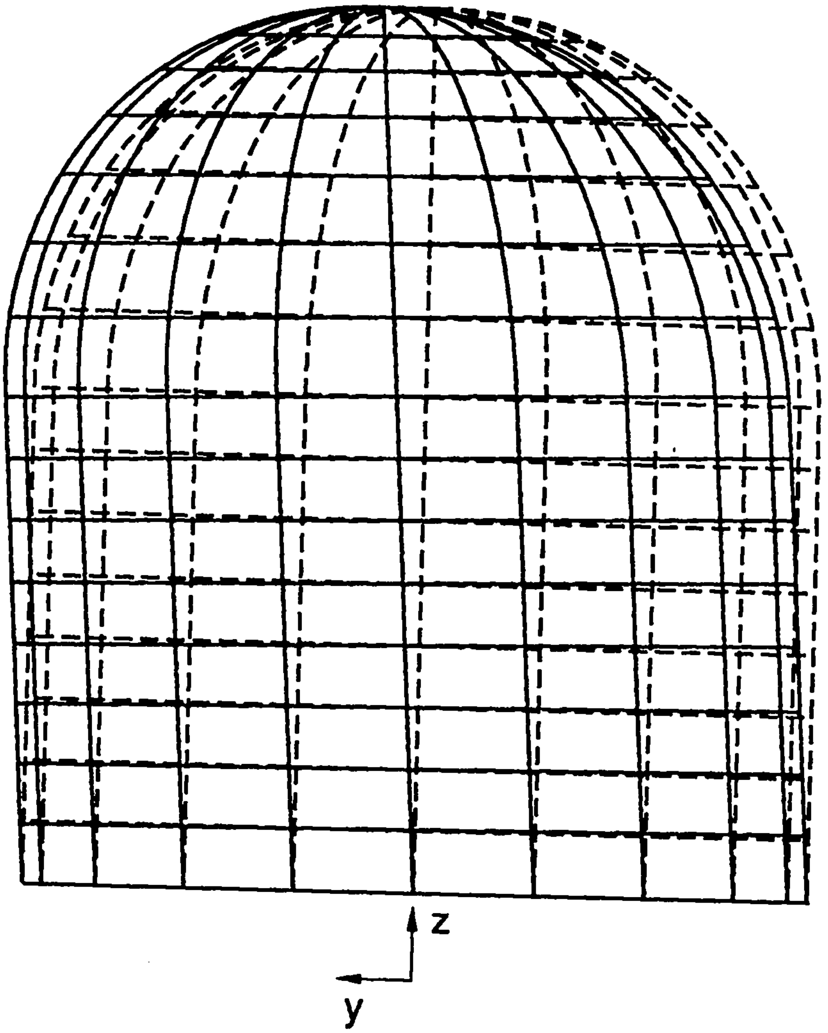

Fig. 13 Fundamental shear-bending mode of the R/t=645 containment calculated with ABAQUS.

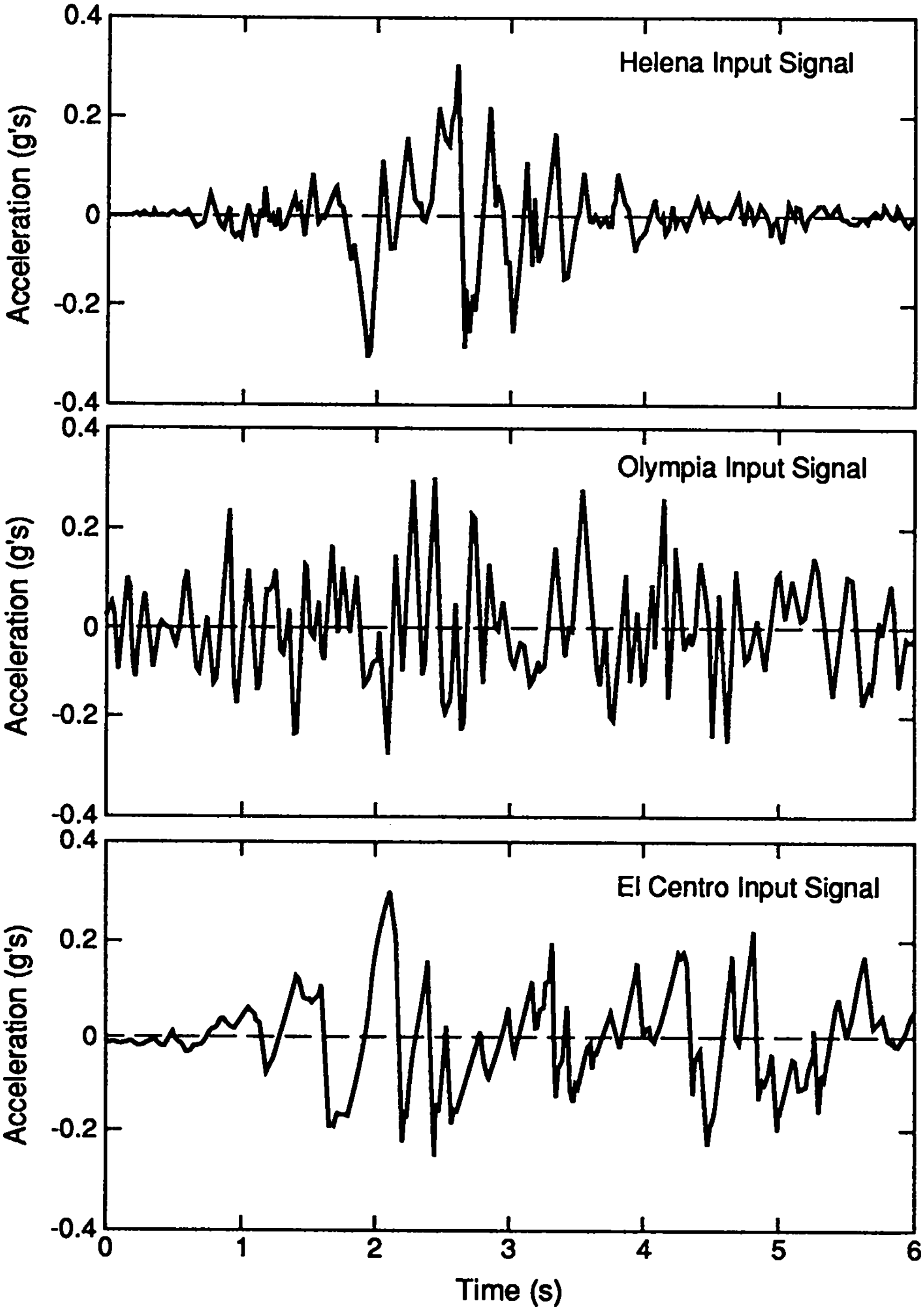

Fig. 14 Measured earthquakes signals used in the time-history analyses.

Next, a computer program was developed that is capable of generating an earthquake time-history whose response spectra will envelope target or design response spectra. The method of generating artificial earthquake signals reported in Ref. 42 was chosen. This method applies an envelope function that has the characteristic build-up, strong motion, and decay portions previously observed in actual measured earthquake time-histories to a random oscillatory function of time. Thus, the time history is generated by the function,

$$\ddot{z}(t) = E(t) \sum_{n=1}^{N} A_n \cos\left(\omega_n t + \phi_n\right), \tag{37}$$

where $\ddot{z}(t)$ = the artificial earthquake acceleration-time history,
$E(t)$ = the envelope function,
ϕ_n = a random phase angle on the interval $(0,2\pi)$,
ω_n = $2\pi n/T$, and
T = the duration of the strong motion portion of the signal.

The number of terms in the summation, N, is chosen such that N/T includes all frequencies in the target spectra. The coefficients A_n are defined in terms of the Fourier transform of the strong motion part of $\ddot{z}(t)$. The strong motion portion of $\ddot{z}(t)$ is referred to as $\ddot{z}_p(t)$. The Fourier transform of $\ddot{z}_p(t)$ is defined as

$$F(\omega) = \int_0^T \ddot{z}_p(t) e^{-i\omega t} dt, \tag{38}$$

and the coefficients A_n can then be defined as

$$A_n = \frac{2}{T} |F(\omega)|. \tag{39}$$

It is necessary to have some starting approximation for A_n, and the one used in this method is based on the fact that the zero-damping pseudovelocity response spectrum curve, $S_v(\omega)$, is closely approximated by the absolute value $|F(\omega)|$. Thus, as starting approximation, we take $A_n = (2/T)\, S_v(\omega)$, which gives a conservative approximation of the target spectra.

Next, for a given set of random phase angles, an iteration is carried out to improve on the A_n values so that

$$A_n' = \frac{(S_v(\omega))_{target}}{S_v(\omega)} A_n , \tag{40}$$

where A_n''s are the new values of the Fourier coefficients to be used in the next iteration of signal generation. The enveloping of the required spectra is enhanced by setting the target spectra a few percent higher than the required spectra.

Once an earthquake has been generated that satisfies the basic spectral requirements, new sets of random numbers can be used to generate another time history that also envelopes the target spectra. The additional signals are necessary when an analysis requires input from multiple components of statistically independent earthquake signals, as most seismic analyses do.

As an example, Fig. 15 shows both the NRC Reg. Guide 1.60 (Ref. 34) pseudovelocity response spectrum for 2% damping that corresponds to a 1-g zero-period acceleration ground motion and the estimated 0% damping curve used as a first approximation for the Fourier coefficients, A_n. Figure 16 shows the enveloping function that was used in this example. Figure 17 shows the artificial earthquake generated using the 0% estimate for a first approximation for A_n, and Fig. 18 shows the 2% damping acceleration spectrum from the generated earthquake, as compared with the 2% damping Reg. Guide 1.60 acceleration spectrum (the smooth curve is the Reg. Guide 1.60 spectrum). Figure 19 shows the improved spectrum that results from three iterations. The zero-period acceleration values from the target spectrum were increased by 5% to aid in the convergence on the desired spectrum. After further iterations and a baseline correction of the signal, Figs. 20 and 21 show the final time history and its corresponding 2% damping acceleration response spectra in comparison with the 2% damping Reg. Guide 1.60 acceleration spectrum.

This computer code was first used to generate three statistically independent, 3-s-long, artificial time histories whose response spectra enveloped the Reg. Guide 1.60 design spectra. These three acceleration-time histories, and the comparison of the response spectra generated from these time histories to the Reg. Guide 1.60 spectrum, are shown in Figs. 22 and 23, respectively. The statistical independence of the three signals was again verified by performing a correlation analysis similar to the one previously described for the Helena, El Centro, and Olympia signals.

Next, three statistically independent artificial time histories, whose response spectra enveloped the spectrum that includes the effects of soil-structure interaction (Ref. 36, Fig. 6), were generated. Figures 24 and 25 show the generated acceleration-time histories and a comparison of the actual and target spectra.

Finally, artificial time histories that enveloped the eastern U.S. design spectra shown in Fig. 5 (Ref. 7) were generated. These acceleration-time histories are shown in Fig. 26. Figure 27 compares the corresponding response spectra to the target

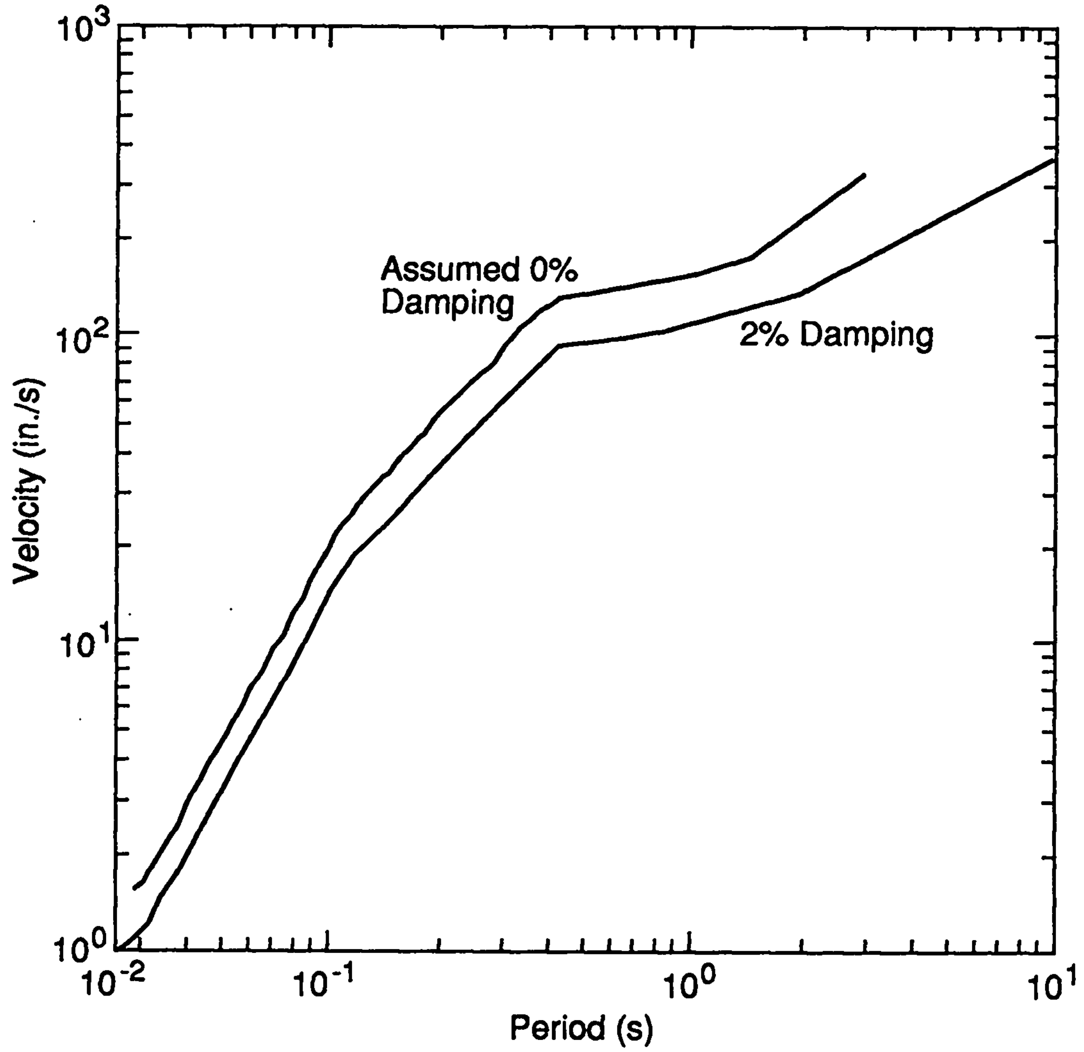

Fig. 15 Reg. Guide 1.60 2% damping response spectrum and the estimated 0% damping response spectrum.

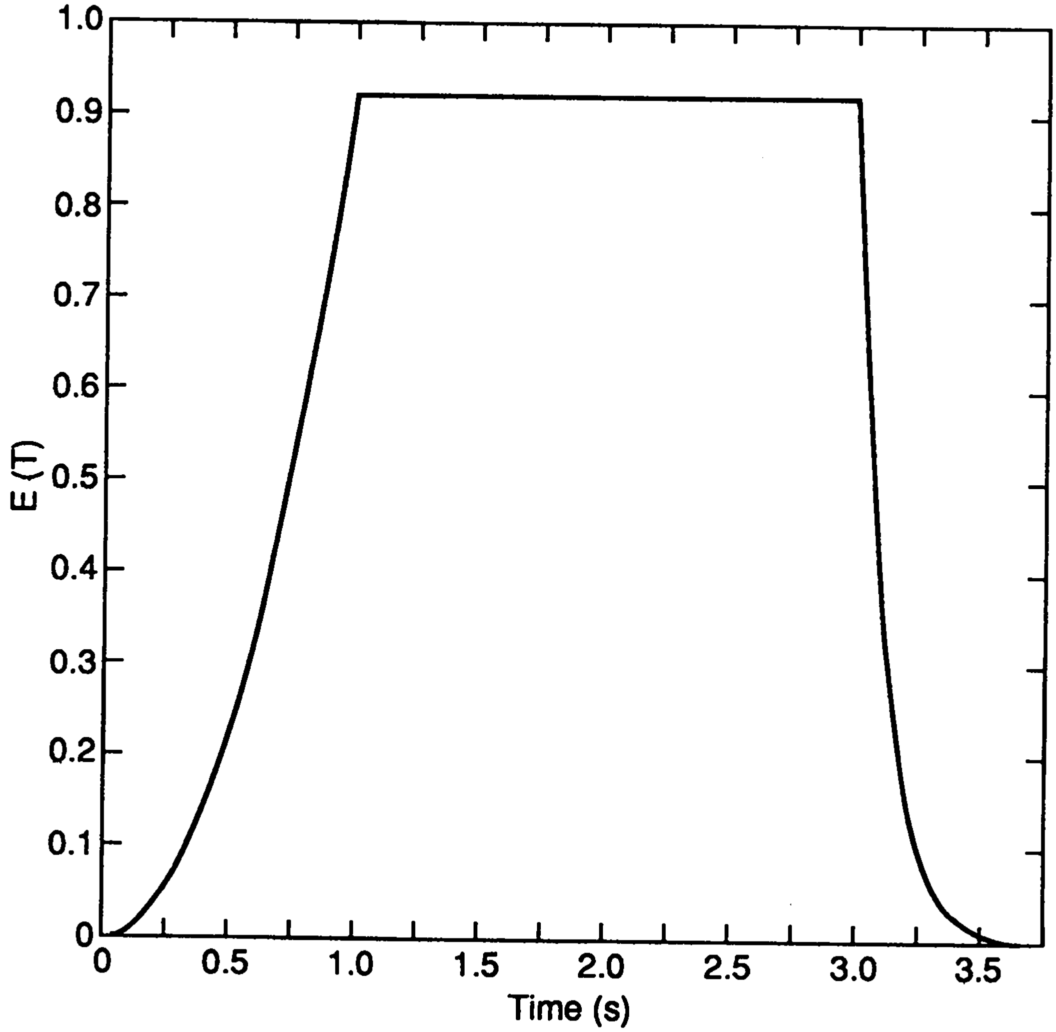

Fig. 16 Enveloping function used to generate the artificial earthquake signals.

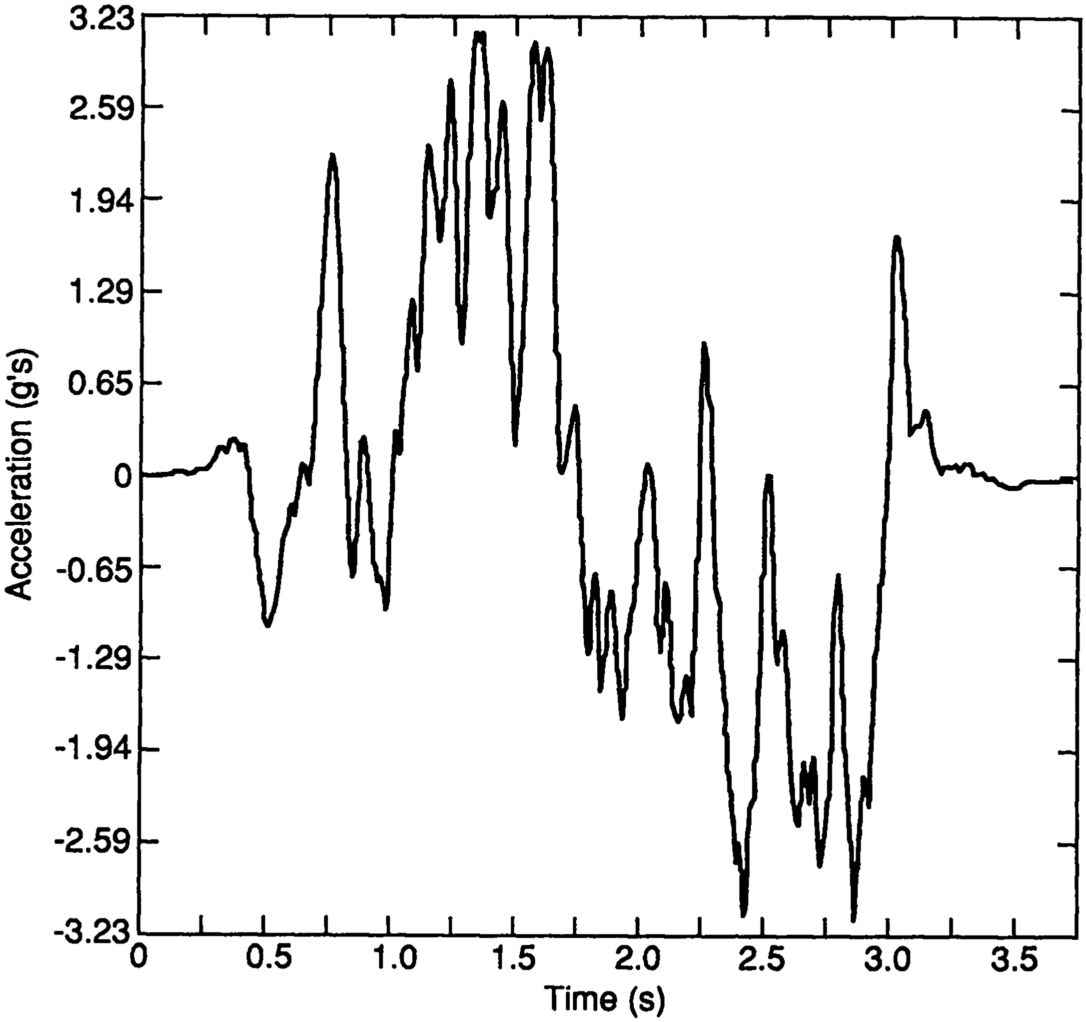

Fig. 17 First approximation artificial earthquake.

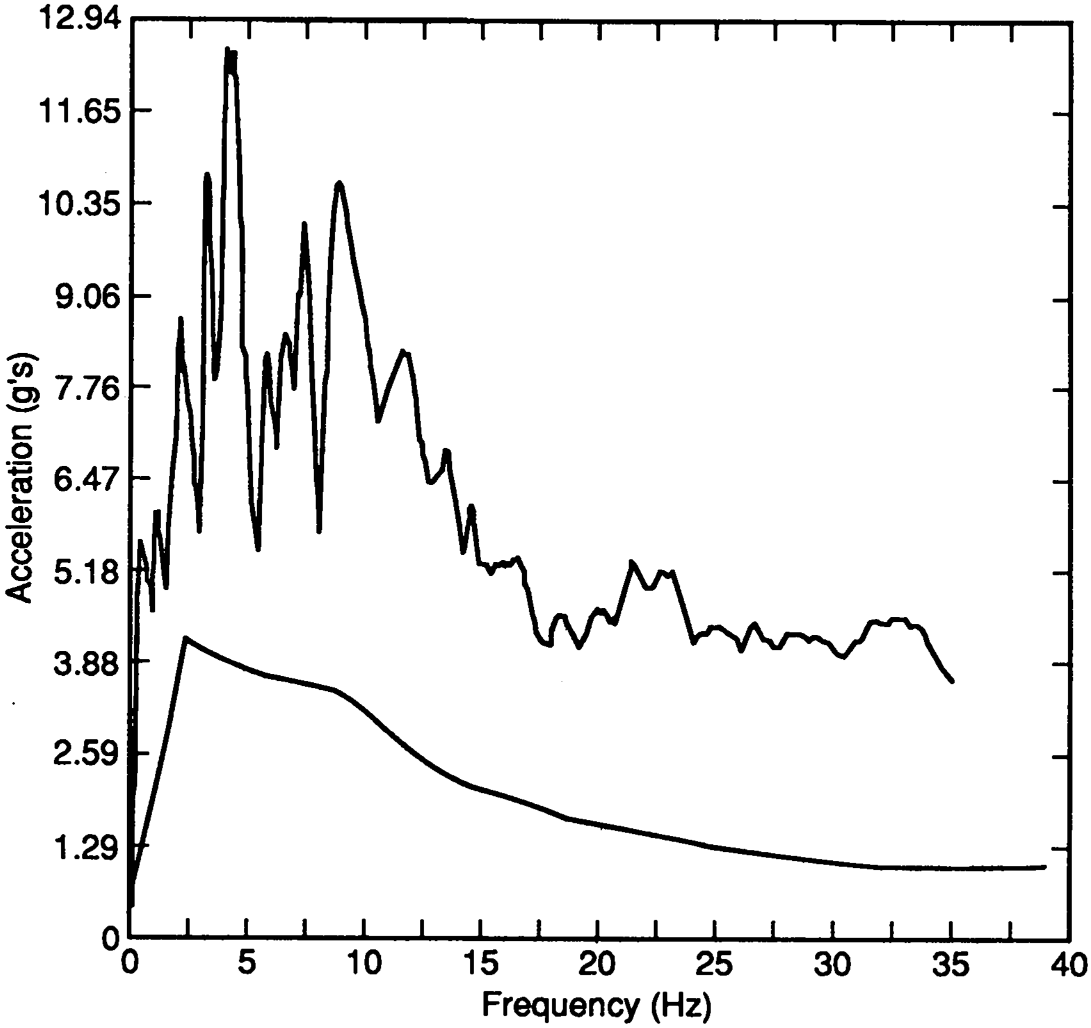

Fig. 18 The 2% damping response spectrum generated from the artificial signal compared with the 2% damping Reg. Guide 1.60 spectrum.

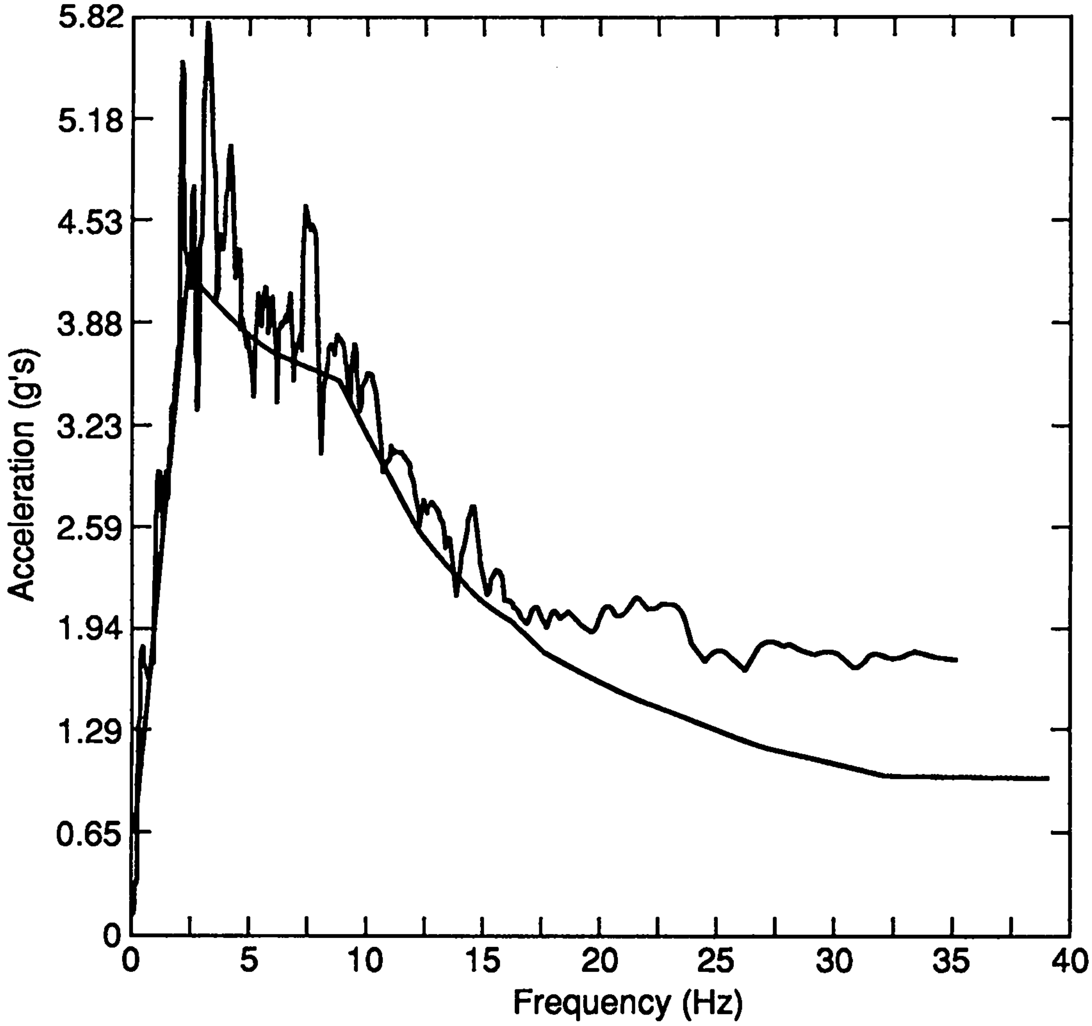

Fig. 19 After 3 iterations, the 2% damping response spectrum corresponding to the artificial earthquake compared with the 2% damping Reg. Guide 1.60 spectrum.

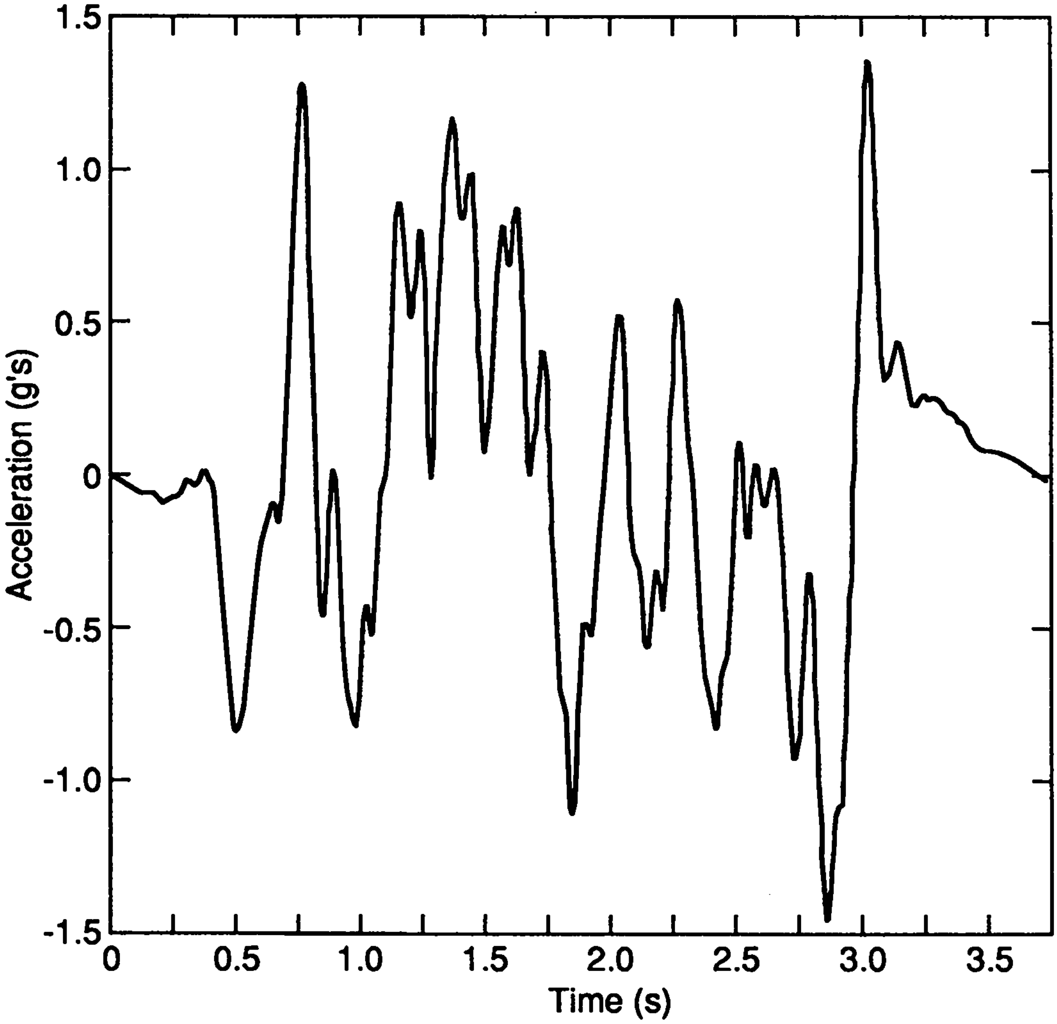

Fig. 20 Final artificial acceleration-time history.

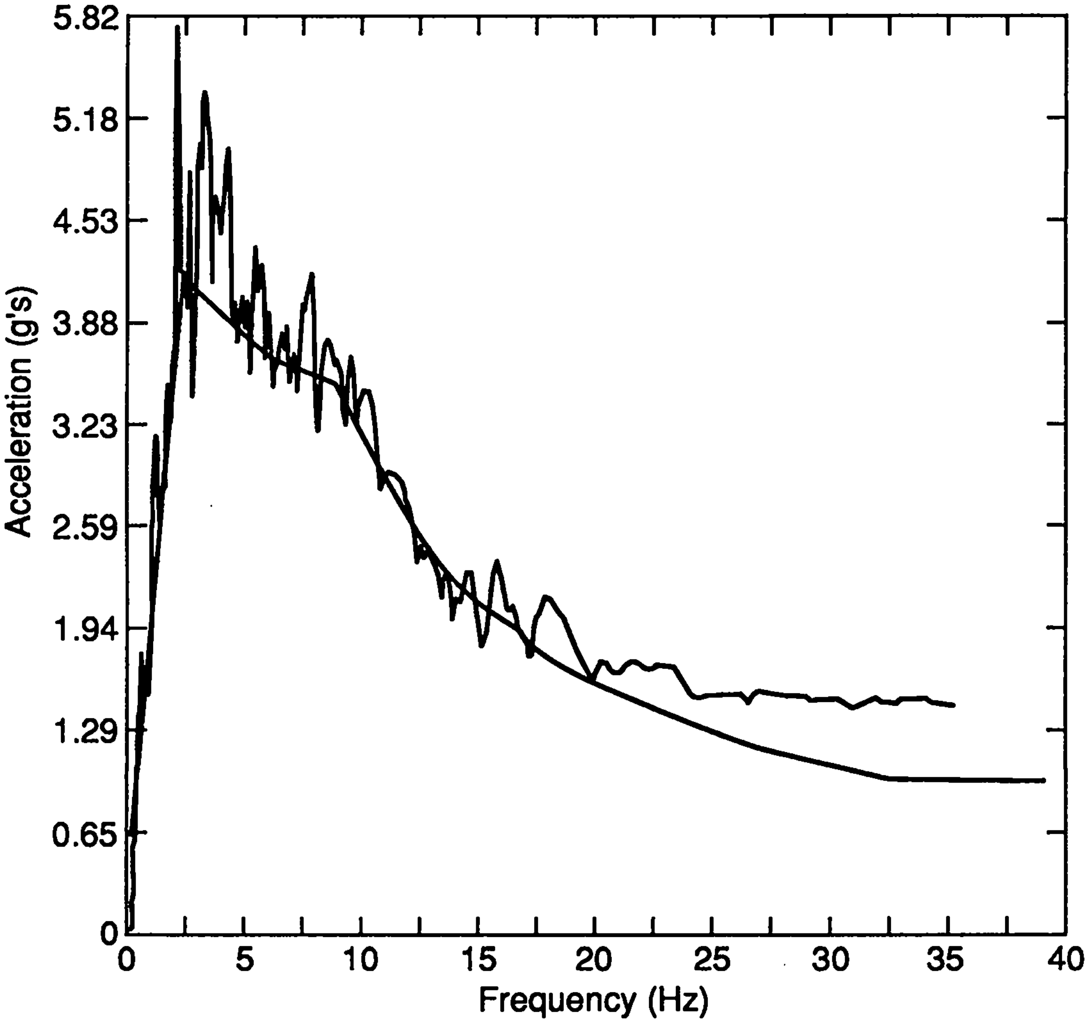

Fig. 21 The 2% damping response spectrum corresponding to the final artificial acceleration-time history compared with the 2% damping Reg. Guide 1.60 spectrum.

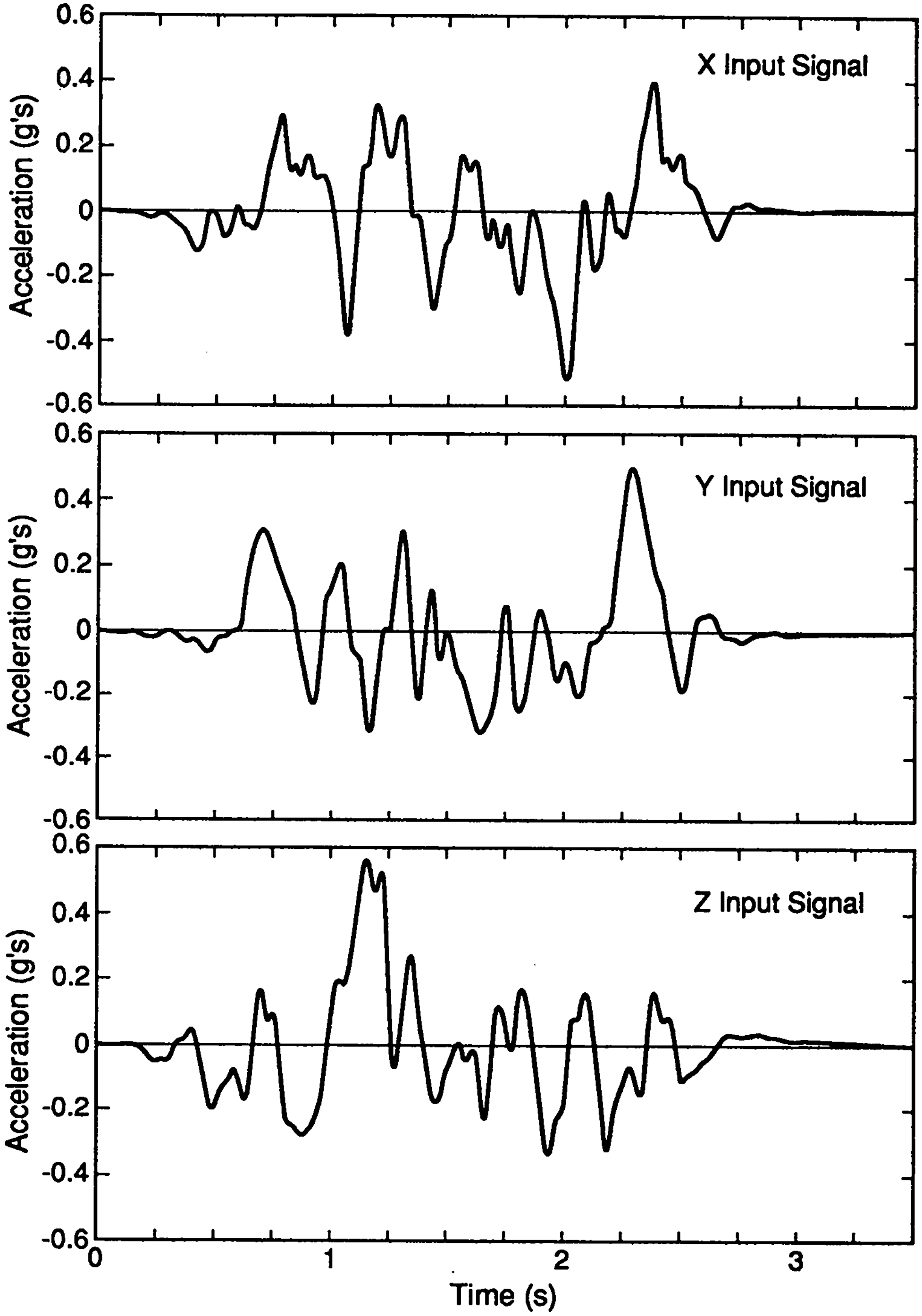

Fig. 22 Artificial time histories whose response spectra envelope the Reg. Guide 1.60 spectra.

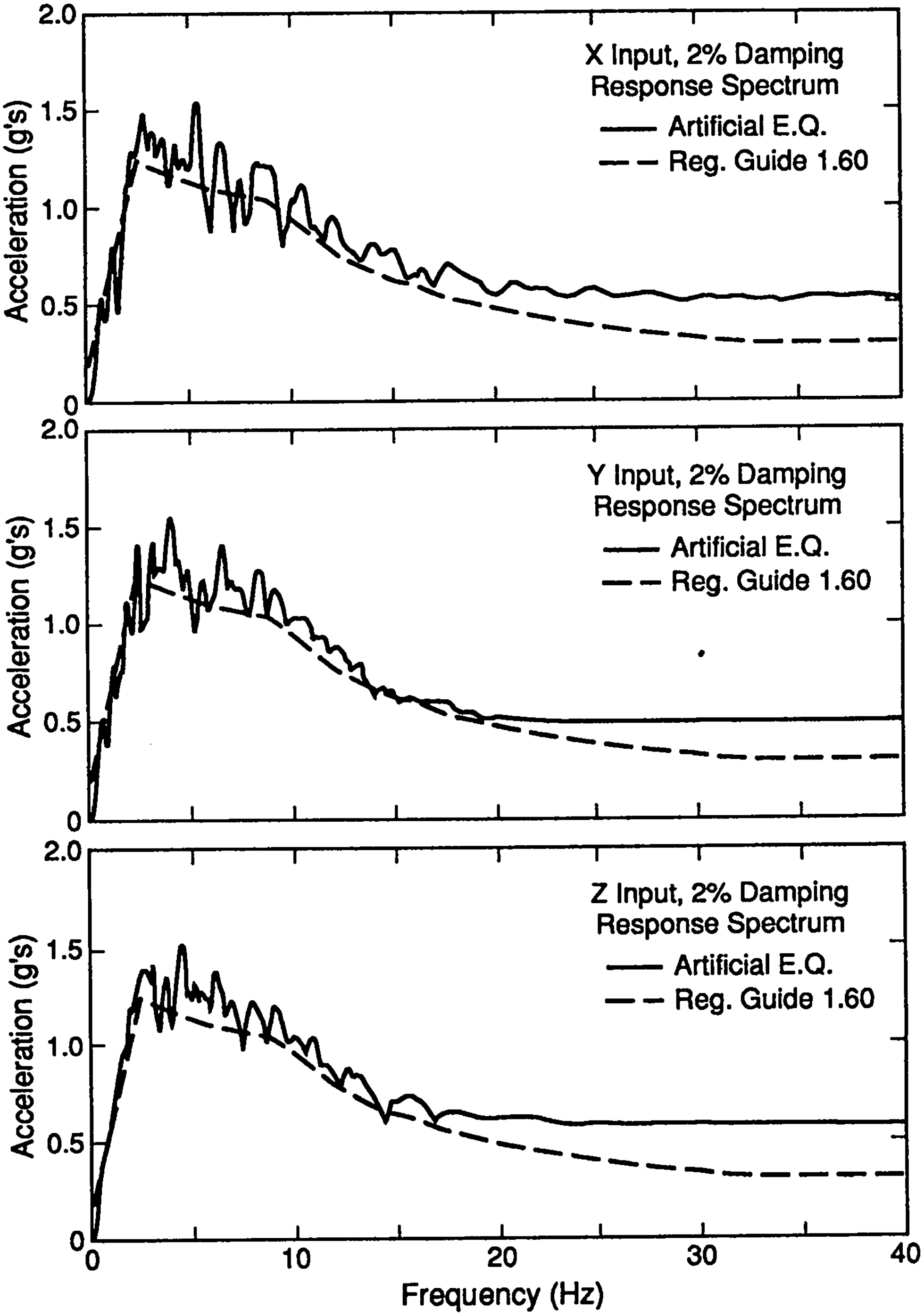

Fig. 23 Comparison of the 2% damping response spectra corresponding to the artificial time histories with the Reg. Guide 1.60 2% damping spectra.

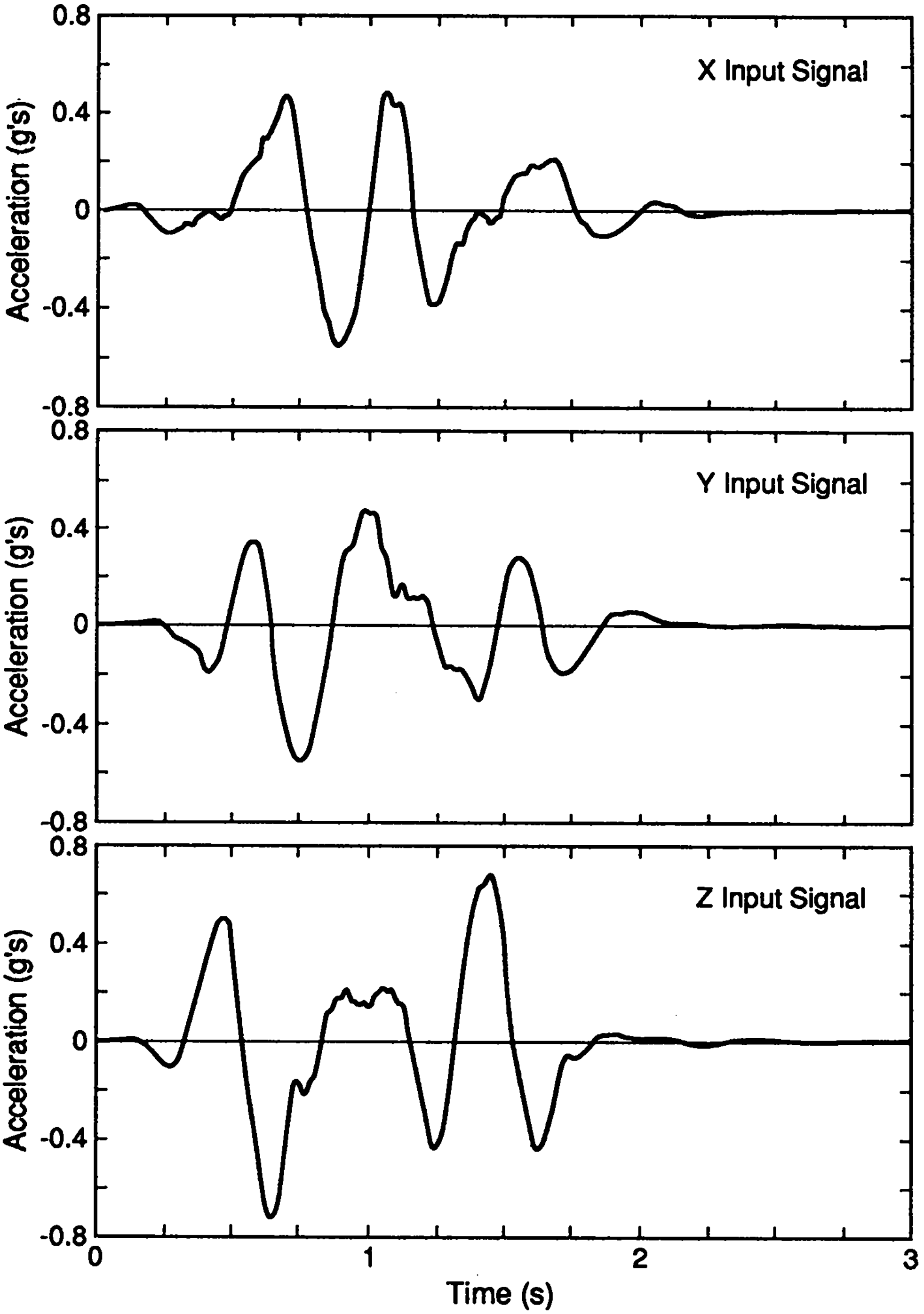

Fig. 24 Artificial time histories whose response spectra envelope the 5% damping spectra generated from a soil-structure interaction analysis.

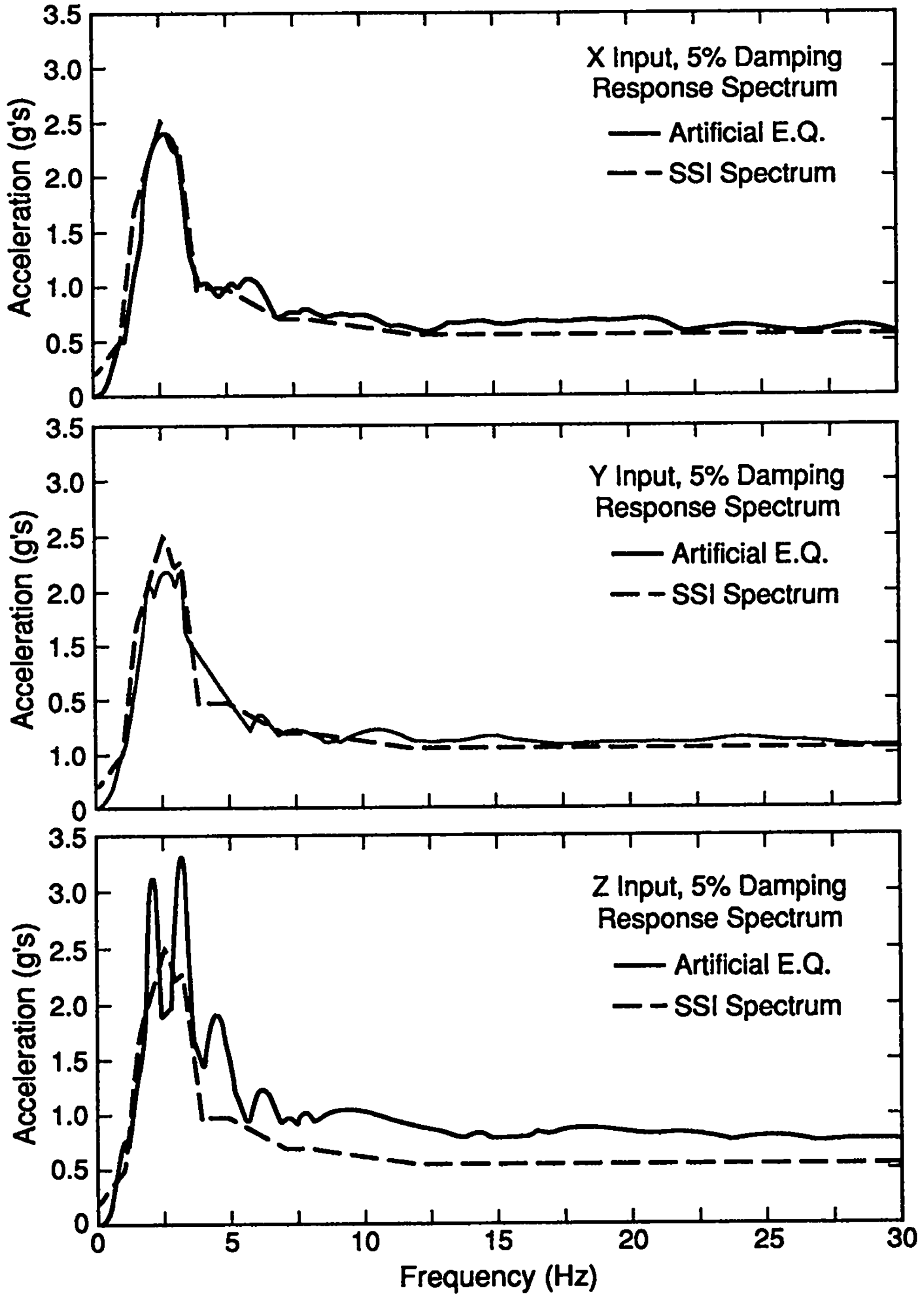

Fig. 25 Comparison of the 5% damping response spectra corresponding to the artificial time histories with the 5% damping spectra generated from a soil-structure interaction analysis.

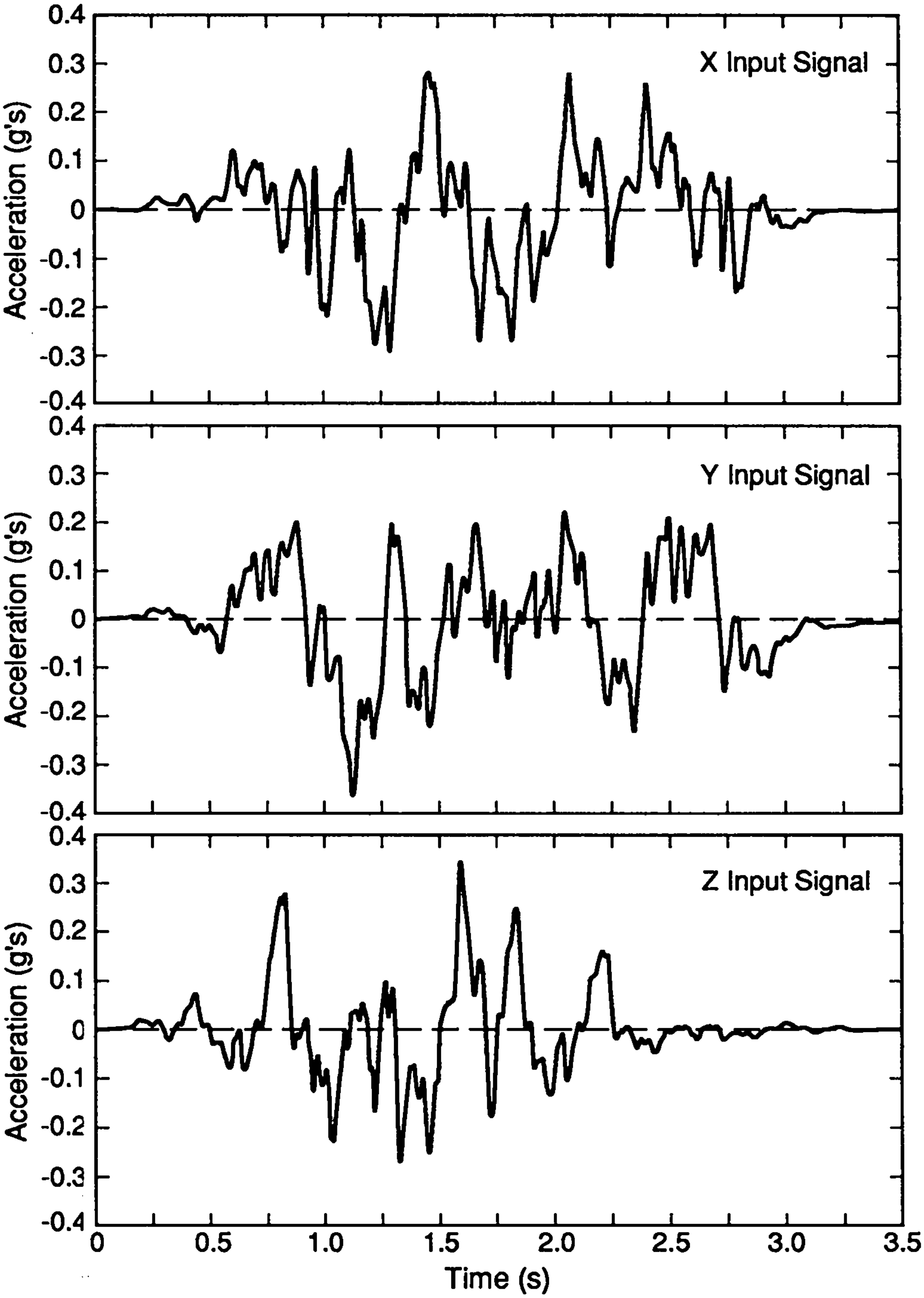

Fig. 26 Artificial time histories whose response spectra envelope an eastern U.S. design spectra.

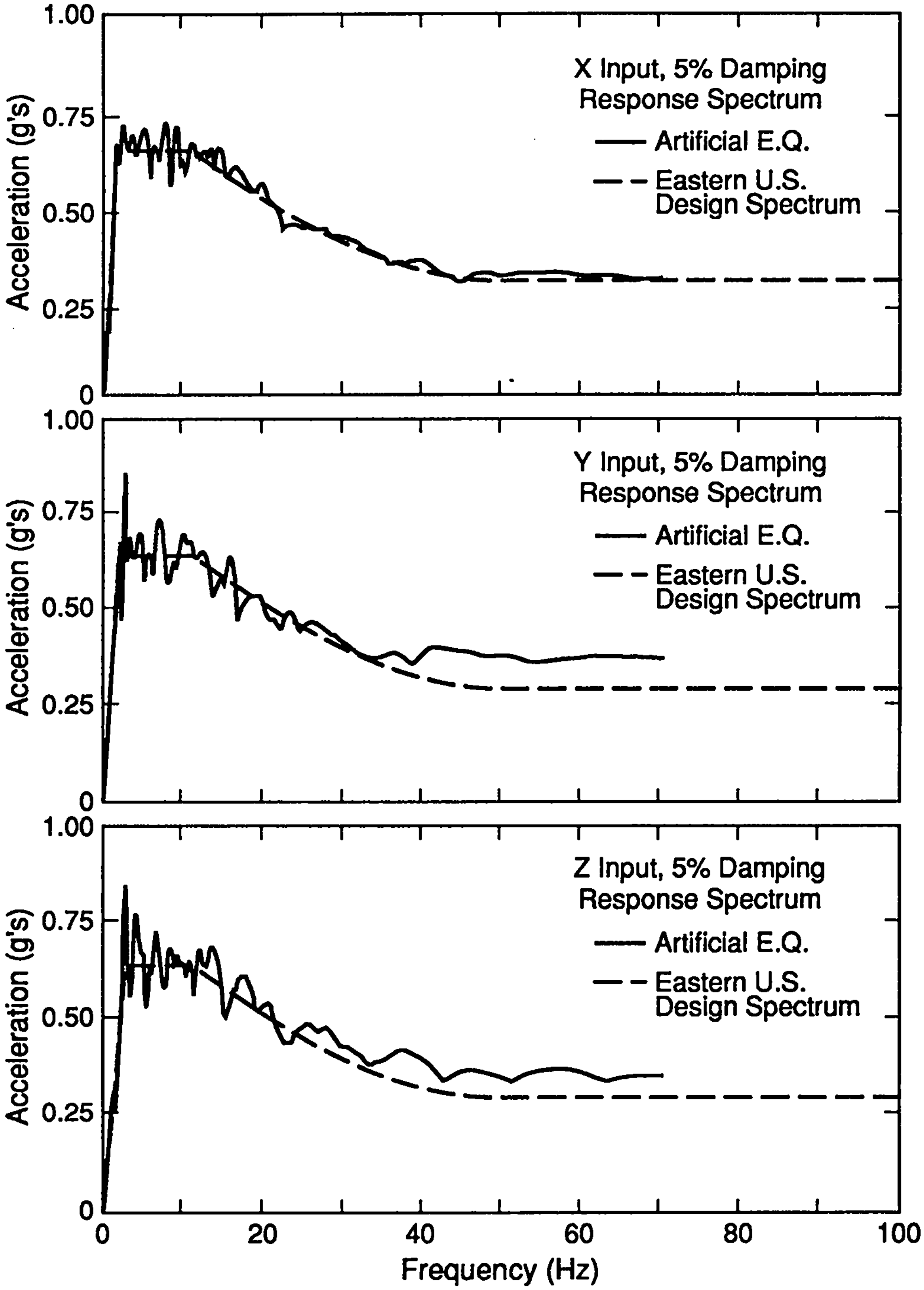

Fig. 27 Comparison of the 5% damping response spectra corresponding to the artificial time histories with an eastern U.S. 5% damping design spectra.

spectrum. All combinations of the three artificial time histories were found to meet the ASCE 4-86 requirements concerning their respective correlation coefficients, thus demonstrating the statistical independence of the three input components.

C. Discussion of Input Acceleration-Time Histories

Acceleration response spectra for the El Centro, Olympia, and Helena (scaled to 1-g peak acceleration) are shown in Fig. 28, for 1% damping. An examination of these figures shows that the peak dynamic amplification at 7.1 Hz, the frequency of the fundamental shear-bending mode, is greatest (8.5) for the Olympia spectrum; the El Centro spectrum has a corresponding amplification of 2.8, and the Helena spectrum's amplification factor is 3.2.

It is interesting to compare corresponding dynamic amplifications for 1% damping at 7.1 Hz, based on Reg. Guide 1.60 (Ref. 34), 4.0, with the eastern-U.S. site-specific design spectra (Ref. 7) 3.2, given in Table II. Clearly, the Olympia acceleration input signal significantly exceeds the site-independent or site-specific amplifications at this frequency. The authors are unaware of any site-independent or site-specific design spectra that would specify such a large amplification factor at 7.1 Hz. The amplification factor for 7.1 Hz given by the Reg. Guide 1.60 site-independent spectra or eastern-U.S. site-specific spectra are typical of all of the design spectra the authors have examined. Amplification factors from the Helena and El Centro spectrums are comparable to those given by these design spectra.

Initially, all earthquake inputs (both measured and artificial) except those resulting from the soil-structure interaction analysis, were scaled to 0.3 g's-peak or ZPA. The vertical components were then scaled by an additional factor of 0.67, as specified in ASCE 4-86 (Ref. 25) and Reg. Guide 1.60. The LLNL design spectra specified a vertical component explicitly; hence, no scale factor was applied to the corresponding vertical component of the artificial earthquake. A 0.3-g's free-field input, corresponding to a Reg. Guide 1.60 spectra, was applied to the SSI model.[36] The resulting input calculated for the base of the containment had a ZPA of 0.55 g's in the horizontal direction and 0.45 g's in the vertical direction. Therefore, a factor of 0.82 was used to scale the vertical component of the artificial earthquake that was generated from the horizontal spectrum.

D. Specification of Damping

When transient time integration is used, the solution of this type of problem is simplified by using proportional damping of the form

$$\mathbf{C} = \alpha\mathbf{M} + \beta\mathbf{K} \tag{41}$$

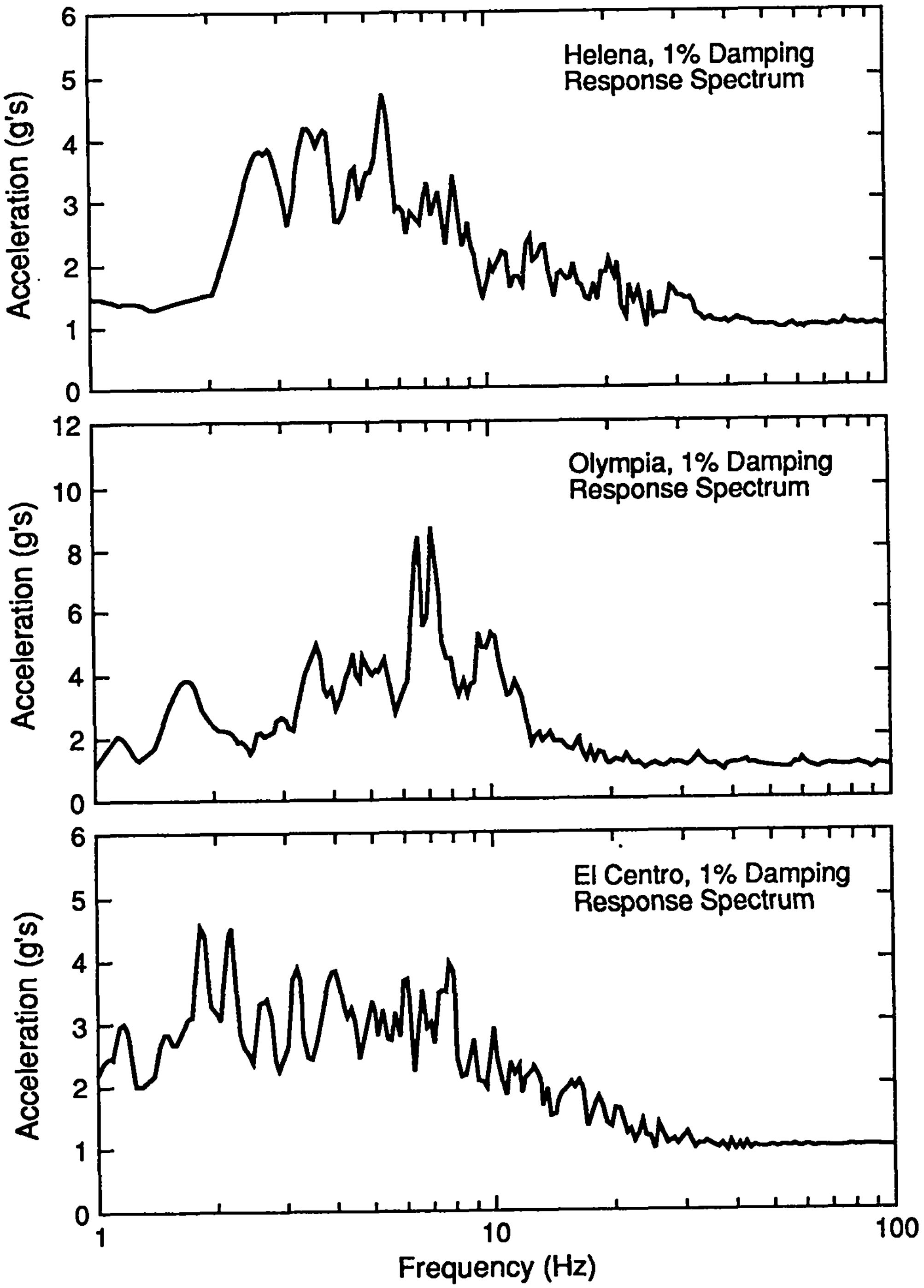

Fig. 28 The 1% damping response spectra corresponding to the El Centro, Olympia, and Helena earthquake components used in the time-history analyses.

rather than viscous damping. Here, **C** is the damping matrix, α and β are constants, **M** denotes the mass matrix of the modeled structure, and **K** denotes the stiffness matrix. This proportional damping is related to modal viscous damping in Ref. 33 by

$$2\zeta_i \omega_i = \alpha + \beta\omega_i^2 \tag{42}$$

where ζ_i and ω_i represent the viscous damping factor (fraction of critical damping) and circular natural frequency of the ith mode of the structure, respectively. Based on a specified viscous damping factor, α and β are determined from Eq. (42). The following approach was adopted for determining these quantities:

1. The response of the containment shell depends heavily on the fundamental shear-bending mode of the shell. Therefore, the proportionality constants, α and β, at that frequency are selected such that Eq. (42) is satisfied for 1% damping.

2. The damping should be equal to (ideally) or greater than the damping of the dominant mode at all other significant modes of the structure. This method of selecting a damping value will introduce some bias in the results of this study because the calculated structural response will be equal to or less than the actual response if the structure does, in fact, respond with 1% damping at all modes.

The proportionality coefficients of $\alpha = 0$ and $\beta = 0.000424$ can be shown to result in an equivalent viscous damping of 1% at a natural frequency of 7.1 Hz (the frequency of the containments' shear-bending mode). With these values, the equivalent viscous damping monotonically increases to approximately 4% at 30 Hz.

E. Finite Element Analysis

Runs were first made to determine the appropriate equilibrium tolerances and the time-step size necessary to obtain convergence. The equilibrium tolerances and time-step size were reduced by factors of 10 until two successive runs gave responses (lateral displacement of the top of the containment) that did not vary by more than 10%, as specified in ASCE 4-86 (Ref. 25). Based on the equilibrium tolerances and specified minimum and maximum allowable time-step sizes, ABAQUS automatically increments the time-step size. The initial time-step size used was 0.0001 s, and the maximum time-step size ABAQUS used was 0.01 s. Acceleration-time history inputs were specified at 0.02-s intervals.

Finite element analyses were performed using 1%, 2%, and 4% damping, to further investigate the sensitivity of peak response to the specified damping. Various combinations of the measured earthquake signals were applied to determine the sensitivity of the response to these signals. The sensitivity of the results to the particular measured earthquake signals chosen was further investigated by applying each signal in all three directions, and the resulting stress components were combined by using the 100-40-40 rule. A typical application of the inputs, based on the 100-40-40 rule, for the Olympia earthquake component was as follows:

X input = 0.4 x 0.3g Olympia
Y input = 0.3g Olympia
Z input = 2/3 x 0.4 x 0.3 g Olympia

F. Superposition of Stresses

For a typical analysis, inputs were first applied in the Y- and Z-directions. A second analysis was then run, with the third input component applied in the Y-direction. Results of the second analysis were then rotated 90° (which simulated X-direction excitation) and superposed with the results of the first run. This superposition of stress components results in the three-dimensional response of the containment shell from transient base excitation in the three orthogonal directions. Superposition of stress components by this method is valid when the response is small-deflection, elastic behavior.

Attention was focused at the two elements (No. 151 and 155, see Figs. 9 and 10), along the base of the containment, at which locations stresses are anticipated to be largest. For the run in which the inputs are specified in the Y- and Z-directions, element 151 corresponds to the location of maximum compressive longitudinal membrane stress, σ_{ϕ}, based on simple beam-bending theory; and element 155 corresponds to that of maximum shear stress, $\sigma_{\phi\theta}$. For the run in which input is specified in the Y-direction only and the results are transformed to represent X input, the roles of elements 151 and 155 are reversed. Thus, the superposition was accomplished by adding axial stresses at element 151 that correspond to the run in which input was specified in the Y- and Z-directions with those of element 155 that correspond to the run in which the input was specified in the Y-direction only; and axial stresses of element 155 (input specified in the Y- and Z-directions) with those of element 151 (input specified in the Y-direction only). Similar superpositions were performed for shear stresses.

Results of combined stresses are shown in the axial compression/shear stress plot in Fig. 29 for an analysis of the R/t = 645 containment, where the X input = El Centro, Y input = Olympia, Z input = Helena, and 1% damping was specified for the containment. The N-284 interaction curve is also shown in Fig. 29, along with all the combined stress points calculated for each time step at integration points 1.90 m (75 in.) above the containment base at the two element locations discussed above. Figure 29 shows that for 1% damping, a substantial number of combined stress points lie outside the design interaction curve, implying that the N-284 buckling criteria have been exceeded.

Because of the linear nature of this problem, these results can be used to determine the peak acceleration level to which the input signals should be scaled such that all points will be on, or within, the interaction curve (see the discussion on calculating the acceleration level that corresponds to the incipient buckling condition in Section III D). When the most severe stress state is considered, the relationship is

$$0.21 + \frac{\sigma_{\phi Dy} \frac{g}{0.3}}{\sigma_{\phi D}} + \left(\frac{\sigma_{\phi \theta Dy} \frac{g}{0.3}}{\sigma_{\phi \theta D}} \right)^2 = 1 \qquad (43)$$

where g is the peak acceleration level to be determined, the 0.21 value corresponds to the portion of the allowable axial buckling stress taken up by the static axial stress, and 0.3 is the acceleration level by which the inputs were originally scaled. When this relation, again quadratic in g, is solved, a value of 0.17 g's is identified as the peak acceleration by which to scale the three inputs to produce an incipient buckling condition.

Results for 2% damping are shown in Fig. 30. As anticipated, considerably fewer stress combinations are outside the interaction curve. These results imply that the input transients would have to be scaled to a peak acceleration level of 0.22 g's to cause a state of incipient buckling. The results for 4% damping, shown in Fig. 31, indicate that the ASME buckling criteria are not exceeded, and that the acceleration levels would have to be scaled to a peak value of 0.31 g's to cause incipient buckling. Two-dimensional interaction curves for all the cases analyzed are shown in Appendix A.

The two-dimensional interaction curves neglect the hoop component of stress. If this third component of stress is considered, a three-dimensional interaction surface results. Figure 32 shows three different views of such a surface that correspond to the 1% damping data. The points shown lie outside the surface and indicate that the N-284 buckling criteria has been exceeded. When the hoop stress component is added, the incipient buckling acceleration level is reduced from 0.17 g's to 0.10 g's, a 59% reduction. Figures 33 and 34 show the corresponding three-dimensional interaction surfaces for the 2% and 4% damping cases, respectively. Appendix B shows the three-dimensional interaction curves, for all cases analyzed, in which incipient buckling occurred at an acceleration level less than 0.3 g's (that is, the cases in which the stress state points lie outside the surface). Tables X and XI summarize the results obtained from all the finite element analyses performed.

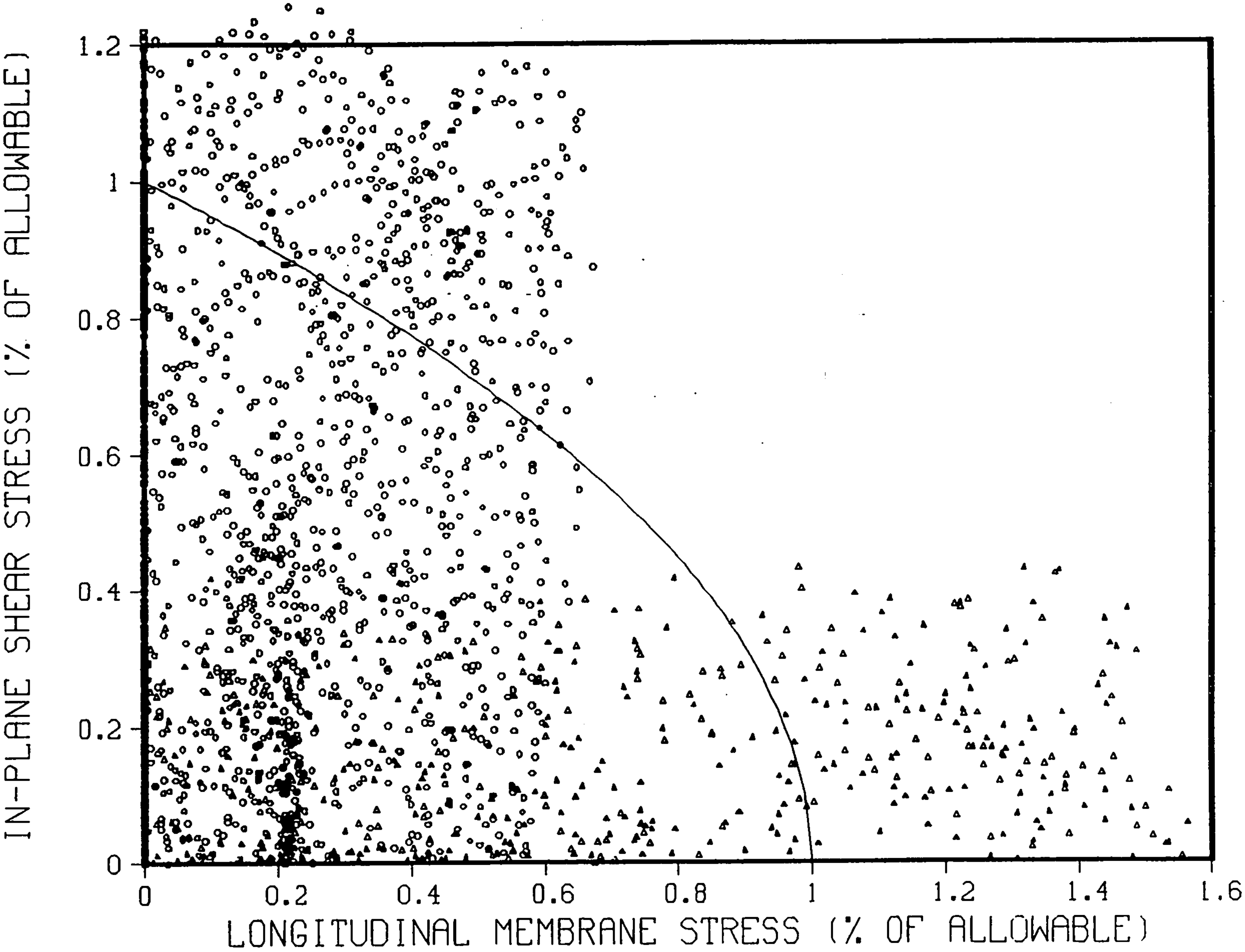

Fig. 29. Two-dimensional interaction equation, R/t=645, x-input = El Centro, y-input = Olympia, z-input = 0.67 Helena, 1% damping.

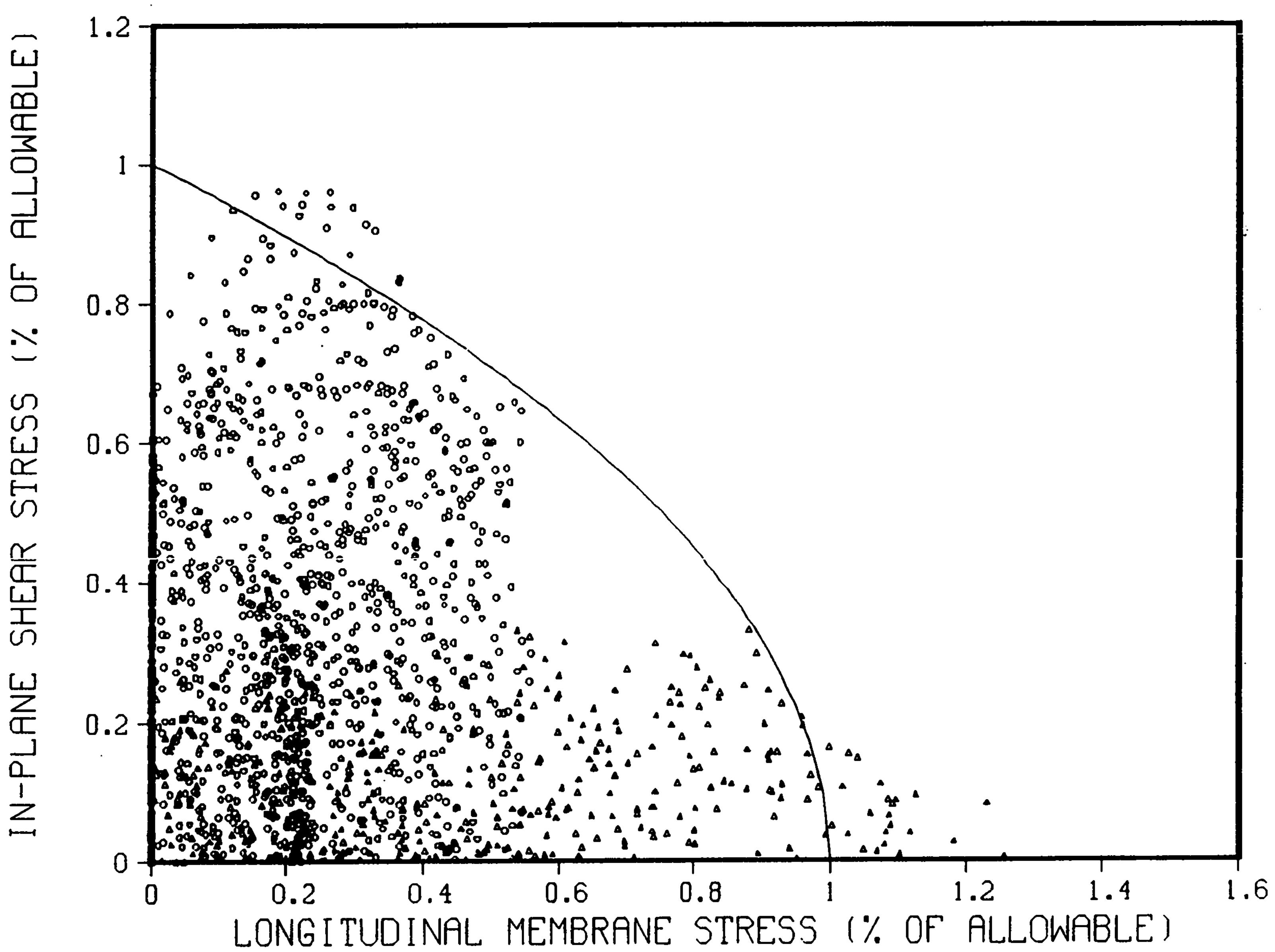

Fig. 30. Two-dimensional interaction equation, R/t=645, x-input = El Centro, y-input = Olympia, z-input = 0.67 Helena, 2% damping.

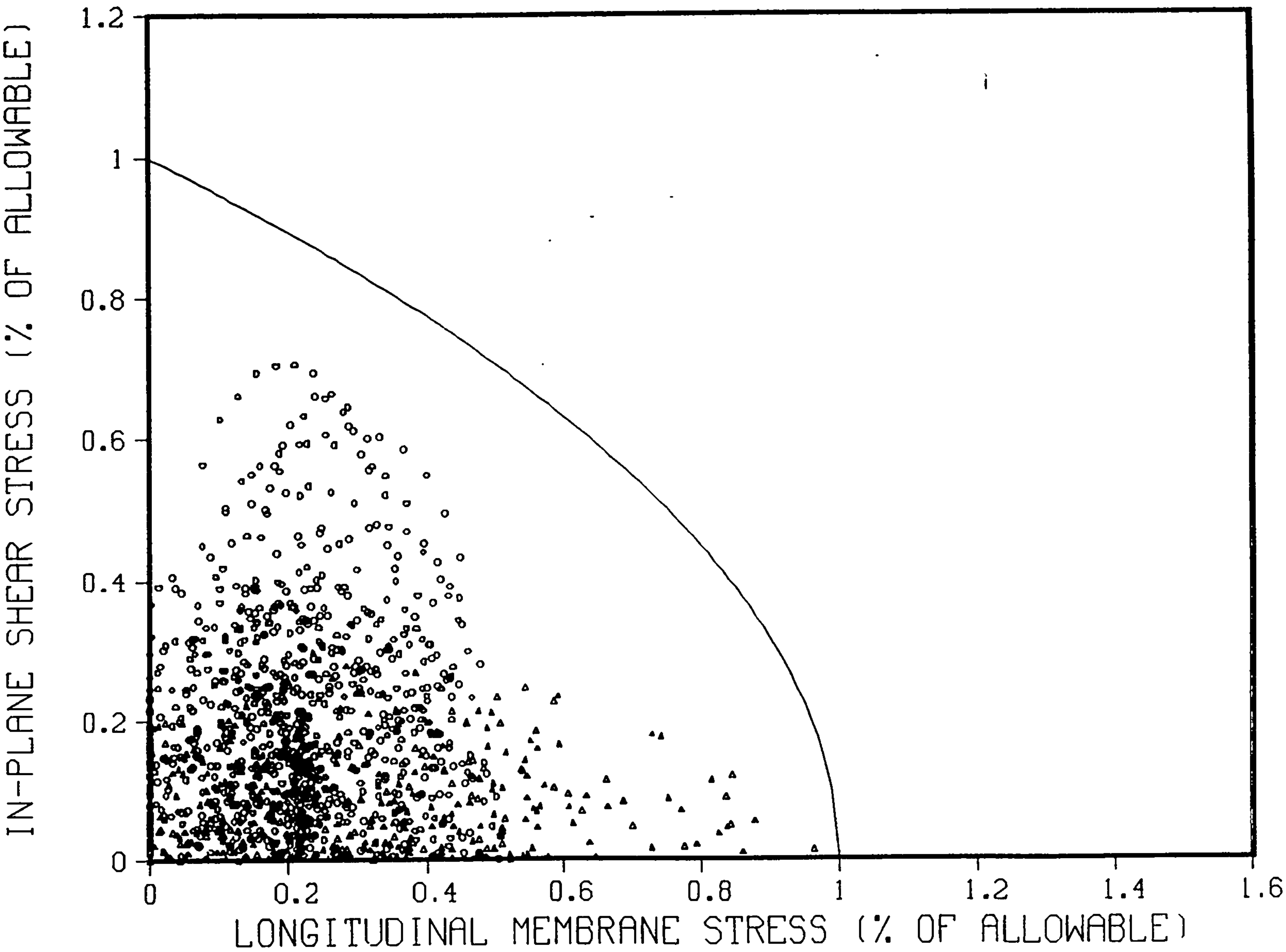

Fig. 31. Two-dimensional interaction equation, R/t=645, x-input = El Centro, y-input = Olympia, z-input = 0.67 Helena, 4% damping.

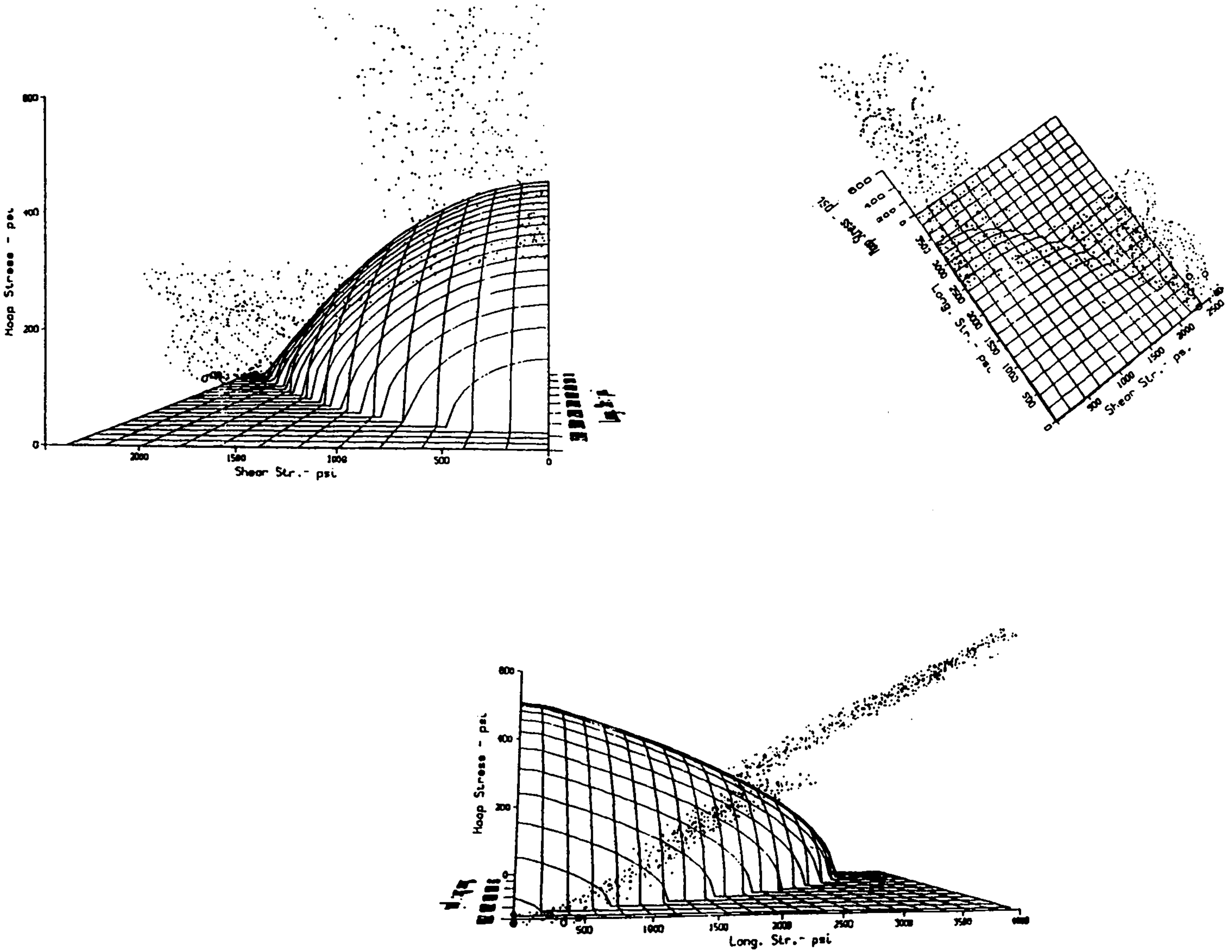

Fig. 32. Three-dimensional interaction equation, R/t=645, x-input = El Centro, y-input = Olympia, z-input = 0.67 Helena, 1% damping.

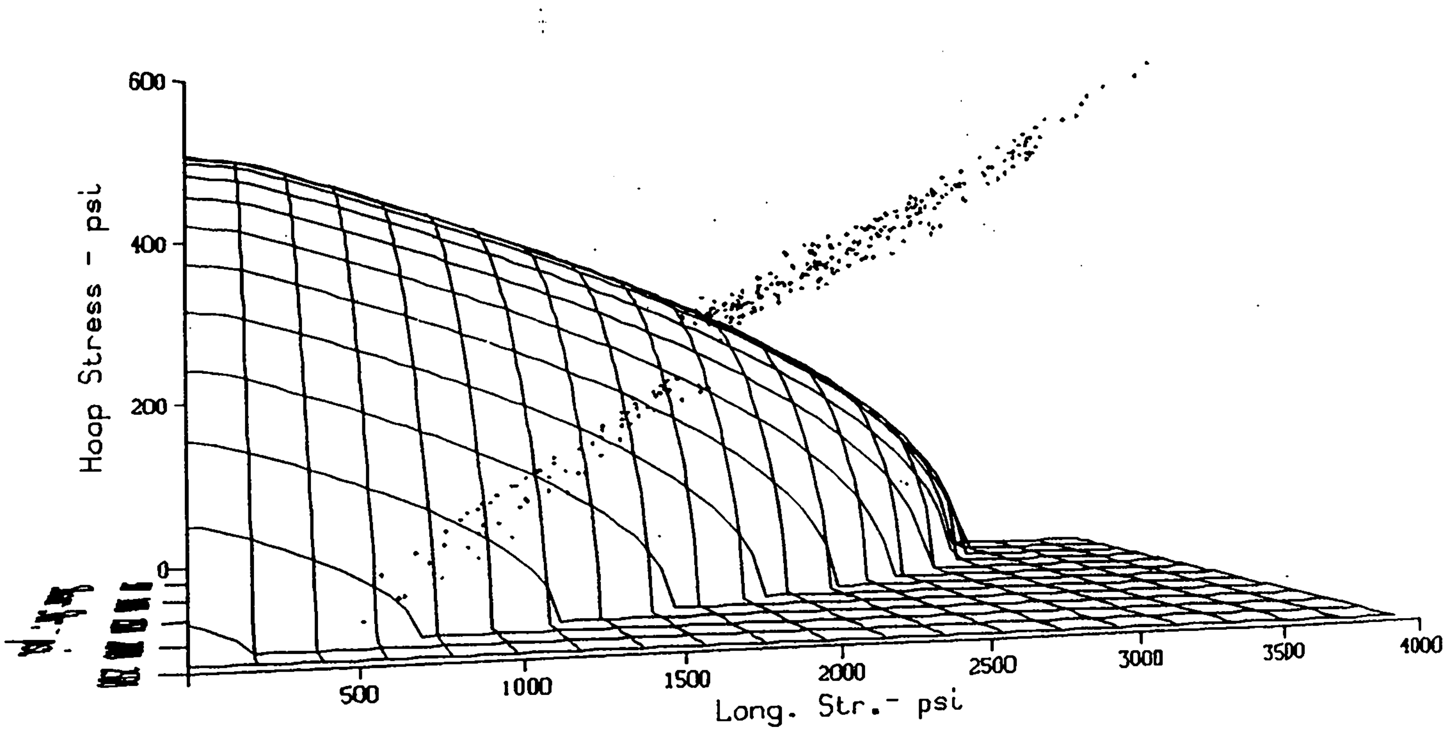

Fig. 33. Three-dimensional interaction equation, R/t=645, x-input = El Centro, y-input = Olympia, z-input = 0.67 Helena, 2% damping.

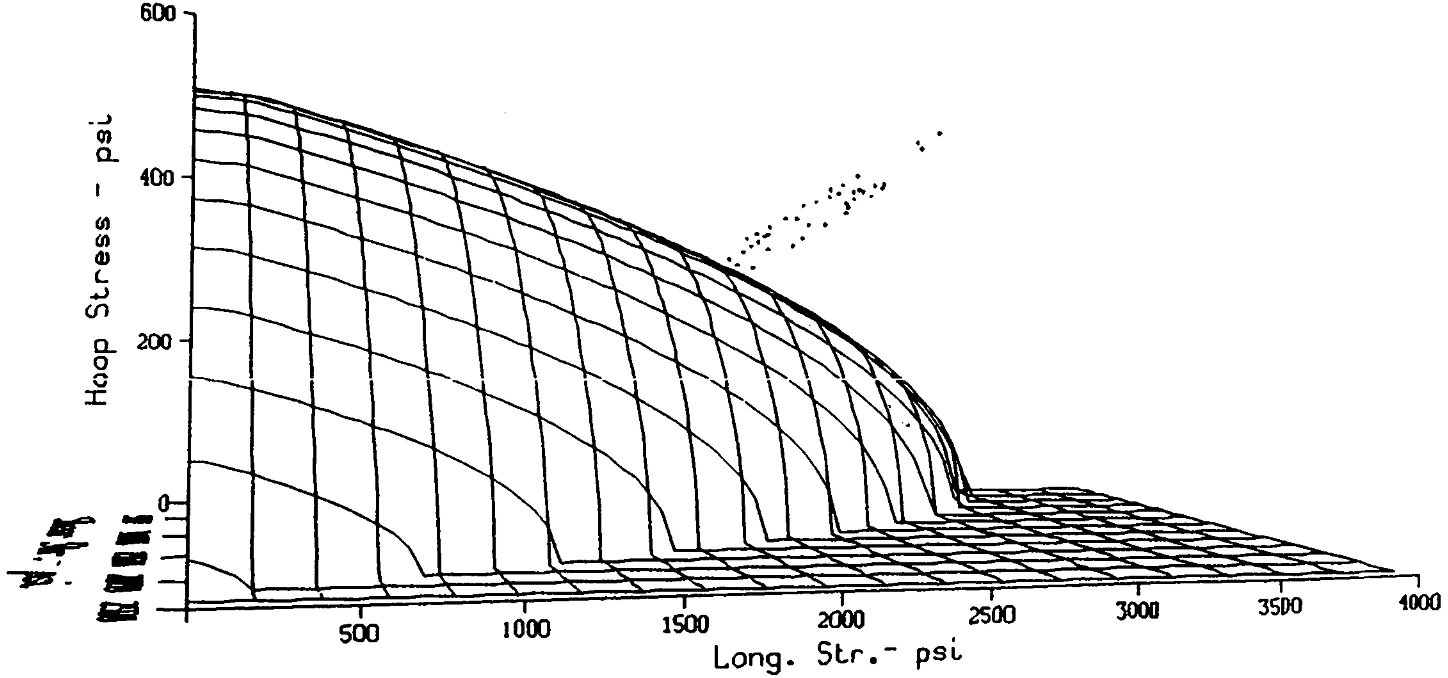

Fig. 34. Three-dimensional interaction equation, R/t=645, x-input = El Centro, y-input = Olympia, z-input = 0.67 Helena, 4% damping.

VII. SUMMARY OF RESULTS

A. Simplified Analysis

The two containments analyzed had nearly identical resonant frequencies for the shear-bending mode and the vertical translation mode; hence, identical amplification factors were applied when the response to a given input was analyzed. For a given input, these analyses showed that the stresses induced in the two containments were similar. Because the R/t=450 containment is more slender, the bending stresses were slightly higher than those calculated for the R/t=645 containment. The shear stresses that result in the R/t=645 containment are larger than those calculated for the R/t=450 containment.

The allowable buckling stresses given in N-284 are considerably different for the two geometries. The shorter length of the R/t=450 containment causes the allowable axial buckling stress to increase 85% above the comparable value for the R/t=645 containment. The allowable shear buckling stress increases 35% and the allowable hoop buckling stress increases 16%. These increases require that the acceleration levels corresponding to the incipient buckling in the R/t=645 containment be increased by an average of 130% to produce an incipient buckling condition in the R/t=450 containment.

The response of the simplified models is most sensitive to the horizontal seismic input component's amplification factor at the frequency corresponding to the fundamental shear-bending mode of the containment because this factor significantly influences both the axial and the shear stresses. Therefore, the site-independent design spectra,[34] where this amplification factor was largest, proved to be the most severe input considered. The spectra resulting from soil-structure interaction analysis,[36] where the fundamental shear-bending mode of the containments was, essentially, in the ZPA portion of the spectrum, was the least severe. It is of interest to note that this input was the least severe even though the ZPA for this signal was 83% greater than the ZPA corresponding to the other signals analyzed.

Results from the simplified analyses show that the acceleration level that produces incipient buckling is sensitive to the damping that the structure is assumed to exhibit. An examination of Table IX shows that the ZPA level that causes incipient buckling either in the R/t = 645 or the R/t=450 containment increases, on the average, by 17% when damping is increased from 1% to 2%. Similarly, the ZPA acceleration level corresponding to incipient buckling increases, on the average, 23% when damping is increased from 2% to 4%. Because the dynamic amplification factors in the SSI spectrum associated with the modes being considered in this simplified analysis do not change significantly for different damping values, the results from the SSI spectrum are insensitive to the assumed damping.

TABLE X

SUMMARY OF RESULTS FROM FINITE ELEMENT ANALYSES, R/t=645

Earthquake Component				Acceleration Level To Produce Incipient Buckling	
X	Y	Z	Damping	Hoop Stress Neglected	Hoop Stress Included
CASE 1					
EL CENTRO	OLYMPIA	0.67 HELENA	1%	0.17	0.10
EL CENTRO	OLYMPIA	0.67 HELENA	2%	0.22	0.125
EL CENTRO	OLYMPIA	0.67 HELENA	4%	0.31	0.18
CASE 2					
EL CENTRO	HELENA	0.67 OLYMPIA	1%	0.46	0.26
EL CENTRO	HELENA	0.67 OLYMPIA	2%	0.49	0.29
EL CENTRO	HELENA	0.67 OLYMPIA	4%	0.57	0.34
CASE 3					
HELENA	OLYMPIA	0.67 EL CENTRO	1%	0.16	0.09
HELENA	OLYMPIA	0.67 EL CENTRO	2%	0.22	0.13
HELENA	OLYMPIA	0.67 EL CENTRO	4%	0.29	0.19
CASE 4					
0.4 OLYMPIA	OLYMPIA	0.27 OLYMPIA	1%	0.15	0.09
0.4 OLYMPIA	OLYMPIA	0.27 OLYMPIA	2%	0.20	0.12
0.4 OLYMPIA	OLYMPIA	0.27 OLYMPIA	4%	0.28	0.17
CASE 5					
0.4 EL CENTRO	EL CENTRO	0.27 EL CENTRO	1%	0.49	0.30
0.4 EL CENTRO	EL CENTRO	0.27 EL CENTRO	2%	0.57	0.35
0.4 EL CENTRO	EL CENTRO	0.27 EL CENTRO	4%	0.68	0.43
CASE 6					
0.4 HELENA	HELENA	0.27 HELENA	1%	0.42	0.25
0.4 HELENA	HELENA	0.27 HELENA	2%	0.44	0.28
0.4 HELENA	HELENA	0.27 HELENA	4%	0.50	0.32
CASE 7					
SSI	SSI	0.82 SSI	1%	0.45	0.34
SSI	SSI	0.82 SSI	2%	0.46	0.35
SSI	SSI	0.82 SSI	4%	0.49	0.38
CASE 8					
R.G. 1.60	R.G. 1.60	0.67 R.G. 1.60	1%	0.26	0.19
R.G. 1.60	R.G. 1.60	0.67 R.G. 1.60	2%	0.29	0.22
R.G. 1.60	R.G. 1.60	0.67 R.G. 1.60	4%	0.34	0.25
CASE 9					
LLNL Prel.	LLNL Prel.	LLNL Prel.	1%	0.45	0.26
LLNL Prel.	LLNL Prel.	LLNL Prel.	2%	0.53	0.32
LLNL Prel.	LLNL Prel.	LLNL Prel.	4%	0.63	0.36

TABLE XI

SUMMARY OF RESULTS FROM FINITE ELEMENT ANALYSES, R/t=450

Earthquake Component				Acceleration Level To Produce Incipient Buckling	
X	Y	Z	Damping	Hoop Stress Neglected	Hoop Stress Included
CASE 1 EL CENTRO	OLYMPIA	0.67 HELENA	1%	0.33	0.16
EL CENTRO	OLYMPIA	0.67 HELENA	2%	0.42	0.21
EL CENTRO	OLYMPIA	0.67 HELENA	4%	0.57	0.28
CASE 2 SSI	SSI	0.82 SSI	1%	0.76	0.54
SSI	SSI	0.82 SSI	2%	0.79	0.57
SSI	SSI	0.82 SSI	4%	0.83	0.61
CASE 3 R.G. 1.60	R.G. 1.60	0.67 R.G. 1.60	1%	0.39	0.27
R.G. 1.60	R.G. 1.60	0.67 R.G. 1.60	2%	0.44	0.30
R.G. 1.60	R.G. 1.60	0.67 R.G. 1.60	4%	0.52	0.36
CASE 4 LLNL Prel.	LLNL Prel.	LLNL Prel.	1%	0.74	0.40
LLNL Prel.	LLNL Prel.	LLNL Prel.	2%	0.85	0.46
LLNL Prel.	LLNL Prel.	LLNL Prel.	4%	1.03	0.58

The primary limitation of this simplified analysis method is that hoop stresses are not adequately accounted for because deformation of the containment cross-section is not considered. The thin-shelled structures being considered are very sensitive to buckling in the hoop direction, as can be seen by comparing the magnitudes of the allowable buckling stress components listed in Section III C. For both containment geometries considered, the allowable hoop buckling stresses are in the range of 3.45 to 4.14 MPa (500 to 587 psi), while the allowable axial and shear buckling stresses are in the range of 15.5 to 42.7 MPa (2250 to 6190 psi). The allowable hoop buckling stresses are relatively insensitive to the R/t ratio, or to the height of the containment, because this allowable stress component increased only 16% when the R/t was decreased from 645 to 450.

Factors that were not considered in this investigation, but which will further reduce the buckling capacity of the containments, are the static and dynamic loads that will result from equipment attached to the containment (such as a polar crane) and the additional shear stresses that can result from torsional response. Interestingly, the fundamental torsional mode occurs at approximately 14 Hz for the structures being considered. The simplified models have the ability to incorporate these types of responses as needed.

B. Finite Element Analysis

The response of the containment is controlled by the ability of the horizontal input component to excite the shear-bending mode of response. For example; Table X and XI show that the Olympia input has the largest amplification factor that corresponds to the frequency of the shear-bending mode and, hence, causes the structure to reach an incipient buckling condition when these signals are normalized to the lowest peak acceleration level. The SSI inputs, where the shear-bending mode amplification factors are lowest and the ZPA is higher, must be normalized to the largest acceleration levels to produce an incipient buckling condition.

Figures 35 and 36 show the influence of damping on the acceleration level that produces a case of incipient buckling. These figures show that increasing the damping from 1% to 4% can increase the acceleration level approximately 10% to 110%. The cases in which the horizontal inputs have large amplification factors at frequencies corresponding to the shear-bending mode were the most sensitive to the changes in damping. Cases 1, 3, and 4 in Table X and Case 1 in Table XI are examples of such inputs. Cases such as the SSI input (Case 7 in Table X and Case 2 in Table XI), where the shear-bending mode is essentially in the ZPA portion of the response, are insensitive to the damping the containment is assumed to exhibit.

For all finite element analyses, including the hoop component of stress, reduced the incipient buckling acceleration level by approximately 25% to 50%. The larger reductions were associated with inputs that significantly amplified the shear-bending mode, for example, Case 1 in Tables X and XI. The smaller reductions are associated with inputs in which the shear-bending mode was nearly in the ZPA portion of the spectrum, as in Case 7 of Table X and Case 2 of Table XI. These results indicate that simple lumped-mass analyses do not accurately assess the seismic buckling capacity of a thin steel shell.

Table XII compares the acceleration level required to produce a case of incipient buckling when the seismic component of hoop stress is neglected in the finite element analyses with the results obtained from the simple lumped-mass models. A review of Table XII shows excellent agreement in some cases (less than 3% difference between the two solutions) and poor agreement in other cases (more than 40% difference in the solutions). One reason for the discrepancies is that the artificial earthquake signals do not always conform to the assumption used in the simplified analyses, that is, when a peak input is applied in one direction, the input in

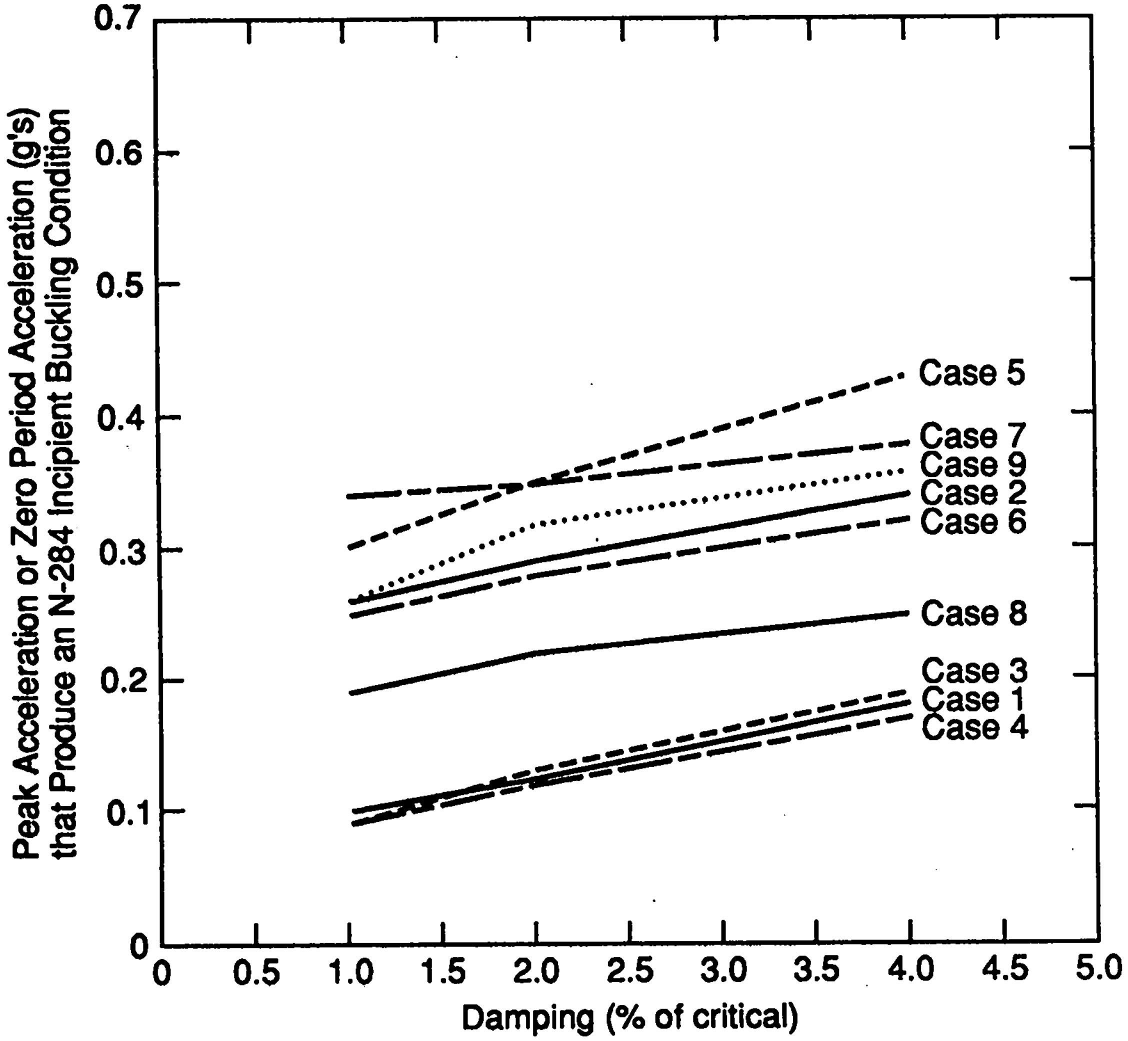

Fig. 35 Influence of damping on the peak acceleration level that will produce a case of incipient buckling in the R/t=645 containment. Refer to Table X for the inputs that correspond to the various cases.

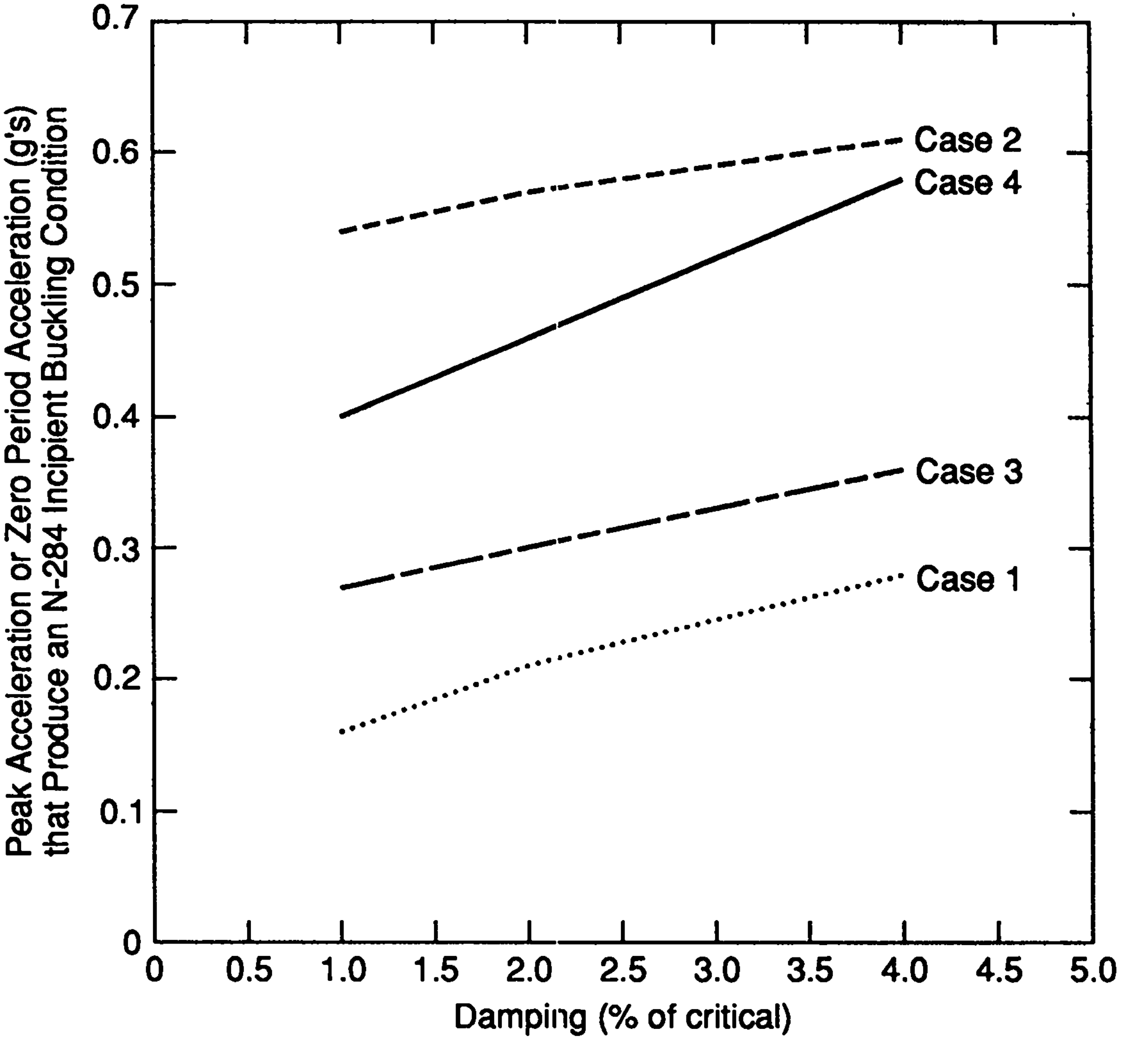

Fig. 36 The influence of damping on the peak acceleration level that will produce a case of incipient buckling in the R/t=450 containment. Refer to Table XI for the inputs that correspond to the various cases.

the other directions are only at 40% of their peak value. Although the artificial earthquake signals were generated with randomly phased inputs, and the correlation coefficients were shown to be less than 0.3, an examination of the signals (Figs. 22, 24, and 26) shows cases in which the peak input is reached in one horizontal direction, while, in the other horizontal direction, the input is significantly greater, or less, than 40% of the peak value in the other horizontal direction.

The two-dimensional interaction plots shown in Appendix A (A-16 through A-24, and A-28 through A-36) further illustrate this point. When examining these plots, one must keep in mind that, for the particular points being plotted, the shear stress is a function of one horizontal input component, while the bending stress is a function of the orthogonal horizontal input component. For example, Figs. A-22 through A-24 show that when the peak axial stress is reached, the shear stress is less than 40% of its peak value. This difference causes the acceleration level determined by finite element analysis to be greater than that determined by the simplified analysis. Conversely, Figs. A-31 through A-33 show that when the peak axial stress is reached, the shear stress is greater than 40% of its peak. Because of this difference, the finite element analysis predicts lower incipient buckling acceleration levels. Further examination of these figures shows that the case in which there is good agreement between the two solutions is coincidental because these cases also violate the 100-40-40 assumption. The fact that good agreement is obtained in one case (the R/t=645, R.G. 1.60 case, for example) and poor agreement is obtained when the same inputs are applied to the other containment, results from the nonlinear nature of the interaction equations and from the fact that the allowable buckling stress components are different and do not change by equal percentages, as previously discussed. When the points from the finite element analysis that correspond to the 100-40-40 assumption are analyzed, they predict the same acceleration level for incipient buckling as from the simple analysis method.

Only one set of artificial earthquake signals corresponding to a given design spectrum was analyzed. Because of the random nature of these signals, it is assumed that if analyses were carried out with many sets of signals, the mean acceleration level that causes incipient buckling would approach the value calculated by the simplified analysis using the 100-40-40 rule. This result suggests that a simplified analysis procedure that empirically accounts for the hoop stress contribution to the cylinder buckling can be developed. The need for a simplified analysis procedure is accentuated by the fact that the time history analyses takes, on the average, 4 h of CPU time on a Cray XMP/416. The application of such a procedure for margins assessment is subsequently discussed in this report.

TABLE XII

COMPARISON OF THE ACCELERATION LEVELS THAT PRODUCE AN INCIPIENT BUCKLING CONDITION DETERMINED FROM THE SIMPLE LUMPED-MASS MODELS, WITH SIMILAR RESULTS DETERMINED FROM THE FINITE ELEMENT MODELS

Earthquake Component				Acceleration Level To Produce Incipient Buckling[a]	
X	Y	Z	Damping	Simple lumped-mass model[b]	Finite element model
R/t=645 SSI	SSI	SSI	4%	0.49	0.50
R/t=645 R.G. 1.60	R.G. 1.60	R.G. 1.60	1%	0.26	0.26
R.G. 1.60	R.G. 1.60	R.G. 1.60	2%	0.29	0.29
R.G. 1.60	R.G. 1.60	R.G. 1.60	4%	0.35	0.34
R/t=645 LLNL Prel.	LLNL Prel.	LLNL Prel.	1%	0.33	0.45
LLNL Prel.	LLNL Prel.	LLNL Prel.	2%	0.38	0.53
LLNL Prel.	LLNL Prel.	LLNL Prel.	4%	0.45	0.63
R/t=450 SSI	SSI	SSI	4%	1.09	0.83
R/t=450 R.G. 1.60	R.G. 1.60	R.G. 1.60	1%	0.58	0.39
R.G. 1.60	R.G. 1.60	R.G. 1.60	2%	0.63	0.44
R.G. 1.60	R.G. 1.60	R.G. 1.60	4%	0.77	0.52
R/t=450 LLNL Prel.	LLNL Prel.	LLNL Prel.	1%	0.72	0.74
LLNL Prel.	LLNL Prel.	LLNL Prel.	2%	0.85	0.85
LLNL Prel.	LLNL Prel.	LLNL Prel.	4%	1.00	1.03

[a] Because the hoop stresses from the normal operating negative air pressure are considered in both analyses, these acceleration levels were determined with the three-dimensional interaction equations.

[b] The 5% damping spectrum was used in the analyses of the simple lumped-mass models when subjected to the SSI input.

The finite element analyses do not include the effects of torsional response because the structures are symmetrical and the inputs were specified along the principal axes of the structure. Typically, accidental torsional effects are considered even when the center of mass and the center of rigidity coincide.[25] Asymmetries that are present in actual containment structures, such as an equipment hatch and the replacement steel around it, were not included in these analytical models. These asymmetries will cause shell modes, which did not contribute to the response of the containments in these analyses, to be excited. Figure 37 shows a typical shell mode calculated for the R/t=645 containment that is within 0.5 Hz of the shear-bending mode. This mode will act as an imperfection and will reduce the buckling capacity, if excited. Finally, these analyses do not include additional masses, such

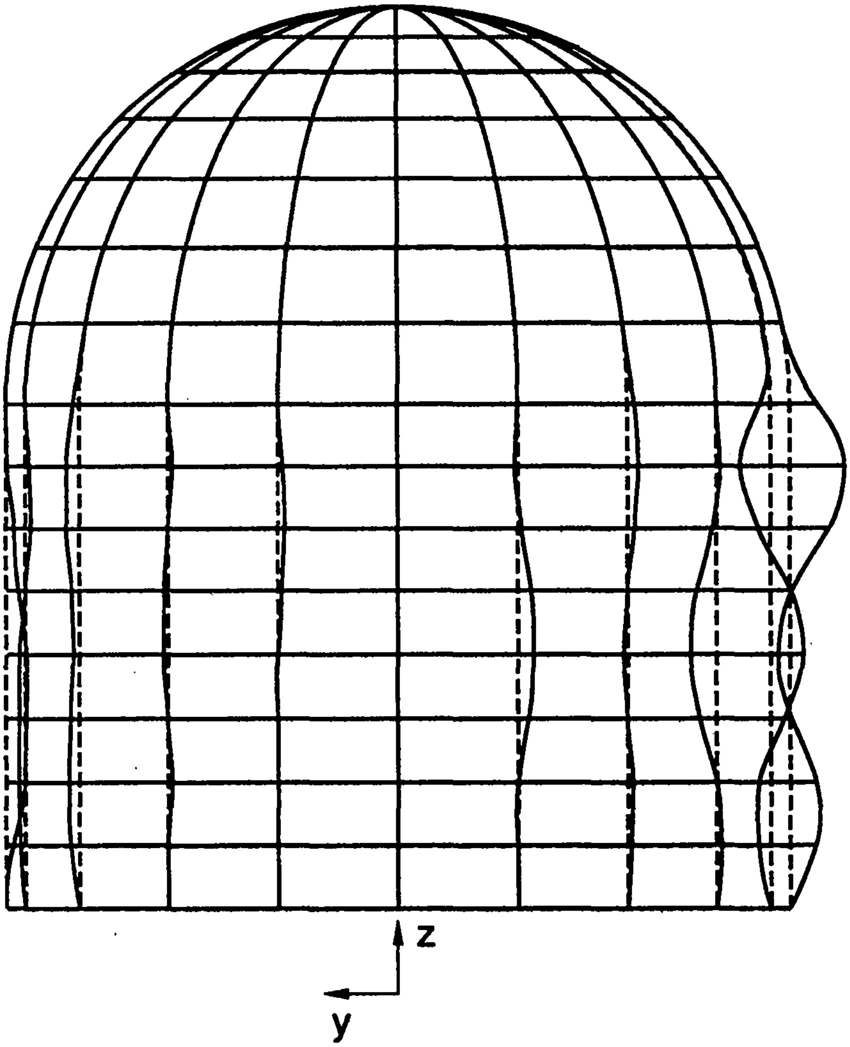

Fig. 37 Typical shell mode within 1 Hz of the shear-bending mode.

as the polar crane, and the dynamic response of such masses. All of these neglected effects tend to reduce the acceleration levels that produce an incipient buckling condition in the containment structures.

C. Other Buckling Considerations

This study has been primarily concerned with buckling caused by seismically induced stresses. Two additional buckling considerations will now be briefly examined. A proposed construction method for the next generation of free-standing steel containments consists of first assembling a series of steel-ring segments on site, then lifting them into place and welding them in a stacked arrangement. Typically, each of the rings will be constructed over a period of 3 months. Therefore, a maximum temperature swing of 44°C (-6 to 38°C) (80°F, 20 to 100°F) is certainly credible during that time period. It is unclear exactly how the dimensions of the rings would be maintained. However, for a 44°C temperature change, the ring radius corresponding to the R/t=645 containment would expand or contract about 1.5 cm (0.6 in.). Assume a difference in radius of 1.5 cm between the newly fabricated ring and that of the last ring welded in place. Then, if there were some means (e.g., thermal or mechanical) to force the new ring to fit the already-erected ring (which appears difficult), then substantial local hoop compressive stresses, 53.1 MPa (7700 psi), would be induced and could cause local buckling. If, on the other hand, the rings are welded as fabricated, then the 1.5-cm offset exceeds the maximum weld offset in the circumferential direction (t/8 = 0.556 cm max.), as specified in the ASME Boiler and Pressure Vessel Code Section III, Division I, NE-4200.

While it may be possible to use this construction method, fabrication to ASME code tolerances may be difficult, and high local compressive stresses that exceed the N-284 allowable buckling stresses may be introduced.

A study was done to determine the external pressure that would result in stresses that exceed the allowable buckling interaction equation value specified in Code Case N-284. If one uses the dead weight that includes the weight of a polar crane 6.67 MN (1.50×10^6 lb), the axial stress, σ_ϕ, for both the R/t=645 and the R/t=450 containments, can be expressed in terms of the external gage pressure, p, as

$$\sigma_\phi = 5.75 \text{ MPa} + pR/2t. \qquad (44)$$

Noting that for the geometry of the R/t=645 containment yields R/2t = 322.5, and for the geometry of the R/t=450 containment yields R/2t = 250, Eq. (44) reduces to

R/t=645

$\sigma_\phi = 5.75\ \text{MPa} + 322.5p$, and

R/t=450

$\sigma_\phi = 5.75\ \text{MPa} + 250p$.

The hoop stress, σ_θ, is 645p and 450p for the R/t=645 and R/t=450 containments, respectively.

The buckling interaction equation from Code Case N-284 for $\sigma_\phi \geq 0.5\sigma_\theta$ (axial compression plus hoop compression) is

$$\frac{\sigma_\phi - 0.5\sigma_h}{\left(\sigma_{\phi_D} - 0.5\sigma_h\right)} + \left(\frac{\sigma_\theta}{\sigma_h}\right)^2 = 1. \tag{45}$$

Substituting the equations for hoop stress and axial stress into Eq. (45) yields a quadratic in p. Noting that for the R/t=645 containment $\sigma_{\phi D} = 23.3$ MPa, $\sigma_h = 3.45$ MPa; for the R/t=450 containment $\sigma_{\phi D} = 42.7$ MPa, $\sigma_h = 4.01$ MPa; and solving this quadratic for p yields gage pressures of 4.55 kPa (0.67 psi) and 8.27 kPa (1.2 psi) that produce an incipient buckling condition in the R/t=645 and the R/t=450 containments, respectively. With respect to buckling in the hoop direction, caused by external overpressure, the next-generation containment is not as safe as the generic containment that is typical of existing unstiffened free-standing steel containments.

Under normal operating conditions, a typical negative air pressure of 0.69 kPa (0.1 psi) is maintained in the containment.[37] If a containment uses sprayers as an emergency cooling system, then the potential exists to exceed the negative pressure, which will cause buckling in the hoop direction. Vacuum breakers must, therefore, be an essential part of the next-generation containment design.

D. Comparison with Existing Containments

An evaluation of the existing U.S. nuclear power plants that utilize steel containments (as of 1988) is presented in Ref. 43. The somewhat qualitative evaluation identified 44 existing stiffened and unstiffened steel containments as follows:

22	Mark I
1	Mark IIs
2	Mark IIIs
8	Ice Condensers
10	PWR Dry Containments
1	Pre-Mark BWR Containment

The R/t ratios for the steel containments fell mostly in the range of 400< R/t <700. Reference 43 states that internal pressure loading controlled the design of these containments.

Five types of loadings listed in Ref. 43 that could cause buckling, including, of course, seismic buckling. The resulting overall factors of safety against buckling and the typical R/t values are given in Ref. 43 as follows:

Mark I	FS approx. 7	(Torus, R/t = 460)
Mark II	FS approx. 3.6	(Cylinder, R/t = 548)
Mark III	--	(Cylinder, R/t = 480)
Ice Condenser	FS > 10	(Cylinder, R/t=650)
Dry Containments	FS > 10	--
Pre-Mark BWR	--	--

The general conclusion of the study in Ref. 43 is that existing steel containment designs have adequate margins against buckling. This work is supplemented by the analysis of the generic R/t=450 containment presented in this study. As seen in Table I, the R/t=450 containment is very similar in geometry to existing unstiffened free-standing steel containment structures. An analysis of this generic containment shows that when the SSI input is considered and the structure is assumed to respond with 1% damping, a free-field input normalized to a peak acceleration or ZPA of 0.54 g's is required to produce a case of incipient buckling. A review of the SARs for these existing plants shows that they have been design for SSE acceleration levels in the range of 0.1 to 0.2 g's. When one considers that the N-284 has a safety factor of 1.67 associated with its buckling criteria, and the limitations of the analyses performed in this study, the results presented in this report confirm the safety factors against buckling given for dry containments in Ref. 43.

Returning to results of the next-generation containment (R/t=645) seismic evaluation presented here, the factor of safety against buckling for this design certainly appears to be below all of the factors of safety listed above, including those for the R/t=450 containment. For example, with 1% damping, and the 0.3 g's peak acceleration input corresponding to the SSI input, the factor of safety approaches 1.89, which is only slightly higher than the 1.67 factor of safety specified in the N-284 . Therefore, from a containment buckling standpoint, this next-generation containment does not appear to be as safe as, or safer than, existing unstiffened free-standing steel containments. It is interesting to note in Table I that the existing unstiffened free-standing steel containments are located in areas of the U.S. that have very low seismic risks associated with them. All of these existing containments were designed for peak acceleration levels significantly less than 0.3 g's (Refs. 2-6).

E. Applications to Margins Assessments

The analyses performed as part of this study can be extended to develop a simplified method for seismic margins assessment of global buckling of an unstiffened, free-standing steel containment. As shown earlier in the comparison with finite element time-history analysis, the simple lumped-mass models based on beam theory, which are analyzed by response spectrum methods, accurately assess the state of stress in the containment shell as long as the hoop stress is neglected. Finite element analysis results analyzed with the two- and three-dimensional buckling interaction curves can be used to empirically account for the hoop stress. A hoop knockdown factor, which will be a function of the amplification factor associated with the fundamental shear-bending mode's natural frequency, can be established from the results presented in this study. With this knockdown factor, the acceleration level that will produce a case of incipient buckling can then be accurately determined from the lumped-mass models. These acceleration levels can then be compared with the containment's SSE acceleration level to determine the margin of failure. This simplified margins assessment procedure is subject to the limitations of the Code Case N-284 buckling criteria, as discussed below.

F. Limitations of Current Dynamic Buckling Criteria

All of the analyses performed in this investigation are based on the buckling criteria given in Code Case N-284. This code case has a number of limitations. For example, it is based on the 'freezing-in-time' analysis method, the limitations of which are discussed in Section II. Further experimental work, similar to that summarized in Ref. 14, coupled with numerical modeling, is necessary to address the accuracy of this analytical method.

A "dynamic knockdown factor" that would further reduce the allowable buckling stress values in N-284 has been suggested.[14] This factor is used to account for reduced buckling capacity that can result from additional stresses and geometric imperfections caused by the excitation of shell modes. In this investigation, the shell modes of the containment were not excited because only symmetric structures were considered. The NRC[44] recently discussed the need for such a knockdown factor. Numerical simulation of the imperfections caused by excitating shell modes, and their effect on the buckling capacity of the containment, can be used to address this issue. However, these results will be somewhat specific to the geometry of the containment being studied and the asymmetries chosen, and will, thus, require several such simulations to obtain bounds on the problem. Experimental verification of these analyses is essential because of the uncertainties associated with the effects of imperfections on the buckling of cylinders

The initial stress state that results from the fabrication method used to construct the containment must also be examined because these stresses can be significant and because they will further reduce the buckling capacity of the structure. It is the authors' opinions that the data on which the knockdown factors given in N-284 are based do not adequately address this issue because all of the specimens were fabricated and tested in a controlled environment. These tests may not be indicative of the construction method or the environment of a prototype containment. These stress states can be estimated with numerical models that simulate the actual construction methods and the environment in which the containment was constructed. The analysis must also consider the tolerances that are allowed in fabrication of the containment, as given in the ASME Boiler and Pressure Vessel Code. Experimental verification of these analyses would add considerable credibility to the numerical results.

Because the buckling of thin cylinders is very sensitive to imperfections, the stress levels that produce a state of incipient buckling in the containments being considered are a factor of 5 to 10 below the yield stress. At these low stress levels, no definitive guidance is given, either in Code Case N-284 or in the NRC Reg. Guides, as to the appropriate damping values that should be used when seismically induced buckling is being considered. Seemingly small changes in the assumed damping can significantly affect the excitation level that will produce incipient damping. This study has shown that decreasing the damping from 2% to 1% can decrease the acceleration level necessary to cause incipient buckling by as much as 38%. Because damping is a material property, the damping ratio must be determined experimentally. Inexpensive tests on small-scale containment models could easily provide the experimental data needed to address this issue.

These safety-related issues must be resolved before the containment design can be considered safe from seismically induced buckling.

REFERENCES

1. "Conceptual System Design Description #12 Containment Building and Containment System," EBASCO Services, Inc. New York, NY (May 1990).

2. WSES-FSAR-UNIT-3, "Waterford Steam Electric Station, Facility Safety Analysis Report," Louisiana Power and Light Company.

3. "Updated Safety Analysis Report," Davis-Besse Nuclear Power Station No. 1, Toledo Edison Company, Toledo, Ohio, Revision 9 (July 1989).

4. "Facility Safety Analysis Report," St. Lucie Plant Unit 2, Florida Power and Light Company (December 1980).

5. "Safety Evaluation of the Kewaunee Nuclear Power Plant," U.S. Atomic Energy Commission Directorate of Licensing, Washington, DC (1972).

6. "Safety Evaluation of the Prairie Island Nuclear Generating Plant Units 1 & 2," U.S. Atomic Energy Commission Directorate of Licensing, Washington, DC (1972).

7. "Preliminary Title 1 Seismic Design Criteria for New Production Reactors (NPR)," Lawrence Livermore National Laboratory draft report, Rev. 2 (August 1990).

8. C. D. Miller, *Metal Containment Shell Buckling Design Methods*, (Chicago Bridge and Iron Company, Plainfield, Illinois, December 1979).

9. ASME Boiler and Pressure Vessel Code, Section III, Division 1, Case N-284, "Metal Containment Shell Buckling Design Methods," Approval date: August 25, 1980.

10. D. L. Anderson and H. E. Lindberg, "Dynamic Pulse Buckling of Cylindrical Shells Under Transient Radial Pressures," *AIAA Journal*, **6**, 589-598 (1968).

11. H. E. Lindberg and R. E. Herbert, "Dynamic Buckling of a Thin Cylindrical Shell Under Axial Impact," *Journal of Applied Mechanics*, **33**, 105-112 (1966).

12. C. D. Babcock, W. E. Baker, J. Fly, and J. G. Bennett, "Buckling of Steel Containment Shells Under Time-Dependent Loading," U.S. Nuclear Regulatory Commission report NUREG/CR-3742 (May 1984).

13. P. Seide, V. Weingarten, and S. Masri, "Buckling Criteria and Application of Criteria to Design of Steel Containment Shell," U.S. Nuclear Regulatory Commission report NUREG/CR-0793, Washington, DC (May 1979).

14. T. A. Butler, W. E. Baker, J. G. Bennett, and C. D. Babcock, "Investigation of Steel Containment Buckling Under Dynamic Loads," *Nuclear Engineering and Design*, **94**, 31-39 (1986).

15. H. Nakamura, S. Matsuura, and A. Sakurai, "Plastic Buckling of Short Cylinders with Axial Temperature Distribution Under Transverse Shearing Loads," in *Transactions of the 9th International Conference on Structural Mechanics in Reactor Technology*, Lausanne, Switzerland, August 17-21, 1987, pp. 219-224.

16. K. Kokubo, M. Shigeta, M. Madokoro, A. Sakurai, and H. Nakamura, "Buckling Behaviors of Short Cylindrical Shells Under Dynamic Loads," in *Transactions of the 9th International Conference on Structural Mechanics in Reactor Technology*, Lausanne, Switzerland, August 17-21, 1987, pp. 167-172.

17. G. D. Galletly and J. Blachut, "Plastic Buckling of Short Vertical Cylindrical Shells Subjected to Horizontal Edge Shear Loads," *Journal of Pressure Vessel Technology*, **107**, 101-106 (1985).

18. R. G. Sauve, W. W. Teper, and R. E. Nickell, "Buckling Design Analysis for Impact Evaluation", *Journal of Pressure Vessel Technology*, **107**, 165-171 (1985).

19. C. D. Miller, "COMMENTARY on the November 13, 1979 Edition of Metal Containment Shell Buckling Design Methods of the ASME Boiler and Pressure Vessel Code, Section III, Division I - Preliminary," Chicago Bridge and Iron Company (December 1979).

20. B. Almroth, C. Rankin, and D. Bushnell, "Buckling of Steel Containment Shells," U.S. Nuclear Regulatory Commission report NUREG/CR-2836, Vol. 3 (December 1982).

21. US AEC Regulatory Guide 1.61, *Damping Values for Seismic Design of Nuclear Power Plants,* US Atomic Energy Commission, Washington, DC, October 1973.

22. M. Amin, P. K. Agrawal, and T. J. Ahl, "An Analytical Study of Seismic Threat to Containment Integrity," U.S. Nuclear Regulatory Commission report NUREG/CR-5098, (July 1989).

23. N. M. Newmark and W. J. Hall, "Seismic Design Criteria for Nuclear Reactor Facilities," in *Proceedings of the Fourth World Conference on Earthquake Engineering*, Vol. II, Santiago, Chile, January 13-18, 1969.

24. N. M. Newmark and W. J. Hall, "Development of Criteria for Seismic Review of Selected Nuclear Power Plants," U.S. Nuclear Regulatory Commission report NUREG/CR-0098 (May 1978).

25. *Seismic Analysis of Safety-Related Nuclear Structures and Commentary on Standard for Seismic Analysis of Safety Related Nuclear Structures*, ASCE 4-86 (American Society of Civil Engineers, New York, September 1986).

26. "A Method for Assessment of Nuclear Power Plant Seismic Margin," Electric Power Research Institute report EPRI NP-6041 (October 1988).

27. M. J. N. Priestley, "Seismic Design of Storage Tanks," New Zealand National Society for Earthquake Engineering (December 1986).

28. *Facility Safety Analysis Report Watts Bar Nuclear Plant Units 1 and 2*, (Tennessee Valley Authority, Chattanoogo, Tennessee, November 1991).

29. P. Seide, V. Weingarten, and S. Masri, "Evaluation of the Buckling Stress Criteria for the Steel Containment of the Watts Bar Nuclear Reactor," U.S. Nuclear Regulatory Commission report, NUREG/CR-2489 (November 1982).

30. *Sequoyah Nuclear Plant Final Safety Analysis Report*, Tennessee Valley Authority, Chattanooga, TN (April 1991).

31. J. D. Stevenson and F. A. Thomas, Selected Review of Regulatory Standards and Licensing Issues for Nuclear Power Plants, U.S. Nuclear Regulatory Commission report NUREG/CR-3020 (November 1982).

32. D. Bushnell, BOSOR 4: Program for Stress, Buckling, and Vibration of Complex Shells of Revolution, in Structural Mechanics Software Series - Vol.1, N. Perrone and W. Pikey, Eds. (University of Virginia Press, Charlottesville, Virginia, 1976).

33. W. T. Thomson, *Theory of Vibration with Applications*, 2nd Edition (Prentice-Hall, Englewood Cliffs, NJ, 1981), 196-197.

34. U.S. AEC Regulatory Guide 1.60, Design Response Spectra for Seismic Design of Nuclear Power Plants, Rev. 1 (U.S. Atomic Energy Commission, Washington, DC, December 1973).

35. D. W. Coats and R. C. Murray, "Natural Phenomena Hazards Modeling Project: Seismic Hazard Models for Department of Energy Sites," Rev. 1, Lawrence Livermore National Laboratory report UCRL-53582, Livermore, California (1984).

36. "Earthquake Loading Assessment Report," EBASCO Services, Inc. New York, NY (May 1990).

37. "Conceptual Design Containment Analysis Report, Rev. 1" EBASCO Services, Inc. New York, NY (May 1990).

38. S. Y. Lu, "Buckling of Cantilever Cylindrical Shell with a Transverse End Load," *AIAA Journal*, **3**, No. 12 (December 1965).

39. M. W. MacCann, "Seismic Hazards Assessment at the Savannah River Site - Input for Seismic PRA," unpublished viewgraphs from a presentation to the DOE Seismic Working Group, Gaithersburg Maryland (March, 1991).

40. *ABAQUS USER'S MANUAL*, Version 4.8, Hibbitt, Karlsson, and Sorensen, Inc., 1989.

41. D. Brook and R. J. Wynne, *Signal Processing*, (Edward Arnold, London, UK 1988).

42. Robert H. Scanlan and Klaus Sachs, "Earthquake Time Histories and Response Spectra," *ASCE Journal of the Engineering Mechanics Division*, **EM4**, 635-643 (August 1974).

43. C. P. Tan, "Evaluation of Buckling Capacity of Steel Containments," U.S. Nuclear Regulatory Commission report (1988).

44. R. L. Baer, U.S. Nuclear Regulatory Commission Memorandum, "Generic Issue B-5, Buckling Behavior of Steel Containments," April 8, 1988.

APPENDIX A

TWO-DIMENSIONAL INTERACTION SURFACES

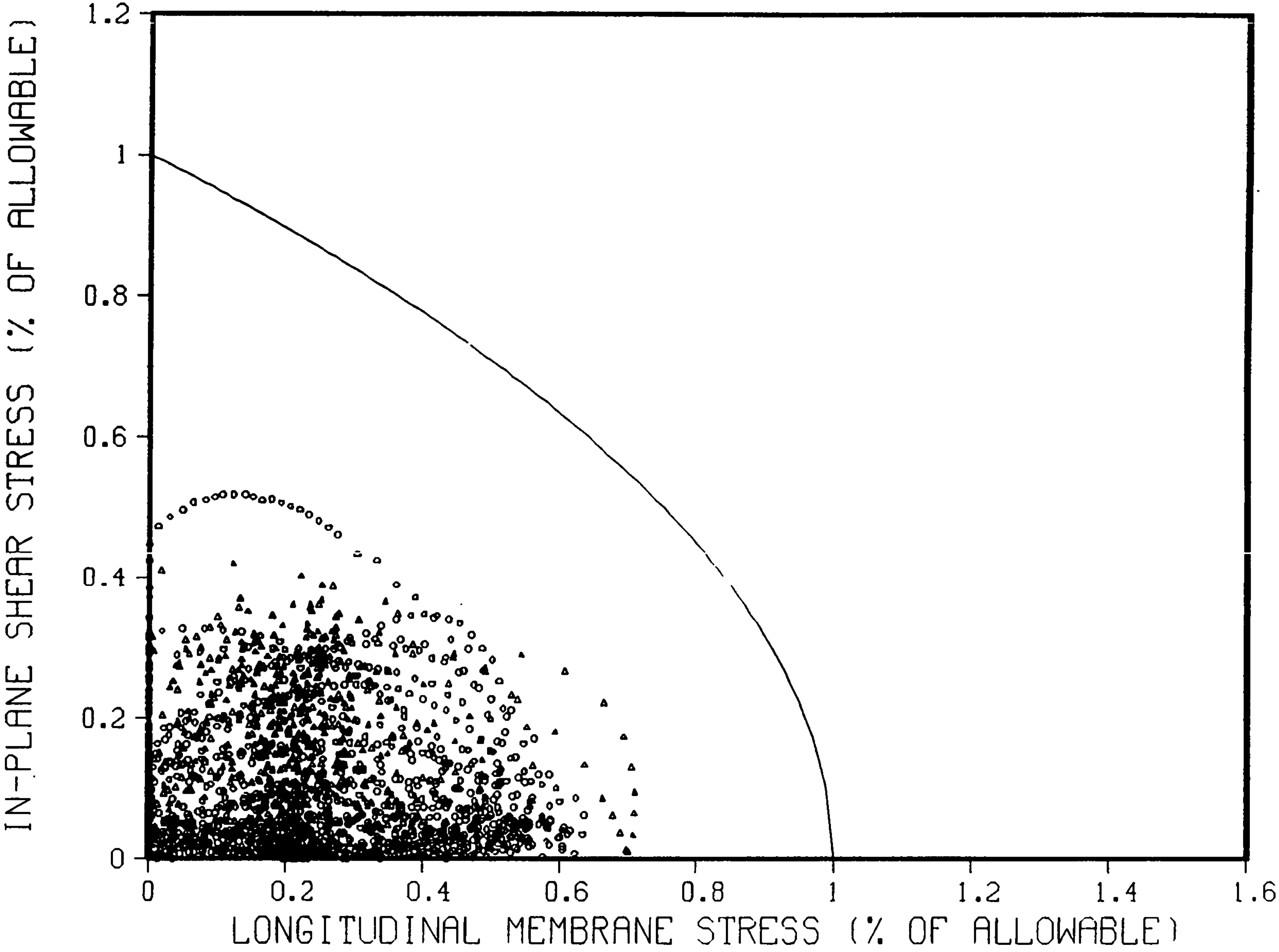

Fig. A-1. Two-dimensional interaction equation, R/t=645, x-input = El Centro, y-input = Helena, z-input = 0.67 Olympia, 1% damping.

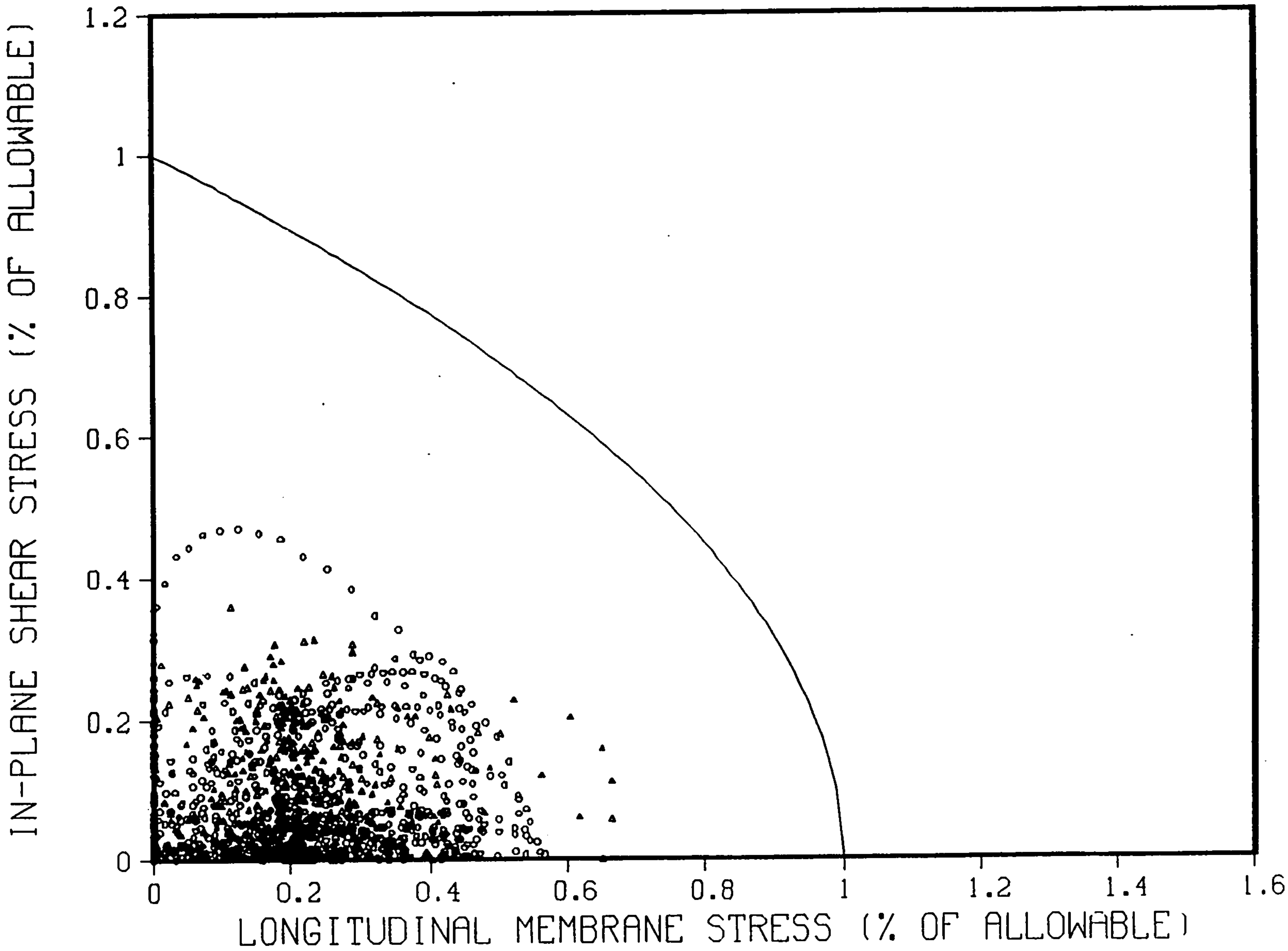

Fig. A-2. Two-dimensional interaction equation, R/t=645, x-input = El Centro, y-input = Helena, z-input = 0.67 Olympia, 2% damping.

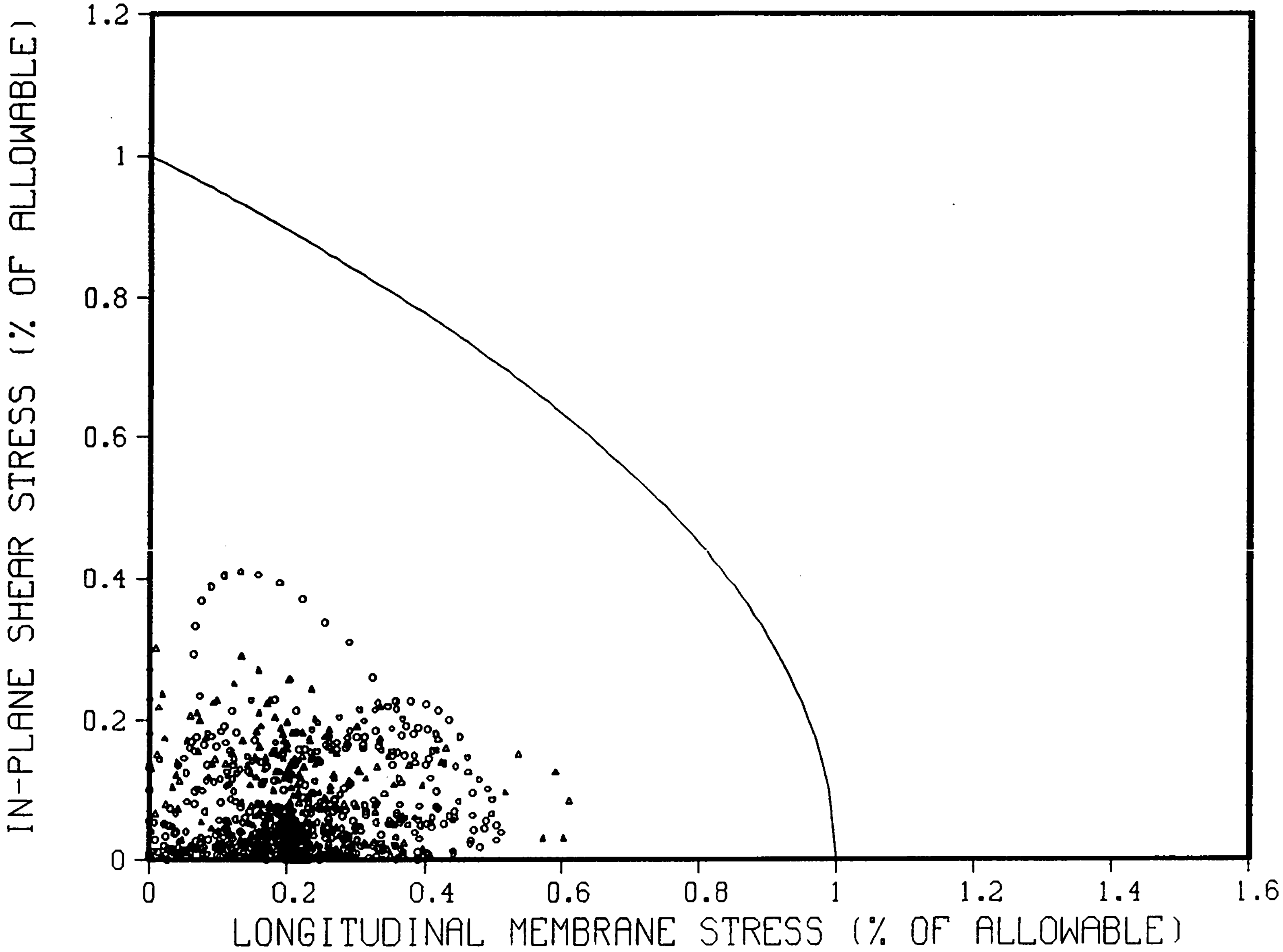

Fig. A-3. Two-dimensional interaction equation, R/t=645, x-input = El Centro, y-input = Helena, z-input = 0.67 Olympia, 4% damping.

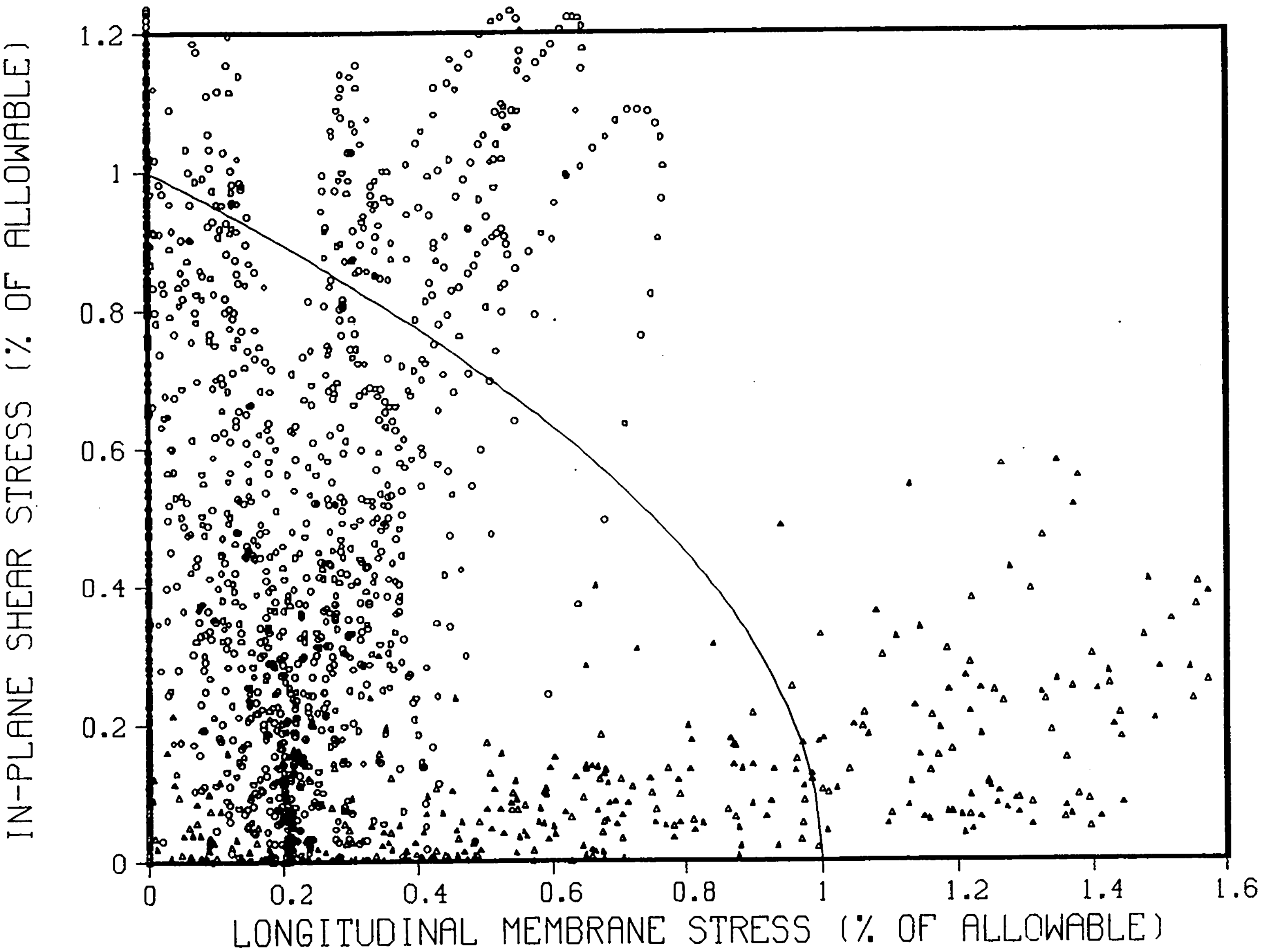

Fig. A-4. Two-dimensional interaction equation, R/t=645, x-input = Helena, y-input = Olympia, z-input = 0.67 El Centro, 1% damping.

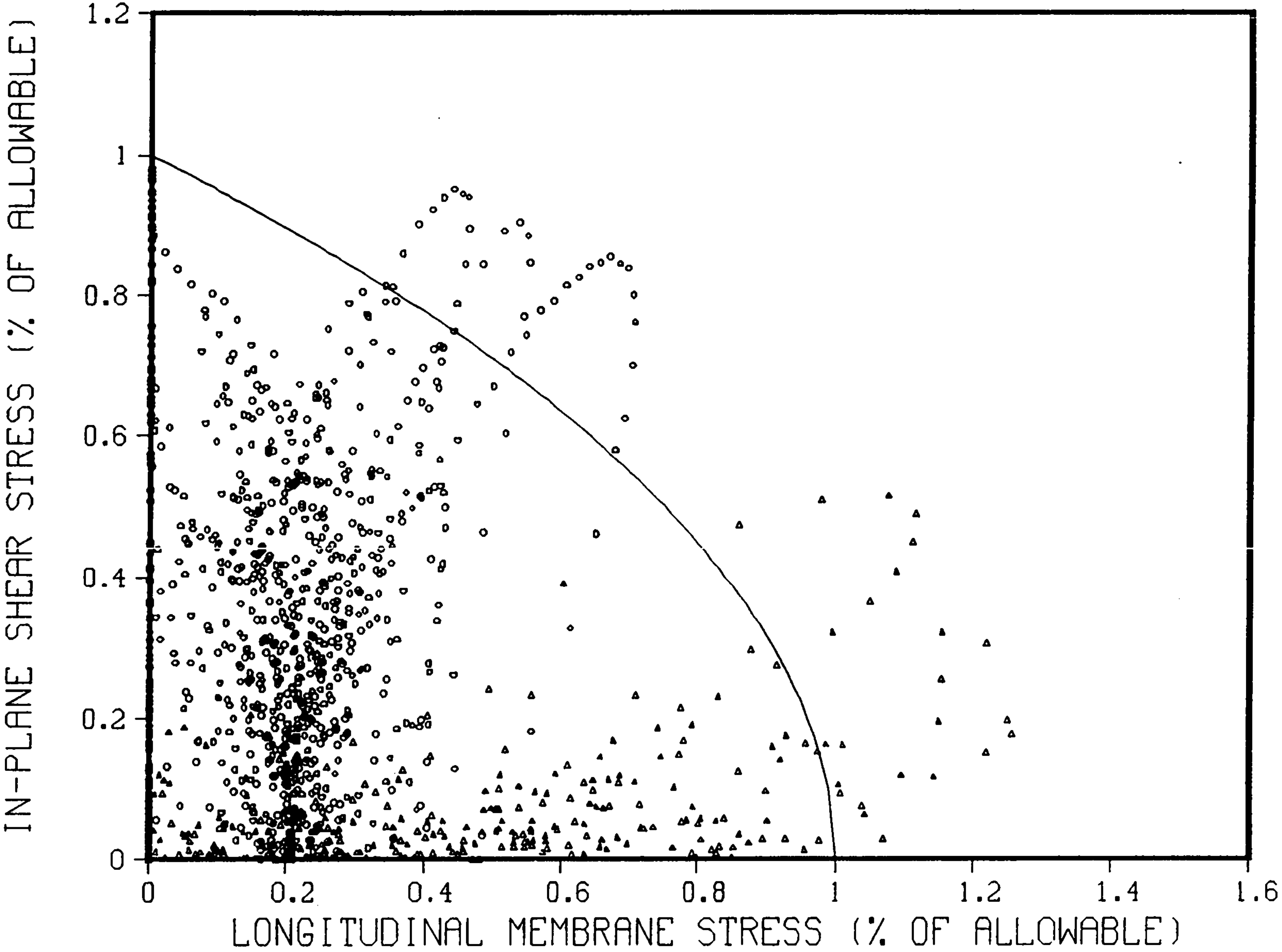

Fig. A-5. Two-dimensional interaction equation, R/t=645, x-input = Helena, y-input = Olympia, z-input = 0.67 El Centro, 2% damping.

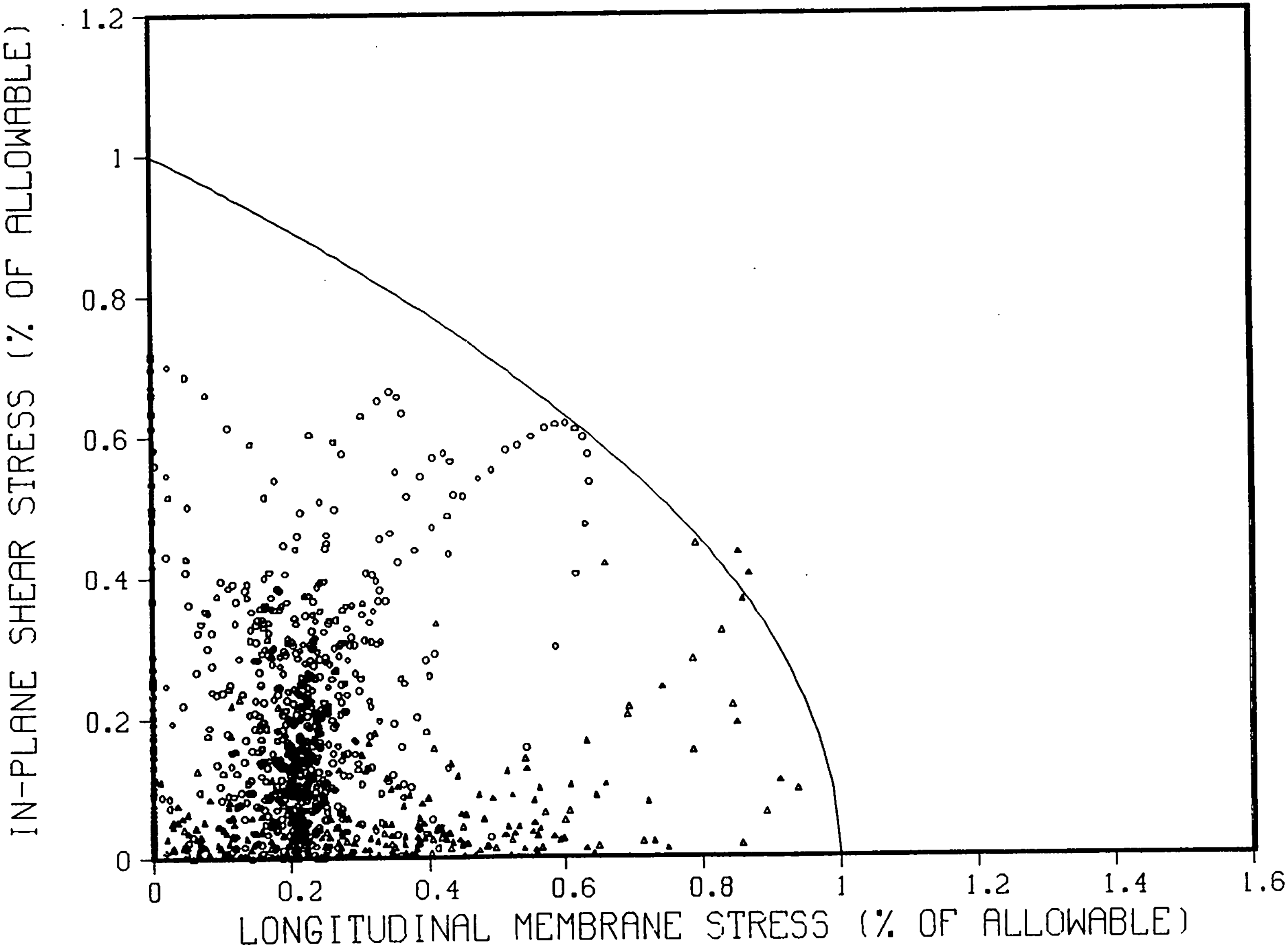

Fig. A-6. Two-dimensional interaction equation, R/t=645, x-input = Helena, y-input = Olympia, z-input = 0.67 El Centro, 4% damping.

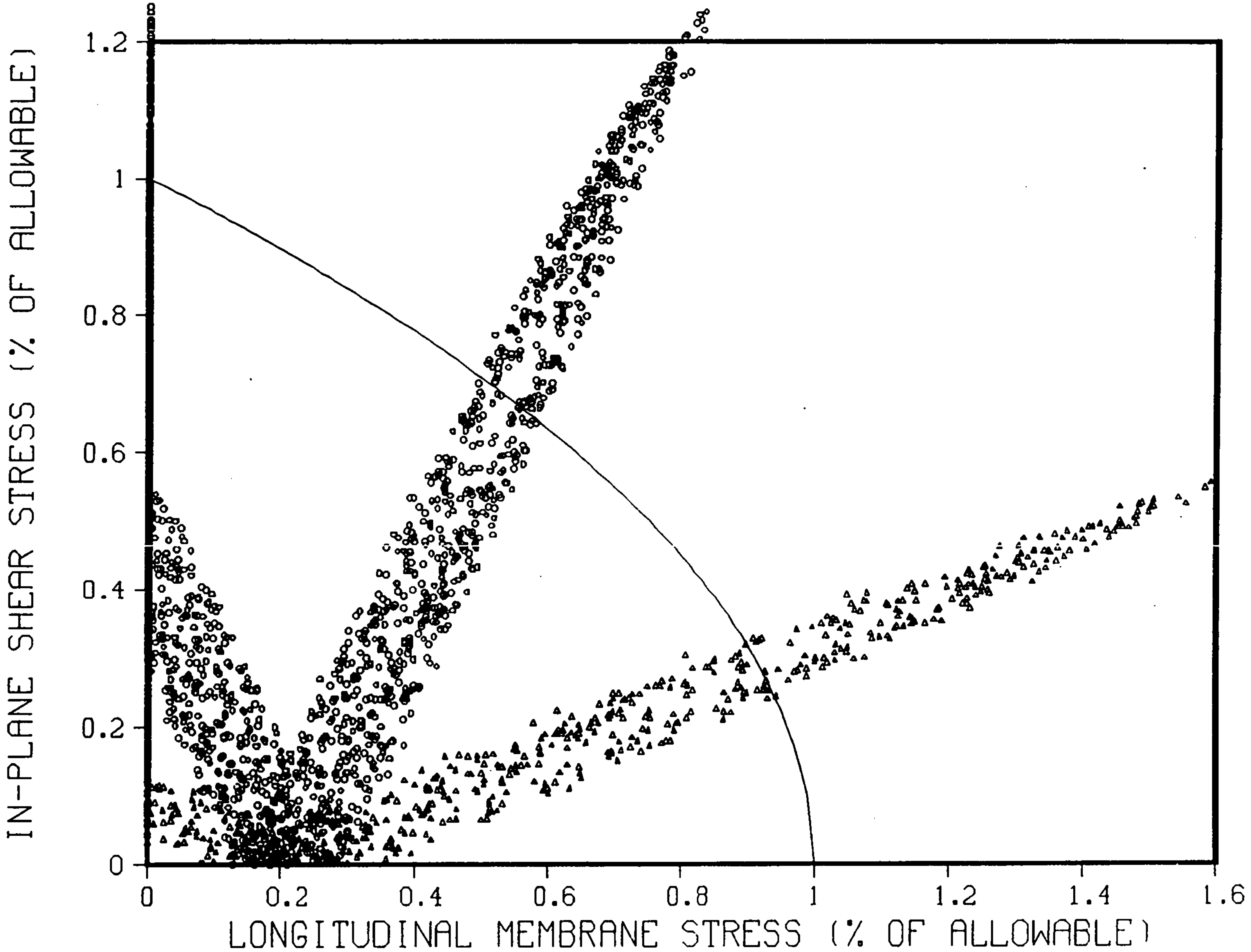

Fig. A-7. Two-dimensional interaction equation, R/t=645, x-input = 0.4 Olympia, y-input = Olympia, z-input = 0.27 Olympia, 1% damping.

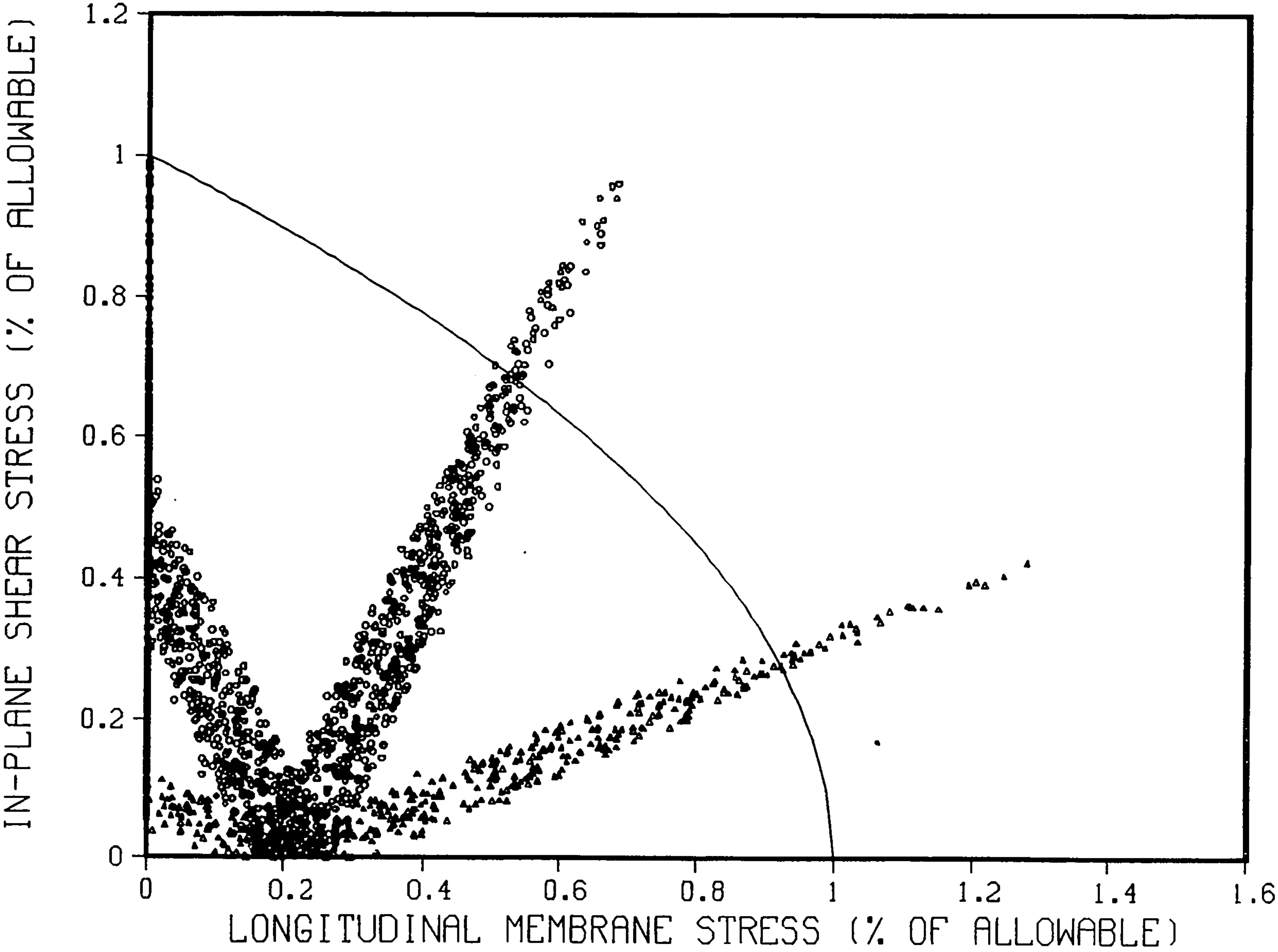

Fig. A-8. Two-dimensional interaction equation, R/t=645, x-input = 0.4 Olympia, y-input = Olympia, z-input = 0.27 Olympia, 2% damping.

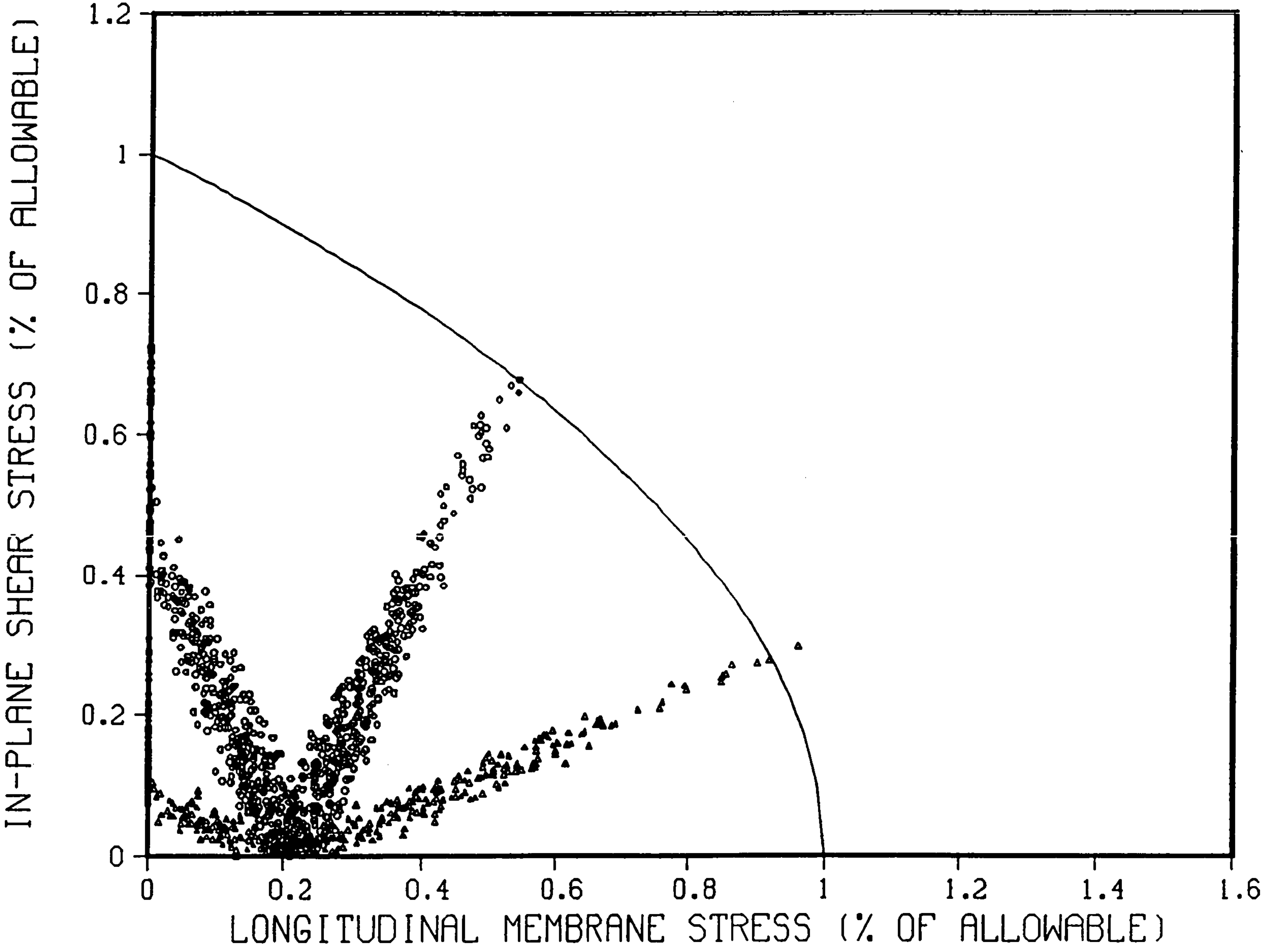

Fig. A-9. Two-dimensional interaction equation, R/t=645, x-input = 0.4 Olympia, y-input = Olympia, z-input = 0.27 Olympia, 4% damping.

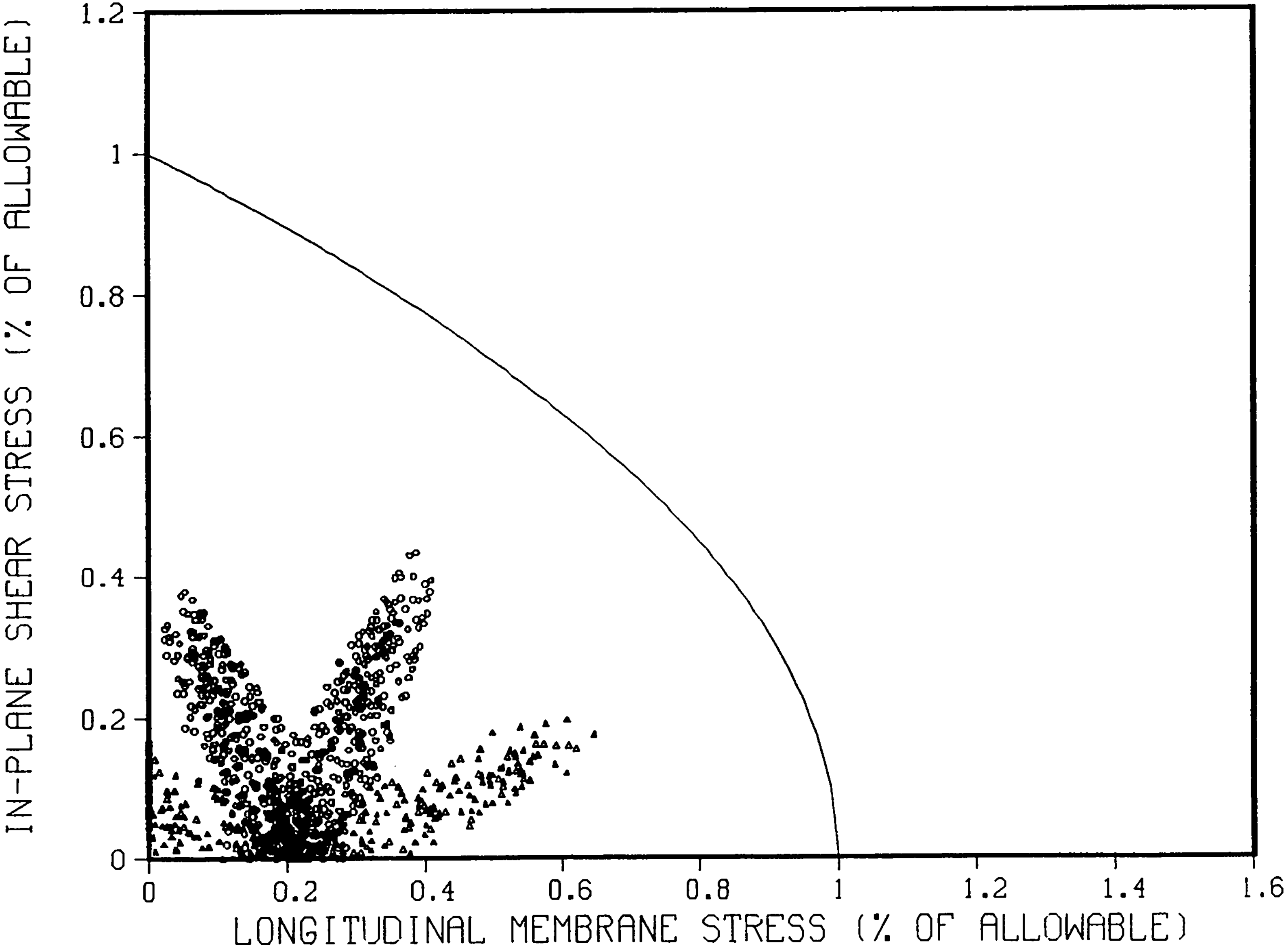

Fig. A-10. Two-dimensional interaction equation, R/t=645, x-input = 0.4 El Centro, y-input = El Centro, z-input = 0.27 El Centro, 1% damping.

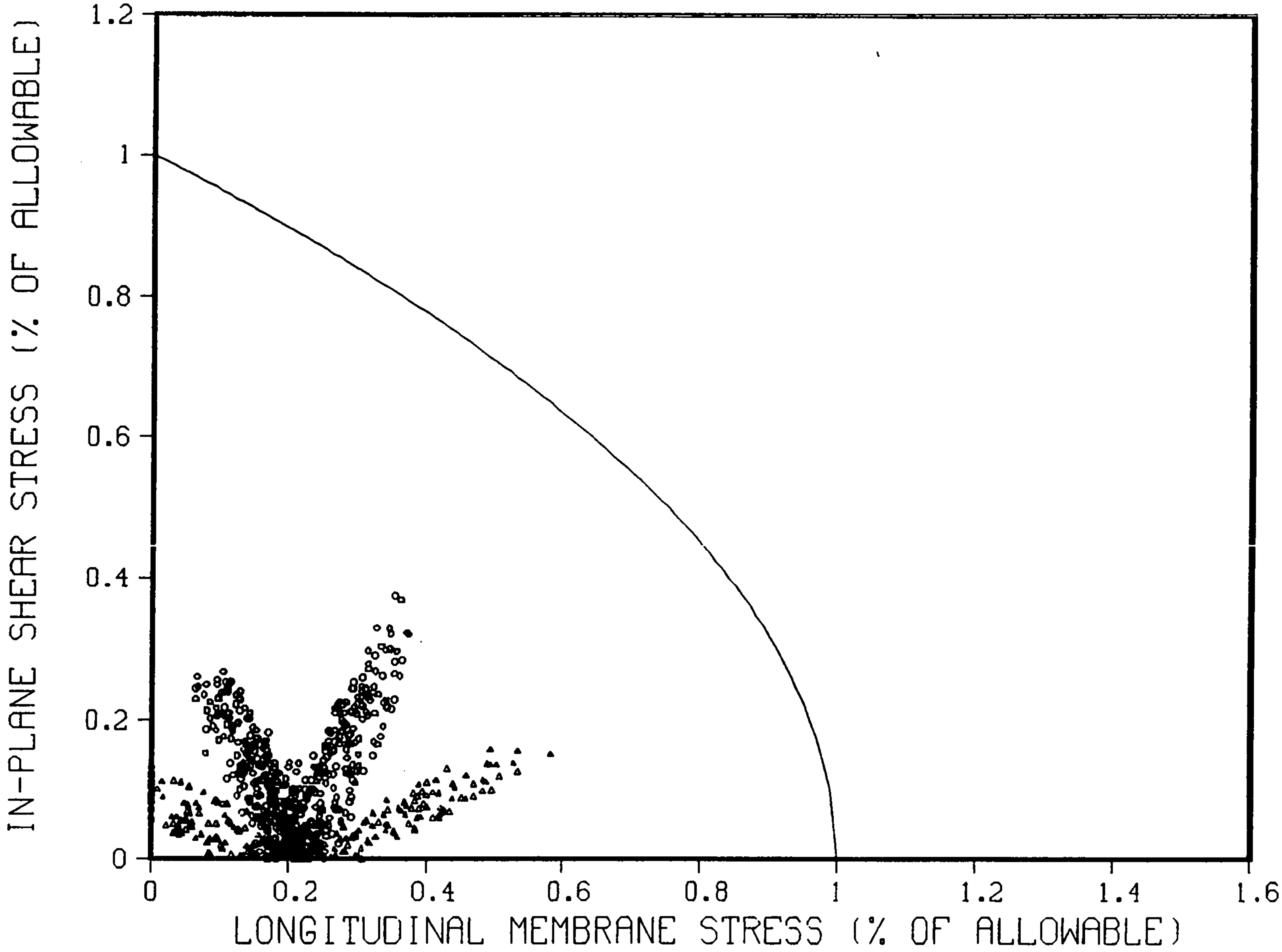

Fig. A-11. Two-dimensional interaction equation, R/t=645, x-input = 0.4 El Centro, y-input = El Centro, z-input = 0.27 El Centro, 2% damping.

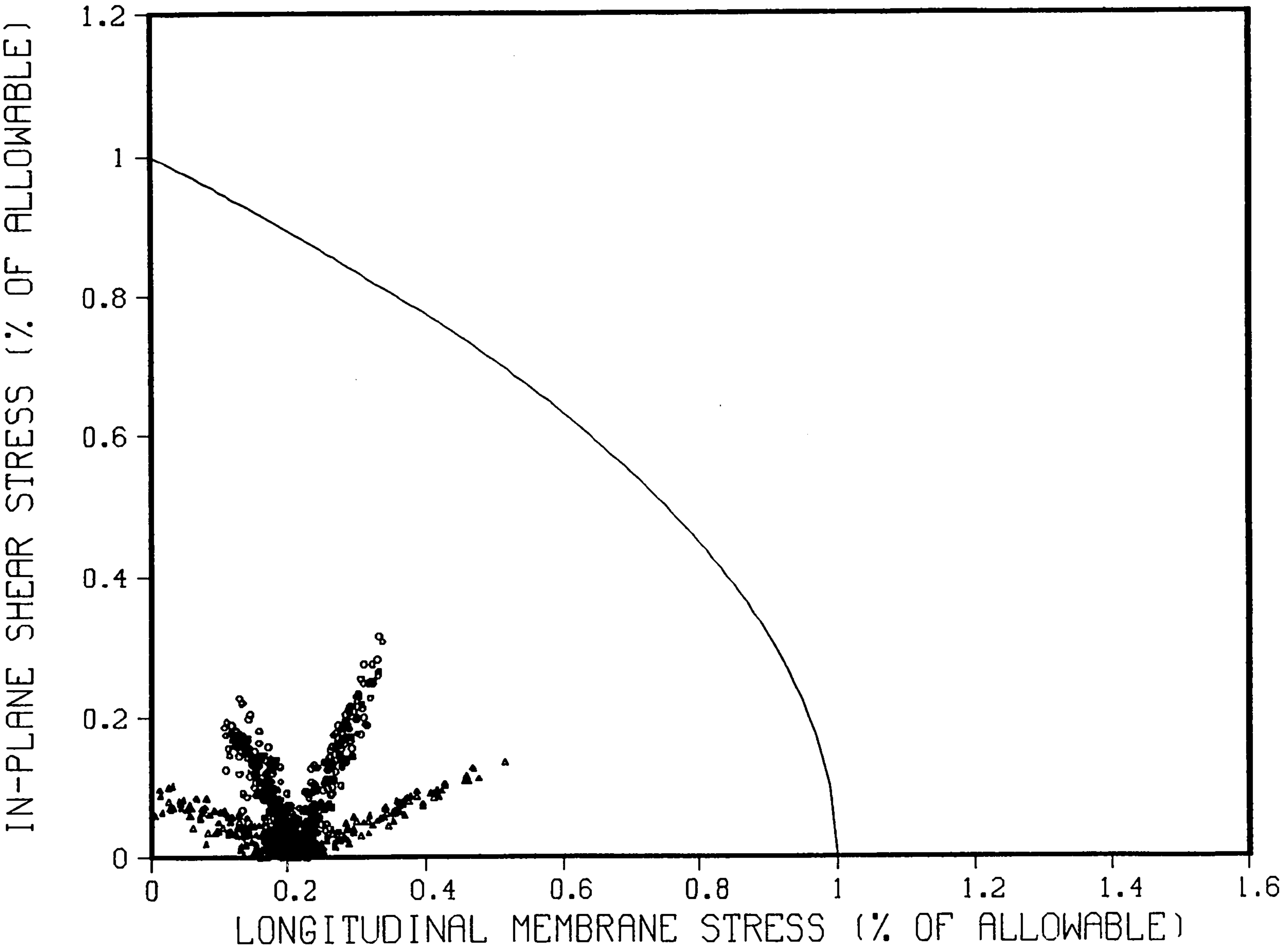

Fig. A-12. Two-dimensional interaction equation, R/t=645, x-input = 0.4 El Centro, y-input = El Centro, z-input = 0.27 El Centro, 4% damping.

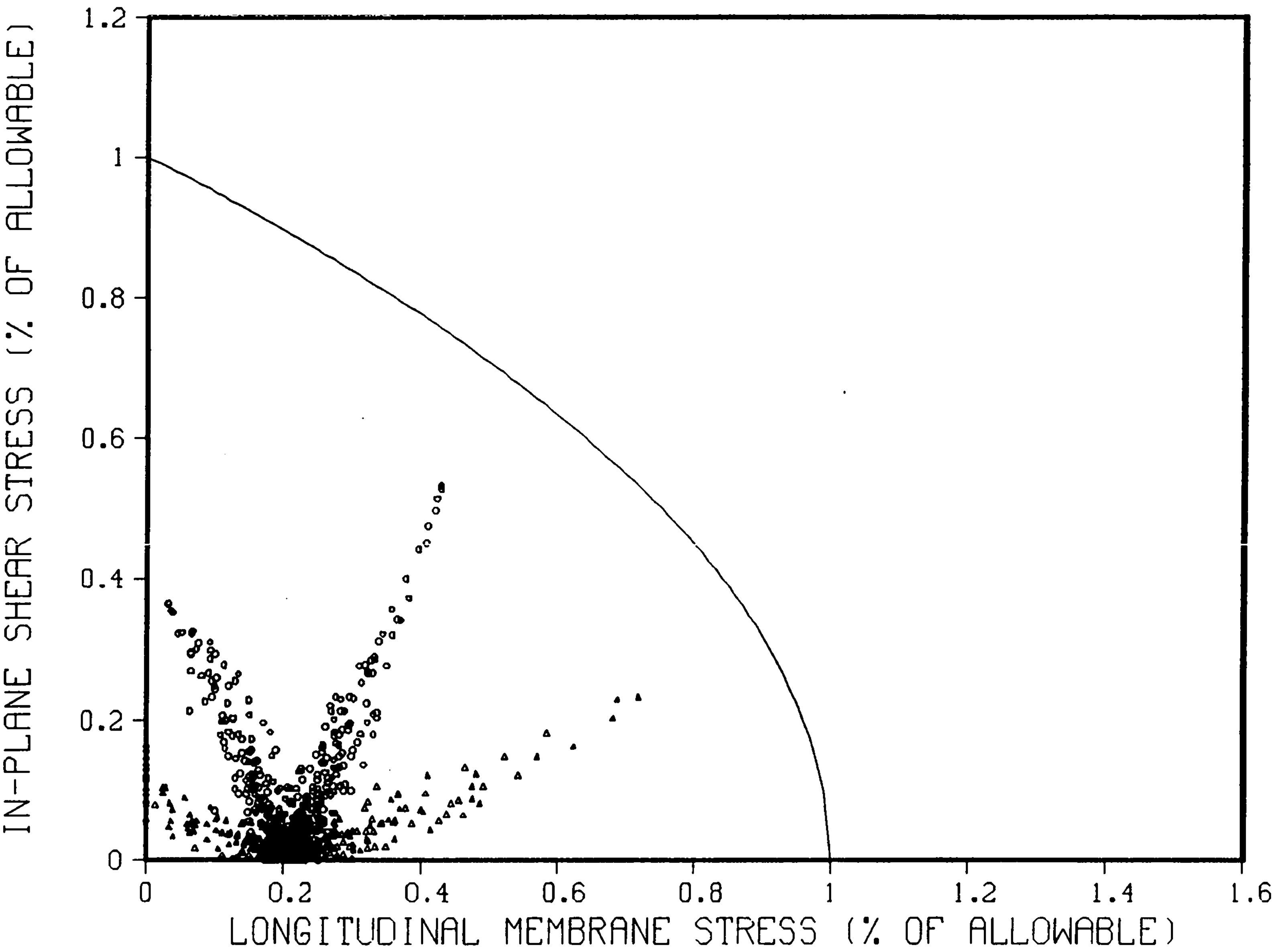

Fig. A-13. Two-dimensional interaction equation, R/t=645, x-input = 0.4 Helena, y-input = Helena, z-input = 0.27 Helena, 1% damping.

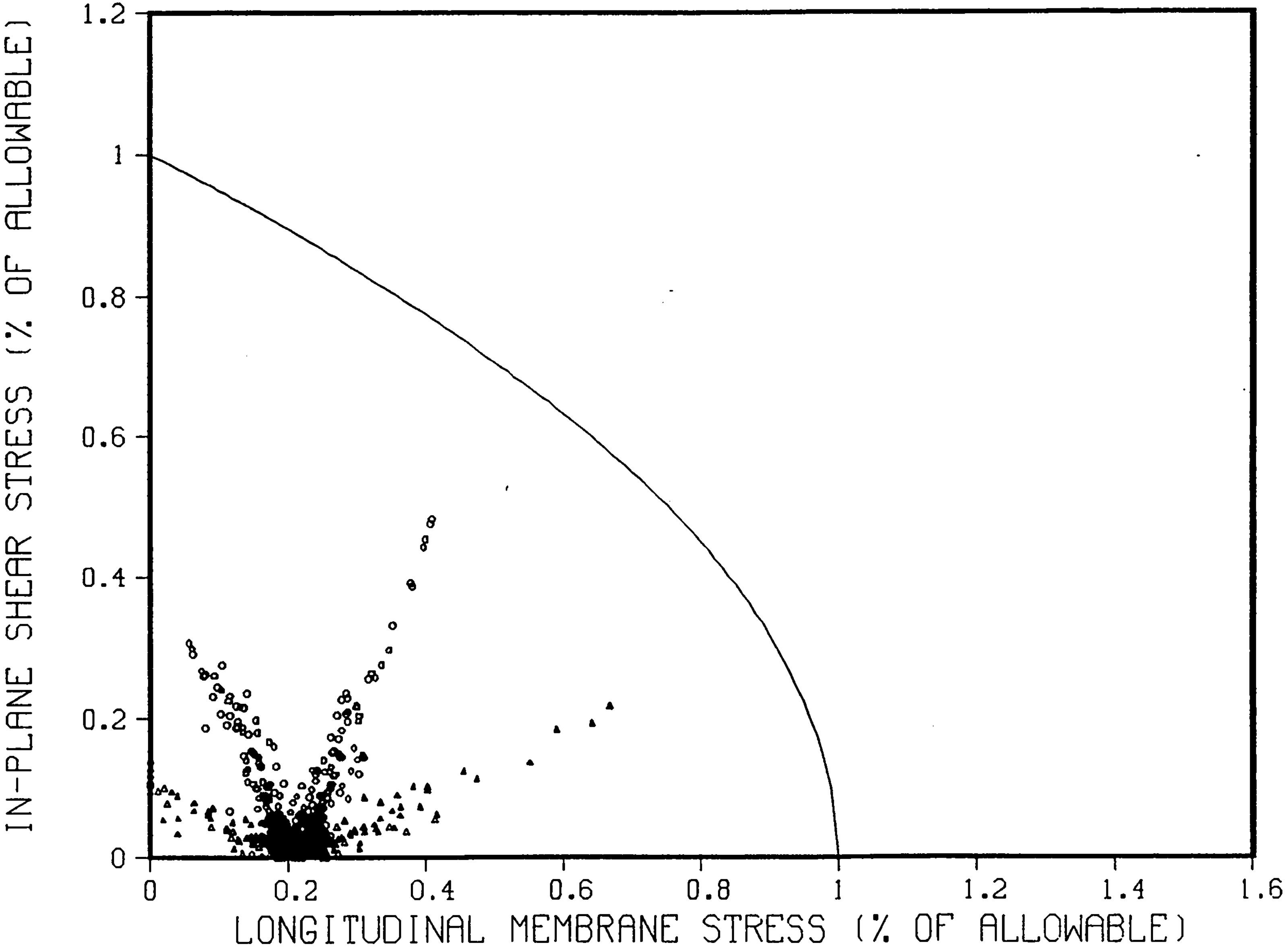

Fig. A-14. Two-dimensional interaction equation, R/t=645, x-input = 0.4 Helena, y-input = Helena, z-input = 0.27 Helena, 2% damping.

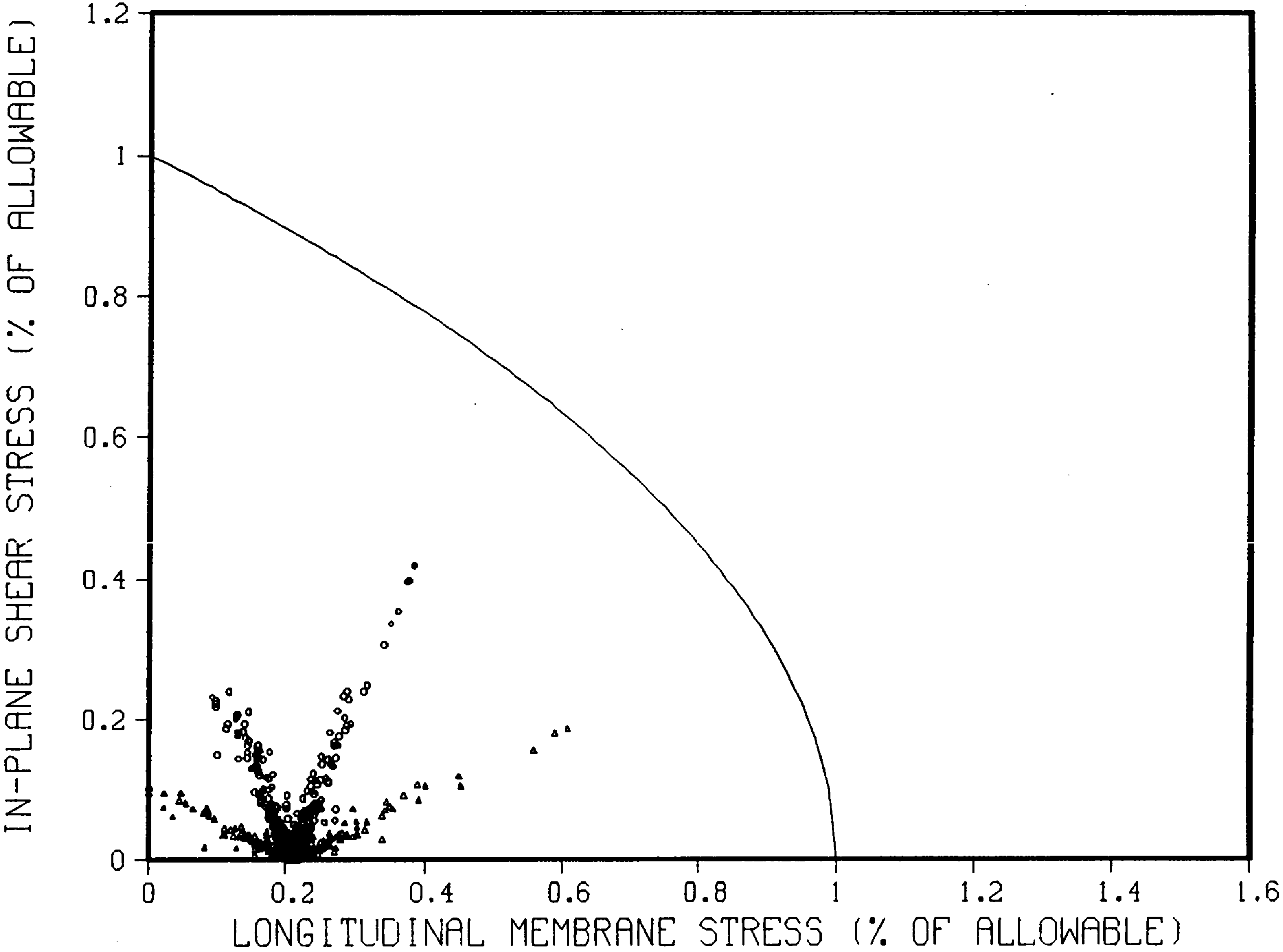

Fig. A-15. Two-dimensional interaction equation, R/t=645, x-input = 0.4 Helena, y-input = Helena, z-input = 0.27 Helena, 4% damping.

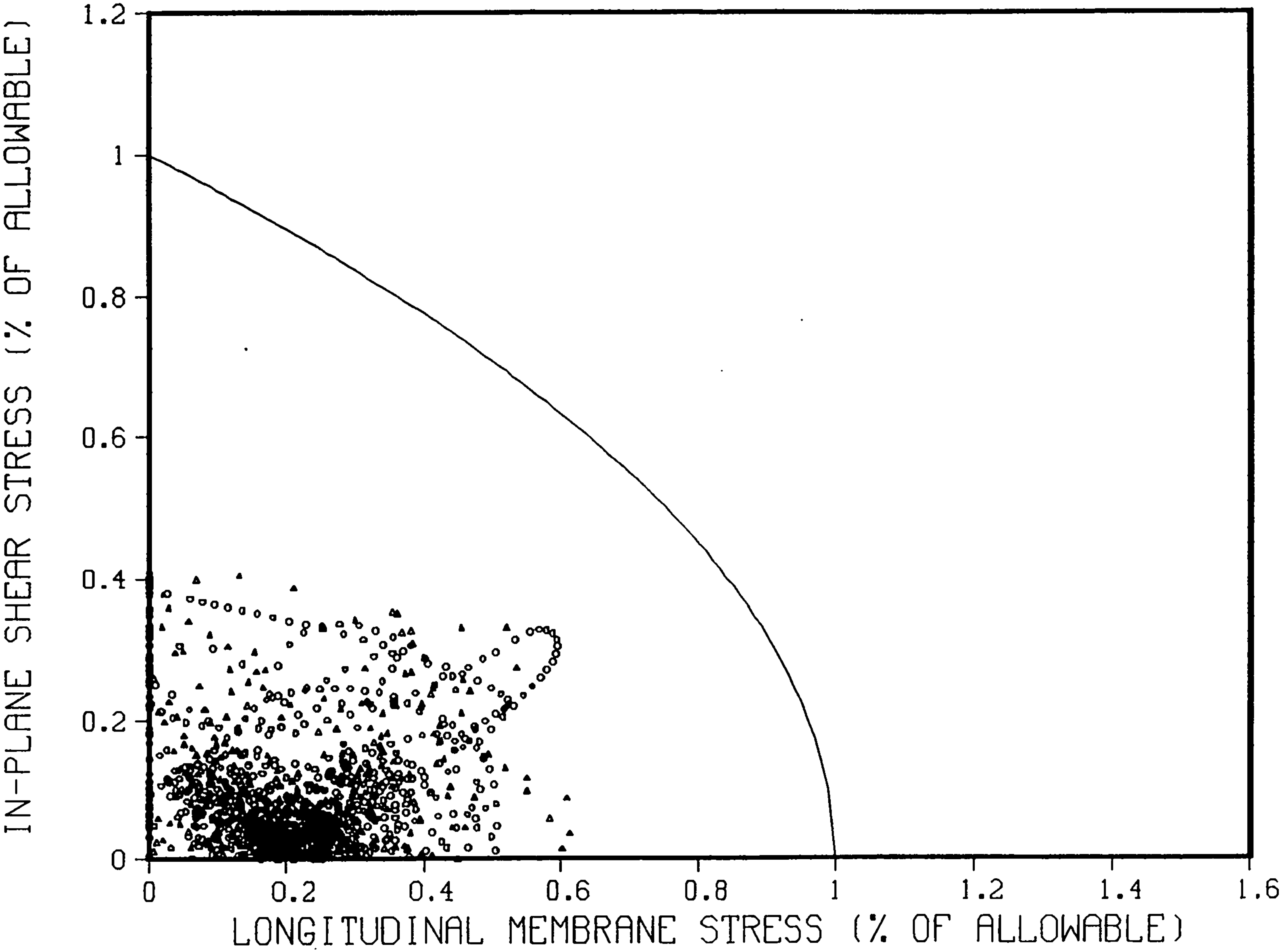

Fig. A-16. Two-dimensional interaction equation, R/t=645, x-input = SSI, y-input = SSI, z-input = 0.82 SSI, 1% damping.

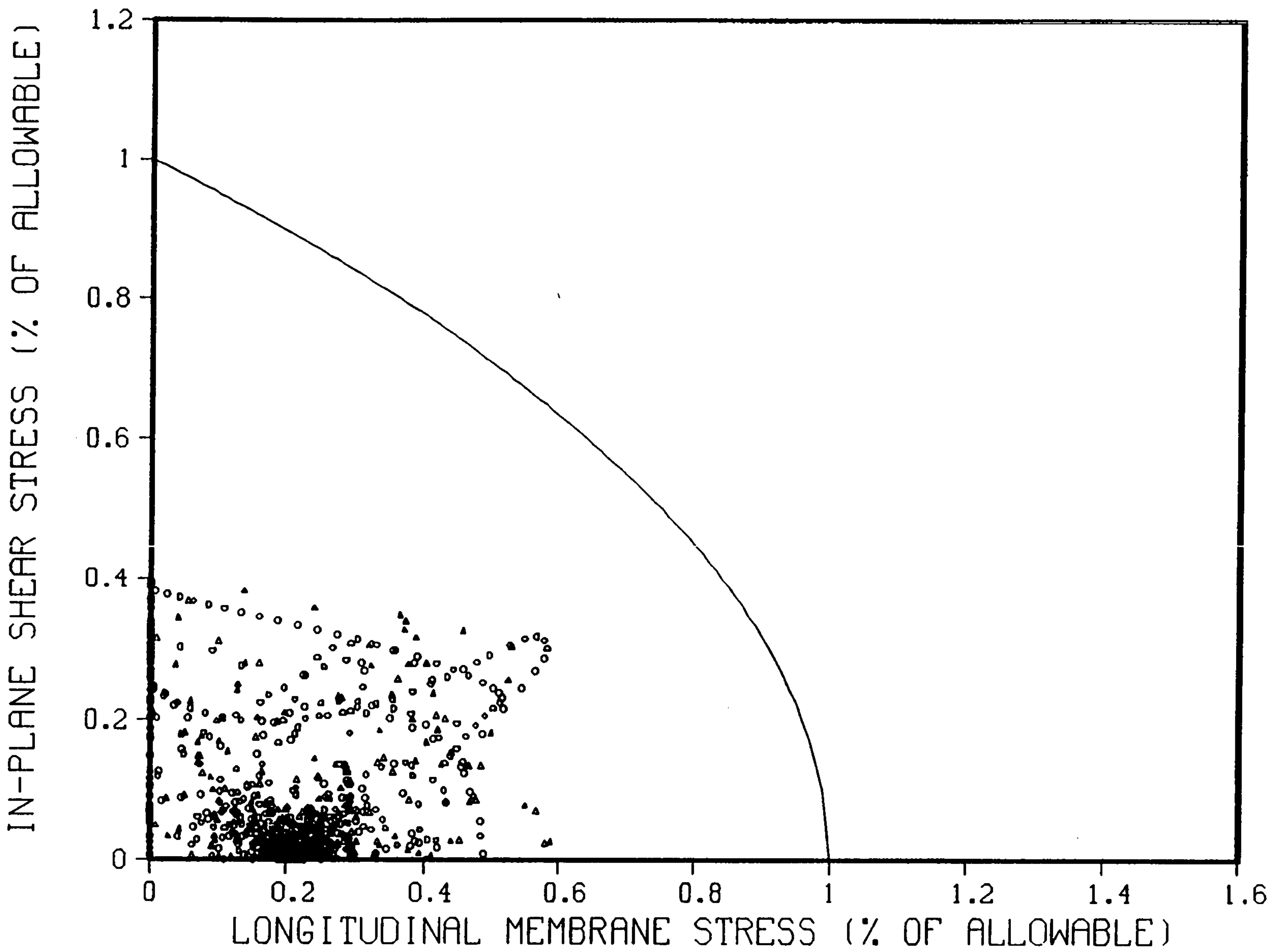

Fig. A-17. Two-dimensional interaction equation, R/t=645, x-input = SSI, y-input = SSI, z-input = 0.82 SSI, 2% damping.

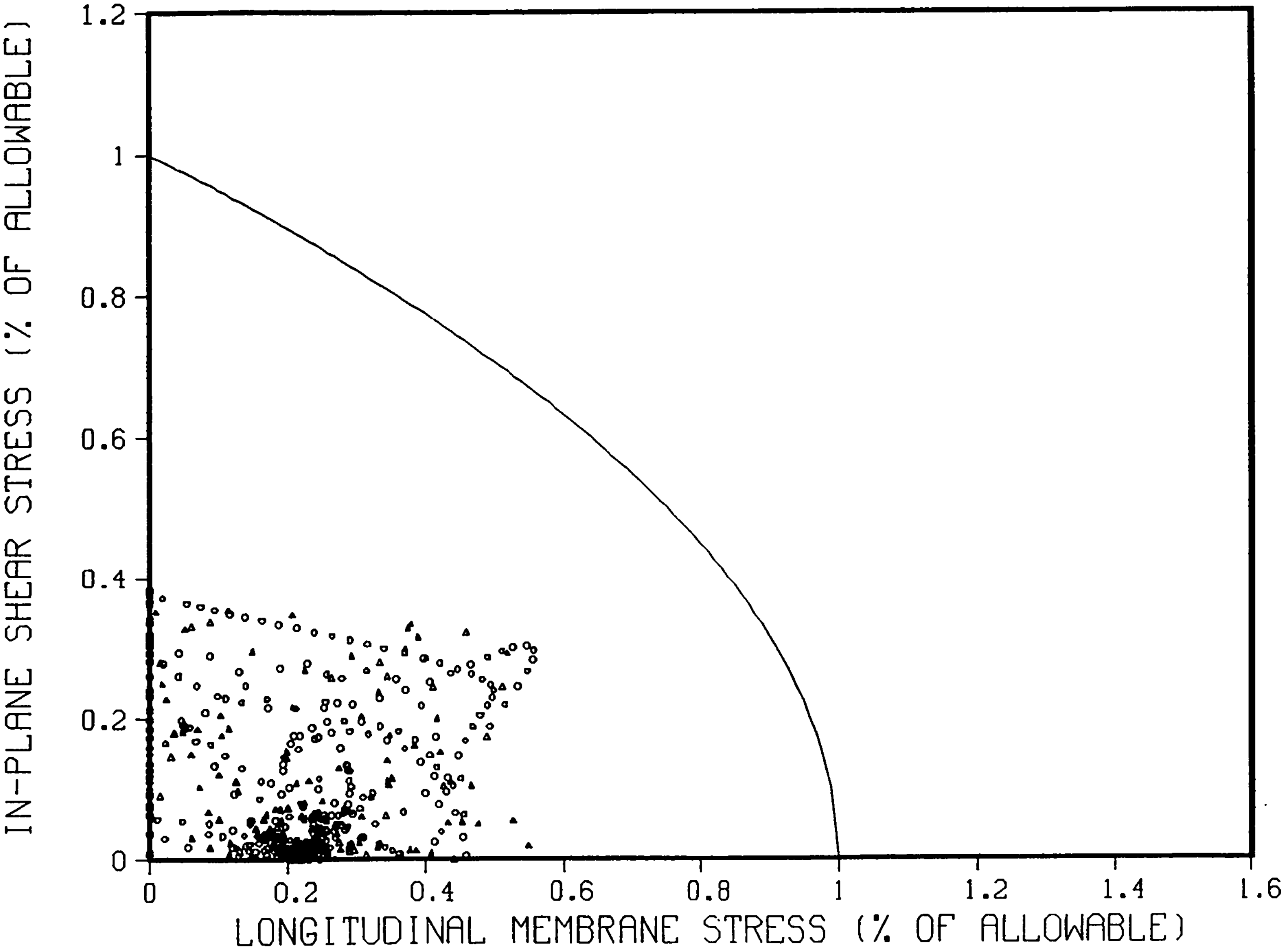

Fig. A-18. Two-dimensional interaction equation, R/t=645, x-input = SSI, y-input = SSI, z-input = 0.82 SSI, 4% damping.

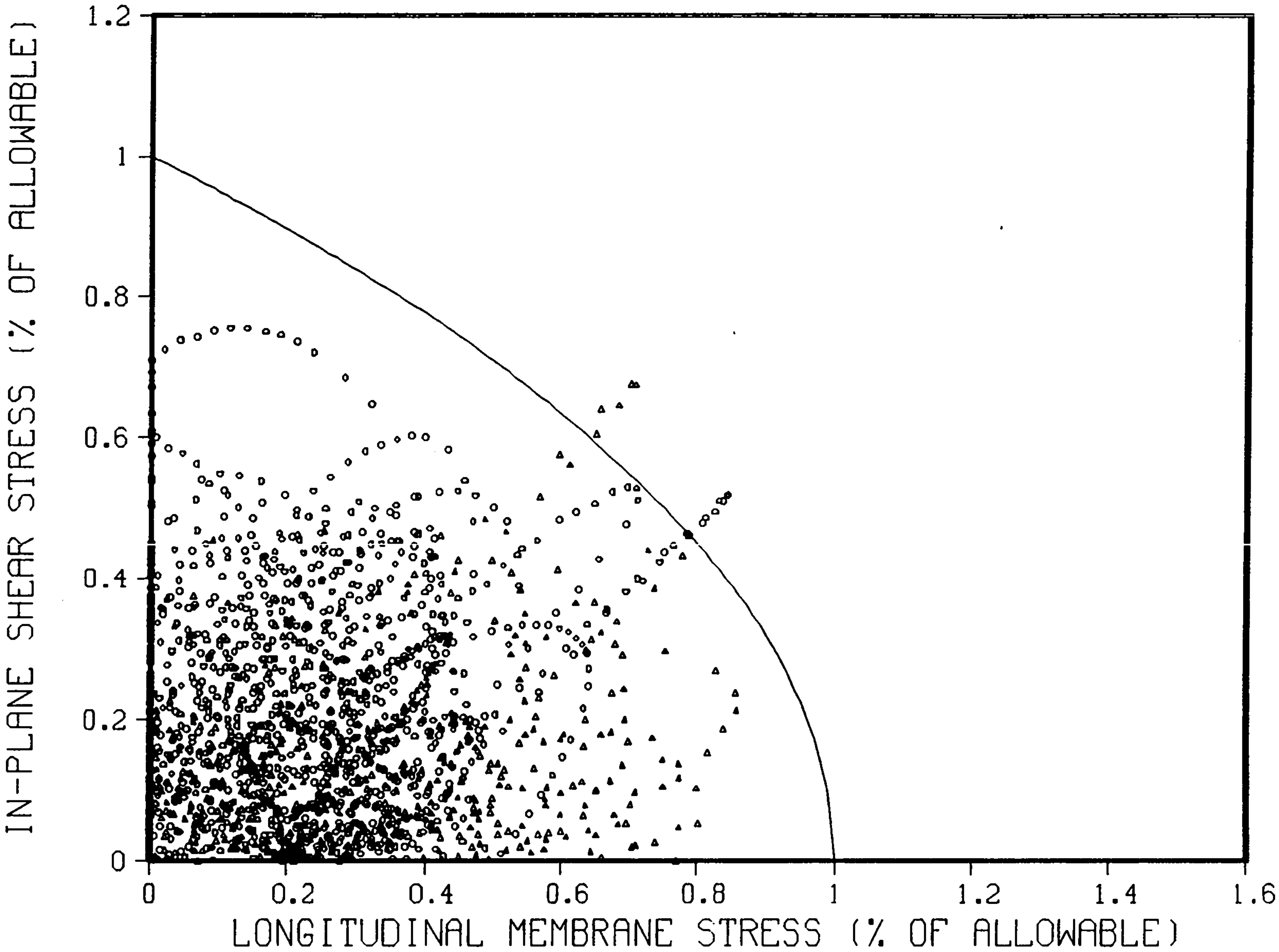

Fig. A-19. Two-dimensional interaction equation, R/t=645, x-input = Reg. Guide 1.60 Spectra, y-input = Reg. Guide 1.60 Spectra, z-input = 0.67 Reg. Guide 1.60 Spectra, 1% damping.

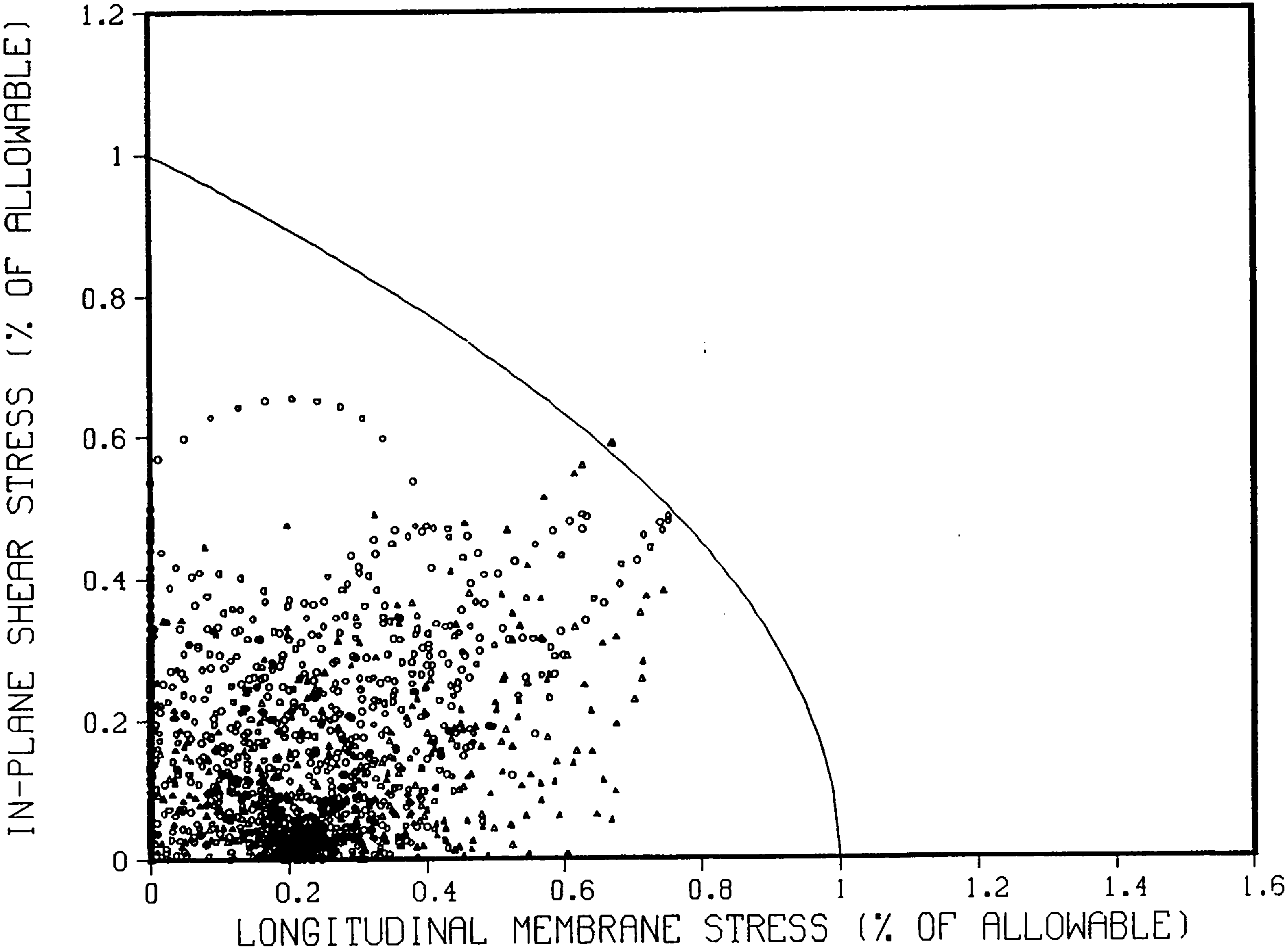

Fig. A-20. Two-dimensional interaction equation, R/t=645, x-input = Reg. Guide 1.60 Spectra, y-input = Reg. Guide 1.60 Spectra, z-input = 0.67 Reg. Guide 1.60 Spectra, 2% damping.

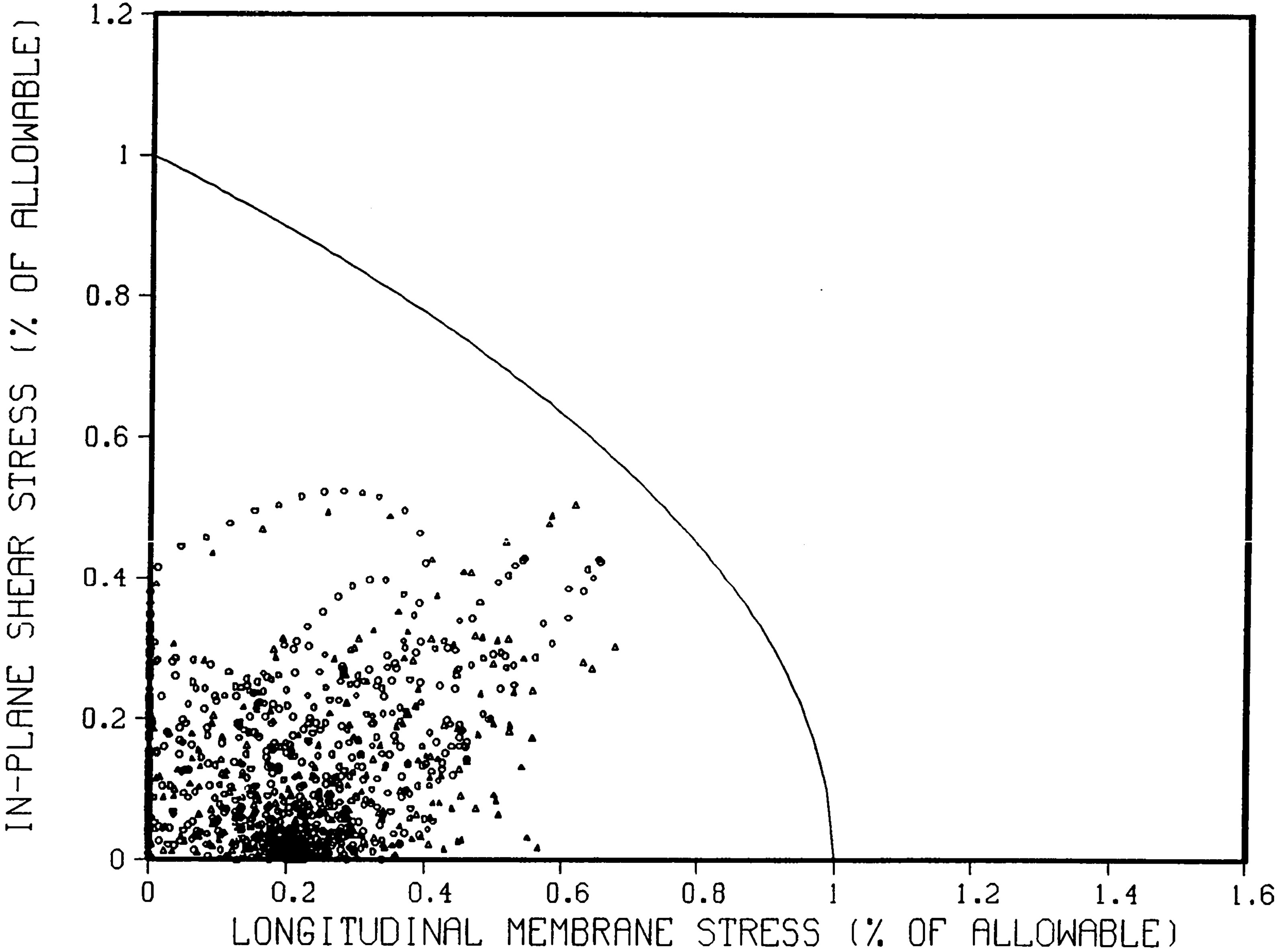

Fig. A-21. Two-dimensional interaction equation, R/t=645, x-input = Reg. Guide 1.60 Spectra, y-input = Reg. Guide 1.60 Spectra, z-input = 0.67 Reg. Guide 1.60 Spectra, 4% damping.

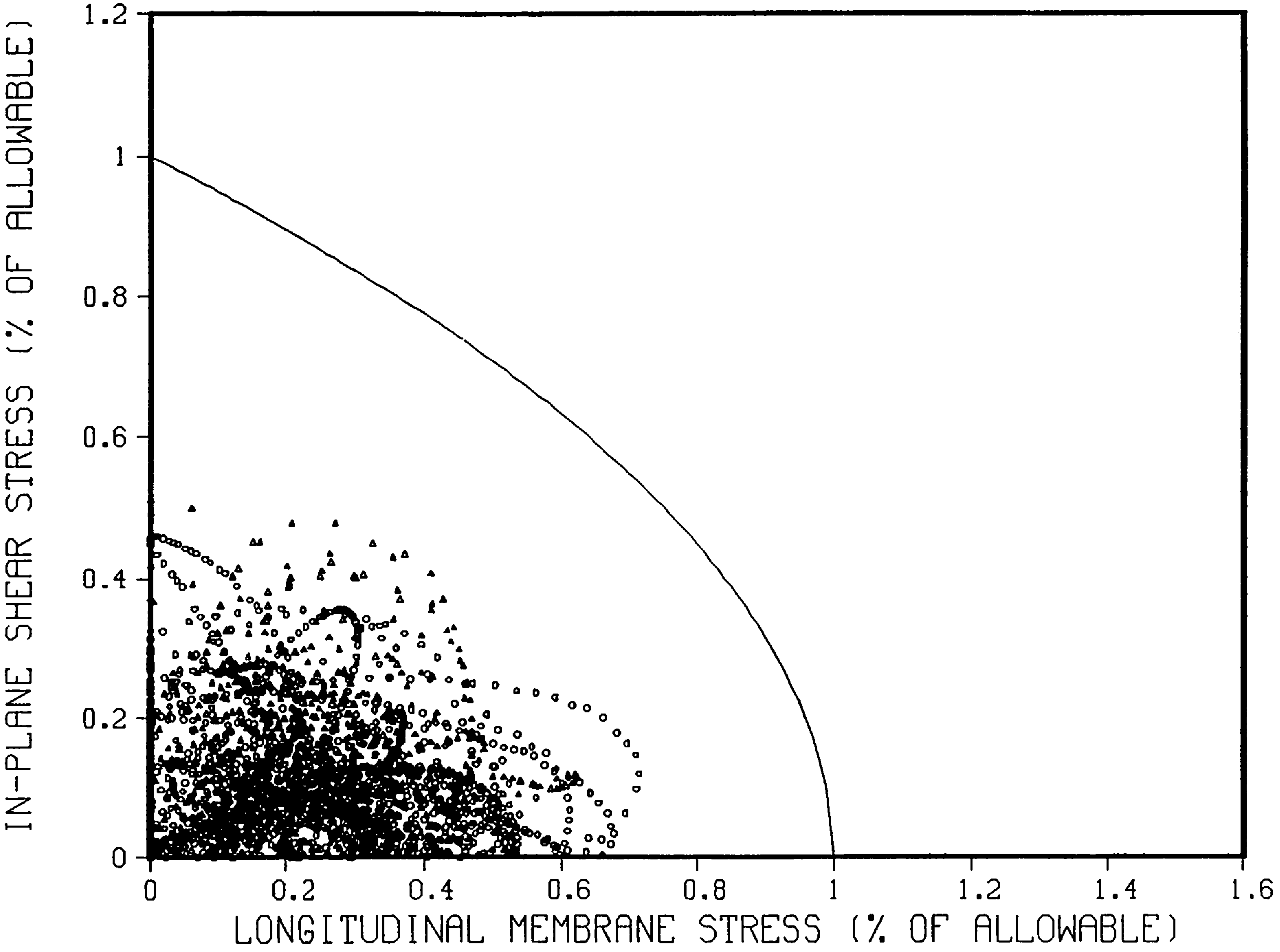

Fig. A-22. Two-dimensional interaction equation, R/t=645, x-input = Ref. 7 spectra, y-input = Ref. 7 spectra, z-input = Ref. 7 spectra, 1% damping.

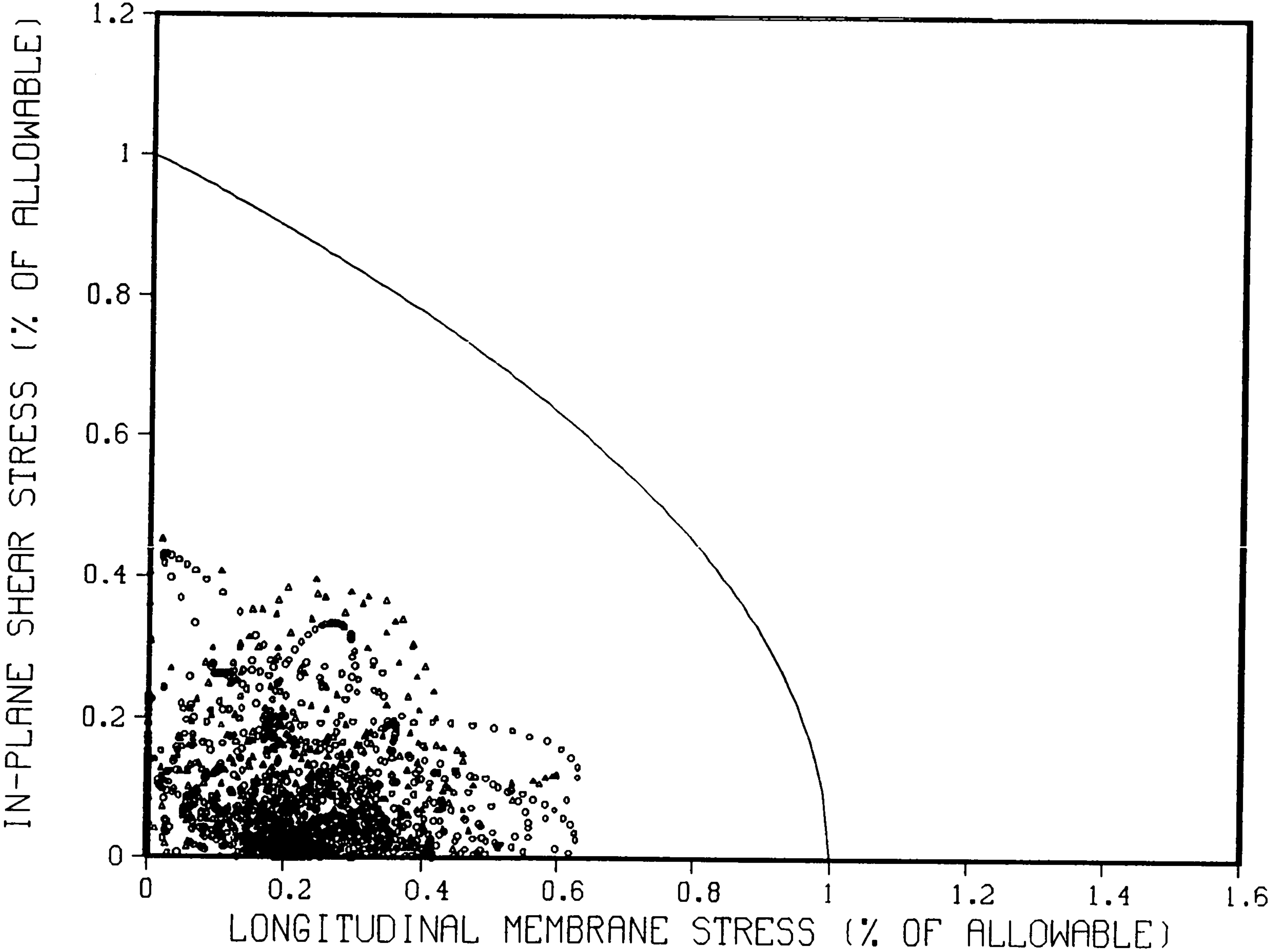

Fig. A-23. Two-dimensional interaction equation, R/t=645, x-input = Ref. 7 spectra, y-input = Ref. 7 spectra, z-input = Ref. 7 spectra, 2% damping.

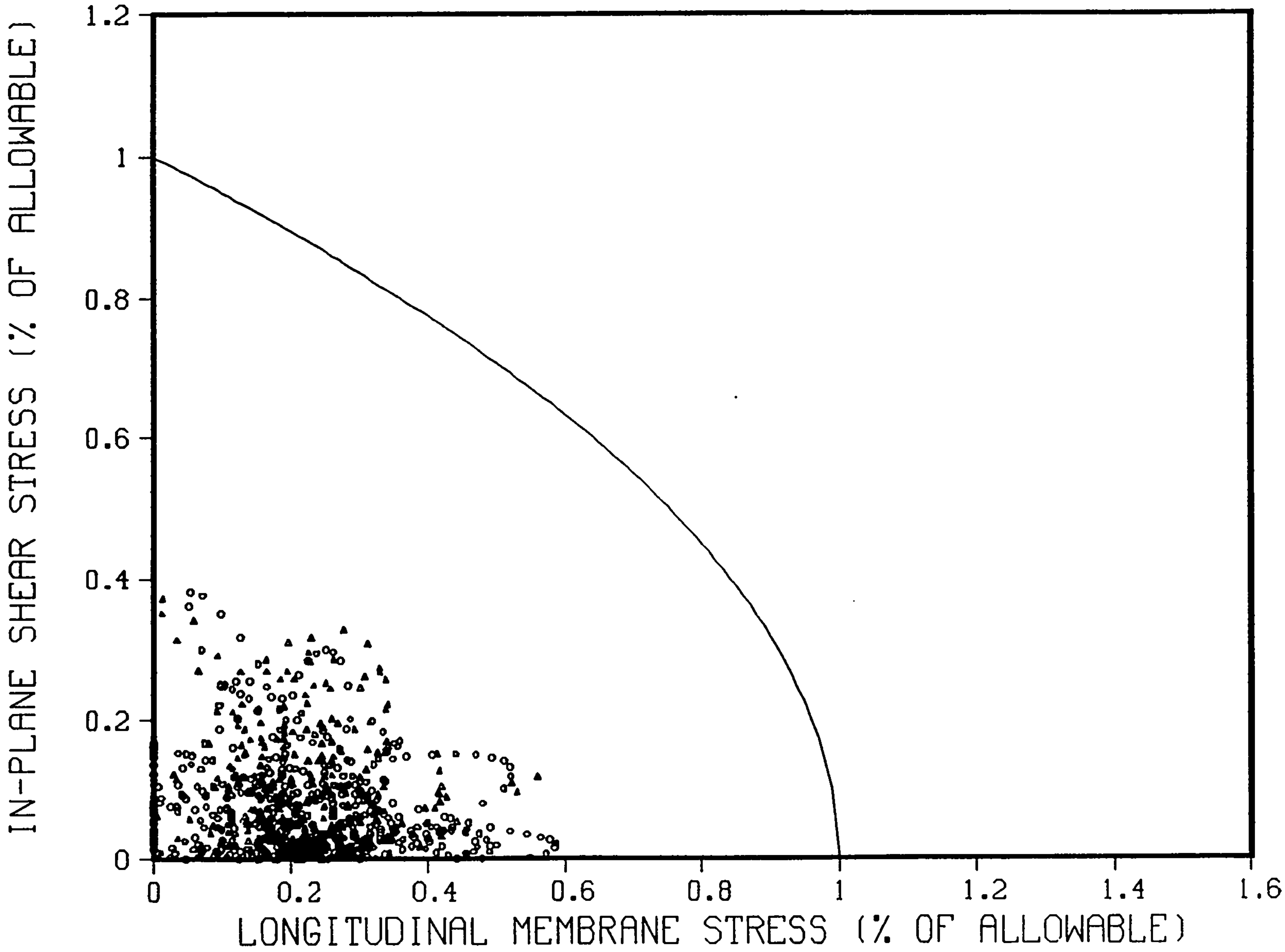

Fig. A-24. Two-dimensional interaction equation, R/t=645, x-input = Ref. 7 spectra, y-input = Ref. 7 spectra, z-input = Ref. 7 spectra, 4% damping.

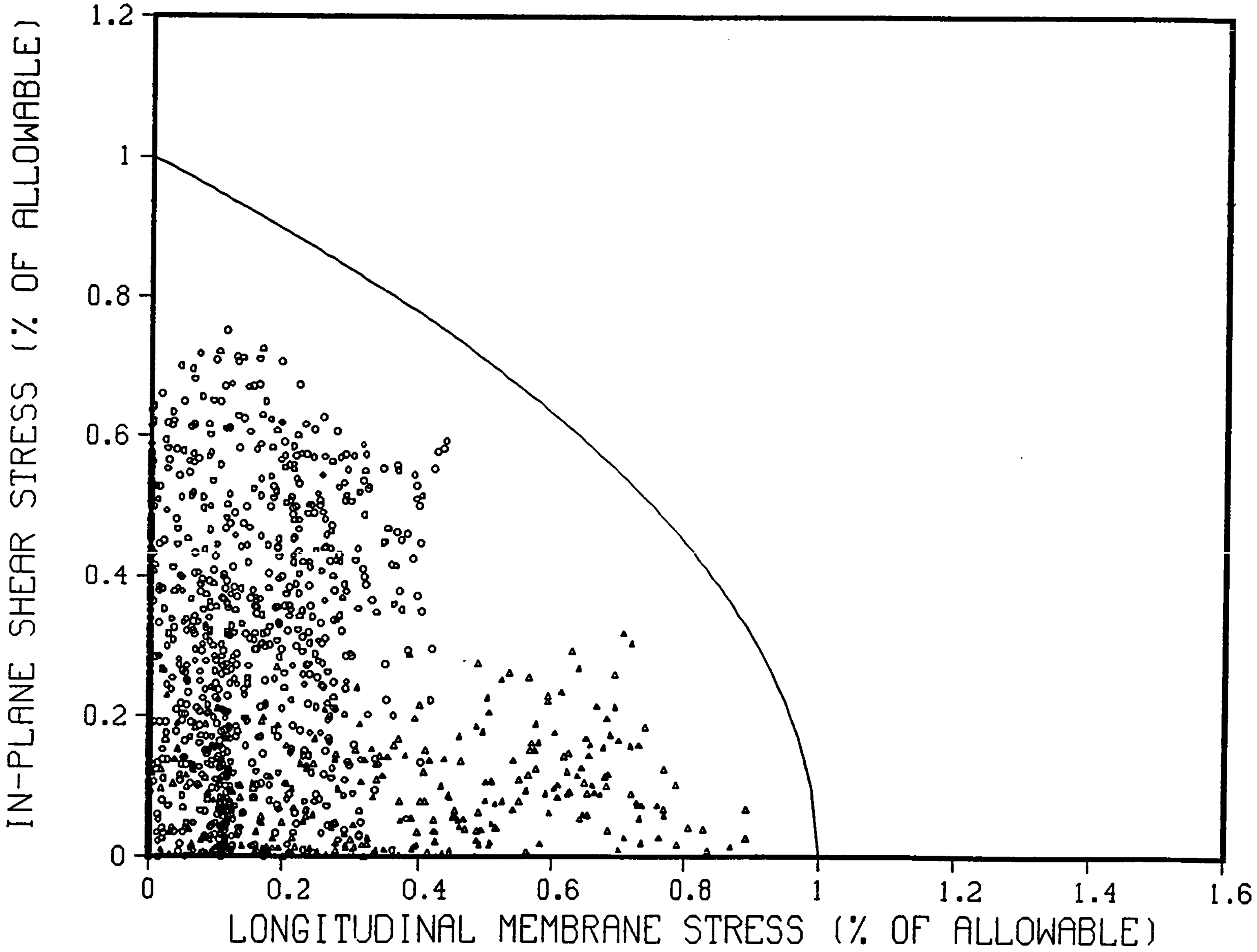

Fig. A-25. Two-dimensional interaction equation, R/t=450, x-input = El Centro, y-input = Olympia, z-input = 0.67 Helena, 1% damping.

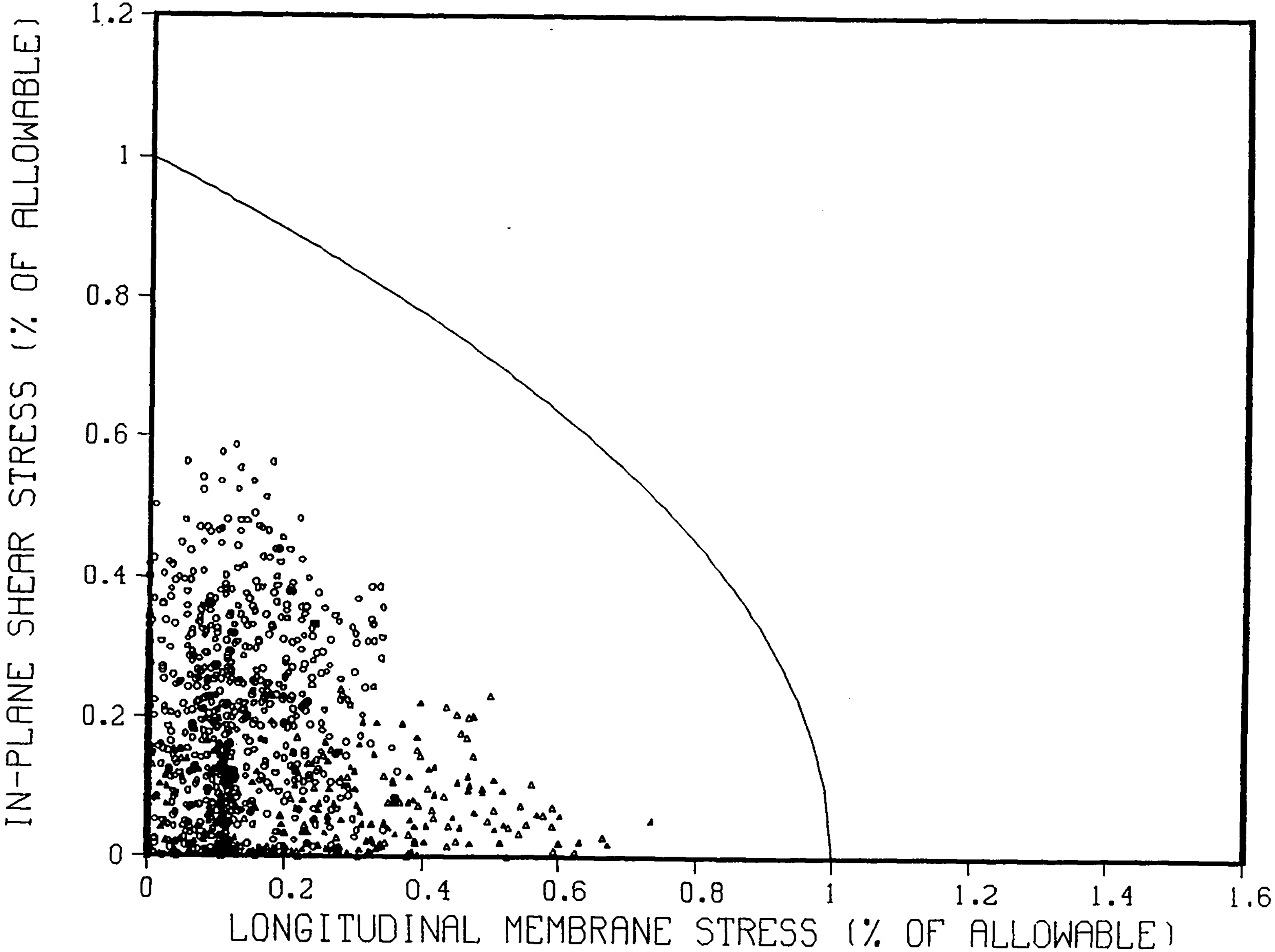

Fig. A-26. Two-dimensional interaction equation, R/t=450, x-input = El Centro, y-input = Olympia, z-input = 0.67 Helena, 2% damping.

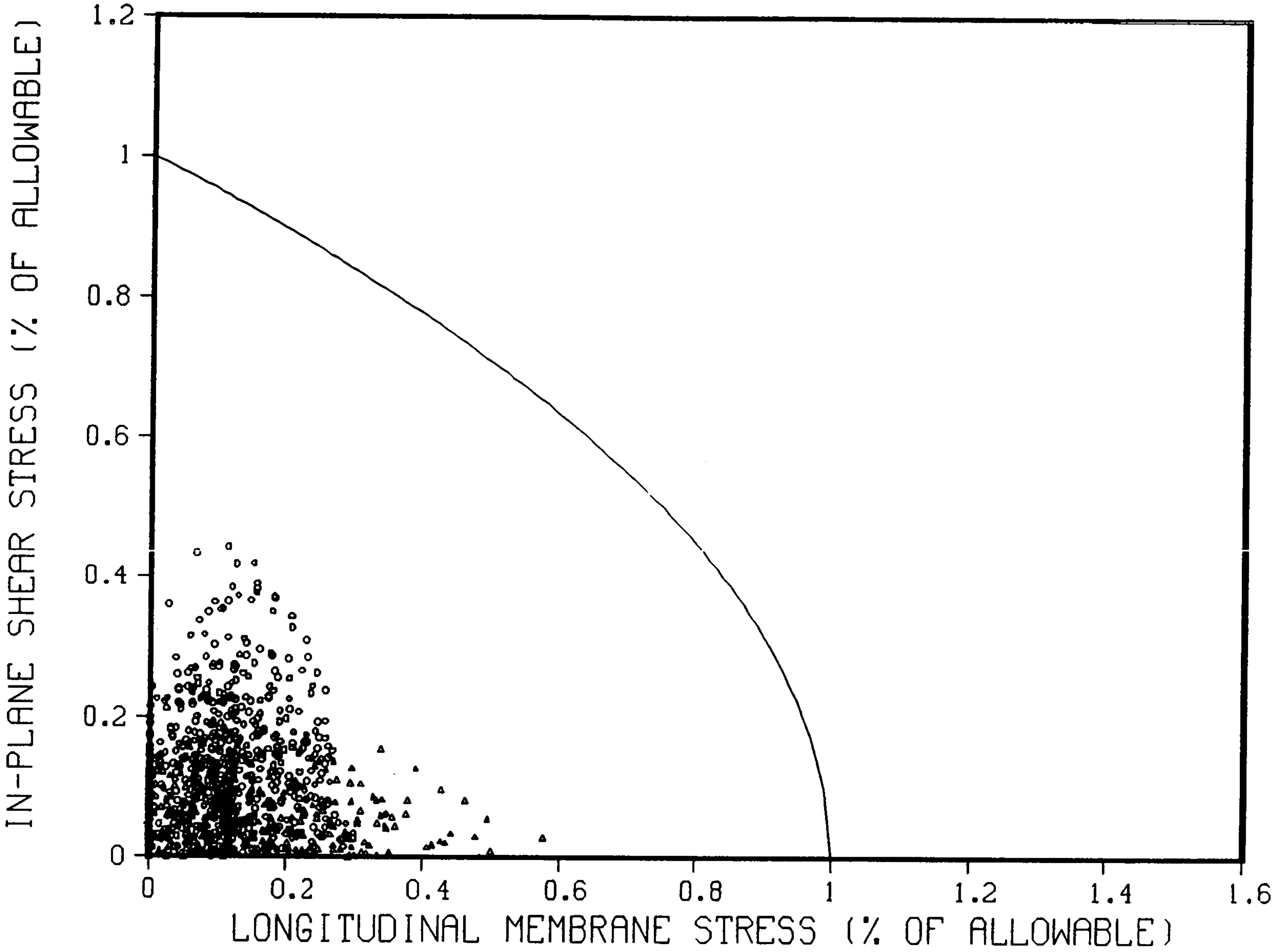

Fig. A-27. Two-dimensional interaction equation, R/t=450, x-input = El Centro, y-input = Olympia, z-input = 0.67 Helena, 4% damping.

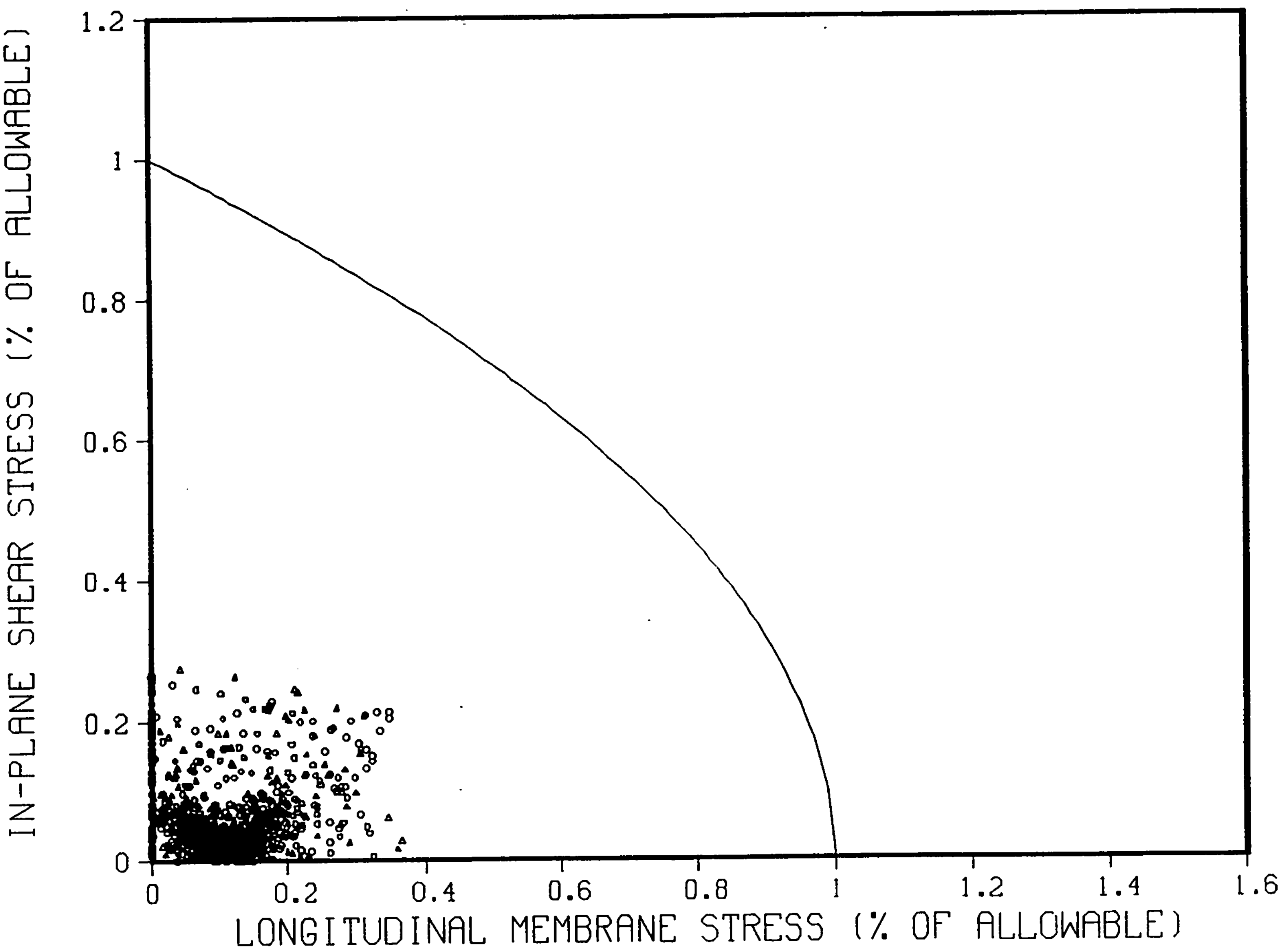

Fig. A-28. Two-dimensional interaction equation, R/t=450, x-input = SSI, y-input = SSI, z-input = 0.82 SSI, 1% damping.

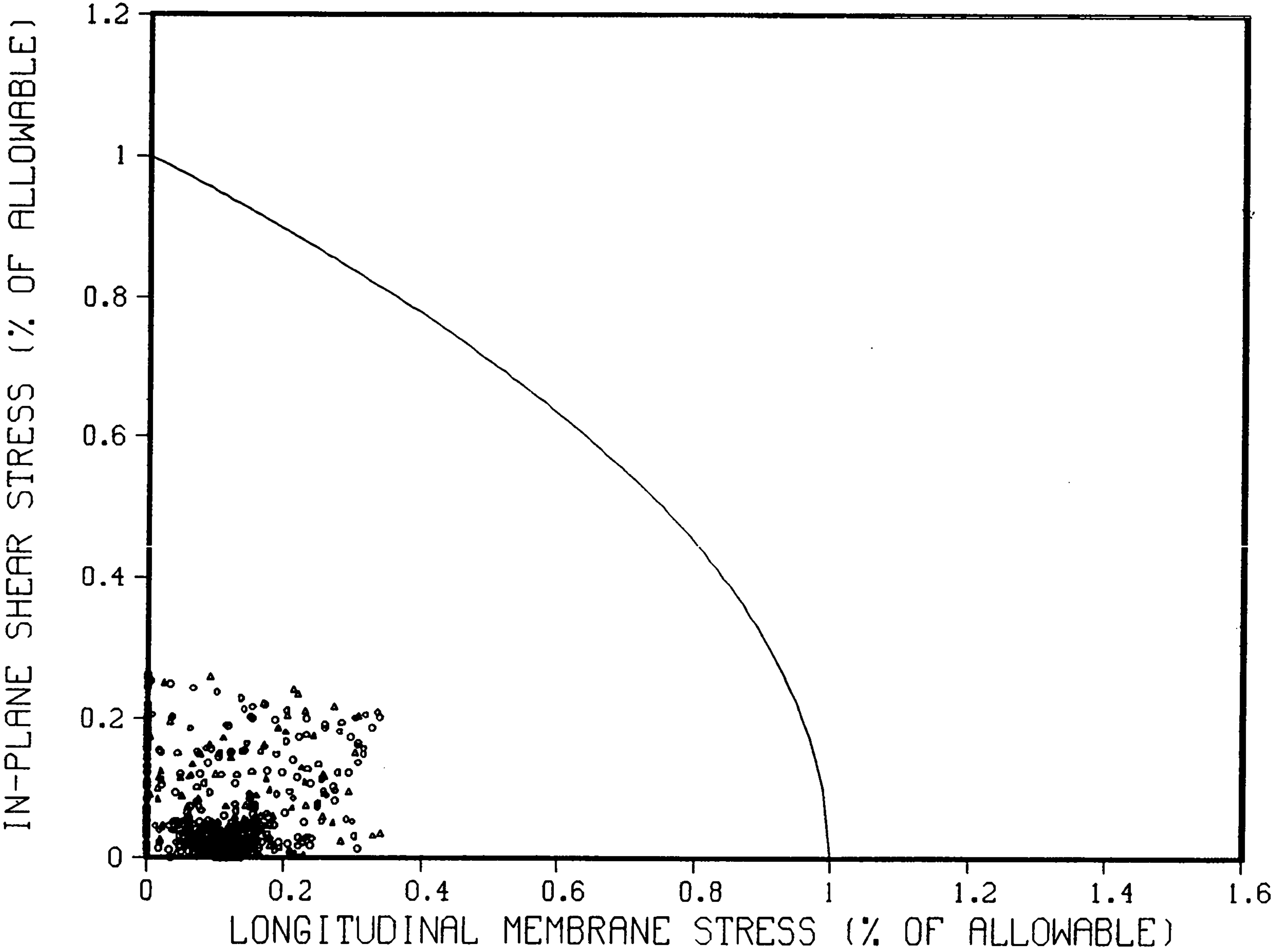

Fig. A-29. Two-dimensional interaction equation, R/t=450, x-input = SSI, y-input = SSI, z-input = 0.82 SSI, 2% damping.

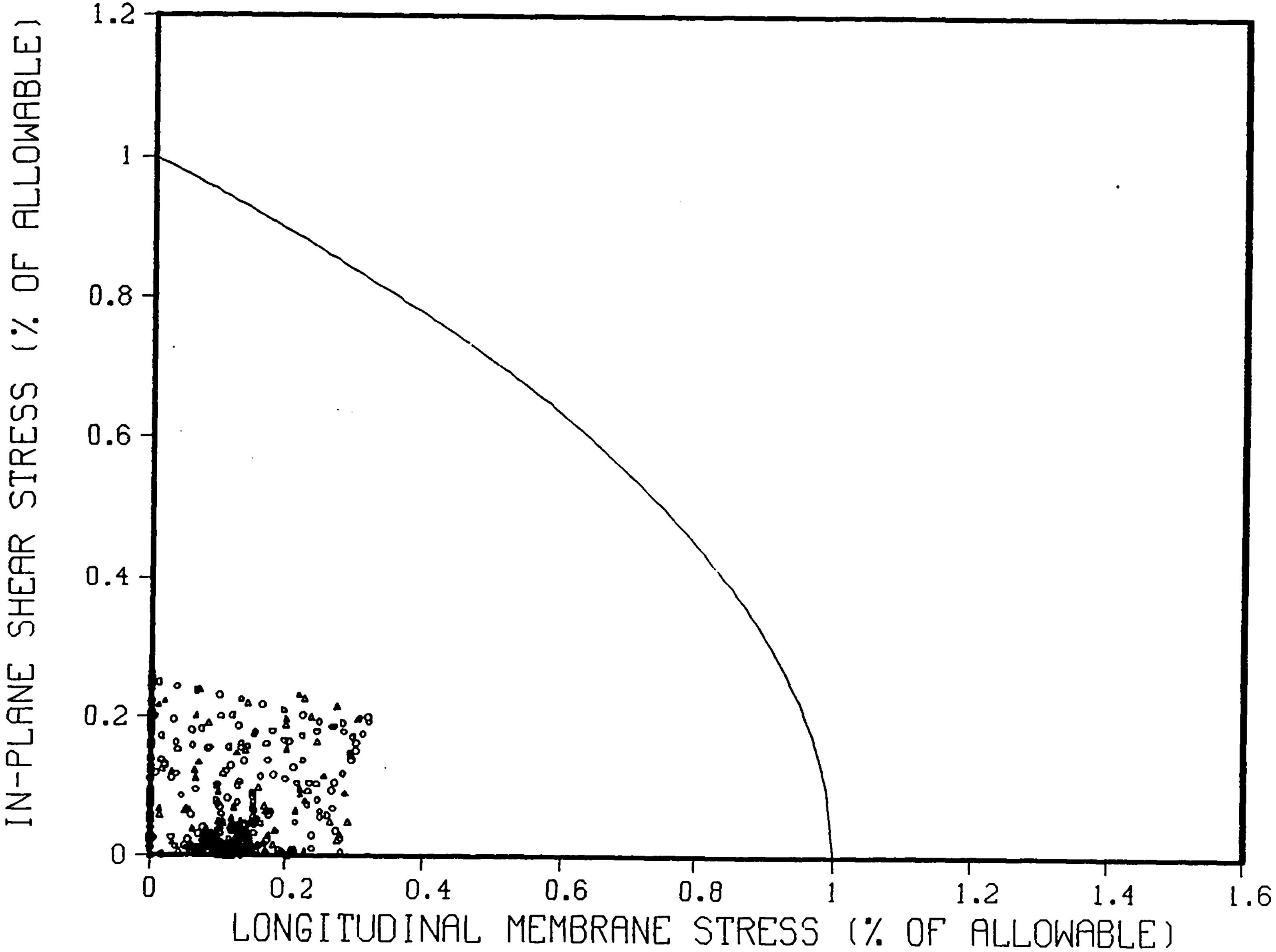

Fig. A-30. Two-dimensional interaction equation, R/t=450, x-input = SSI, y-input = SSI, z-input = 0.82 SSI, 4% damping.

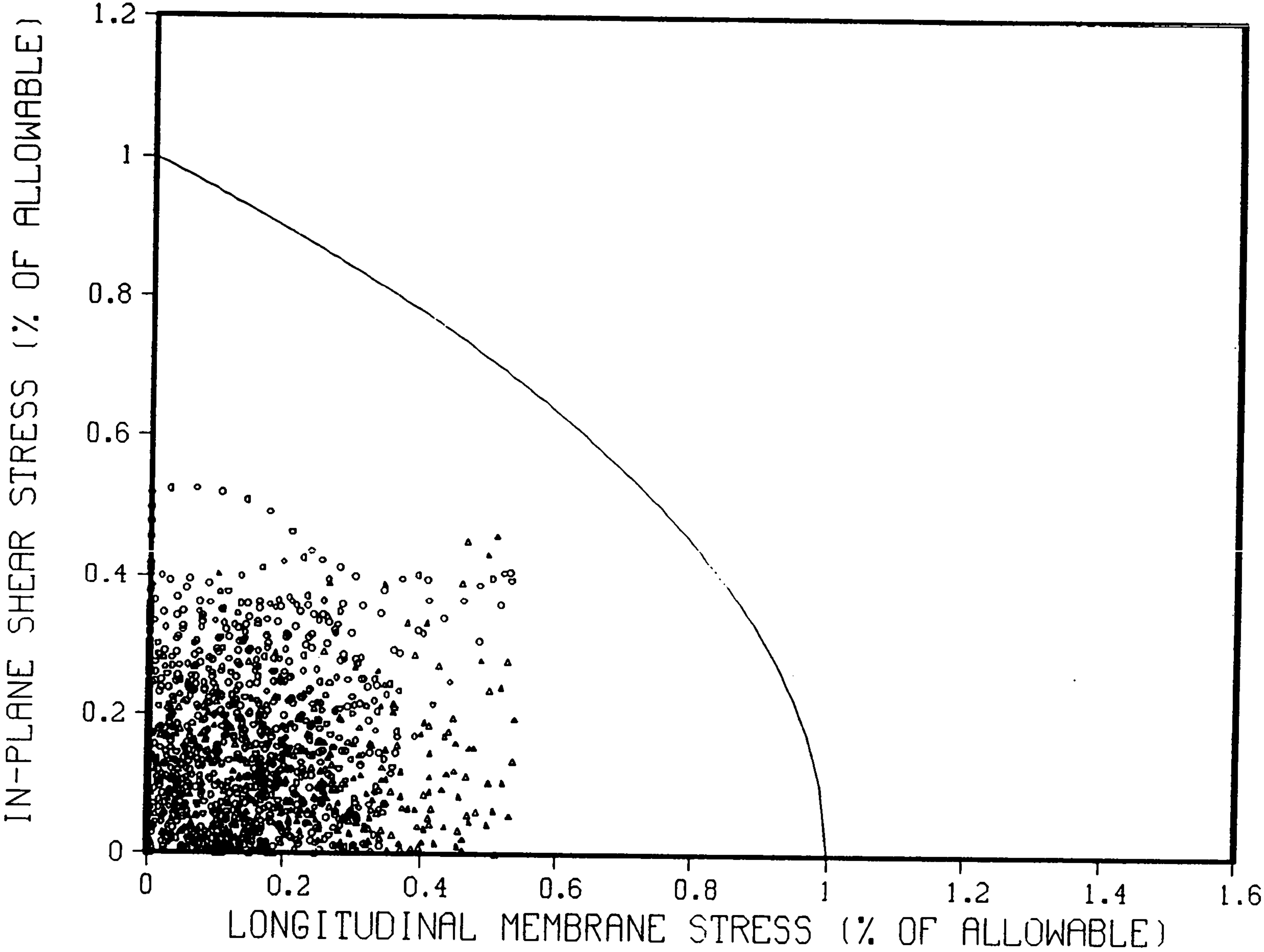

Fig. A-31. Two-dimensional interaction equation, R/t=450, x-input = Reg. Guide 1.60 Spectra, y-input = Reg. Guide 1.60 Spectra, z-input = 0.67 Reg. Guide 1.60 Spectra, 1% damping.

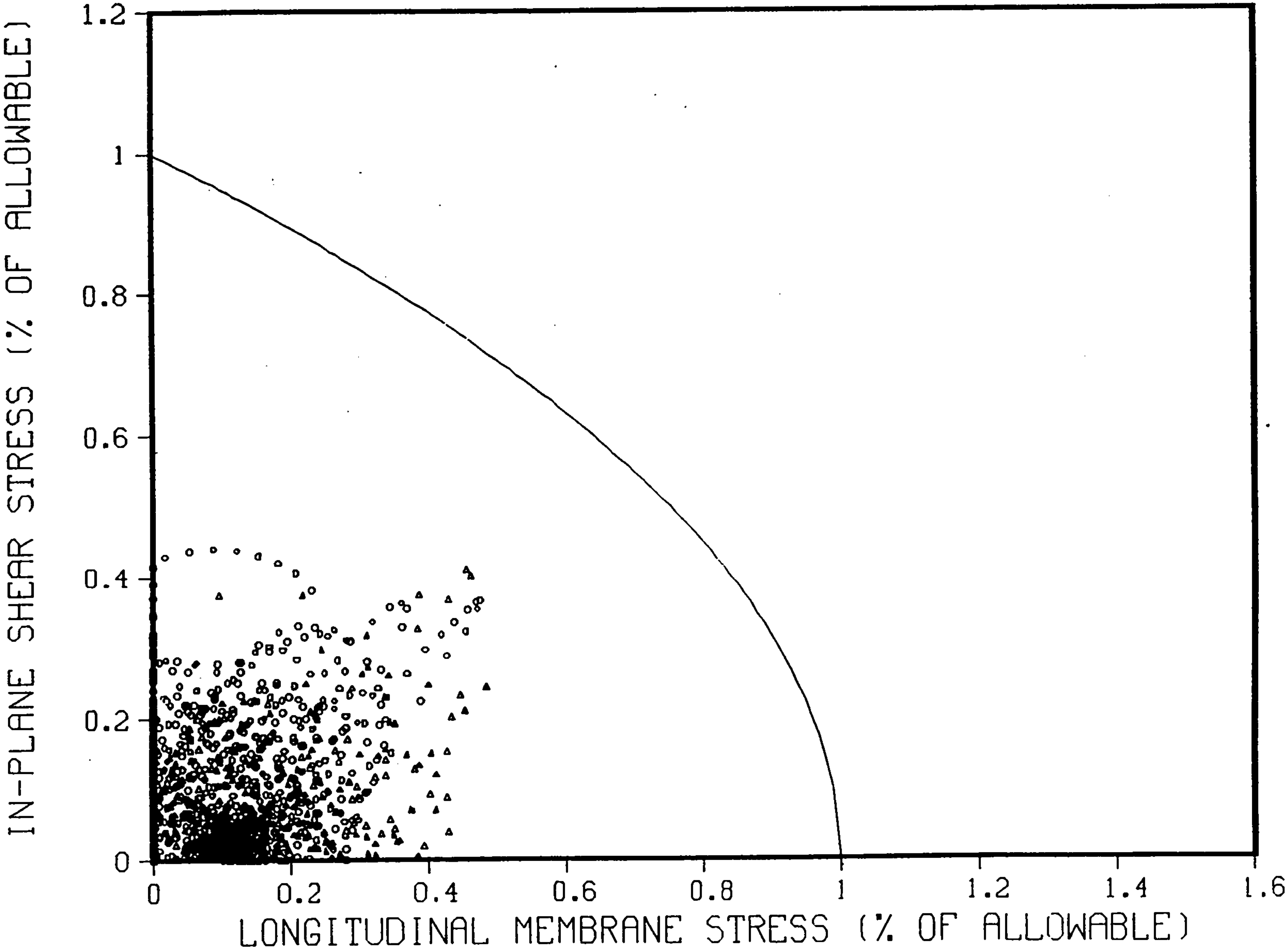

Fig. A-32. Two-dimensional interaction equation, R/t=450, x-input = Reg. Guide 1.60 Spectra, y-input = Reg. Guide 1.60 Spectra, z-input = 0.67 Reg. Guide 1.60 Spectra, 2% damping.

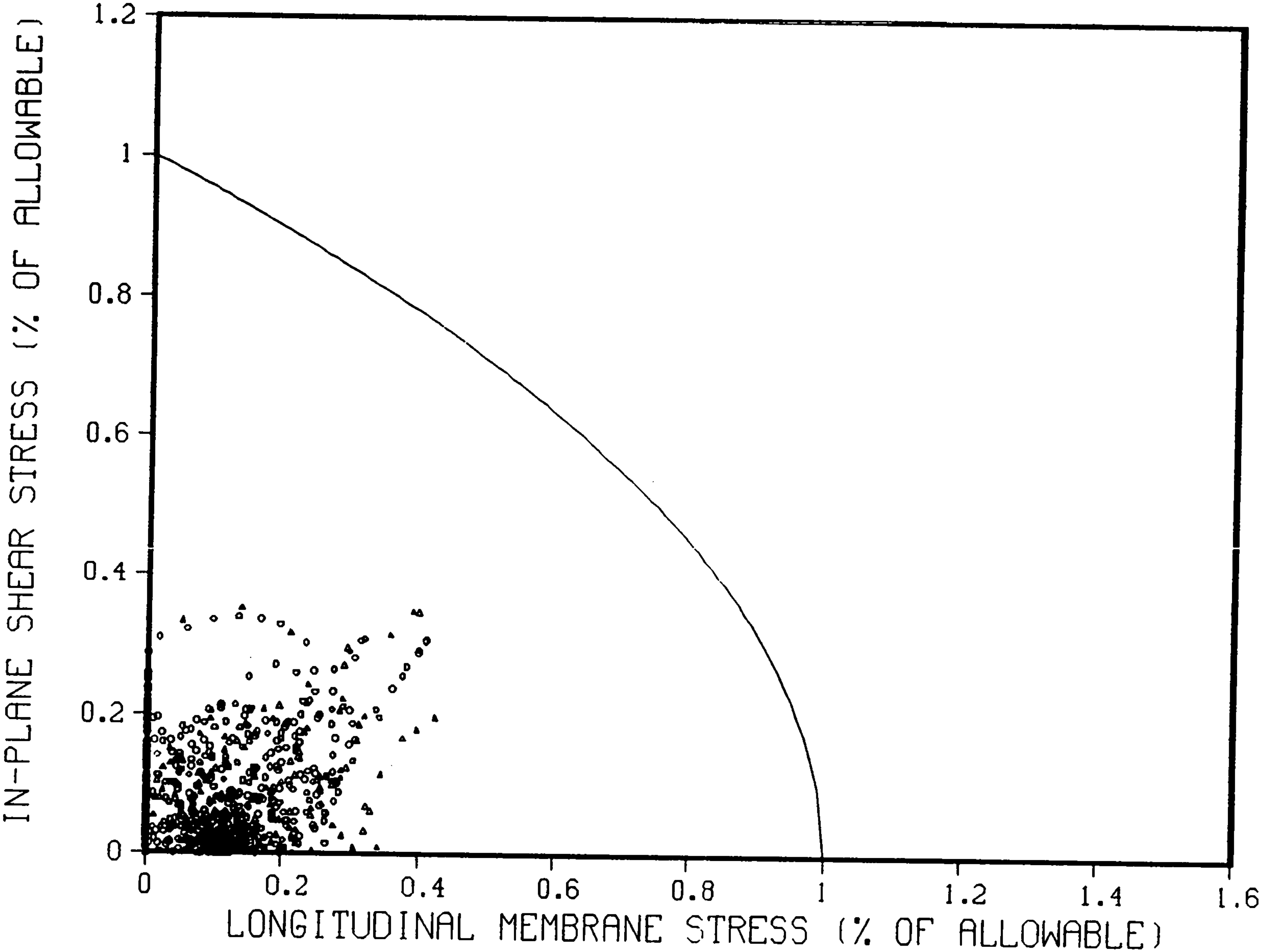

Fig. A-33. Two-dimensional interaction equation, R/t=450, x-input = Reg. Guide 1.60 Spectra, y-input = Reg. Guide 1.60 Spectra, z-input = 0.67 Reg. Guide 1.60 Spectra, 4% damping.

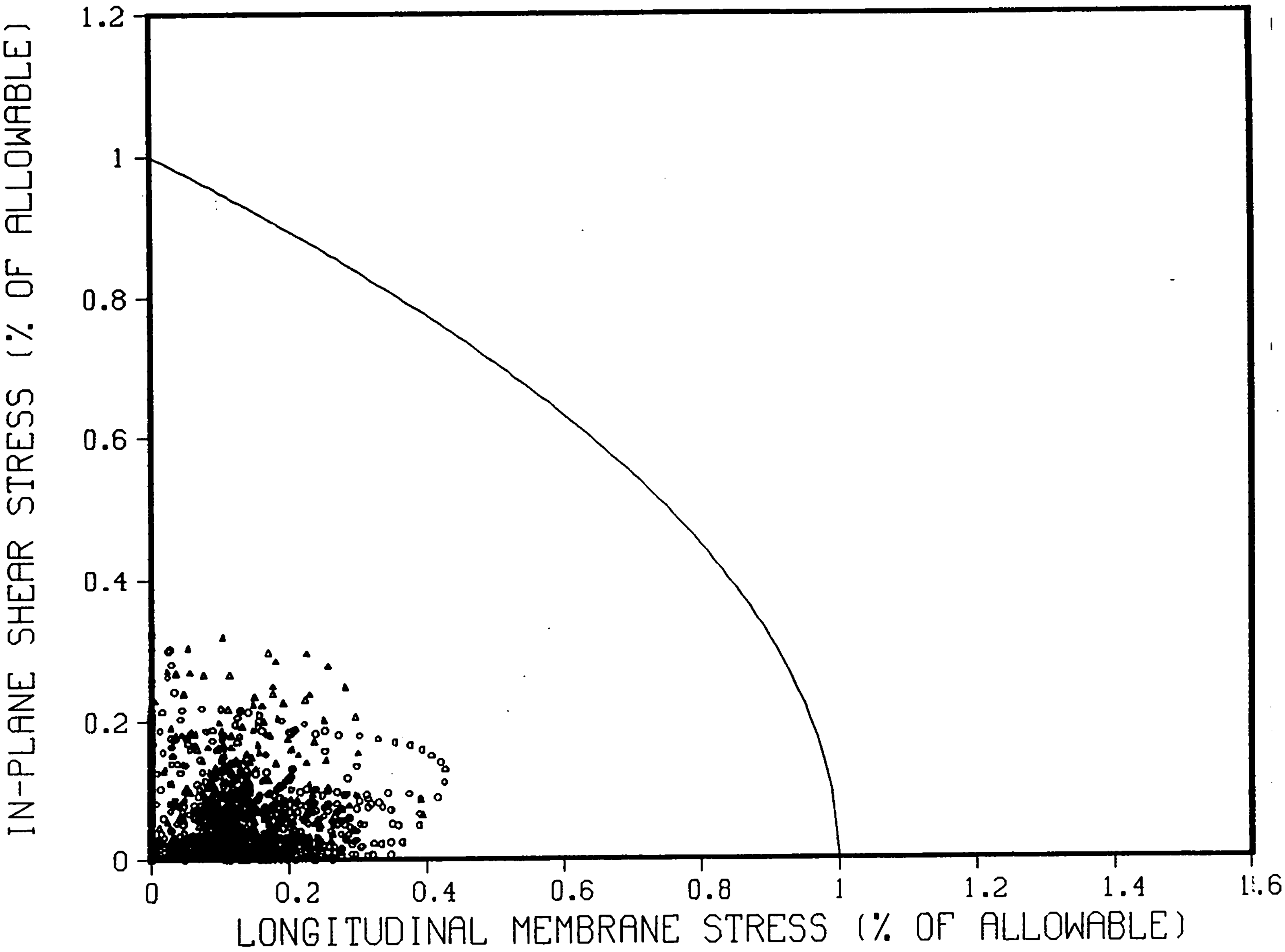

Fig. A-34. Two-dimensional interaction equation, R/t=450, x-input = Ref. 7 spectra, y-input = Ref. 7 spectra, z-input = Ref. 7 spectra, 1% damping.

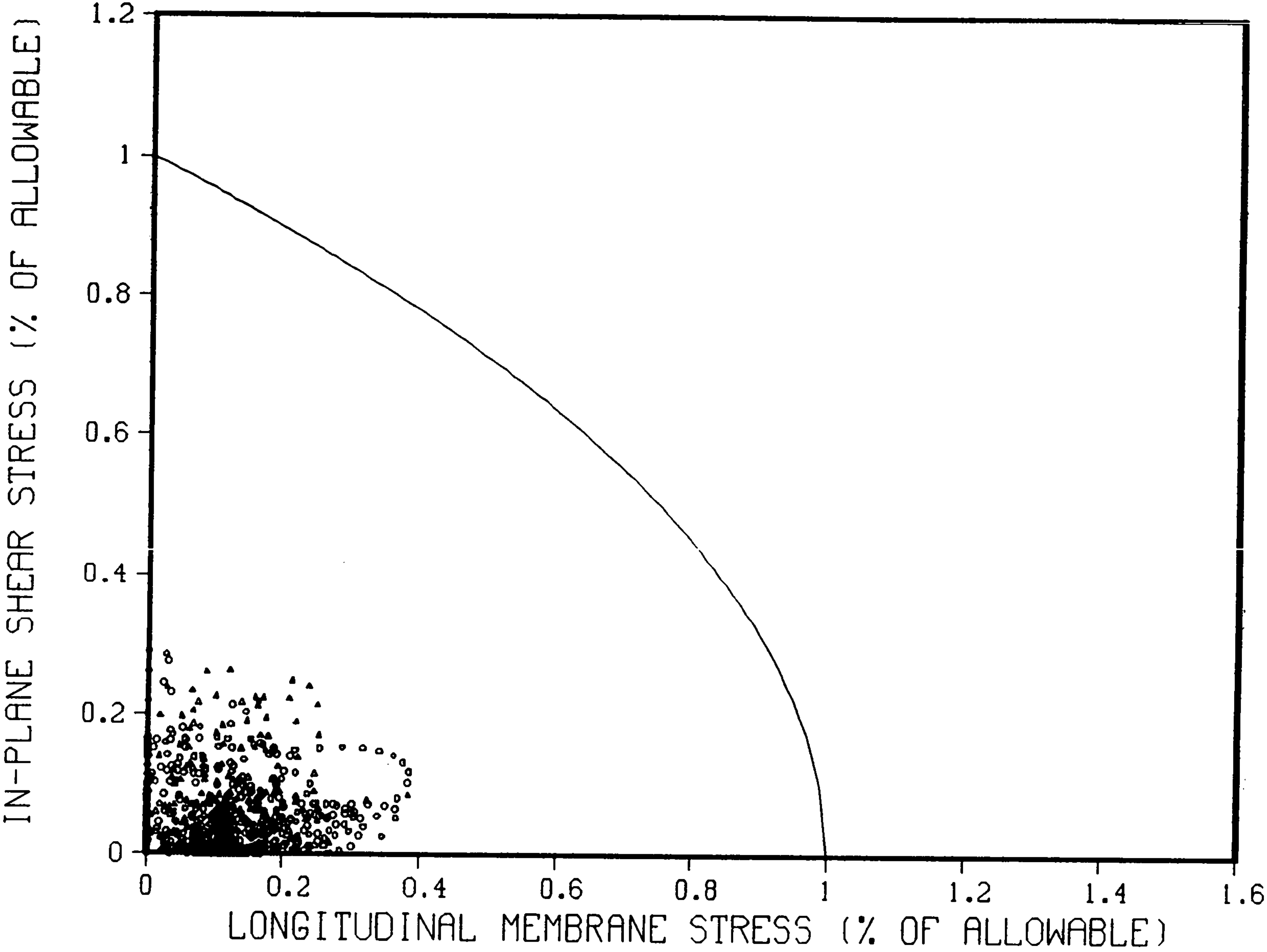

Fig. A-35. Two-dimensional interaction equation, R/t=450, x-input = Ref. 7 spectra, y-input = Ref. 7 spectra, z-input = Ref. 7 spectra, 2% damping.

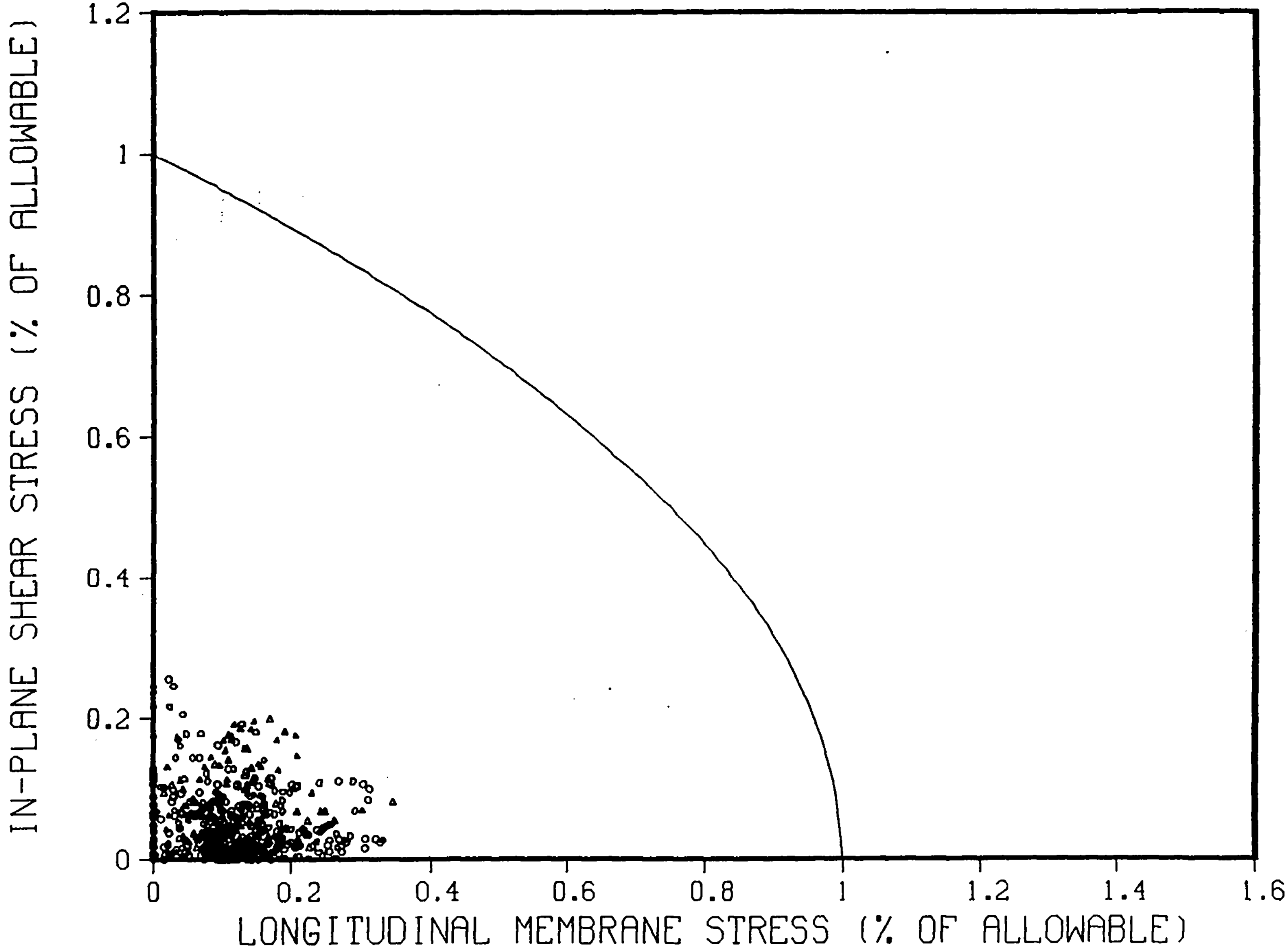

Fig. A-36. Two-dimensional interaction equation, R/t=450, x-input = Ref. 7 spectra, y-input = Ref. 7 spectra, z-input = Ref. 7 spectra, 4% damping.

APPENDIX B

THREE-DIMENSIONAL INTERACTION SURFACES

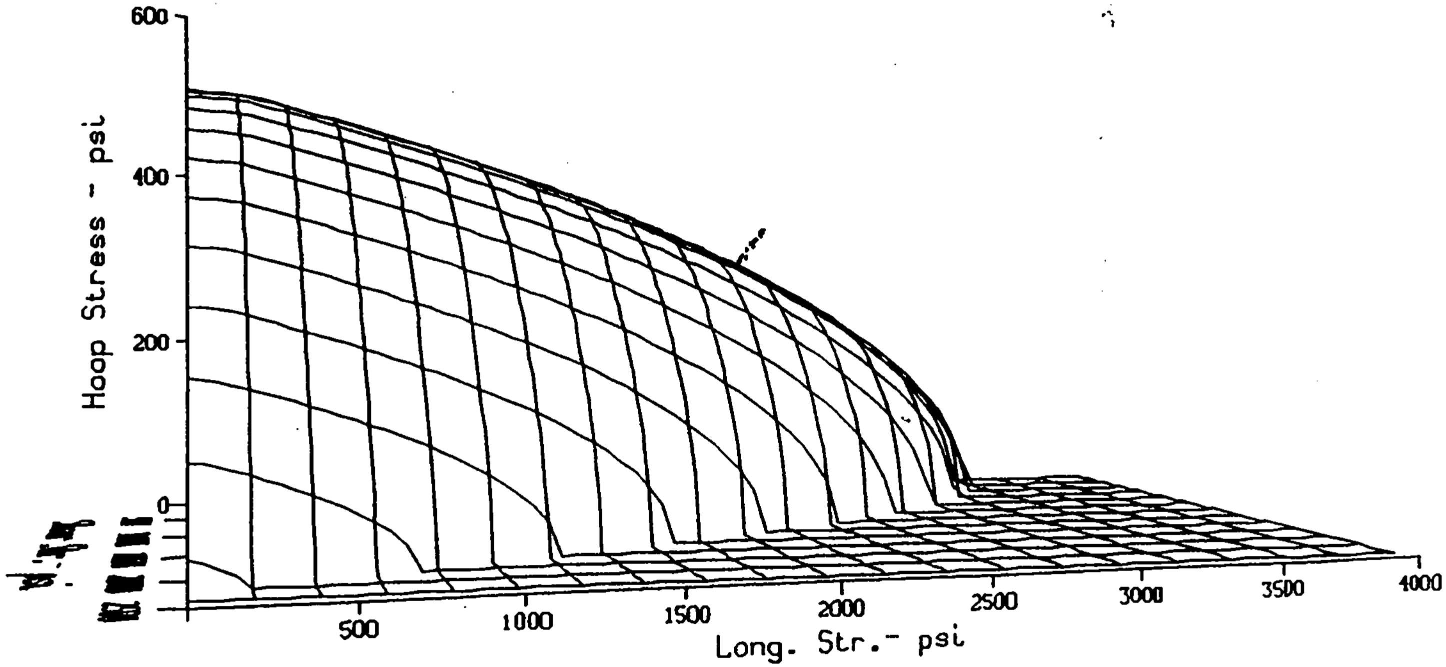

Fig. B-1. Three-dimensional interaction equation, R/t=645, x-input = El Centro, y-input = Helena, z-input = 0.67 Olympia, 1% damping.

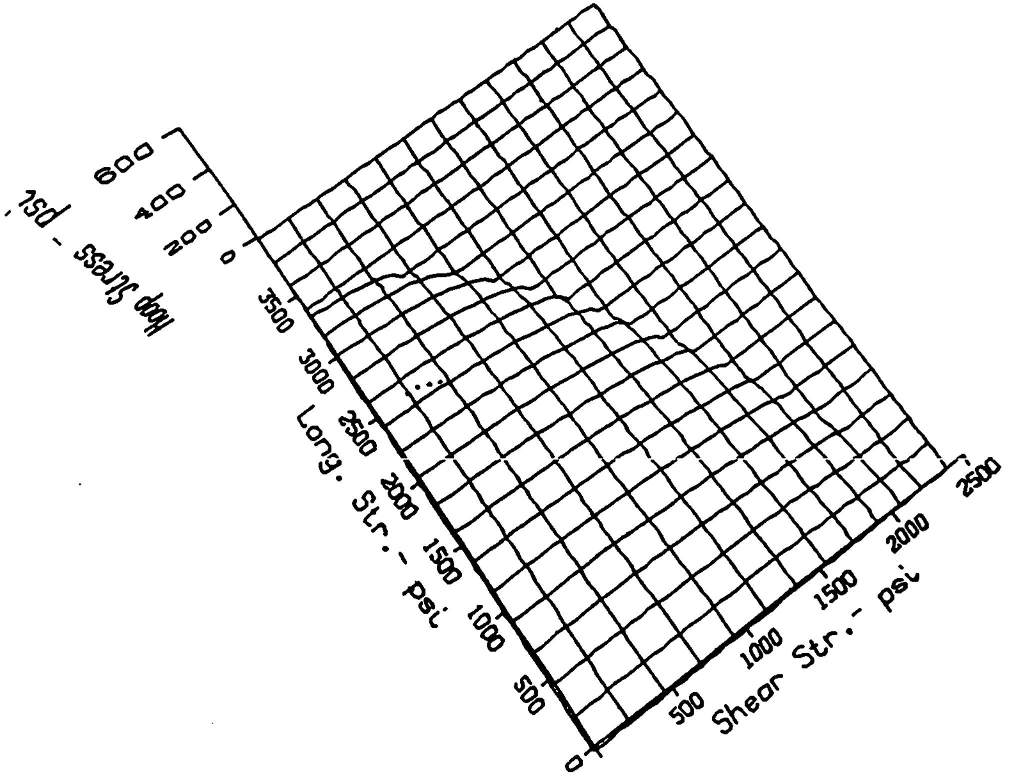

Fig. B-2. Three-dimensional interaction equation, R/t=645, x-input = El Centro, y-input = Helena, z-input = 0.67 Olympia, 2% damping.

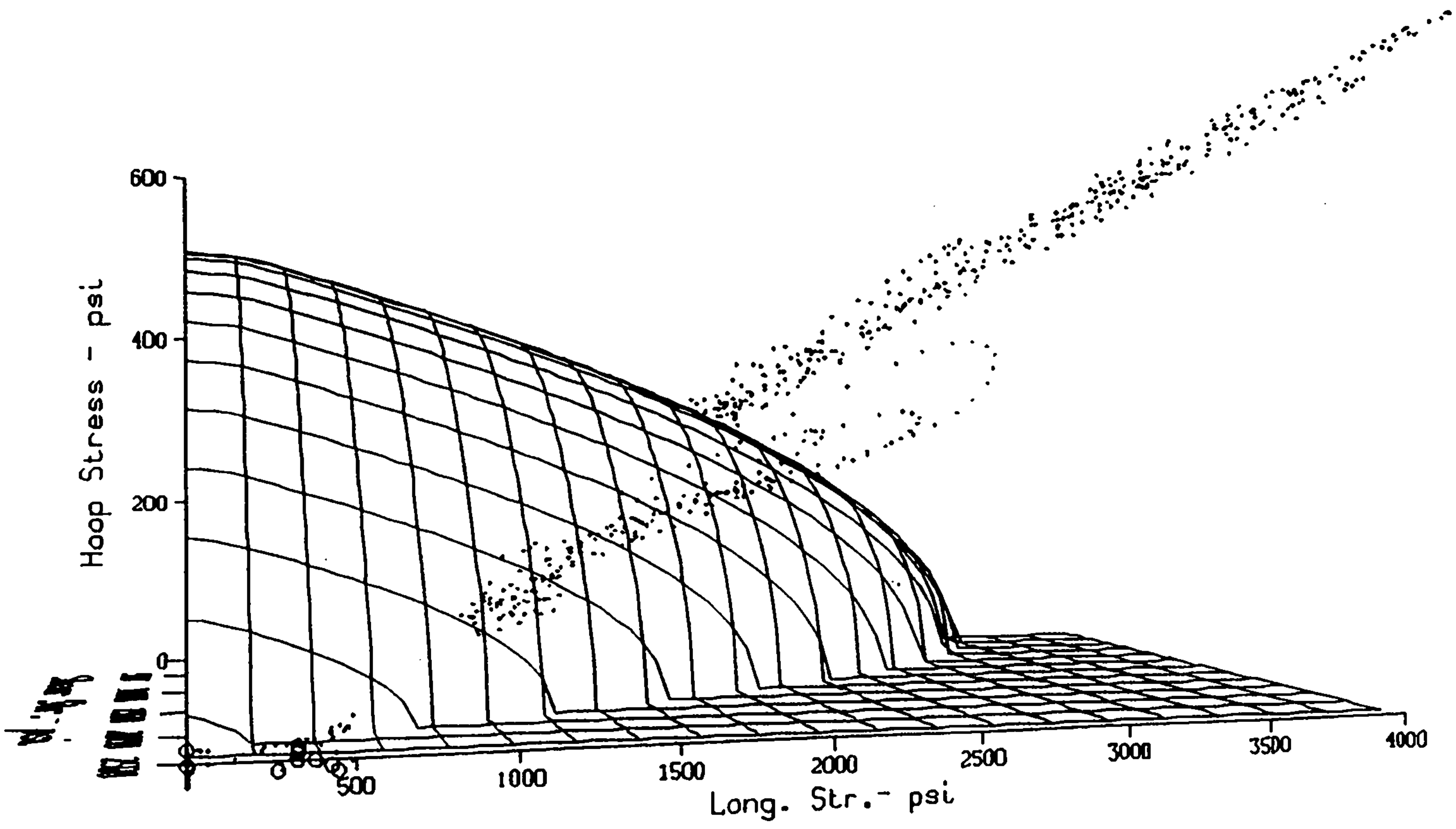

Fig. B-3. Three-dimensional interaction equation, R/t=645, x-input = Helena, y-input = Olympia, z-input = 0.67 El Centro, 1% damping.

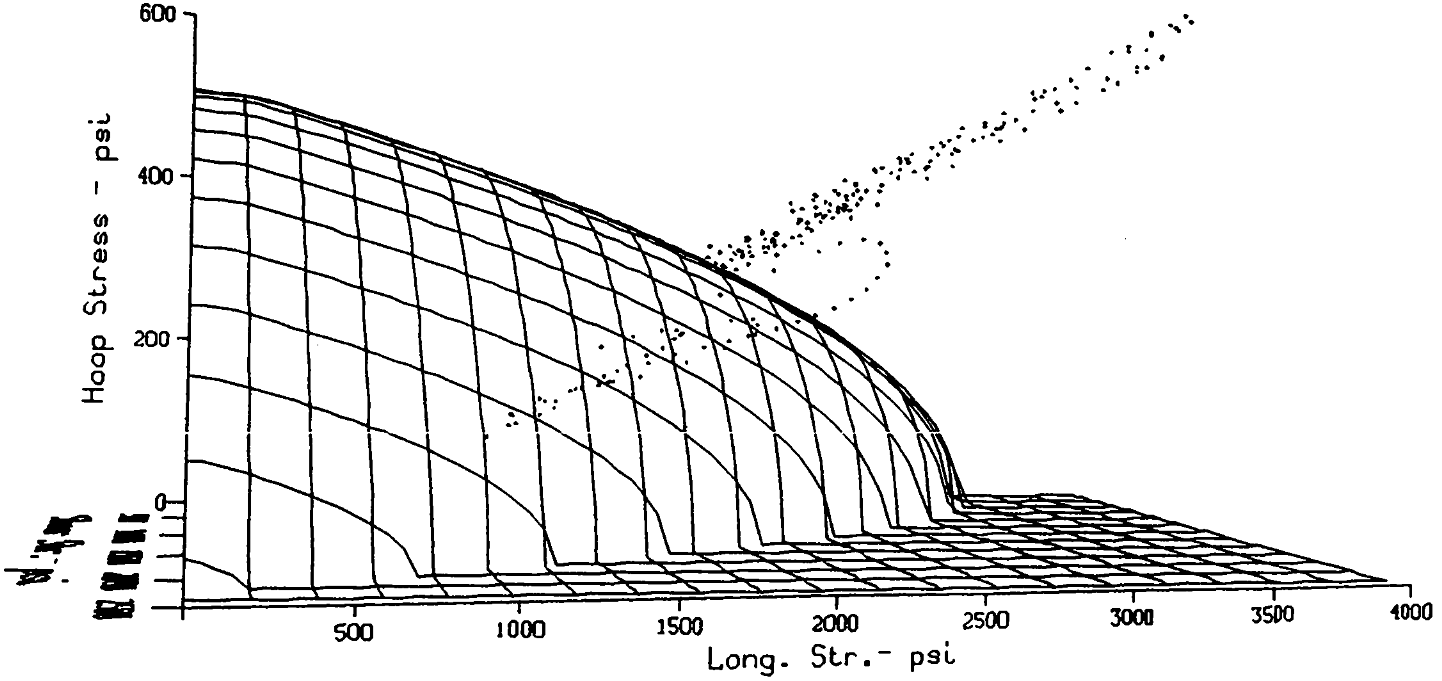

Fig. B-4. Three-dimensional interaction equation, R/t=645, x-input = Helena, y-input = Olympia, z-input = 0.67 El Centro, 2% damping.

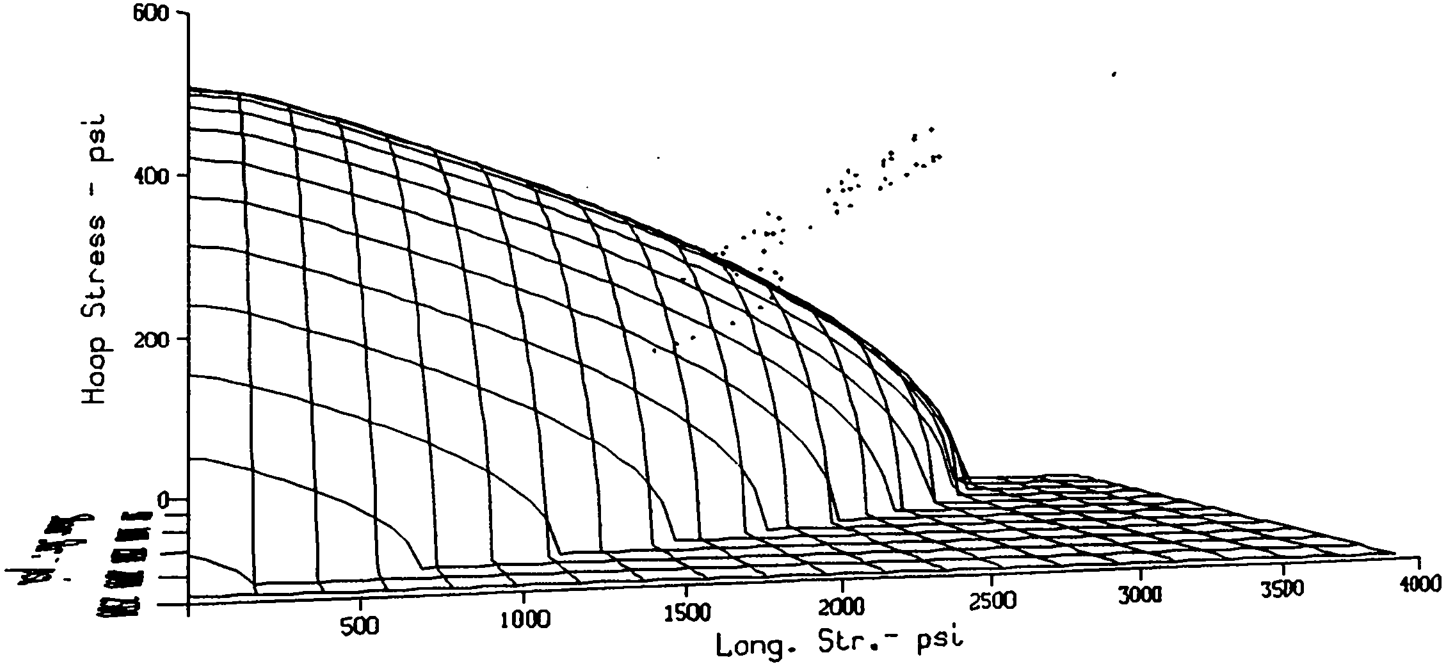

Fig. B-5. Three-dimensional interaction equation, R/t=645, x-input = Helena, y-input = Olympia, z-input = 0:67 El Centro, 4% damping.

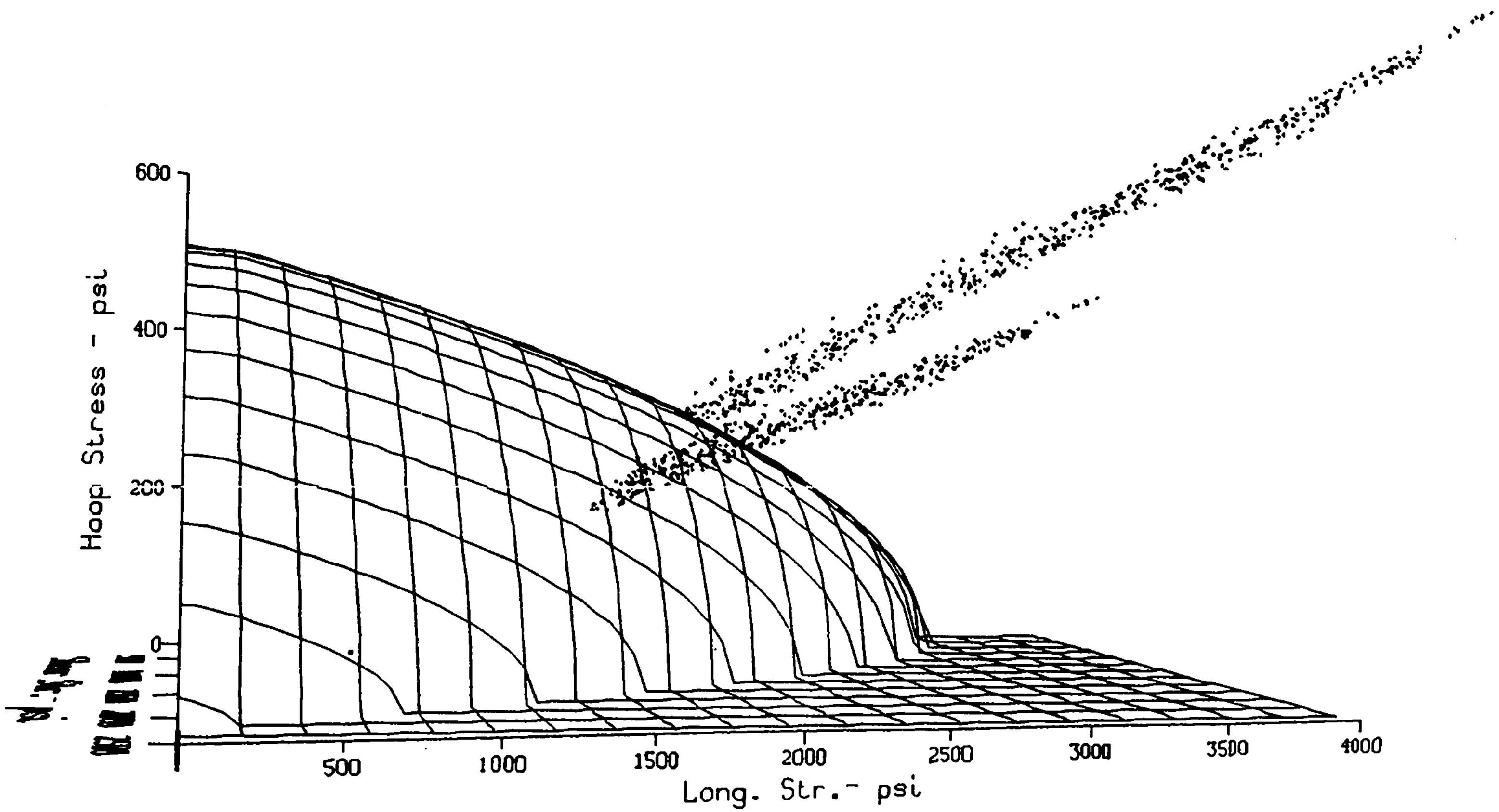

Fig. B-6. Three-dimensional interaction equation, R/t=645, x-input = 0.4 Olympia, y-input = Olympia, z-input = 0.27 Olympia, 1% damping.

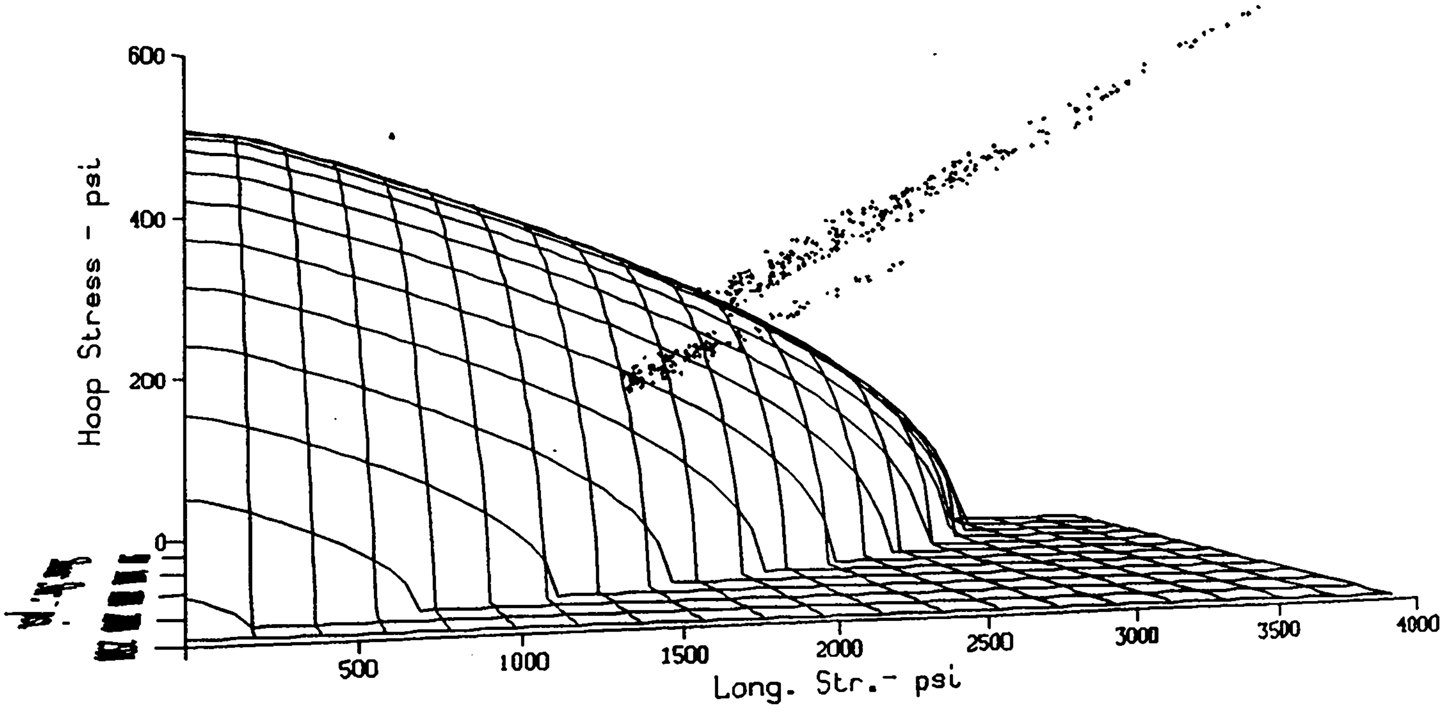

Fig. B-7. Three-dimensional interaction equation, R/t=645, x-input = 0.4 Olympia, y-input = Olympia, z-input = 0.27 Olympia, 2% damping.

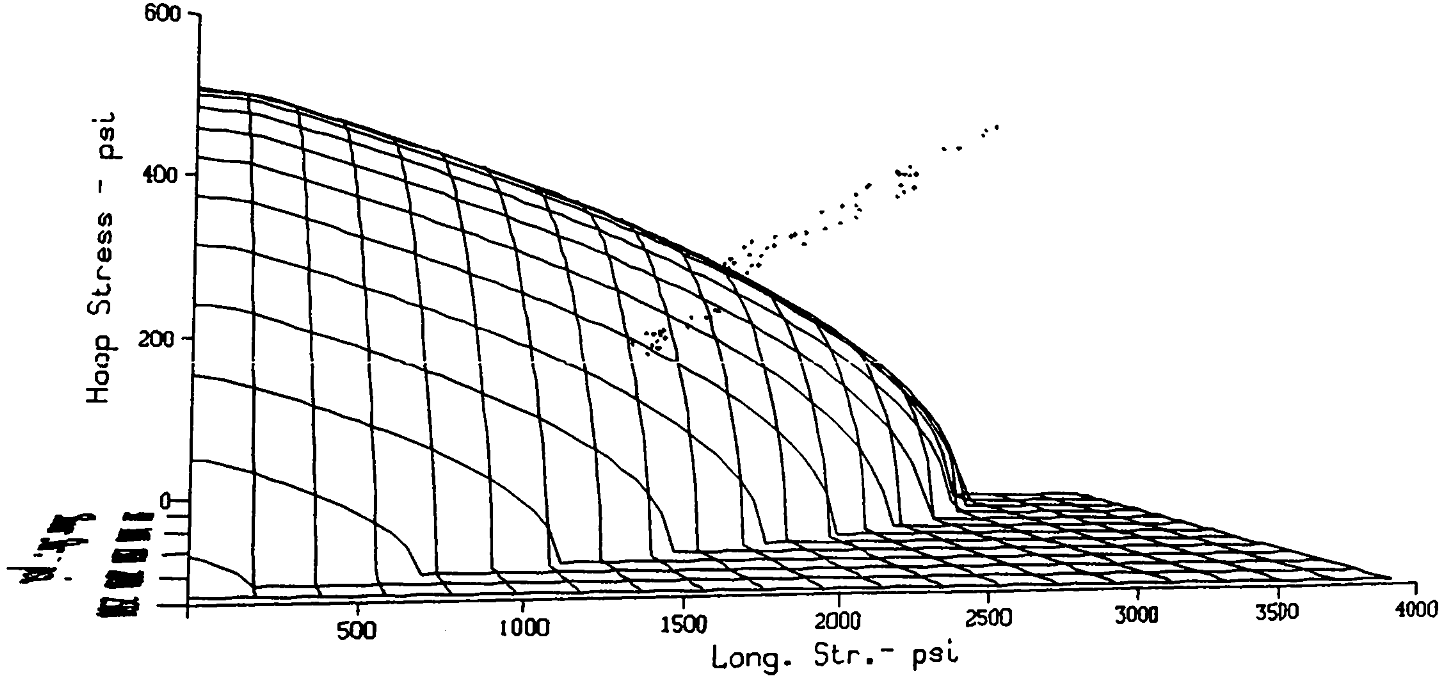

Fig. B-8. Three-dimensional interaction equation, R/t=645, x-input = 0.4 Olympia, y-input = Olympia, z-input = 0.27 Olympia, 4% damping.

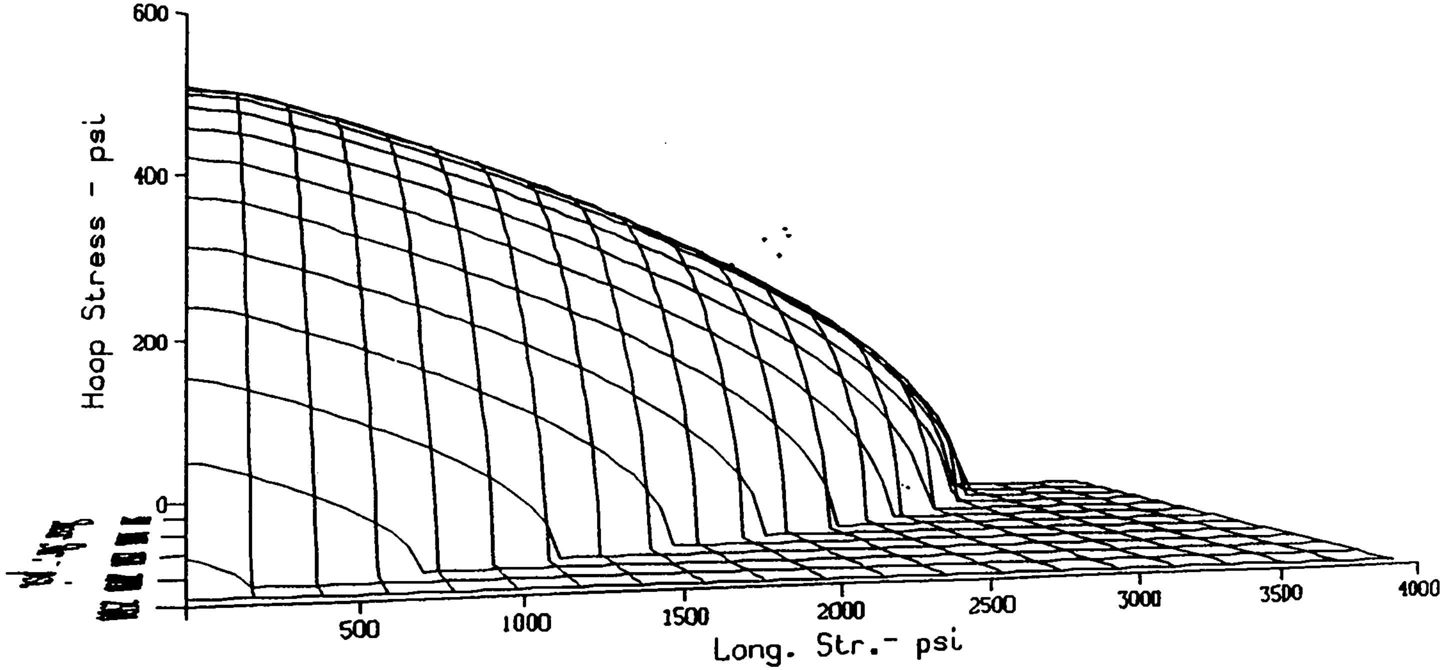

Fig. B-9. Three-dimensional interaction equation, R/t=645, x-input = 0.4 Helena, y-input = Helena, z-input = 0.27 Helena, 1% damping.

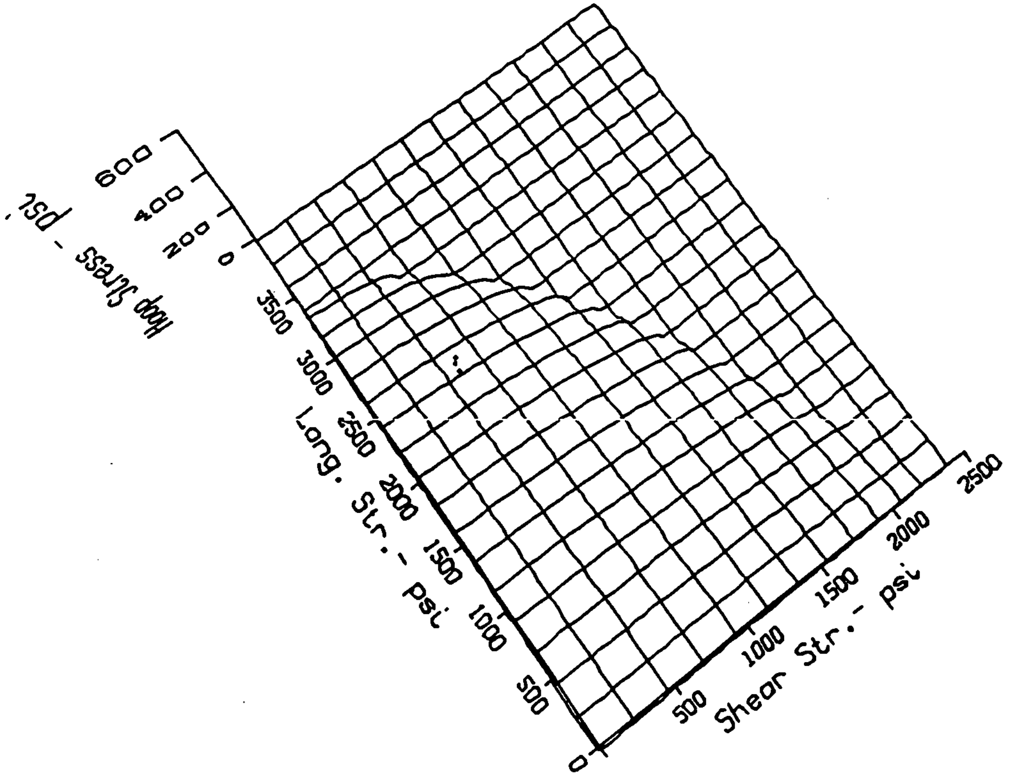

Fig. B-10. Three-dimensional interaction equation, R/t=645, x-input = 0.4 Helena, y-input = Helena, z-input = 0.27 Helena, 2% damping.

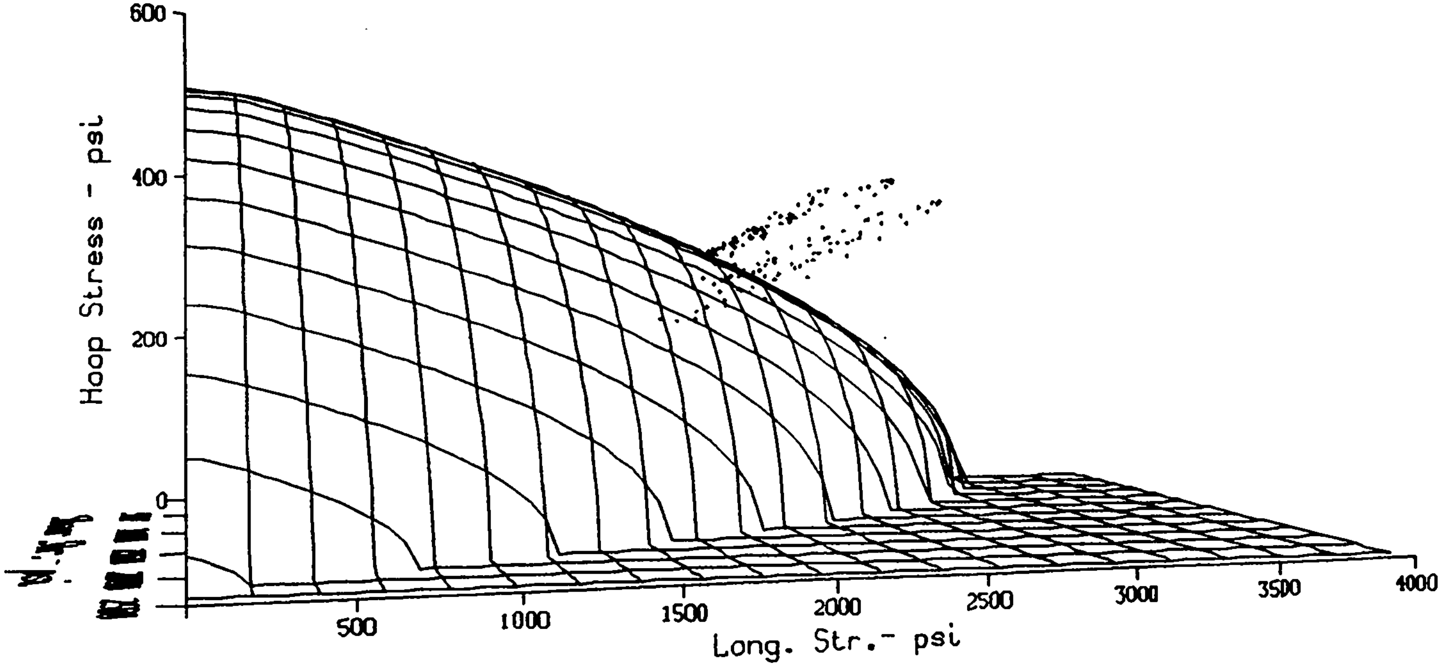

Fig. B-11. Three-dimensional interaction equation, R/t=645, x-input = Reg. Guide 1.60 Spectra, y-input = Reg. Guide 1.60 Spectra, z-input = 0.67 Reg. Guide 1.60 Spectra, 1% damping.

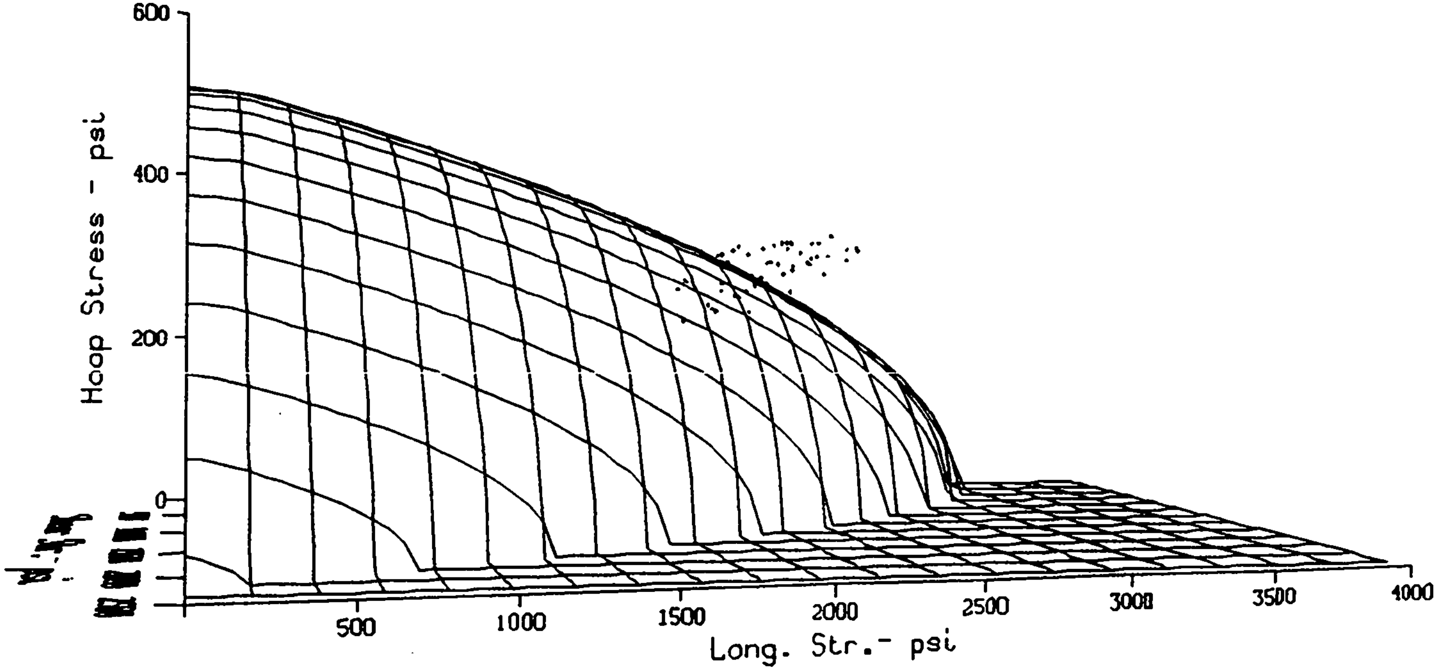

Fig. B-12. Three-dimensional interaction equation, R/t=645, x-input = Reg. Guide 1.60 Spectra, y-input = Reg. Guide 1.60 Spectra, z-input = 0.67 Reg. Guide 1.60 Spectra, 2% damping.

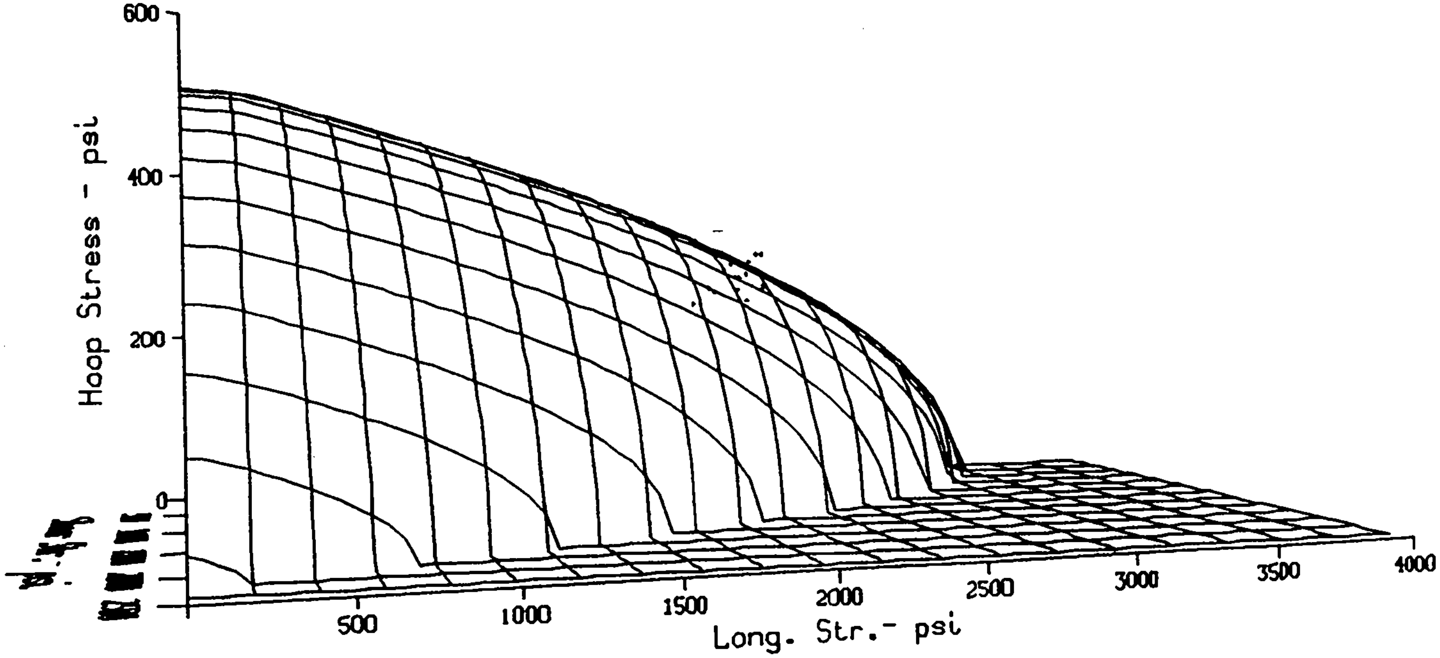

Fig. B-13. Three-dimensional interaction equation, R/t=645, x-input = Reg. Guide 1.60 Spectra, y-input = Reg. Guide 1.60 Spectra, z-input = 0.67 Reg. Guide 1.60 Spectra, 4% damping.

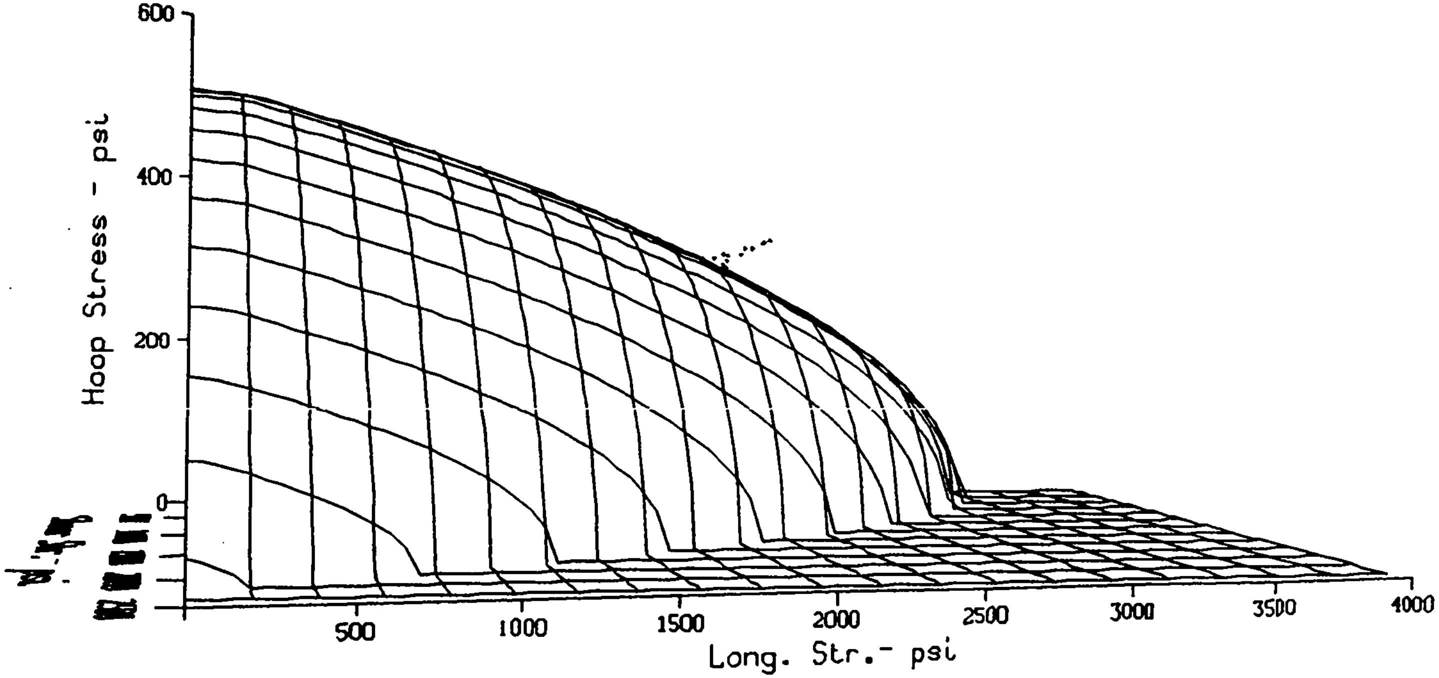

Fig. B-14. Three-dimensional interaction equation, R/t=645, x-input = Ref. 7 spectra, y-input = Ref. 7 spectra, z-input = Ref. 7 spectra, 1% damping.

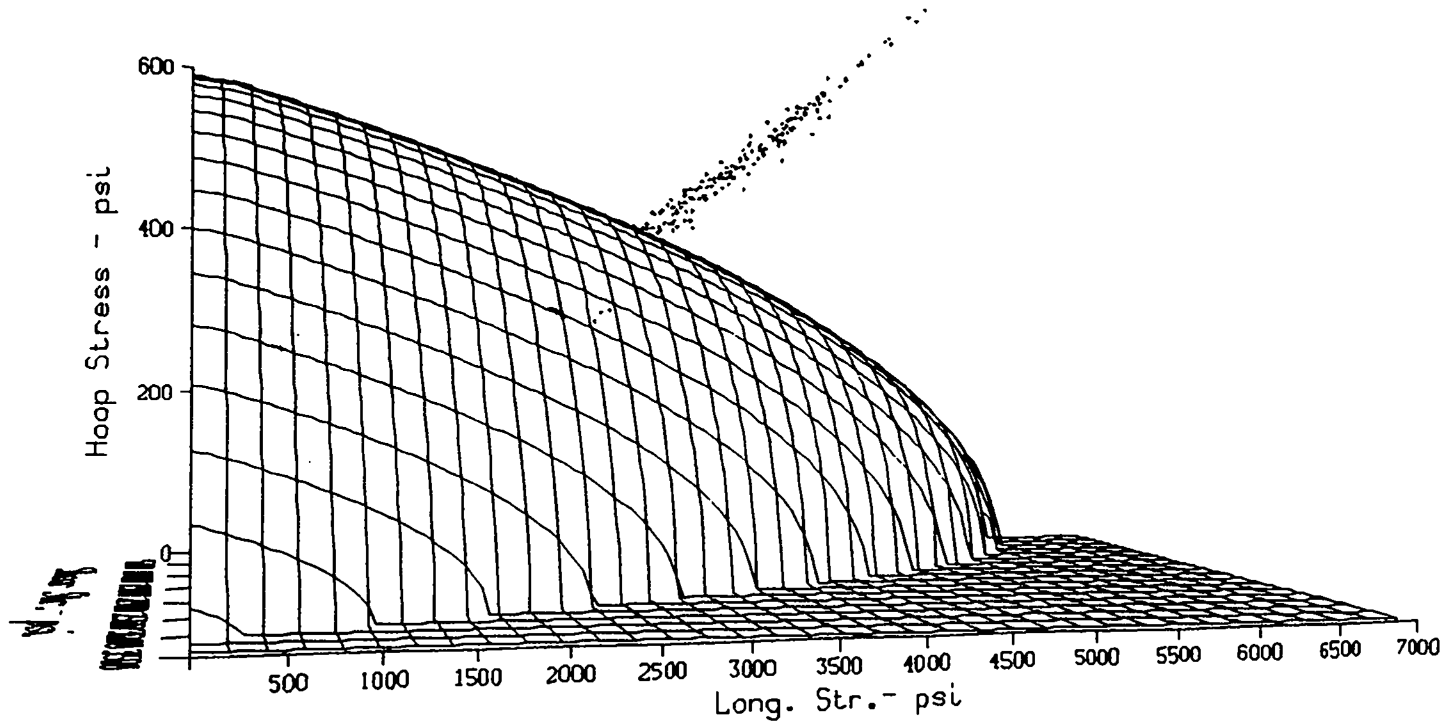

Fig. B-15. Three-dimensional interaction equation, R/t=450, x-input = El Centro, y-input = Olympia, z-input = 0.67 Helena, 1% damping.

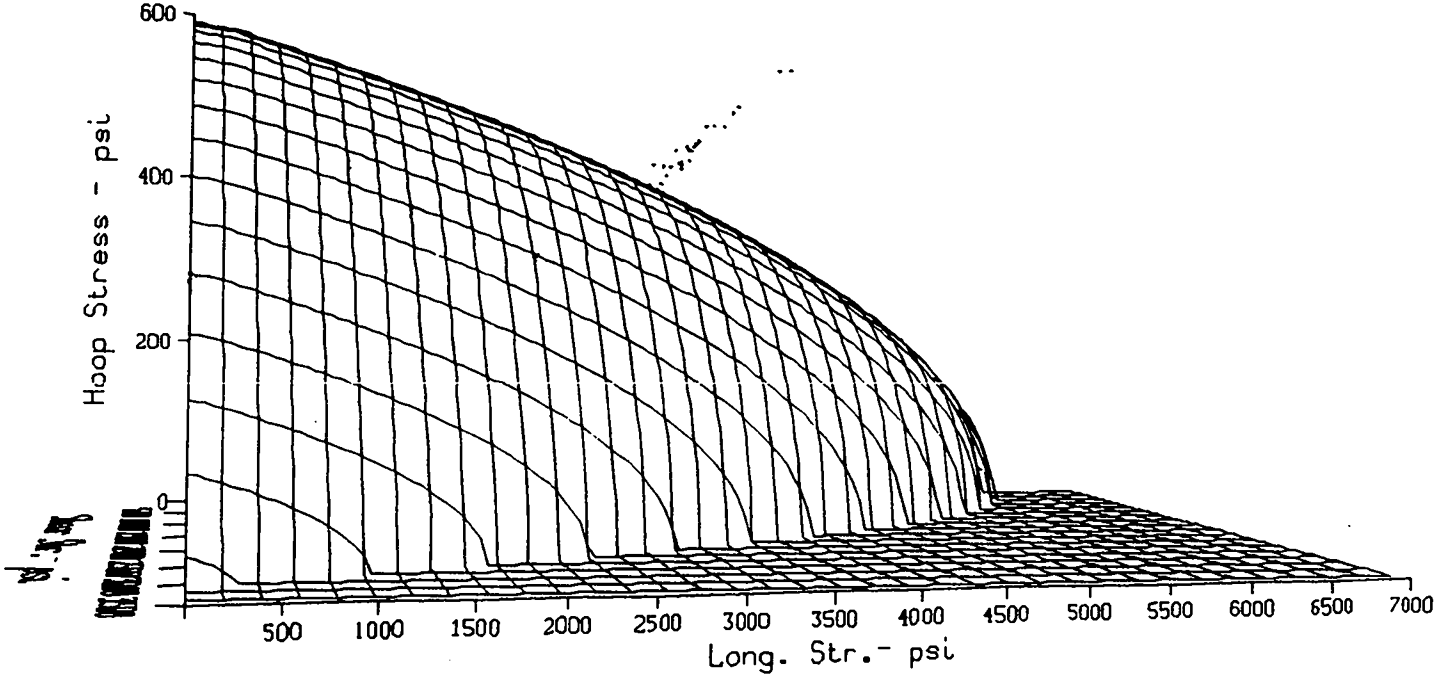

Fig. B-16. Three-dimensional interaction equation, R/t=450, x-input = El Centro, y-input = Olympia, z-input = 0.67 Helena, 2% damping.

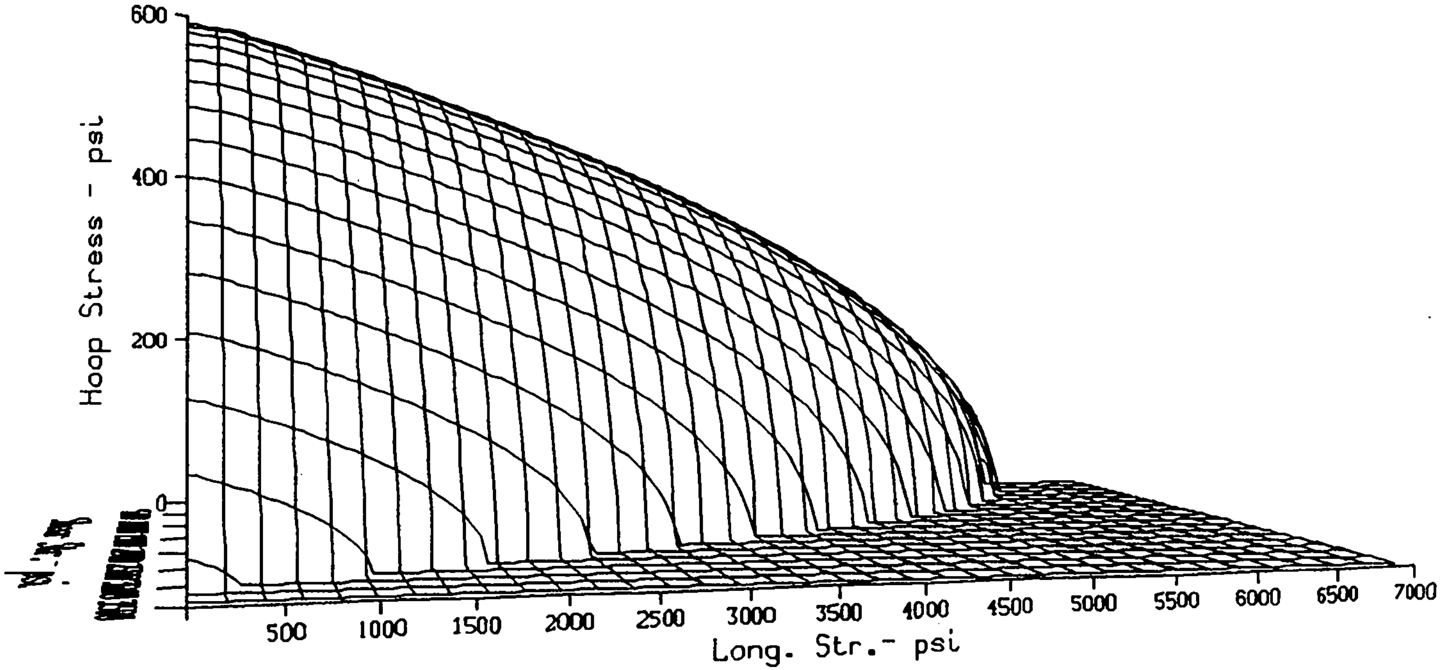

Fig. B-17. Three-dimensional interaction equation, R/t=450, x-input = El Centro, y-input = Olympia, z-input = 0.67 Helena, 4% damping.

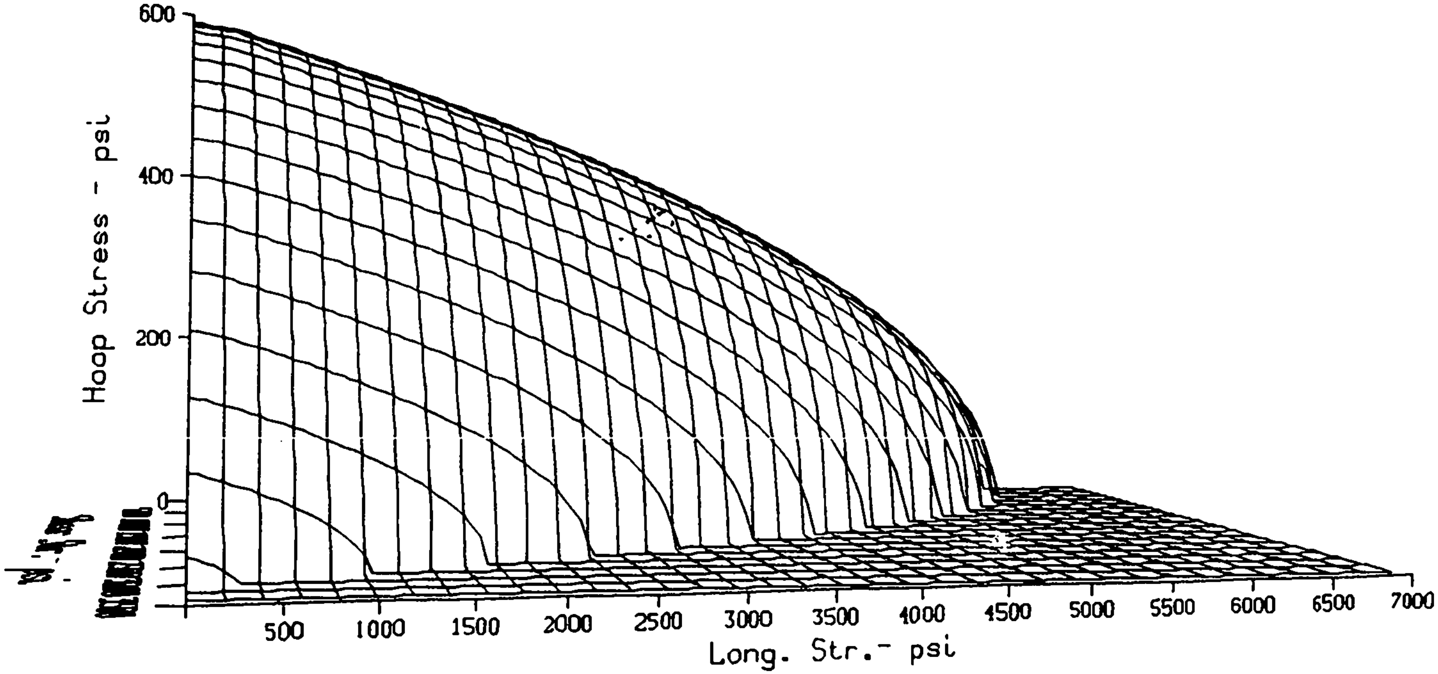

Fig. B-18. Three-dimensional interaction equation, R/t=450, x-input = Reg. Guide 1.60 Spectra, y-input = Reg. Guide 1.60 Spectra, z-input = 0.67 Reg. Guide 1.60 Spectra, 1% damping.

*U.S. Government Printing Office: 1992-673-036/67016